In situ growth of silicon and germanium nanowires in the metastable hexagonal-diamond phase

Eric Ngo

▶ **To cite this version:**

Eric Ngo. In situ growth of silicon and germanium nanowires in the metastable hexagonal-diamond phase. Materials Science [cond-mat.mtrl-sci]. Institut Polytechnique de Paris, 2021. English. NNT : 2021IPPAX020 . tel-03284317

HAL Id: tel-03284317

https://theses.hal.science/tel-03284317v1

Submitted on 12 Jul 2021

HAL is a multi-disciplinary open access archive for the deposit and dissemination of scientific research documents, whether they are published or not. The documents may come from teaching and research institutions in France or abroad, or from public or private research centers.

L'archive ouverte pluridisciplinaire **HAL**, est destinée au dépôt et à la diffusion de documents scientifiques de niveau recherche, publiés ou non, émanant des établissements d'enseignement et de recherche français ou étrangers, des laboratoires publics ou privés.

INSTITUT POLYTECHNIQUE DE PARIS

NNT : 2021IPPAX020

Thèse de doctorat

In situ growth of silicon and germanium nanowires in the metastable hexagonal-diamond phase

Thèse de doctorat de l'Institut Polytechnique de Paris
préparée à l'École polytechnique

École doctorale n°626 École Doctorale de l'Institut Polytechnique de Paris (ED IP Paris)
Spécialité de doctorat: Physique de la matière condensée

Thèse présentée et soutenue à Palaiseau, le 13/04/2021, par

M. ERIC NGO

Composition du Jury :

Frank Glas Directeur de recherche, Université Paris-Saclay, CNRS (C2N)	Président
Vladimir Dubrovskii Professeur, Université ITMO et Académie des sciences de Russie	Rapporteur
Martien den Hertog Chargée de recherche, habilitée, Institut Néel	Rapporteur
Frances Ross Professeure, Massachusetts Institute of Technology (DMSE)	Examinateur
Anna Fontcuberta i Morral Professeure, École polytechnique fédérale de Lausanne (LMSC)	Examinateur
Jean-Luc Maurice Directeur de recherche, École polytechnique (LPICM)	Directeur de thèse
Martin Foldyna Chargé de recherche, École polytechnique (LPICM)	Co-directeur de thèse
Pere Roca i Cabarrocas Directeur de recherche, École polytechnique (LPICM)	Co-directeur de thèse Invité

Acknowledgments

Prior to the start of my prospective research for a PhD, people have promised me only pain and suffering from the beginning until the very end. Well, it has turned out to be the case. Equipment that let you down at the worst possible time, failed experiments that make you wonder what you are working for and world-traveling viruses that do not even allow you to experience those letdowns for a full year, those three years could definitively be nerve-wracking. Fortunately, there are people along the path that make life as a PhD student bearable and occasionally fun and with whom to celebrate all the small victories. This section is dedicated to those who made this achievement possible and enjoyable: yes, you too were a part in this project.

Let us start with the celebration. I was immensely lucky to meet my PhD supervisors at LPICM: Jean-Luc Maurice, Martin Foldyna and Pere Roca i Cabarrocas. During those three years, you have taught me the skills to conduct a proper research project: planning, resilience, critical thinking and a sense for details which were decisive in the success of this thesis. Jean-Luc, you always pushed me to go even deeper into the results while preventing me to draw some hasty conclusions. You also taught me how to use a TEM. Martin, the unending discussions we had on the results were uplifting and an important part on me not giving up. Pere, you always found time to listen despite a tight schedule, especially when faced with even more responsibilities. Your sharp feedback, vast knowledge on nanowires and suggestions were a huge help. To the three of you, I would like to express my sincerest gratitude for the opportunity to work on this wonderful project.

My thanks go to the NanoMAX team at CIMEX which was incredibly supportive and full of ideas to bring this unique and cutting-edge instrument into life. With an ever tighter time frame to do their own experiments, they were willing to postpone their own to put mine first. This paragraph is for you: Ileana, Federico, Daniel, Jean-Christophe, Laetitia, Charles, Gilles and Laurent. I also thank Éric and Mélanie from LPMC for their work on the Jeol and the SEM. Many thanks to Mathias from LSI for introducing me to the delicate art of teaching.

Appreciations go towards the HexaNW partners: Romuald and Olivier from LSI. You provided major insights thanks to your numerical simulations that were welcome to find this oh-so elusive structure.

The colleagues at LPICM also deserve a mention. I would like to especially thank Pavel for providing a critical upgrade to the microscope and for never hesitating to get his hands dirty to help my project. I also thank the research engineers François, Cyril, Jérôme, Dmitri, Jacqueline and Jean-Charles for their continuous work on the laboratory equipment. Thanks to the IT engineer for the same reason: Éric and Frédéric. The administrative personal also deserves some recognition, so thank you to Laurence and Fabienne. Then there are all these amazing persons with whom I had the pleasure of sharing an office with or discuss together with,

scientifically or not. Andjelika, Romain, Lukas, Maria, Mutaz, Lucas, Marta, Chloé and Letian, you will be remembered. Special thanks to Weixi as her contributions to this thesis cannot be overstated. I would say that this was a nice display of teamwork!

Many thanks to my friends who accompanied me during all these years at university and beyond. I cannot count the number of laugh and backstabbing that we exchanged between us during board game sessions, the long discussions and stories, the emotional support that we shared during those tough times as we all went on our ways. To you, Luis, Léon, Gabriel, Lucie, Hugo, Floriant, David, Maxime and Yanis, I will say this: you guys are legends!

Be it parents, brother or cousins, you were never short on good words and encouragements. That gave me the extra drive to pursue this endeavor until the very end. For that, you have my thanks. I hope that this fills you with as much joy and pride as it did for me.

Contents

Introduction

Research in the field of materials has never been so fertile as over the last century. In the pursuit of improved performance in regard of mechanical, electrical and optical properties, new materials were discovered and already known ones improved. From new and old materials, new physics were discovered such as superconductivity [1], leading to breakthroughs in the field of particle physics, medical diagnosis and train transportation. Superconducting Nb_3Sn magnets are instrumental for the production of high intensity magnetic fields, permitting the bending of the trajectories of charged particles traveling at a velocity close to the speed of light in particle accelerators. Powerful magnetic fields, produced by rare-earth compound magnets, are the center piece behind magnetic resonance imaging (MRI) scanners. Similar magnets are used in special train tracks allowing for a friction-free means of transportation.

New materials are also the focal point of the upcoming energy revolution. With the climate change generated by excessive CO_2 emissions, energy production is expected to abandon fossil fuels for renewable resources eventually. In particular, the development of solar energy allows for inexpensive, carbon-free energy production. A cumulative photovoltaic energy production reaching the terawatt is planned for 2023 [2] with the help of the increased number of available technologies and their continuous improvement [3]. A particularly hot field concerns the elaboration of solar cells using organic/inorganic hybrid compounds such as the $MAPbI_3$ perovskite [4].

Several strategies exist for devising new materials and modifying their properties. In the case of semiconductors for light-emitting diodes, a first strategy has been to explore the chemical substitution of column-III and V elements. This strategy was successful for the elaboration of light emitting devices for all wavelengths in the visible spectrum. Originally, the first compound used for near-infrared light was GaAs [5]. Then, different wavelengths from the visible spectrum followed, AlGaAs/GaAs quantum well [6] for red, AlGaP for green and finally GaN [7] for blue. The latter color was particularly difficult to obtain with a good efficiency. As a result, its invention by the team of Nakamura was awarded the Physics Nobel Prize in 2014 [8].

Another strategy is to reduce the materials dimensionality. Unique and new properties are known to rise from this approach because of quantum confinement effects [9]. From 3D crystals, researchers move to 2D semiconducting films and finally 2D materials such as MoS_2 or graphene. Graphene [10], for instance, is known to exhibit peculiar electron transport properties such as a high electron-hole mobility. Its discovery by Geim and Novoselov was also awarded with a Physics Nobel Prize in 2010 [11]. By further reducing the dimensionality, we can go from 2D materials to 1D materials such as nanotubes and nanowires.

Finally, one last possible approach is to modify the spatial arrangements of atoms in the material. Tin, for example, is known to undergo a phase transition at 13.2 °C between α-Sn and β-Sn, two solid forms of tin but with a different crystal structure, cubic diamond for the former and body-centered tetragonal for the latter. α-Sn is brittle and nonmetallic while β-Sn is ductile and conductive.

Of course, these three approaches can be combined. In this thesis, dimension reduction and change in the crystalline order are put together in order to elaborate silicon and germanium one-dimensional nanowires with a "non-standard" hexagonal diamond crystalline structure, which would have remarkable optical properties (see Section 1.4.2). While this structure is no longer a novelty, it had not been obtained with standard growth techniques until recent years, when J. Tang, a PhD student in the Laboratory of Thin Film Physics and Interfaces (LPICM), obtained such nanowires by chance. The aim of this thesis is "to replace chance by understanding" and explore the growth conditions that deliver this structure.

Chapter 1 of this thesis introduces silicon and germanium nanowires, as well as the hexagonal-diamond crystalline structure. The motivations for choosing silicon and germanium are stated. Some notions are given about nanowires, notably what are their unique properties and what are the techniques used to grow them. Following this, a brief reminder about crystals is given, with the aim of better introducing the hexagonal diamond structure, and what separates it from the standard cubic diamond structure. The state of the art on their synthesis is then detailed.

Chapter 2 describes the strategy employed in the present work to obtain these hexagonal diamond nanowires. For that purpose, several experimental apparatuses were used. They will be introduced. In particular, we will present NanoMAX, an *in situ* transmission electron microscope where nanowire growth will be carried out, and we will detail the unique challenges that it poses, notably in terms of sample preparation and irradiation damage. Some elements on how to identify the hexagonal diamond structure through numerical simulations are also given.

Chapter 3 reports all the experimental results gathered from the growth of germanium nanowires using Au nanoparticles. Two types of germanium precursors were used, a gas and a solid source that led to structural differences in the nanowires. We will compare and explain the structural differences that rise from the two sources. Several aspects of the growth are also discussed here. Notably, the important role of hydrogen is investigated.

Chapter 4 will demonstrate the relevance of the experimental results obtained in the *in situ* microscope by confronting them with those produced in standard chemical vapor deposition reactors. We chose the growth of silicon nanowires catalyzed by Au particles as the subject of comparison.

Chapter 5 is dedicated to the plasma-assisted growth of silicon nanowires catalyzed by complex particles composed of different amounts of copper and tin. Depending on the copper/tin ratio, nanowire characteristics and growth dynamics vary greatly. *In situ* data analysis provides key insights that disclose an original mechanism of growth with dual-phased, liquid-solid catalysts.

In Chapter 6, we present and discuss the results obtained on the hexagonal diamond structure. In particular, the growth parameters that promote this structure in silicon nanowires are examined. Using all the results established in previous chapters, we propose a model that could explain how this unique structure forms.

Finally, the conclusion summarizes the work and gives some perspectives for further studies.

CHAPTER 1

Polytypism in column-IV semiconductor nanowires

In this introductory chapter, basic properties and growth principles about silicon and germanium nanowires (Si and Ge NWs) are introduced. In particular, we highlight their advantages as building blocks for devices and the methods used to grow them. Following this, the notion of crystal allotropes is explained as a way to define the 2H polytype in Si and GeNWs, which is the main focus of this thesis. Attention is then shifted towards the motivations for their study. The state of the art on their synthesis will then conclude this chapter.

1.1 Silicon and germanium nanowires for devices

1.1.1 The use of Si and Ge in modern day electronics

Silicon, a group-IV element, is omnipresent in microelectronics and, therefore, in today's society. It is, indeed, the basic material in metal-oxide-semiconductor field effect transistors (MOSFET), a critical component in computers, smartphones and many other electronic devices. Several reasons explain its widespread use. At start of microelectronics, the fact that it possesses a stable and insulating oxide, SiO_2 that can be formed by oxidation of bulk Si, played a role in its leading position. Now that gate oxides are no longer made of SiO_2, other advantages keep it in demand. Indeed, Si is also less expensive and readily available in comparison to other semiconductors. It is the second most abundant element in Earth's crust after oxygen [12] (Figure 1.1). Thus, there is no risk of depletion unlike other semiconductor compounds. Finally, it is non-toxic as it is present naturally in various living organisms. Pure Si in the form of a wafer is a common substrate used in micro-electronics and the absorbing material in c-Si solar cells. In addition, the chemical element Si is widespread in construction materials, such as glass.

One major characteristic of a semiconductor is its band gap. Band theory states that electrons populate a continuum of electronic states, called bands, defined by their energies and wavevectors. Some bands are filled and others are not. In semiconductors, the valence band defines the band with the highest energy which is filled with electrons. The conduction band is the band just above the valence band in terms of energy, and it is empty of electrons when in a

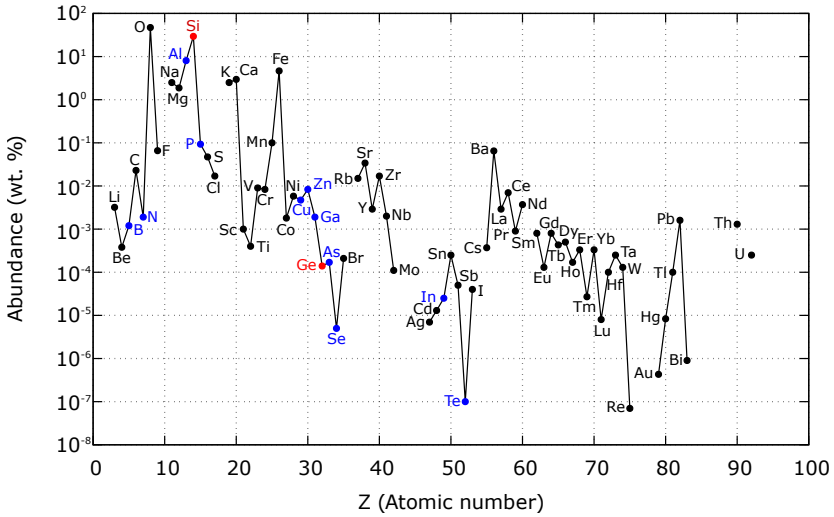

FIGURE 1.1: Abundance of various elements of the periodic table in Earth's crust in weight percentage. Si and Ge are indicated in red. Other elements that are relevant for the semiconductors industry are marked in blue. Data from [12].

ground state at 0 K. Energies between the valence band and the conduction band are forbidden. The energy difference between those two bands is the so-called band gap of the material, and is usually given in eV. In other words, it is the energy required for an electron in the valence band to be promoted to the conduction band. This physical quantity is of extreme importance since it determines the energy threshold where the material starts absorbing or emitting photons in statistically significant amounts. Crystalline Si with cubic structure, for instance, has a band gap of 1.12 eV, so that only light with equal or higher energy can be absorbed. A characteristic of a band gap is its direct or indirect nature. As stated above, an electronic state is defined by its energy and wavevector. Therefore, the energy maximum of the valence band does not always coincide with the energy minimum of the conduction band in terms of wavevectors. Because of the law of conservation of momentum, if an electron is to be promoted to the conduction band and there is no coincidence, it also needs to acquire momentum in addition to energy. In general, this momentum is provided by vibrations in the material, modeled by phonons. In such situation, the band gap is qualified as indirect. If the energy maximum of the valence band and the energy minimum of the conduction band are positioned at the same wavevector, the band gap is direct. The distinction between the two types of band gaps is important due to the lower probability for an electron to be promoted in the case of an indirect band gap. Even if radiations of sufficient energy interact with an indirect band gap material, the promotion of an electron from the valence band to the conduction band must be assisted by a phonon. The macroscopic consequence of an indirect band gap is less efficient light emission or absorption in the spectral region close to the bandgap when compared to materials with a direct bandgap.

Due to its indirect band gap, Si is neither a good light emitter nor a good absorber of photons in the visible spectrum. This is why Si is rarely used in light emitting devices, where other - direct band gap - semiconductor compounds are preferred. In solar cells, Si is chosen for its combination of low cost and performance. Although it is not a good absorber, strategies like the use of back reflector or surface modulation help alleviate this problem in exchange of more process steps.

Germanium is also a column-IV semiconductor and also has an indirect band gap, worth

0.67 eV this time. It still has several applications thanks to improved properties compared to Si, specifically its higher charge carrier mobility. In particular, it has one of the highest hole mobility values of all semiconductor materials [13]. It is thus suitable for high-frequency applications. Due to its high hole mobility, it was actually the main semiconductor in bipolar-transistor based early stages of microelectronics, before Si MOSFET technology took over. What ultimately prevented its dominance is the lack of a stable oxide. GeO_2 is soluble in water and often amorphous. Contrary to SiO_2, GeO_2 cannot simply be grown thermally from Si. Ge is also used in the bottom cell of high-performance multi-junction solar cells because of its low bandgap.

Ge research has recently regained interest. Its better performance became more appealing due to the physical limits reached by the scaling down of Si devices. Indeed, further miniaturization poses problem due to quantum effects. For instance, in MOSFETs, a leakage current can occur due to quantum tunneling through ultrathin gate oxides, rendering the transistor useless. The improvement of lithography techniques also comes with increased financial cost and complexity. The complete replacement of Si by Ge is unlikely however. This is due to the lack of complementary metal oxide semiconductor (CMOS) compatible processes with Ge, which are standard techniques used in the industry for Si to bring the cost down. One of the main points of CMOS-compatible processes is the use of Si substrate. For devices using Ge layers, using a Si substrate is especially problematic as there exists a lattice misfit between Si and Ge of about 4 %. Thus, strain will appear and will need to be relaxed in some ways. Interface between Si and Ge will be therefore filled with dislocations and other defects, reducing the charge carrier mobility, one of the selling points of Ge, and degrading the resulting device performances.

Mixing Si and Ge forms the Si_xGe_{1-x} alloy. It combines the high performance of Ge and easier integration on a Si substrate compared to pure Ge. A successful utilization of this alloy is the heterojunction bipolar transistor (HBT), capable of handling high frequency operations and consuming a small amount of power. SiGe alloys are also used to create complex heterojunctions. Indeed, by modifying the ratio of Si/Ge, electronic and mechanical properties are altered. This opens up the possibility of band and strain engineering, techniques that prove useful in present day devices [14]. Strain engineering could also bring the use Si_xGe_{1-x} as a buffer layer between Si and Ge [15].

1.1.2 "One-dimensional" object advantages

The use of Si as a substrate limits the number of usable compounds for the elaboration of devices, to those which have a lattice parameter close to that of Si. One way to circumvent this issue is to use nanowires: objects with high aspect ratio where their lengths is far larger than their width. Depending on their purpose, their length can range from tens of nanometers up to several micrometers, while their width, or diameter, is generally below the micrometer scale. An assembly of Si nanowires (SiNWs) is shown in Figure 1.2. One of the prime interests of nanowires is their ability to grow on a wide variety of substrates, while retaining good crystallinity and little structural defects. This is due to nanowires being able to easily accommodate stress. Such property allows for the growth of SiNWs on flexible substrate [16]. The used substrates should be able to tolerate the growth process conditions. Most processes involve high temperatures so the selected substrates must be thermally stable. Recent advances in growth techniques are pushing for low temperature processes though, which allowed growth on plastic substrates [17].

Another strong property concerning nanowires is their high surface to volume ratio. This is

a) b)

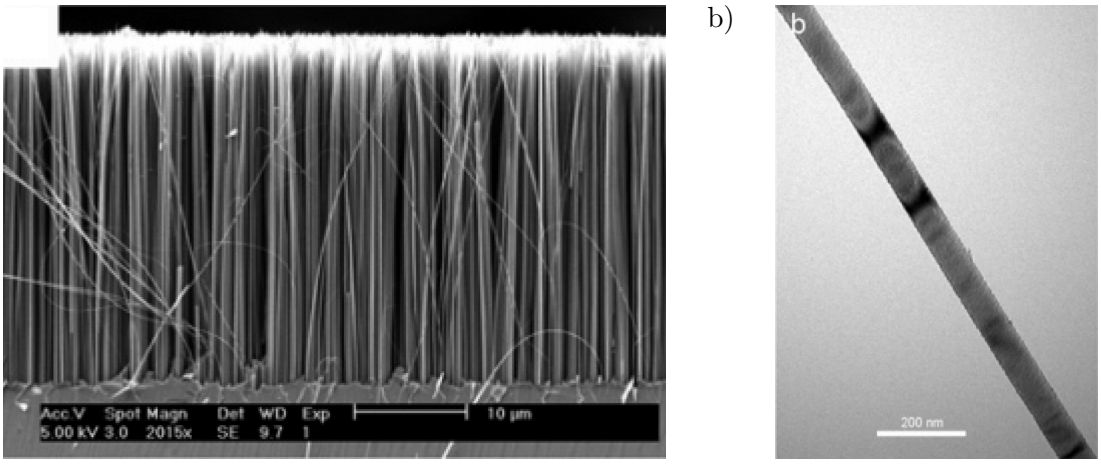

FIGURE 1.2: a) Scanning electron microscopy image of an ordered array of SiNWs produced by selective etching of a p-doped Si (100) wafer. b) Transmission electron microscopy image of a single SiNW. Reproduced from [18].

of interest when the surface has to be maximized in order to increase the number of interactions between the nanowires and the external environment. In the case where chemical reactivity is sought, one can vary the diameter and length of the nanowire to tune the surface to volume ratio of the object. The decoration of nanowire sidewalls by catalytic particles also constitutes a promising pathway to increase reactivity. Functionalization of nanowire surfaces can also create chemical selectivity and tailor the surfaces for specific applications.

Standard devices often involve the stacking of two or more chemically different layers of varying thicknesses. This is the case in thin-film solar cells and light-emitting quantum dots for example. Similar stackings are achievable using nanowires but the number of possible structures is richer: the direction of stacking can either be perpendicular to the axis of the nanowire, or parallel to it. The former case yields heterojunctions while the latter gives core-shell nanowires. Without using nanowires, creating a horizontal stacking requires the use of selective area deposition techniques, which are often very long and complex processes.

1.1.3 Bottom-up approaches to grow nanowires: VLS and VSS

Several techniques exist to synthesize nanowires which all have their own advantages. They can be separated into two categories:

- Top-down approaches: objects are obtained by carving them from bulk crystals. Lithography combined with other etching techniques are commonly used for that purpose [19, 20, 21]. They provide a high amount of control on the final structure and properties of the nanowires. The quality of the nanowires is generally good because it is an inherited property from the material. These approaches require many process steps which limits their applicability in an industrial context.
- Bottom-up approaches: objects are obtained by the growth on a substrate through the supply of atoms. Processes that fall into this category are scalable and the resulting nanowires are more cost efficient. Precise control over the growth is more complicated though, as the growth process depends on many parameters. Arrays of nanowires grown

with this kind of approach are often disordered, with nanowires growing in every possible direction. However, they can also be ordered, when prepared on patterned substrates [22].

In this thesis, we are interested in the growth of Si and GeNWs in the non-standard hexagonal diamond structure and our goal is to elucidate the growth mechanisms of this structure. As such, we are aiming for bottom-up techniques. One that is especially suited for Si and GeNWs is the vapor-liquid-solid (VLS) method and its variants, which was reported for the first time in 1964 [23] to grow SiNWs. It was also successful in the growth of other semiconductor nanowires such as GaAs, GaP and others. This technique rests on the precipitation of a solid nanowire by enrichment in atomic precursors, through a vapor phase, of a liquid catalytic metallic seed, hence the name of the technique. The metallic catalyst can also be solid; in that case, the method is known as the vapor-solid-solid (VSS) technique.

In order to fabricate SiNWs by VLS, a Si source is required. That source can be a melting Si pellet in the case of molecular beam epitaxy [24] (MBE) or a gaseous precursor in the case of chemical vapor deposition (CVD). For other types of nanowires, other techniques exist. For instance, III-V nanowires are often grown by metalorganic chemical vapor deposition (MOCVD). Suppose we want to grow SiNWs with a gaseous precursor. In this case, prior to the growth, metallic seeds, Au for instance, are deposited on a substrate. The substrate is then loaded into a CVD reactor. In this reactor, the substrate is heated up to 400 °C (for example) while the reactor chamber is filled with precursor gases. Silane (SiH_4) or tetrachlorosilane ($SiCl_4$) are often used for that purpose. Such molecules crack upon contacting the catalyst surface, so that single silicon atoms are adsorbed by the metallic particles (Figure 1.3a). From that point, the catalytic seeds are no longer pure Au but rather a mixture of Au and Si. With time, the concentration of Si increases. When the concentration in Si reaches a value around 19 %, the initially solid Si and Au alloyed seeds melt, forming a liquid eutectic. If further Si is added to the mix, the eutectic melt becomes supersaturated in Si, thus the precipitation of a solid Si nucleus begins and the SiNW starts growing (Figure 1.3b). From the Si nucleus, the growth occurs in a step-flow manner. The solid expands laterally under the catalyst, creating an atomic monolayer. After the monolayer is completed, a new Si nucleus appears on top when the conditions are favorable, and the cycle restarts (Figure 1.3c-d). The time between the introduction of gases in the chamber and the start of the growth is called the incubation time of the growth. At a given pressure of gaseous silicon, it depends on both the temperature and the choice of the catalyst. The catalyst will also influence the growth rate of the nanowire, the supersaturation threshold is different between chemical elements [25]. The growth rate also evolves with temperature by an Arrhenius law:

$$\frac{\mathrm{d}l}{\mathrm{d}t} = k \exp\left(-\frac{E_a}{k_B T}\right) \tag{1.1}$$

where k is a kinetic constant, E_a the activation energy of the growth, k_B the Boltzmann constant and T the temperature.

The diameter of the grown nanowires is initially given by the size of the catalyst particle. Thus, if a specific distribution of nanowire diameters is required, using the catalyst size engineering is a good way to control nanowire diameter. When the catalyst is deposited thanks to a colloidal suspension of nanoparticles, a laser ablation technique can help reduce the size of the particle and thus yield smaller diameter nanowires [26]. If the catalytic seeds come from the thermal evaporation of a metallic nugget, the evaporation time can be tuned in order to give the desirable diameter distribution by controlling the total amount of the evaporated material which will naturally form particles. As the nanowire growth advances, the diameter can change. The diameter close to the base of the nanowire may thicken due to sidewall deposition and,

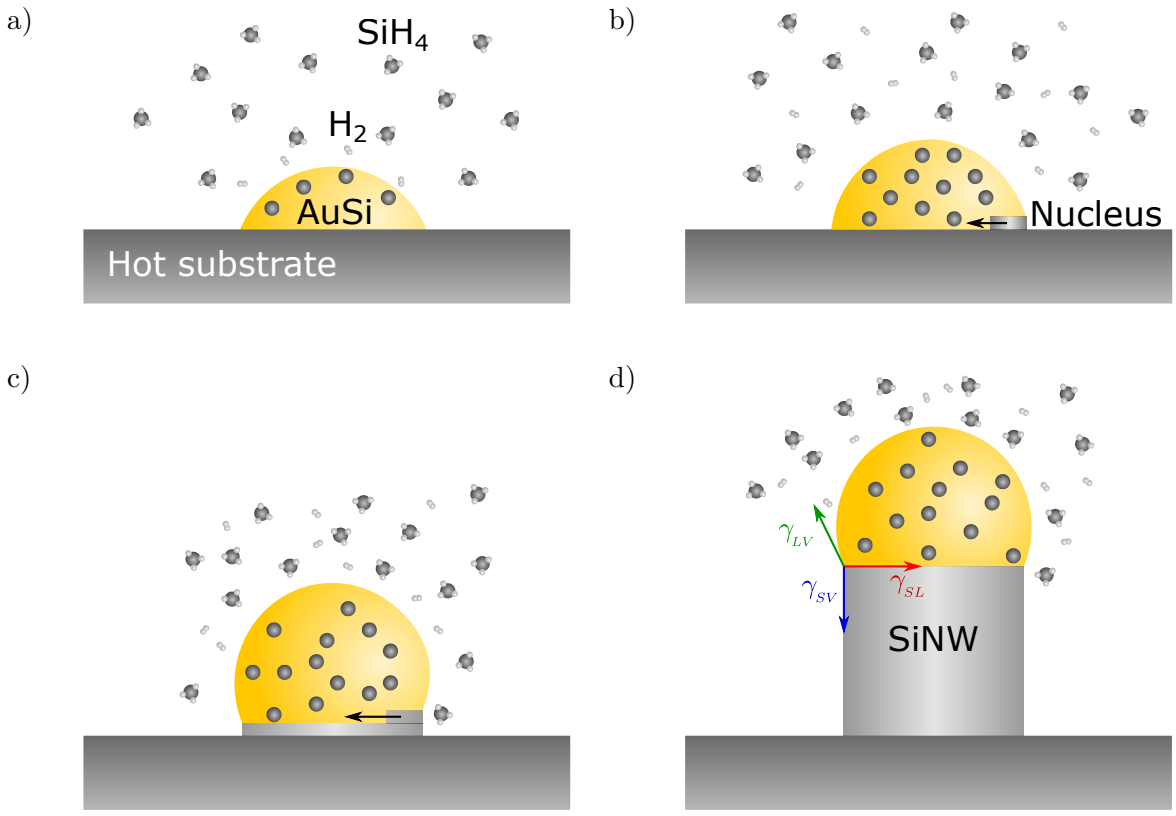

FIGURE 1.3: Schematics of the VLS growth of a SiNW using SiH4 as a precursor. a) Si atoms are adsorbed by the Au catalyst while H2 gas is created through the dissociation of SiH4 molecules. b) Supersaturation in Si in the seed is achieved, giving a solid precipitate known as the nucleus. This nucleus then expands laterally to form a complete layer thanks to the continuous incorporation of Si atoms. d) Additional layers are formed and a nanowire is born. The forces acting on the triple phase-boundary - liquid (L), solid (S) and vapor (V) - that are responsible for the droplet staying on top of the nanowire are also indicated.

inversely, the nanowire diameter may decrease at the top due to eventual losses of the catalyst. These two phenomena can create tapered nanowires [27, 28].

Several catalysts for VLS growth have already been tested. Among them, Au [29, 30, 31, 32], Cu [33, 34], Sn [35, 36, 37], Ga [38, 39, 40], In [35] and Al [41] can be cited. The choice of the catalyst for the growth of nanowires requires the careful consideration of several physical and technical factors. For the physical factors, the first one is the ability of the metallic catalyst to form a liquid alloy with the material of the nanowire. Then, the liquid catalyst must be pinned to the top of the solid precipitate. The surface tension of the liquid catalyst is the deciding factor on whether it can stay on top or not. Indeed, if the liquid catalyst is destabilized during the growth by fluctuations of forces acting on the droplet (Figure 1.3d), it may slide down from the nanowire it created. Metals with high surface tension, like Au or Cu for example, are relatively stable; while low surface tension metals are more easily destabilized. In theory, a metal like Sn should not allow the growth of SiNWs because of its very low surface tension [42] but growth can still be achieved under a plasma environment. The plasma modifies the surface energies involved in the droplet equilibrium. For the technical factors, the maximum temperature that can be reached with the growth equipment dictates the choice of catalyst for

the VLS technique. Indeed, the eutectic temperature of Si-metal alloys varies with the metal. Si-Cu eutectic temperature is 802 °C while for Si-Au it is 363 °C. Si-Sn eutectic temperature is even lower, at 232 °C. Thus, if low temperature growth is important, Au or Sn catalysts are better. It is also important to know that the choice of catalyst has an impact on the quality of the nanowires. Some catalysts, like Cu, are known to generate more faults and defects in the nanowire. On the other hand, Au creates deep level electronic defects which act as charge carrier recombination centers [43]. Thus, it is unsuited if electronic or photovoltaic devices are to be created from the grown nanowires.

In the case of the vapor-solid-solid growth (VSS) [44], the temperature of the growth is below the eutectic temperature of the alloy. An immediate consequence of the solid nature of the catalyst is a reduced growth rate compared to VLS. The main reason for this is primarily related to the slower diffusion in solids compared to liquids. This effect is moreover increased by the fact that, for a given catalyst, the growth temperature is lower for VSS [45]. The VSS technique, coupled with the VLS technique, is particularly useful when both fast and slow growths are desirable. This is the case when one wants a chemically abrupt heterojunction in a nanowire. When a pure section is grown, a fast growth by VLS helps reducing the process time. When a heterojunction is grown, one can lower the temperature to switch to the VSS mode, which gives better control over the growth allowing for the formation of chemically-abrupt heterojunctions [46].

Single element metallic catalysts are frequently used for the growth of nanowires. However, it is possible to mix two metals together in order to create a single alloyed catalyst. Thus, when a precursor is added to the catalyst, it creates a ternary system. Using an alloyed catalyst may enable one to tune specific parameters of the growth. For instance, AuAg catalysts have varying eutectic temperatures with Si depending on the Au/Ag ratio [47] which gives flexibility in the choice of growth temperature. Doping of nanowires can also be achieved with an alloyed catalyst such as Bi-Sn [48] by incorporation of a small amount of Bi inside growing nanowires.

1.1.4 Application of nanowires in devices

1.1.4.1 Nanowires in solar cells

Let us briefly remind the working principle of a solar cell using an amorphous Si layer (a-Si:H). A standard photovoltaic cell consists in a semiconductor p-i-n junction with a front and back conductive contact. The first step towards electricity production is the absorption of a photon of energy above the band gap of the material. When a photon is effectively absorbed, an electron-hole pair is created. In the case of a p-i-n structure (Figure 1.4a), an electric field exists within the whole cell, which separates the photogenerated charge carriers. In the layout shown in Figure 1.4a, positive charges (holes) will drift towards the p-doped layer and join the front contact. Negative charges (electrons) on the other hand go towards the n-doped layer to join the back contact. This results in the formation of an electrical current.

The most used semiconductor material in the photovoltaic industry is crystalline Si. Some reasons for that were mentioned previously. The main problem with c-Si is its indirect band gap which reduces light absorption, especially in the near infra-red part of the spectrum. For that reason, thick layers (around 200 μm) are common in order to maximize the amount of absorbed light. This comes with several drawbacks [49]. The most obvious one is the quantity of Si used to

manufacture a cell. A second, more subtle, issue concerns the diffusion of charge carriers through the thicker layers. Indeed, thicker layers increase the distance traveled by charge carriers. Thus, the likelihood of charge recombination is higher, creating losses of performance. One solution is to improve the absorbing layers quality by using highly pure and defect-free Si.

Using SiNWs can solve this issue [49, 50], because it allows for a different architecture of solar cells. Typical solar cells use planar p-n junctions. With arrays of SiNWs, it is possible to create radial junctions [51] (Figure 1.3b), which present vertical interfaces between layers, thus creating core-shell structures. In this application, the primary nanowires, the growth of which we are interested in, are used as p-doped cores for the radial-junction solar cells. Their main role is to carry the photovoltaic current produced by individual radial cells towards the back-surface electrode. This architecture presents several advantages: the diffusion of charge carriers through the junction is facilitated by the proximity of the doped layer. Charge separation now occurs in radial direction. Furthermore, less Si is used overall compared to standard planar junctions. Also, the radial architecture gives an appealing solution to the reflectivity problem caused by planar junctions, where the light can be reflected back, although this problem can be mitigated by adding anti-reflective coating or micro-texturing [52]. By using radial junction devices this problem is not so detrimental because light can be trapped by bouncing several times between individual junctions, thus increasing the absorption. Optimizing the length and density of the SiNWs helps in achieving the maximum efficiency [53, 54].

To this day, the maximum efficiency obtained by an array of single radial junction a-Si:H solar cells made from SiNWs grown by VLS developed at LPICM is 9.2 % [55]. Improving this efficiency requires overcoming some technical challenges. Better conformal interfaces between doped layers and the top transparent contact may help increase performance. Additionally, surface passivation is necessary to prevent the surface recombination of charge carriers, which is an important channel of loss in nanowire solar cells [56]. This is especially true for cells using InP III-V nanowires where the record efficiency between planar (17.8 %) and radial junctions (6.35 %) differs greatly [57].

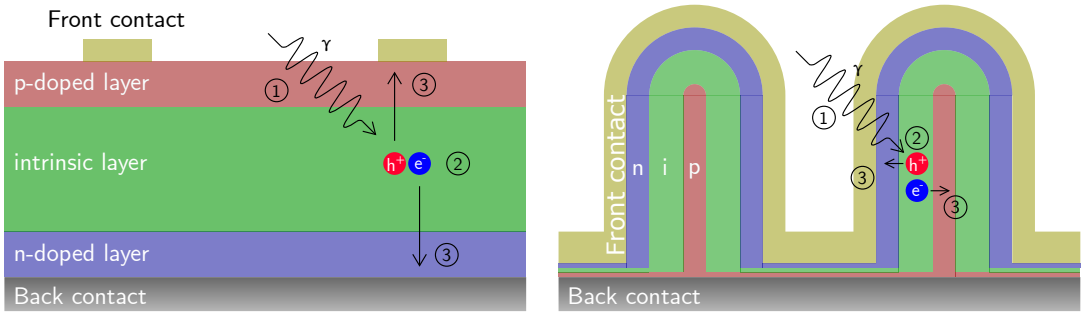

a) b)

FIGURE 1.4: Schematics of two a-Si:H solar cell architectures. a) Planar junction solar cell. Light is absorbed in the intrinsic layer, creating an electron-hole pair which is then separated by the electric field produced by the p-n junction towards the front and back contact. b) Radial junction nanowire solar cell. The front contact is made out of a transparent conductive oxide (TCO) to allow entry of photons.

1.1.4.2 Nanowire sensors

Thanks to their high aspect ratio, SiNWs are good building blocks for many types of highly-sensitive sensors. Also, due to their very small size, they can be implemented into high-density sensor arrays. Current research aims towards the integration of SiNWs into field-effect transistors (FETs) as shown in Figure 1.5. A p or n-doped SiNW is placed between the source and drain terminals and acts as the conductive channel. When a chemical agent interacts with the surfaces of the SiNW, the threshold voltage V_T of the device changes and this affects the current flowing through the SiNW I_{DS} when in the linear regime:

$$I_{DS} = \mu \frac{CW}{L}(V_G - V_T)V_{DS} - \frac{1}{2}V_{DS}^2 \tag{1.2}$$

where μ is the charge carrier mobility, C the capacitance of the gate oxide, W corresponds to the width of the SiNW, L its length, V_G the gate voltage and V_{DS} the channel voltage. Thus, the change in the current indicates a modification in the chemical environment around the SiNW.

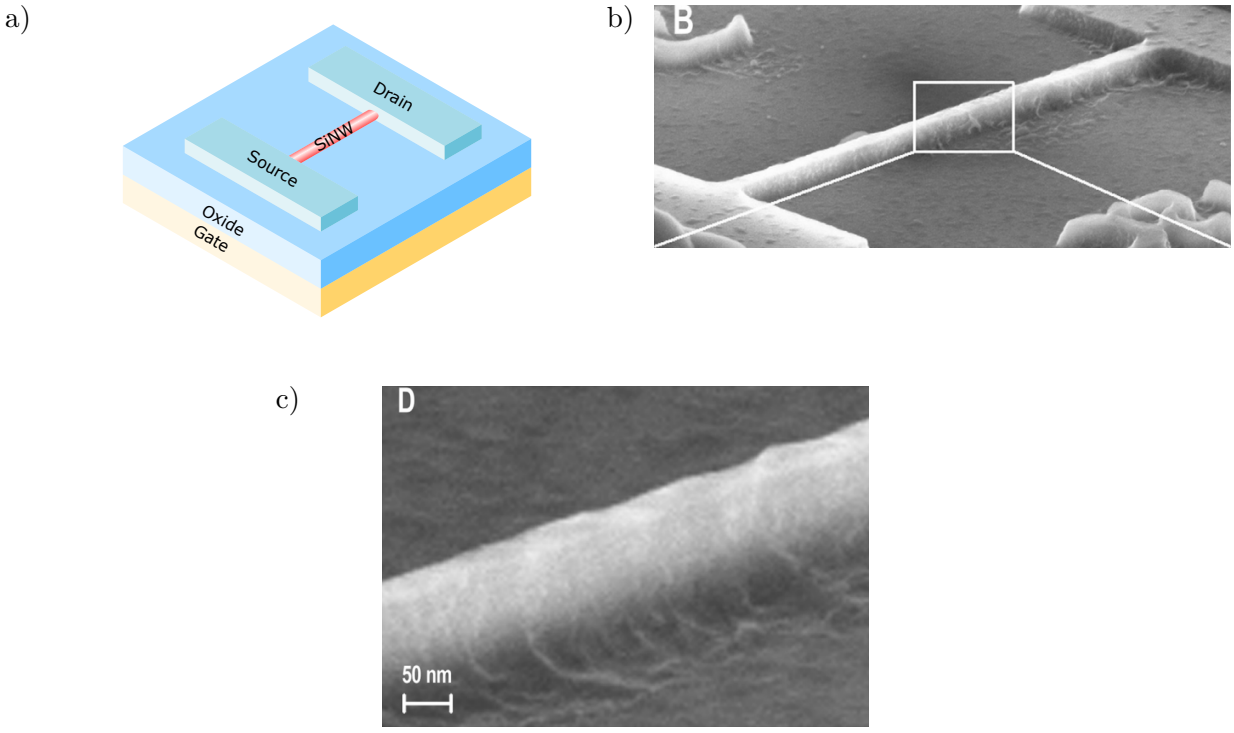

FIGURE 1.5: a) Schematics of a FET where a SiNW is used as the conductive channel. b) Scanning electron microscopy image of a SiNW FET functionalized with APTMS. c) Close-up view of the white squared area. Reproduced from [58].

In order to make the sensor specific to a chemical compound, the SiNWs have to be functionalized with a receptor. For pH sensors, a common technique is to use 3-aminopropyltrimethoxysilane (APTMS) as an agent [58]. In this geometry, the surface of the SiNW is terminated by both amine groups and silicon-hydroxyl groups. In the presence of a low pH, the amine groups are protonated, depleting the majority carriers in the SiNW conductive channel, and thus decreasing the conductance. At high pH, the silicon-hydroxyl groups are deprotonated, increasing the conductance instead. Other functionalizing agents can be used for other purposes. Sensors for heavy metal ions, such as Pb^{2+} [59] or Hg^{2+} [60] for the evaluation of water quality were reported. Nucleic acids were also successfully detected with nanowire sensors, which opened the path for the biological sensors [61, 62, 63].

1.1.4.3 Energy storage

Portable energy storage relies mainly on the Lithium-Ion battery technology, which, in present-day devices relies in turn on the back and forth movement of Li^+ ions between an oxide cathode and a graphite anode. One of the bottlenecks of the current technology is the low electrode capacity. This can be improved by using other compounds for the electrodes. However, it must be noted that the chosen material for the electrode must tolerate the repeated alloying with Li, known as lithiation, which changes the structural properties of the anode. In that respect, Si bulk material is a rather poor candidate for replacing graphite for the anode. Indeed, while it has a very high capacity compared to graphite, it undergoes significant structural changes when alloyed with Li [64]. This includes an increase in the volume of the LiSi alloy, resulting in mechanical failures after few charging-discharging cycles. This does not happen with graphite, as the volume expansion after lithiation is negligible.

This problem can be circumvented by using SiNWs instead of bulk Si [65, 66]. An example of architecture is given in Figure 1.6. Contrary to bulk Si, nanowires are able to accommodate much larger strain, and thus handle the volume expansion experienced during lithiation. There is still however one caveat to the use of SiNWs as anode. When alloyed with Li, the initially crystalline Si becomes amorphous [67]. After delithiation, Si remains in this amorphous state. This is not ideal because it reduces the conductivity of the anode. Consequently, the rate of charge-discharge is reduced after a single cycle. Solutions to this include the use of core-shell structured SiNWs [68]. The core is crystalline while the outer shell is amorphous. In this configuration, lithiation is limited to the shell while the transport of charge carriers occurs through the pristine crystalline core. It is also possible to coat the SiNWs with a layer that is both conductive and permeable to Li ions. Cu seems to be a good candidate in that regard [69].

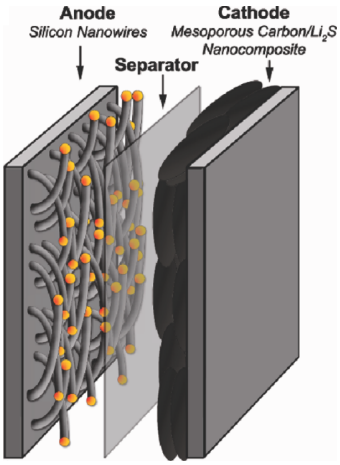

FIGURE 1.6: Schematic of the structure of a Li-ion battery with an anode composed of a random array of SiNWs. Reproduced from [65].

1.2 Crystallography and allotropes of Si and Ge

In this section, we introduce the concept of crystallographic phase for solid state materials. We will also see that some of these phases, while they should theoretically not exist at a given temperature and pressure, can still be synthesized under very specific conditions. This will prove

useful to understand what is the diamond hexagonal phase in group-IV elements, which is the main subject of this thesis.

1.2.1 Basic concepts of crystallography

In a solid, atoms are arranged in a certain way which depends on their chemical properties. If the solid is said to be amorphous, then there is no long-range order in the material, i.e, there is no correlation in the positions of distant atoms belonging to the solid (Figure 1.7a). Amorphous materials can be obtained by rapid quenching of their liquid state, which is the case for glass, of main compound SiO_2, a typical example of an amorphous solid. If the solid is said to be crystalline, then atoms are arranged in a way that presents long-range order: it is possible to find a geometrical operation (such as a rotation, a mirror symmetry, a translation...) which leaves the positions of atoms unchanged. The arrangement of atoms is also periodic (Figure 1.7b). This means that the arrangement of the unit cell is the same, regardless of where we look. In other words, there is translational invariance of the crystal along some axes.

Thus, to generate a crystal, we only need two things: a lattice, which tells us how to translate, and a motif, which is the shape that is translated. In three-dimensional space, one can show that all the different combinations possible of lattice and motif give 230 unique possibilities. These possibilities are called space groups, and each group has its own symmetry. The Hermann-Mauguin notation system can be used to label each space group depending on their symmetries.

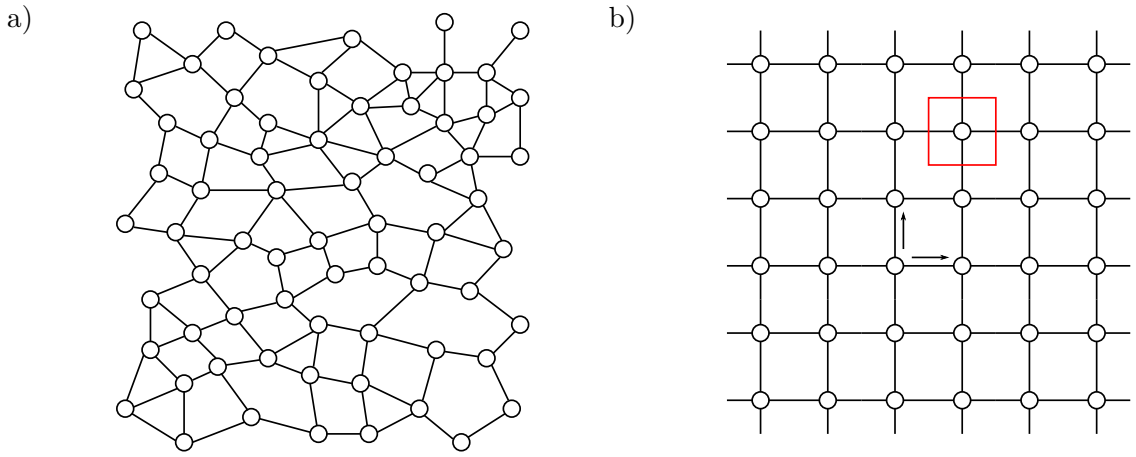

FIGURE 1.7: 2D representations of a material with either amorphous or crystalline structure. a) Schematic of an amorphous material, lacking any long-range order. b) Schematic of an example of a crystalline material. Arrows represent directions with translational invariance. A unit cell is marked by the red square.

Because a crystal is periodic, we can simplify its study by only considering the smallest finite volume which presents all its symmetries. This volume is called the unit cell of the crystal. Then, the crystal can be generated by simply translating the unit cell along the directions with translational invariance. The unit cell has several important characteristics. The size and shape are completely defined by six numbers: a, b and c, also known as the lattice parameters, which are the lengths of the edges of the unit cell; and α, β and γ the angles between the unit cell edges. From these, the unit cell vectors $\mathbf{a}$, $\mathbf{b}$ and $\mathbf{c}$ are defined. Another set of characteristics are the positions of the atoms in the unit cell. Because of symmetries, only certain sets of atomic

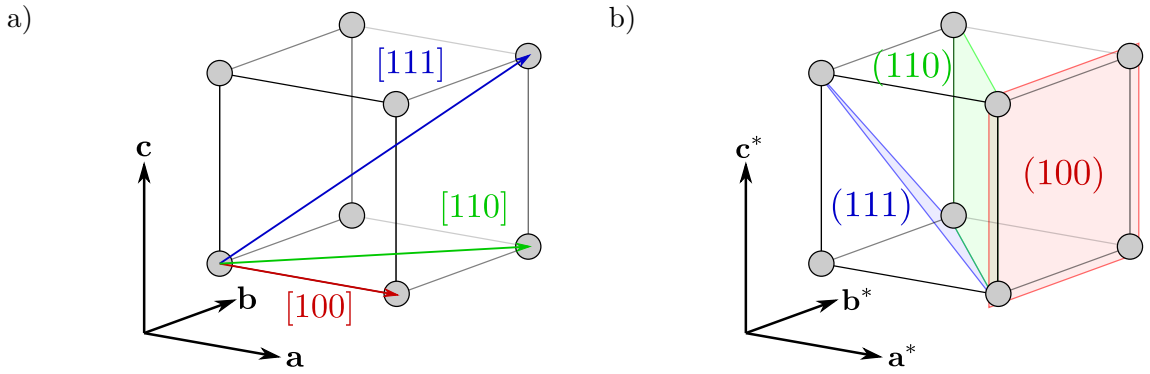

FIGURE 1.8: Example of directions and planes in a cubic unit cell. a) Three different directions and their notation using direction indices. The unit cell vectors **a**, **b** and **c** are represented. b) Three different planes and their notation using Miller indices. The reciprocal lattice vectors $\mathbf{a}^*$, $\mathbf{b}^*$ and $\mathbf{c}^*$ are represented.

positions are possible. All the possible sets can be labelled given their multiplicity, which is the number of positions the set defines. This is known as the Wyckoff notation.

Atoms in the unit cell are located by coordinates which can be expressed as fractions of the lattice parameters. Reticular directions in the unit cell (Figure 1.8a) are represented by vectors **r**, written as linear combinations of the unit cell vectors:

$$\mathbf{r} = u\mathbf{a} + v\mathbf{b} + w\mathbf{c} \tag{1.3}$$

where u, v and w are three numbers. If **r** corresponds with an atomic position, then one can find a (u, v, w) triplet where u, v, w are all integers. Such directions are noted $[uvw]$. The (u, v, w) triplet are the direction indices. Note that, due to symmetries in the unit cell, some directions are equivalent and can be regrouped in a family of directions. They are noted $\langle uvw \rangle$. To define planes, we use the reciprocal lattice unit vectors $\mathbf{a}^*$, $\mathbf{b}^*$ and $\mathbf{c}^*$, obtainable from the unit cell vectors:

$$\mathbf{a}^* = \frac{\mathbf{b} \times \mathbf{c}}{\mathbf{a} \cdot (\mathbf{b} \times \mathbf{c})}; \mathbf{b}^* = \frac{\mathbf{c} \times \mathbf{a}}{\mathbf{b} \cdot (\mathbf{c} \times \mathbf{a})}; \mathbf{c}^* = \frac{\mathbf{a} \times \mathbf{b}}{\mathbf{c} \cdot (\mathbf{a} \times \mathbf{b})} \tag{1.4}$$

Thus, directions **g** in the reciprocal space are written as linear combinations of the reciprocal space unit vectors:

$$\mathbf{g} = h\mathbf{a}^* + k\mathbf{b}^* + l\mathbf{c}^* \tag{1.5}$$

The direction **g** defines (hkl) planes perpendicular to it (Figure 1.8b). Similar to directions, some planes are equivalent and are regrouped in a family noted $\{hkl\}$. In the cubic system, any given unit cell vector is parallel to its corresponding reciprocal lattice unit vector, so that the direction indices $[uvw]$ defines planes with Miller indices (uvw).

For hexagonal lattices, one defines for planes a notation with four indices for planes is used, known as the Bravais-Miller indices, so that planes are noted $(hkil)$ where $i = -(h+k)$. Members of a family of planes $\{hkil\}$ can all be obtained by a cyclic permutation of the h, k and i indices. For directions, it is more complicated. A fourth index is also used, but going from the three-index system to the four-index one is not as straightforward. Let $[uvw]$ be a direction in the

three-index system, the same direction in the four-index system is written $[uvtw]$ where:

$$\begin{cases} u' &= \frac{1}{3}(2u - v) \\ v' &= \frac{1}{3}(2v - u) \\ t &= -(u' + v') \\ w' &= w \end{cases} \tag{1.6}$$

The reason for this system is to clearly distinguish families of planes and directions. For instance, the planes $(1\bar{1}0)$ and (010) seem to be from different families at first sight. However, when the four-index system is used, this gives $(1\bar{1}00)$ and $(01\bar{1}0)$. We see that a cyclic permutation shows that these two planes belong to the same family.

1.2.2 Equilibrium structure of Si and Ge

For both Si and Ge, the crystalline structure at room temperature and ambient pressure is the cubic diamond structure, of space group $Fd\bar{3}m$ in Hermann-Mauguin notation, dubbed Si-I and Ge-I respectively. This structure has a cubic unit cell with Si and Ge having a lattice parameter a of 5.431 Å and 5.658 Å, respectively. It is a face-centered cubic structure, but with a two-atom motif at $(0, 0, 0)$ and $(1/4, 1/4, 1/4)$. With this structure, both Si and Ge are indirect band gap semiconductors. The wafers, which are widely used for the fabrication of devices, typically have this structure.

The cubic diamond structure shares some similarities with the zinc blende (ZnS) structure. Both have a cubic symmetry and have exactly the same atomic sites. However, the zinc blende term is used for crystals with at least two different elements in their two-atom motifs, such as ZnS indeed or GaAs, another widely used semiconductor.

By significantly changing the pressure and temperature, the equilibrium crystalline structure of solid materials can change. It means that the material still retains its solid crystalline state but the arrangement of atoms is different. A specific stable crystalline arrangement of atoms is called an allotrope. A given compound can possess several allotropes. An example is carbon, where the equilibrium structure at standard temperature and pressure is graphite, but at high pressure, typically several GPa, the equilibrium one is cubic diamond. For the same material, allotropes can have different mechanical, electronic and optical properties. Going back to carbon, graphite is an opaque, black and brittle conductor while diamond is a transparent, colorless and hard semiconductor.

To summarize all the possible allotropes a specific compound can have, we can build a phase diagram for this compound that gives the equilibrium allotrope for a specific temperature and pressure. The phase diagram of Si and Ge were both explored experimentally and numerically, and are remarkably similar below 15 GPa (see Figure 1.9). Both Si and Ge undergo a phase transition at high pressure to a tetragonal structure [70] (space group $I4_1/amd$), similar to β-Sn, another group-IV element. They are respectively named Si-II and Ge-II. Experiments using diamond anvils have shown that other allotropes could form at even higher pressure for both Si and Ge [71]. For Si, these include two hexagonal phases Si-V and Si-VII [72], a face-centered cubic phase Si-X [73] and an orthorhombic phase Si-XI [74]. For Ge, we have two hexagonal, hcp-Ge and sh-Ge, and two orthorhombic phases, $Imma$-Ge and $cmca$-Ge [75, 76].

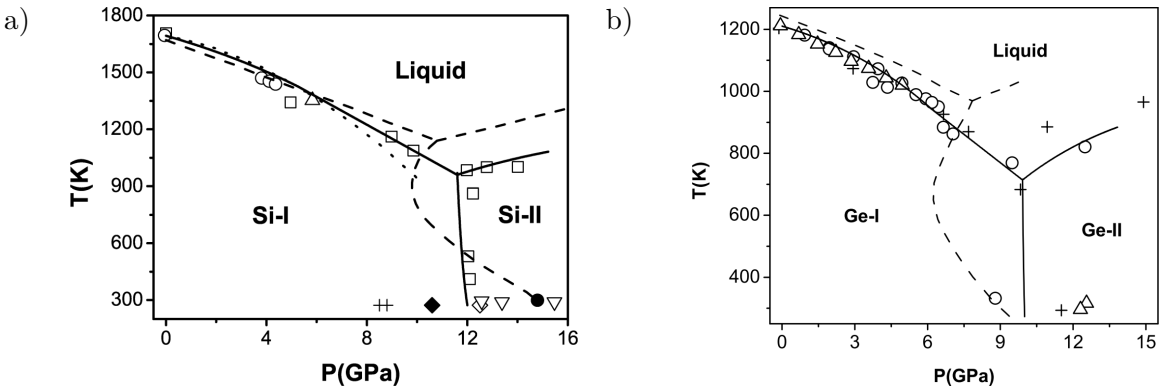

FIGURE 1.9: Si and Ge pressure and temperature phase diagrams for pressures below 16 GPa. Lines are theoretical predictions and symbols are experimental results. a) Si phase diagram. Data are collected from literature and graph was reproduced from [77]: solid lines [77], dashed lines [78], dotted lines [79], open circles [80], open squares [81], open pointing up triangles [82], open pointing down triangles [82], crosses [83], open diamonds [83], filled diamonds [83], filled circles [78]. b) Ge phase diagram. Data for solid lines [84], dashed lines [78], open circles [80], crosses [81], open triangles [82]. Reproduced from [84].

1.2.3 The 2H metastable phase and other polytypes

The allotropes that were mentioned in the previous section are all obtained by increasing pressure to several GPa. Upon reversal at atmospheric pressure, one could expect that the high-pressure phases should revert back to the usual cubic diamond phase, as indicated by both Si and Ge phase diagrams. It is however not always the case as pressure release can yield allotropes at pressure and temperature that are not predicted in the original phase diagram. Allotropes produced that way or by other means, that are not in the phase diagram, are qualified as metastable. An allotrope that is of interest because of its properties is the hexagonal diamond phase, also called lonsdaleite, for both Si (named Si-IV [85]) and Ge [86].

To better visualize the diamond hexagonal phase, we can go back to the standard cubic diamond phase, and observe it in an orientation where the [111] direction points to the right and the [110] direction is perpendicular to the plane defined by the paper. This is shown in Figure 1.10b. From this viewpoint, it can be seen that the cubic diamond phase consists in a stacking of three alternating layers along the [111] direction, that we can name A, B and C, which is then repeated, generating the crystal. Because the periodicity of this structure is three layers (ABC), and because it has a cubic symmetry, we can also label this phase 3C. This is called the Ramsdell notation for polytypes. From now on, we can create other structures by modifying the stacking along the [111] direction. For instance, 4H is a stacking of periodicity four (ABCB) and has a hexagonal symmetry (Figure 1.10c). 6H is a stacking of periodicity six (ABCACB) and again has hexagonal symmetry (Figure 1.10d). All the possible stackings are regrouped under the name polytype.

A polytype that is of special interest for us in this work is 2H, a stacking with a two-layer periodicity (AB) and hexagonal symmetry (Figure 1.10a). It is also known as the diamond hexagonal phase or lonsdaleite and belongs to the space group $P6_3/mmc$. The lattice constants of this structure are $a = 3.84\,\text{Å}$ and $c = 6.27\,\text{Å}$. A parallel can be drawn between the 2H and wurtzite structure, as both belong to the hexagonal system and have the same atomic structure, except that wurtzite alternates the two types of atoms of a binary compound material. Hence

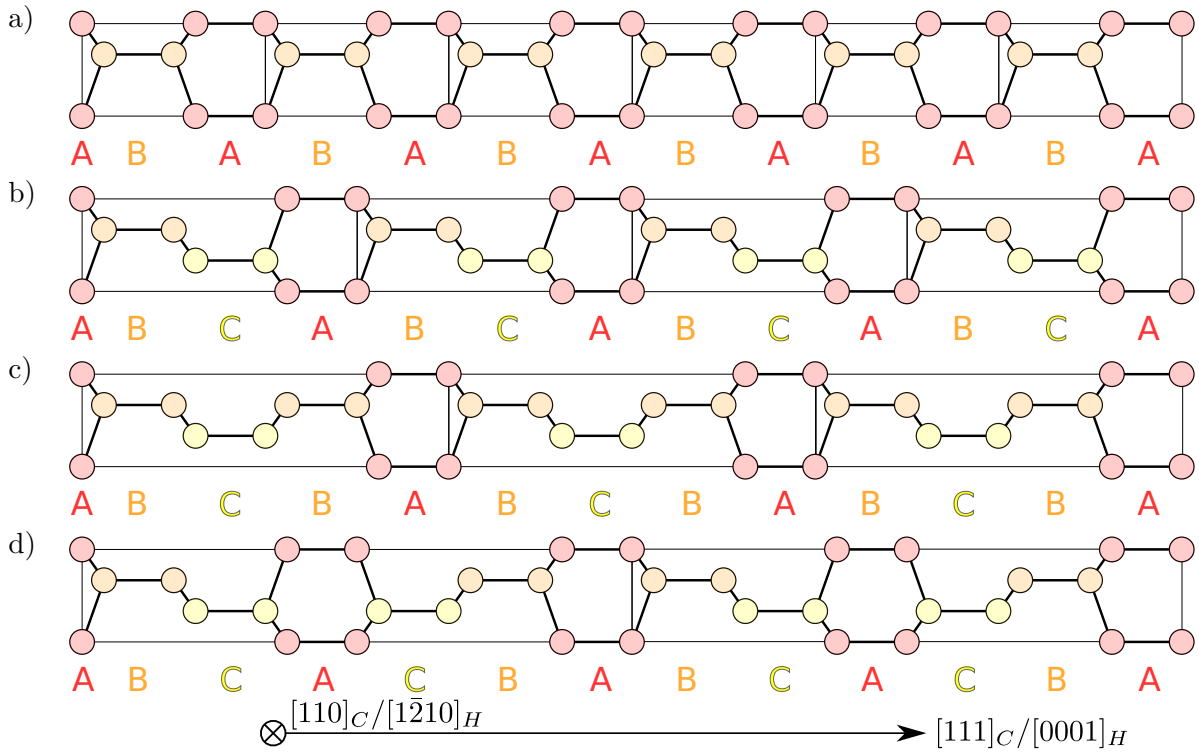

FIGURE 1.10: Examples of Si and Ge polytypes projected along the [110] direction. Black lines show the unit cells limits. a) Polytype 2H (hexagonal diamond). b) Polytype 3C (cubic diamond). c) Polytype 4H. d) Polytype 6H.

why the term wurtzite silicon is sometimes encountered in the literature although it is not the correct name in the case of a single element. Typical compounds with the wurtzite structure include GaN, a common semiconductor used in LED, and ZnS. The latter is metastable at standard temperature and pressure as the 3C phase (the generic zinc blende) is the equilibrium one.

Concerning the 6H polytype, it is interesting to note that the reversal of the stacking ABC-A-CBA is akin to a twin plane, a type of planar defect. In crystallography, twin planes act as a mirror plane, so that one atomic site on one side of the twin plane has its symmetric image on the other side. However, the reversal of the stacking in 6H is not a twin as it is not a localized single defect in the structure, but is present in every 6H unit cell. Incidentally, twin planes can occur in polytype crystals as well as stacking faults. These defects complicate the characterization of polytypes. For instance, studies using Raman spectroscopy have shown that twins and stacking faults can shift Raman peaks, overlapping with the Raman peaks associated with the polytypes [87, 88], although Ge might be a special case [89]. In TEM studies, such defects can give patterns that are similar to those obtained with pure polytypes [90, 91].

1.3 Synthesis of the 2H phase

We have introduced the 2H crystalline structure in the previous section. The different ways of synthesizing it will be the focus of this section.

1.3.1 Stress application in bulk

The first report of the 2H polytype was on bulk crystalline Si. Wentorf and Kasper [85] noticed that after the compression and recovery of a pure cubic diamond Si piece, an irreversible change in its electric resistivity occurs. They attributed this change to the appearance of a new phase in Si with a hexagonal symmetry, related to the wurtzite structure, and presented by X-ray diffraction data. The authors however conceded that they could not exclude the possibility that stacking faults were responsible for the intriguing X-ray pattern. It was later Eremenko and Nikitenko [92] who carried out the first transmission electron microscopy (TEM) study of the 2H polytype. By Vickers indentation above 400 °C, they generated a high amount of stress on a Si single crystal. After retrieval of the sample, they found several dislocations, twin defects and ribbons of 2H Si, giving additional reflections in electron diffraction patterns that could not be explained by defects. The synthesis of the 2H phase in Si was later reproduced through the same technique [93] and characterized using high-resolution transmission electron microscopy (HRTEM) (see Figure 1.11a). Models based on crystallographic analysis were proposed [94, 95], showing that the 2H structure could appear because of the intersection of twin planes. This created a shear stress, relaxed through the formation of diamond hexagonal Si ribbons. In such a case, the cubic diamond to hexagonal diamond transformation is martensitic, meaning that it does not involve diffusion processes.

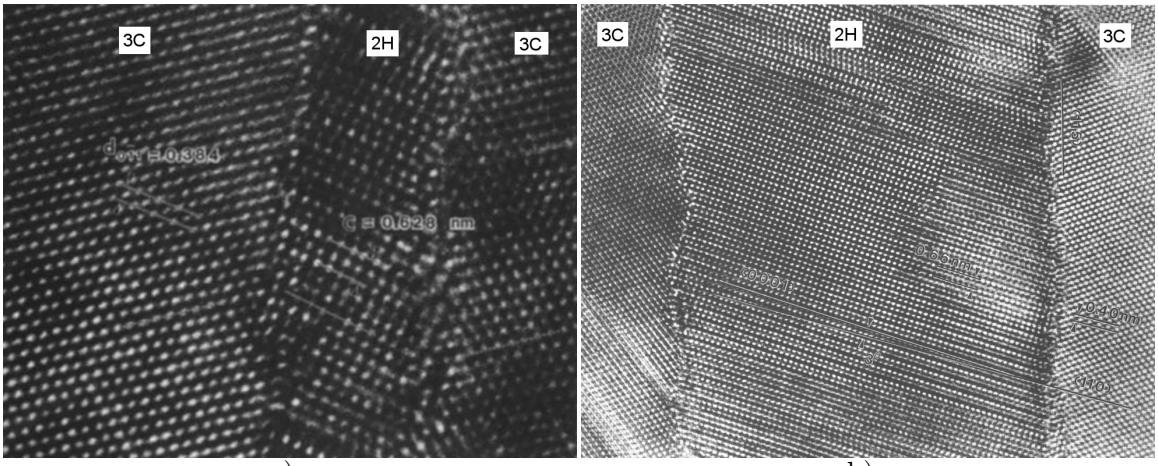

a) b)

FIGURE 1.11: HRTEM images of ribbons of 2H polytypes. a) 2H Si. Reproduced from [93]. b) 2H Ge. Reproduced from [86].

Ion implantation was also found to induce shear stress, resulting in the formation of hexagonal diamond Si. This technique consists in bombarding a target with high-energy ions, which creates irradiation damage in the crystalline materials, causing heating and change in physical or chemical properties. Beams of As^+ [96, 97] and Ar^+ [98] ions were used to attempt the synthesis of hexagonal diamond Si. While these studies claimed to have obtained it, no clear evidence was provided. The polytype 9R was also obtained with a beam of N+ ions [99]. Hexagonal diamond Ge was realized through indentation [86, 100, 101] and observed by HRTEM (Figure 1.11b). There are also reports that pulsed laser ablation [102], locally heating a sample, could form films of hexagonal diamond Ge.

1.3.2 Shear stress in nanowires

Thermo-mechanical treatments can also be used to obtain the 2H polytype in both Si and Ge nanowires. Vincent *et al.* [103] pioneered the technique on GeNWs. Cubic diamond GeNWs were first grown epitaxially by the bottom-up VLS approach in a UHV-CVD reactor with Au as catalyst on a Si (111) surface. The precursor used for Ge was a mixture of Ge_2H_6 and H_2. The substrate was then heated at 320 °C before the start of the growth. The obtained GeNWs were then embedded in a hydrogenated silesquioxane (HSQ) resist, an organosilicon compound. The whole sample was then transferred in an oven, and brought to 400 °C. The densification of the HSQ mold, followed by its transformation into SiO_2 and the subsequent cooling, created a high amount of shear stress on the GeNWs. This stress was then relaxed by formation of ribbons of hexagonal diamond Ge in the GeNWs. The GeNWs thus presented an alternance of cubic diamond and hexagonal diamond structure over their lengths, creating heterostructures (Figure 1.12c-d).

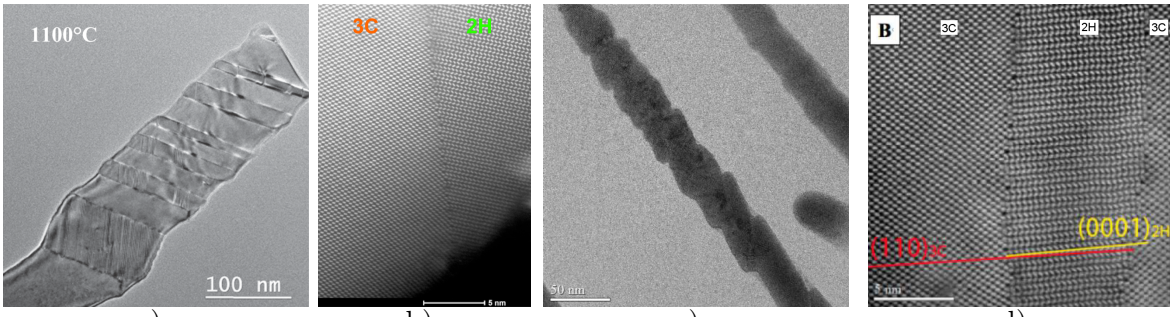

a) b) c) d)

FIGURE 1.12: SiNWs with ribbons of 2H polytypes obtained by a shear-driven process. a) TEM micrograph of a SiNW with an alternance of 3C and 2H polytypes. b) STEM micrograph of an area with a 2H-3C interface. c) TEM micrograph of a GeNW with an alternance of 3C and 2H polytypes. d) HAADF-STEM image an interface. a), b) reproduced from [104], c) and d) from [103].

The same technique was used successfully to synthesize SiNWs with 2H structure [105]. Diamond cubic SiNWs were fabricated through the etching of a Si wafer. Tetraethyl orthosilicate was then deposited by CVD on the substrate in order to fill the spacings between the SiNWs. The sample was then baked, resulting in the oxide densification. Ribbons of 2H on SiNWs were observed by TEM and analyzed similarly to the study of Vincent *et al.* The same authors later published another study using again HSQ resist to realize 2H SiNWs [104] (Figure 1.12a-b). They found that the baking temperature influences the size and the number of 2H ribbons in SiNWs.

1.3.3 Epitaxy of the 2H phase in core-shell GaP/Si nanowires

Shear-driven transformations have the disadvantage of lacking precise control on the size, position and number of 2H domains. Bottom-up approaches are thus more appealing as more strategies can be applied to tune their characteristics. To circumvent the metastable nature of this phase, one promising pathway is to grow hexagonal diamond nanowires epitaxially from a template with a similar structure. This is known as the crystal structure transfer technique [106]. For hexagonal diamond SiNWs, wurtzite GaP NWs proved to be an efficient platform

[107]. First, GaP NWs were grown with the VLS method using Au as catalyst on a GaP (111) substrate. Then, Si precursors were introduced to grow hexagonal diamond Si from the GaP NW sidewalls, forming a GaP/Si core-shell nanowire with an atomically sharp interface. Wurtzite GaAs/Ge core-shell nanowire, with Ge presenting the 2H polytype, were also grown using a similar technique [108] (see Figure 1.13).

Temperature was found to be an important parameter during this process, as it increases the growth rate of the Si 2H shell [109]. Using higher order silanes, the growth temperature could be reduced, while retaining a relatively fast growth of the Si hexagonal shell. This is helpful if one desires a constant diameter shell along the whole nanowire. Indeed, there is an inverse tapering of the Si shell when grown at high temperature. The Si hexagonal shell is thicker at the top, while the bottom part, closer to the substrate is thinner. The authors suggest that the substrate acts as a sink for Si atoms. Because of the reduced length of diffusion of Si atoms, those arriving at the top of the wire are incorporated into the Si shell, while those impinging at the bottom diffuse towards the substrate. The end result is an uneven growth rate along the wire. This is exacerbated by growth at high temperature due to the reduced length of diffusion of Si atoms at these temperatures thanks to the high density of dangling bonds. At lower temperature, these dangling bonds are passivated by hydrogen.

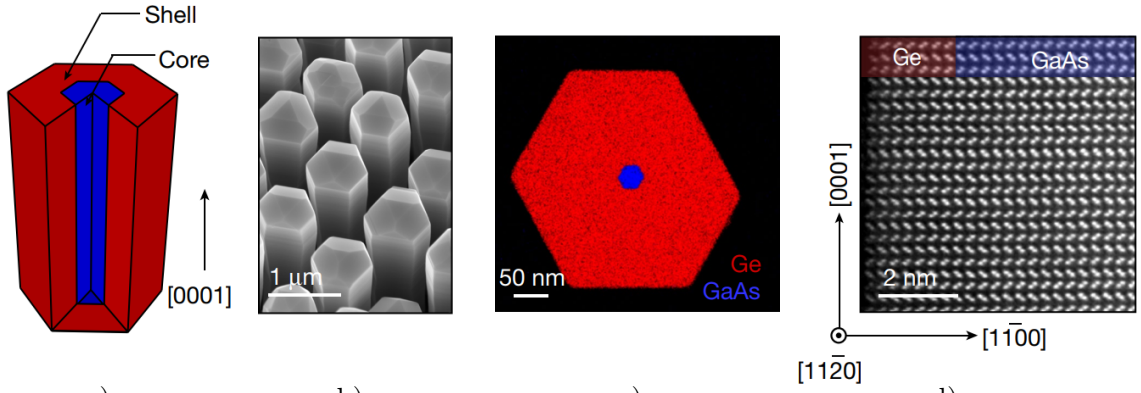

FIGURE 1.13: Epitaxy of the 2H polytype on a core-shell GaAs/Ge NW. a) Schematic of a core-shell GaAs/Ge NW. b) SEM image of an array of core-shell GaAs/Ge NWs. c) HAADF-STEM image combined with EDX data of the nanowire. d) HAADF-STEM image of the interface between the Ge shell and the GaAs core. Reproduced from [108].

1.3.4 Direct synthesis of the 2H polytype through the VLS method

The previously described techniques have a common point in that they require several treatments to synthesize the 2H polytype, thus increasing the number of steps during the process. This is a potential obstacle for the implementation of polytype growth in the fabrication of low-cost devices. Furthermore, none of these approaches gave NWs that were pure 2H. The crystal transfer technique would only give a 2H shell and the shear-induced transformation technique yields only random ribbons. However, it was found that this structure could also be prepared using the bottom-up VLS SiNW growth approach. Tang *et al.* [110] successfully obtained the 2H polytype, while providing unambiguous proof through HRTEM analysis. These SiNWs were obtained in a plasma-enhanced chemical vapor deposition (PECVD) reactor by the VLS method with Sn catalyst. The precursor used was a gas mixture of SiH_4 and H_2. SiNWs were grown on a

TEM Cu grid. Some of the NWs were fully hexagonal, contrary to what has been obtained with previously described methods, see Figure 1.14. This suggests that the mechanism of formation of the 2H phase in this experiment may be fundamentally different from the shear-driven methods. The reason why the 2H phase formed was however not clear, as plasma processes completely change the growth environment: presence of radical species, ion bombardment, temperature gradient and presence of electric fields.

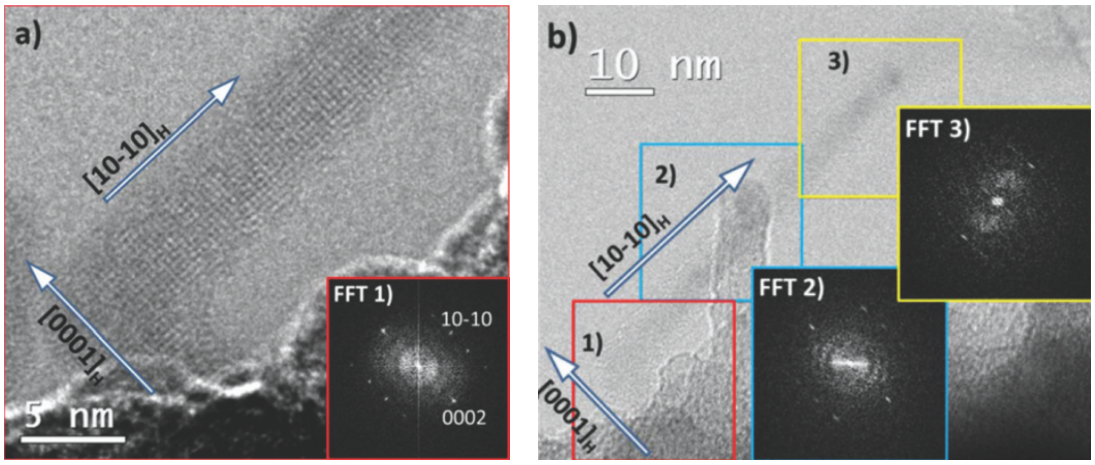

FIGURE 1.14: Hexagonal diamond SiNW grown by the plasma-assisted VLS method. a) HRTEM micrograph of a fully 2H SiNW. b) Low magnification view of the full wire of a). Reproduced from [110].

Another study [111] showed that the 2H structure could also be grown without the use of plasma-assisted process. Using In nanoparticles, the authors obtained faulted SiNWs, with twin planes. Those twin planes were found to be either perpendicular to the growth axis or parallel. Some SiNWs have kinked, changing their growth direction during the process. Because of this, some twin planes could intersect, creating a grain in the SiNW with the hexagonal diamond structure. The mechanism of formation of the 2H polytype in this study seems similar to what Dahmen *et al.* have proposed [94] that 2H occurs due to two or more twin planes intersecting.

While the spontaneous growth of GeNWs with the 2H polytype with the VLS method has not yet been reported, it is worth noting that the 4H polytype was obtained [112] by LPCVD, where an organometallic Ge gas precursor was used.

1.4 Properties of the 2H phase

In the previous section, we have reviewed different approaches of synthesis of Si and GeNWs presenting the 2H polytype. Here we discuss the properties of such objects and their potential use in novel devices.

1.4.1 Modifications in the band structure

Both bulk Si and Ge, in their standard cubic diamond structure, are indirect band gap semiconductors with a gap width of respectively 1.12 eV and 0.66 eV at 300 K. Because of the structural

differences between polytype 3C and 2H, there will be modifications in the electronic properties of Si and Ge, as they depend on the overlap of atomic orbitals. These modifications have been investigated in the literature for both Si and Ge by *ab initio* calculations using the density functional theory [113] (DFT).

For bulk diamond hexagonal Si, the band gap is predicted to be narrower, when compared with the standard cubic diamond structure; it decreases to 0.95 eV and remains indirect [108, 114, 115] (Figure 1.15a, c). The lowering of the gap is also accompanied by a splitting of the valence bands. The application of strain to the hexagonal diamond Si lattice modifies the lattice parameters, and allows to change the value of the gap [114]. In particular, biaxial strain acting on the lattice parameter a of the 2H polytype was predicted to modify the nature of the gap, making it direct. For Ge, calculations also predict a lowering of the band gap [108, 115, 116] from 0.72 eV at 0 K to 0.32 eV. Contrary to Si, the band gap becomes direct without the need of lattice deformation (Figure 1.15b, d). Again, a splitting of the valence band is predicted.

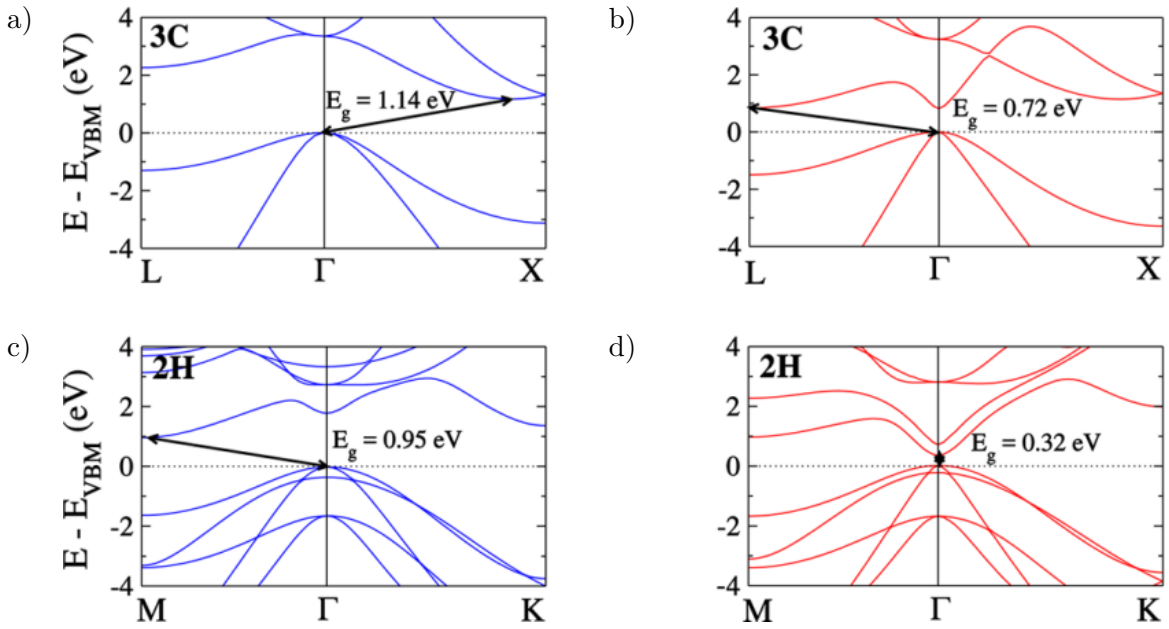

FIGURE 1.15: Band structure of bulk Si and Ge given by DFT calculations. a) Bulk cubic diamond Si. b) Bulk cubic diamond Ge. c) Bulk hexagonal diamond Si. d) Bulk hexagonal diamond Ge. Reproduced from [115].

As I write this manuscript, there are no experimental reports confirming the bulk 2H band structure predicted by the simulations, in either Si or GeNWs because the synthesis of large quantities of the 2H polytype remains a challenge. However, it is interesting to note that hexagonal diamond $Si_{1-x}Ge_x$ core-shell nanowires were investigated experimentally [108]. Photoluminescence measurements have shown that the value of the gap could be tuned by changing the composition. Furthermore, for $x \sim 0.65$, the authors measured a strong variation in the photoluminescence intensity of the nanowires. This suggests an indirect-to-direct band gap transition for $x > 0.65$. Given that hexagonal $Si_{1-x}Ge_x$ should have an intermediate behavior between hexagonal Si and Ge, this gives us an important clue pointing towards the plausibility of the predictions of the above mentioned simulations.

For the moment, only the bulk was considered. In the case of nanowires, size effects may occur. For Si and GeNWs with diameter greater than 10 nm, results in bulk are also valid

[117, 118]. For very thin nanowires, electrons are in a state of quantum confinement, as their motion is restricted in directions perpendicular to the nanowire axis. A textbook analogy would be like a particle inside an infinite potential well in a two-dimensional space. As a result, there will be differences in the band structure of the material. *Ab initio* calculations [119, 120], validated experimentally in cubic SiNWs by scanning tunneling spectroscopy [121] (STS), show that the band gap should increase with the reduction in diameter. The variation of the gap value in SiNWs can be fitted using this equation [120]:

$$E_{gap}^{NW}(d) = E_{gap}^{bulk} + \frac{C}{d^{\alpha}} \tag{1.7}$$

where $E_{gap}^{NW}(d)$ is the value of the gap in the nanowire of diameter d, E_{gap}^{bulk} the value of the gap in the bulk and C and α are positive fitting parameters. Figure 1.16 illustrates this variation for both cubic and hexagonal SiNWs. Thus, careful control of the diameter allows for the tuning of electronic properties. Additionally, the band gap becomes direct for small diameter hexagonal SiNWs, without the need for a strain. Both theoretical and experimental studies on quantum confinement in GeNWs are lacking at the time of the writing of this thesis.

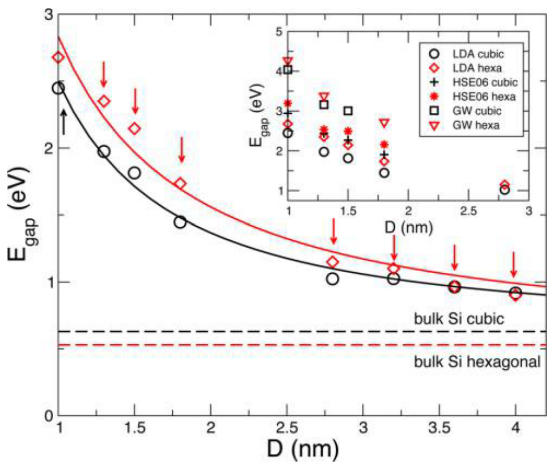

FIGURE 1.16: Effect of quantum confinement in SiNWS on the value of the band gap. The calculations are done by DFT using local-density approximation (LDA). The arrows denote direct band gap. The inset shows results obtained with other methods. Reproduced from [120]. Note that only the relative trend of band gap values can be considered reliable, the absolute values are not reliable due to the used DFT approach.

The differences between the band gap values of the 2H and 3C polytypes immediately bring out a potential application. When cubic Si (Ge) is connected with hexagonal Si (Ge), a homo-junction is created. At the interface, the mismatch in band gap creates a misalignment of the bands, called band offset. Thus, on one side of the junction, the valence (conduction) band is lower in energy than the other side valence (conduction) band. Two types of band offset are possible [115, 120]:

- Type I refers to a situation where the lowest valence band and the highest conduction band are located on the same side of the interface. Here, both types of charge carriers, electrons and holes, will have the tendency to move towards the same side of the heterojucntion (Figure 1.17a).
- Type II refers to a case where the lowest valence band and the lowest conduction band

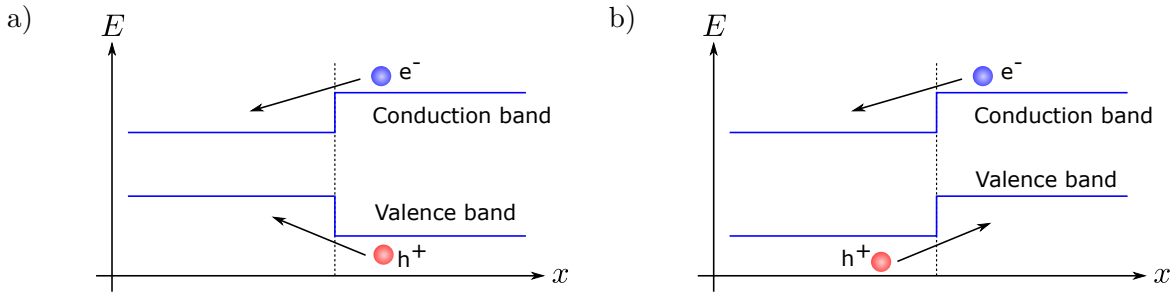

FIGURE 1.17: Examples of band diagrams that depict: a) a type I band offset or b) a type II band offset.

are on the same side. Electrons and holes will drift towards opposite directions of the heterojunction (Figure 1.17b).

This situation is of interest for devices because, by providing a band profile similar to that of a p-n junction, it suppresses the need for dopants. Semiconductor doping requires additional processes, which often involve toxic gasses. Thus, type I heterojunctions could be used for light-emitting devices, while type II are better for solar cells. Because of the quantum confinement, the value of the gap can be theoretically tuned, changing the type of band offset. Consequently, Si (Ge) heterojunctions could be multi-purpose objects.

The fact that the band gap becomes direct in Si and GeNWs is of crucial importance. As stated in Section 1.1.1, the indirect band gap limits the usefulness of Si and Ge, making them neither a good light absorber nor emitter. This is why direct band gap semiconductors, such as GaAs or InGaN, are preferred for LEDs, although toxic and less abundant. Thus, direct band gap Si or Ge could be important platform for future devices.

1.4.2 Optical absorption and emission

By means of DFT simulations, the optical absorption at 0 K of hexagonal Si can be predicted as shown in Figure 1.18 [114, 120]. Contrary to cubic Si, hexagonal Si should present an ordinary and an extraordinary axis because the a and c lattice parameters are different. Thus, the absorption should be different depending on the direction of polarization with respect to the c axis. It can be seen that hexagonal Si starts absorbing sooner, especially along the extraordinary axis ([0001] direction). Furthermore, the absorption is higher for energies in the range 1 eV-4 eV, which correspond to those present in the solar spectrum. Because of this, hexagonal Si can be relevant as an absorbing layer in solar cells allowing to reduce the thickness of the latter. The reduced band gap might be a problem if the Schockley-Queisser limit is considered, but the loss in performance should not exceed a few % [122]. If shear strain is considered, the calculations show that the hexagonal Si starts absorbing even sooner as the imaginary part of the dielectric function becomes non-zero at lower photon energies. Coupled with the predicted direct band gap transformation, it can be seen how hexagonal Si can become an appealing material. There is however concern over the fact that the direct band gap transition is dipole forbidden. For Ge, calculations show that the radiative lifetime is several orders of magnitude higher in hexagonal Ge than in cubic Ge in a range of temperature from 0 K to 400 K, giving smaller carrier recombination rate [116] and greater absorption. The 0.32 eV direct transition should be dipole forbidden according to the study.

Very few experimental studies on the optical characterization of SiNWs with the 2H structure exist, due to the difficulty of synthesizing large quantities of SiNWs presenting this structure [123, 124]. B-doped SiNWs were characterized by cathodoluminescence and were found to radiate in the near infrared. While the NWs were called "wurtzite" the characterization studies never provided a proof that the objects had the 2H structure. However, the structure of cubic SiNWs often includes a high density of microtwins and stacking faults which, in turn, may look like 2H regions. Thus, the published results could give an interesting trend of the evolution of the optical properties when a structure changes towards 2H. According to a photoluminescence study [123], high density arrays of such SiNWs give intense luminescence peaks around 2.14 eV, corresponding to the green-yellow part of the visible spectrum. When p-doped with B_2H_6 [124], emissions are observed in the near-infrared (0.76 eV) and in the red (1.5 eV) while bulk Si emits around 1.1 eV with an intensity three orders of magnitude lower. The situation is different for 2H-GeNWs, as such objects (actually microtubes) have been obtained and their structures duly characterized [108]: their band gap is direct; emissions are observed mainly in the infrared at 0.3 eV. By alloying with Si, the band gap can be shifted towards higher energy. An emission at 0.66 eV is observed for $Si_{0.35}Ge_{0.65}$, while still keeping the direct band gap [108].

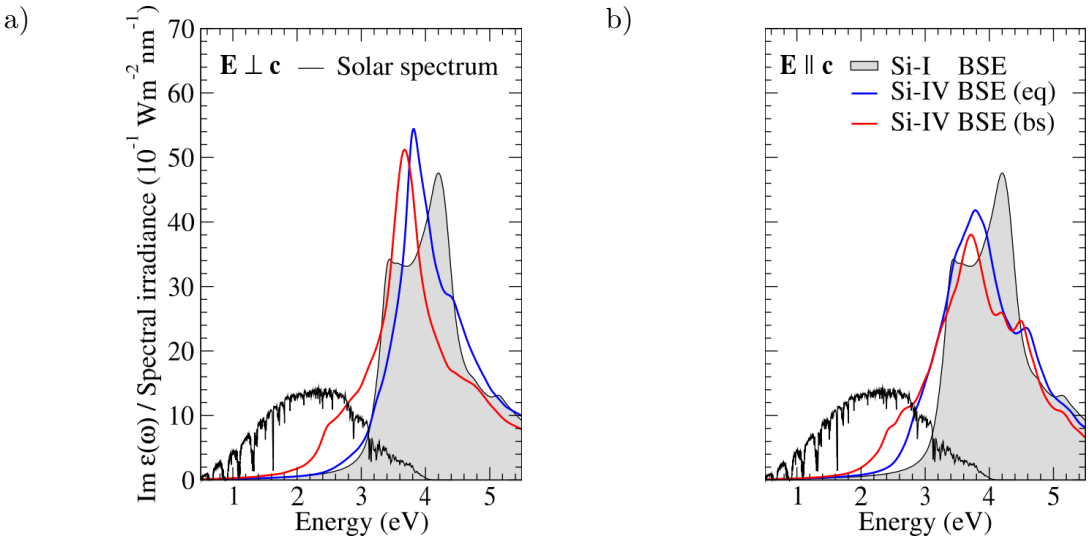

FIGURE 1.18: Imaginary part of the dielectric function as a function of photon energy, predicted from *ab initio* calculations. Grey line corresponds to cubic diamond Si, blue line to hexagonal diamond Si, red line to biaxial strained hexagonal diamond Si and black line to the solar emission spectrum. a) Imaginary part for ordinary polarization. b) Imaginary part for extraordinary polarization. Reproduced from [116].

1.4.3 Reduction in thermal conductivity

Thermoelectricity describes the physical effect that links heat flux and electrical current. It is particularly used for portable cooling, such as Peltier module, and autonomous power generation for spatial applications. The efficiency of a thermoelectric device is given by its figure of merit, noted ZT which depends on the temperature T and intrinsic physical quantities of the used material. It is given by:

$$ZT = \frac{\sigma S^2 T}{\kappa} \tag{1.8}$$

where σ is the electrical conductivity, S the Seebeck coefficient and κ the thermal conductivity of the material. A figure of merit $ZT > 1$ is considered good. Thus, high electrical conductivity and Seebeck coefficients are desirable for efficient energy conversion, while thermal conductivity must be as low as possible. In practice, it is quite difficult to achieve this since metals typically have both high electrical and thermal conductivity. On the other hand, semiconductors have lower electrical and thermal conductivity, but the electrical conductivity can be improved by doping. Typical semiconducting compounds with widespread uses include Bi_2Te_3 [125] or SiGe [126]. Bulk Si is a very poor choice for thermoelectric devices because of its high thermal conductivity [127] ($150\,\mathrm{W}\cdot\mathrm{m}^{-1}\cdot\mathrm{K}^{-1}$), yielding $ZT = 0.01$ at room temperature.

There are two main contributions to thermal conductivity. The first one is linked to heat transport by electrons which depends on the density of free electrons in the semiconductor. A second contribution is from lattice vibrations modeled by phonons. Consequently, increasing phonon scattering is a good strategy to reduce thermal conductivity and thus improve the figure of merit. Incidentally, it was found that low dimensionality materials, such as nanowires, create spatial confinement for phonons, reducing the thermal conductivity [128]. This is true for SiNWs [129, 130]: experiments showed that the figure of merit could be improved to 0.7. Creating heterostructured devices is also a good pathway towards lowering thermal conductivity, as interfaces and defects lower phonon mean free path [131]. In particular, interfaces between polytypes is expected to lower thermal conductivity [132].

DFT calculations have predicted that the 2H polytype in SiNWs should have a lower thermal conductivity than 3C nanowires, regardless of the temperature or the nanowire diameter, as shown in Figure 1.19 [133]. For instance, room temperature hexagonal diamond SiNWs have a predicted thermal conductivity of $25\,\mathrm{W}\cdot\mathrm{m}^{-1}\cdot\mathrm{K}^{-1}$, giving a six-fold reduction compared to bulk Si. This concept, coupled with heterostructures, was demonstrated experimentally in both Si-2H/3C NWs and Ge-2H/3C NWs [134]. By using scanning thermal microscopy (SThM), the authors were able to measure a reduction in the thermal conductivity with the increasing number of 2H/3C interfaces. Thus, heterostructured Si and GeNWs can be good candidates for future thermoelectric devices.

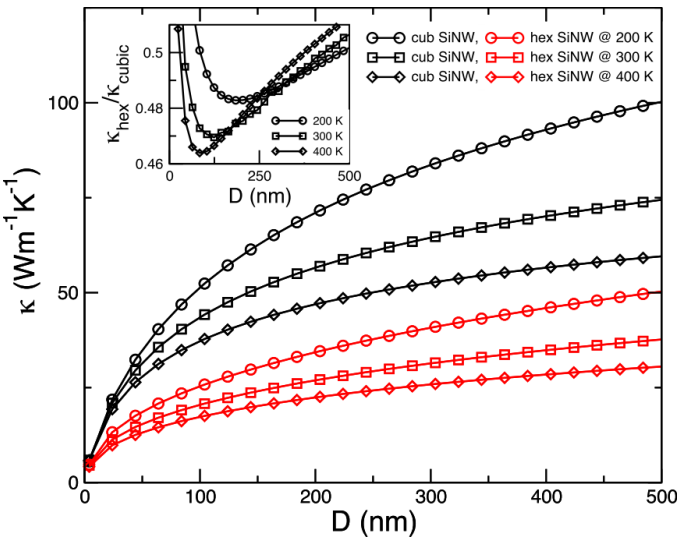

FIGURE 1.19: Thermal conductivity of cubic and hexagonal SiNWs as a function of diameter for a temperature of 200, 300 and 400 K. The inset shows the ratio between the thermal conductivities of hexagonal and cubic SiNWs. Reproduced from [133].

1.5 Theoretical predictions on the presence of the 2H phase in group-IV nanowires

The metastability of the 2H polytype in Si and Ge was referred to in Section 1.2.2. We now discuss this aspect in further details, by considering it from the equilibrium and kinetical points of view.

1.5.1 Stability and metastability of crystalline allotropes

In general, for a given number of atoms in a system, the total energy of the system is lowered if interactions exist between the atoms than if each of them is taken individually. This can also happen for crystals, where atoms and electrons interact with each other through the electrostatic force. This difference is the so-called bulk cohesive energy, and its value, positive or negative, determines if the crystal is stable or not. Positive values mean that the system is more stable if atoms are not interacting with each other, thus the crystal is unstable and will most likely dissociate spontaneously. Negative values signify the stable or metastable nature of the crystal. If a specific structure achieves the lowest bulk cohesive energy for a given temperature and pressure, then this structure should be stable under these conditions while all the other structures with negative cohesive energy are metastable instead. Thus, the bulk cohesive energy constitutes a clue towards the likelihood of achieving a specific crystalline structure since each one has its own cohesive energy.

A higher temperature increases lattice vibrations, while increasing the pressure changes the equilibrium lattice parameters. Both modify how atoms are positioned relatively to each other, changing the interaction energies, and thus changing the bulk cohesive energy. Because of these modifications, it is possible that at some temperature or pressure threshold, another crystal structure becomes the one with the lowest bulk cohesive energy. Understanding how the bulk energy evolves is critical to evaluate the stability of polytype 2H.

For both Si and Ge, the cubic diamond structure is the stable one, i.e the one that achieves the lowest cohesive energy of all possible allotropes. A clearer picture on the likelihood of obtaining hexagonal polytypes, mentioned in Section 1.2.3 can be harnessed if we assess the difference in bulk cohesive energy between the cubic diamond structure and the other hexagonal polytypes. In that regard, *ab initio* calculations, based on the density functional theory (DFT), are capable of computing these bulk cohesive energies [135] and provide theoretical predictions on the polytype stability. Such calculations confirm that, for both elements, the cubic diamond phase has the lowest total energy, and hence is the stable one. When the stacking sequence deviates from the cubic diamond one, the total energy of the system increases. Polytype 6H for example has an excess of energy of 1.0 meV/atom in Si and 4.3 meV/atom in Ge crystal, respectively. Polytype 4H is even more energetic with an excess of respectively 2.4 and 6.9 meV/atom. Polytype 2H deviates the most, where the excess reaches 10.7 meV/atom for Si and 16.1 meV/atom for Ge. From these numbers, the metastable nature of the 2H phase is clearly visible. If the polytypes are arranged depending on their degree of hexagonality (3C followed by 6H, 4H and finally 2H), we see that the energy increases with the hexagonality of the polytypes (see Figure 1.20). The nature of the element also plays a role, as the increase in energy for increasing hexagonality is steeper for Ge as compared to Si. Thus, in theory, Ge 2H should be much more difficult to obtain than Si.

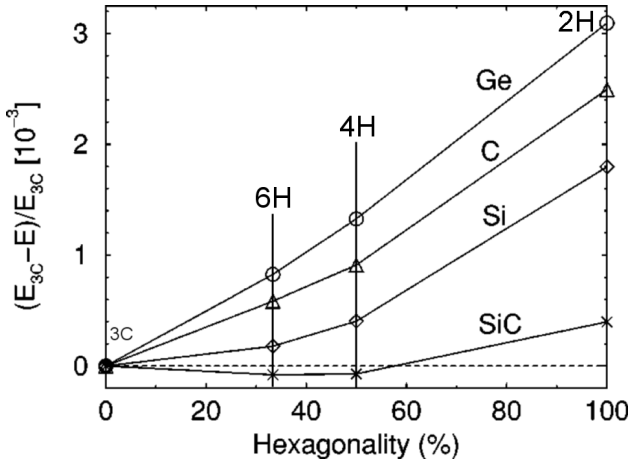

FIGURE 1.20: Relative energy of hexagonal polytypes compared to the stable cubic diamond structure for four different compounds of group-IV elements. The values are calculated using DFT method in [135], image is adapted from this publication.

When hydrostatic pressure is applied to a bulk material, the interatomic distances change and so does the bulk cohesive energy. The latter is then expected to evolve with changing pressure. For polytypes that are sufficiently close to each other in terms of cohesion, it is possible that their energy curves cross at a specific value of pressure. Pressures below or above this value favor different phases. For Si and Ge, the study [135] predicts that these changes in energy could allow for phase transitions between the cubic diamond phase and the 6H and 4H hexagonal polytypes, as they are not so far apart in terms of bulk cohesive energy. However, because the 2H polytype is much more energetic than the others, hydrostatic pressure would not be sufficient to trigger a phase transition in both Si and Ge. Obtaining bulk Si 2H and Ge 2H from simple pressure change is therefore much more difficult. Experiments mentioned in Section 1.3.1 confirm this, as the observed ribbons of polytype 2H were most likely due to a mechanism involving twin intersections and not compression only [95].

1.5.2 Influence of surfaces on the stability of polytype 2H in nanowires

Figure 1.20 shows how difficult obtaining the 2H polytype can be. It only concerns bulk material though. In nanowires, these results can be different since both surfaces and edges have to be considered for the calculation of the total energy of the system. The chemical environment is also expected to play a role, as adatoms may change surface energies. As the dimension of nanowires decreases, the surface to volume ratio increases. Consequently, the contribution of surfaces to the total energy becomes more and more important. For extremely thin nanowires of diameter below 2 nm, it was shown that the cubic diamond phase might not be the stable phase anymore in Si [136]. Another study predicted that the 2H polytype should become stable in SiNWs for all diameters below 100 nm [137]. However, the cubic diamond structure remains the norm even for nanowires below this diameter threshold [30, 31, 138].

The two reported studies [136, 137] were on $[111]_C/[0001]_H$ grown SiNWs with an hexagonal cross-section. This is quite limited since SiNWs can have different morphologies. For instance, growth of SiNWs with a [110] or [112] growth direction is feasible. Because the growth direction can be different, so do the displayed facets. Reports of dodecagonal SiNWs also exist [139],

indicating that this structure should increase the contribution of edges to the total energy. For all these reasons, if a clear picture concerning the stability of polytype 2H is to be achieved, testing multiple SiNW and GeNW configurations is mandatory.

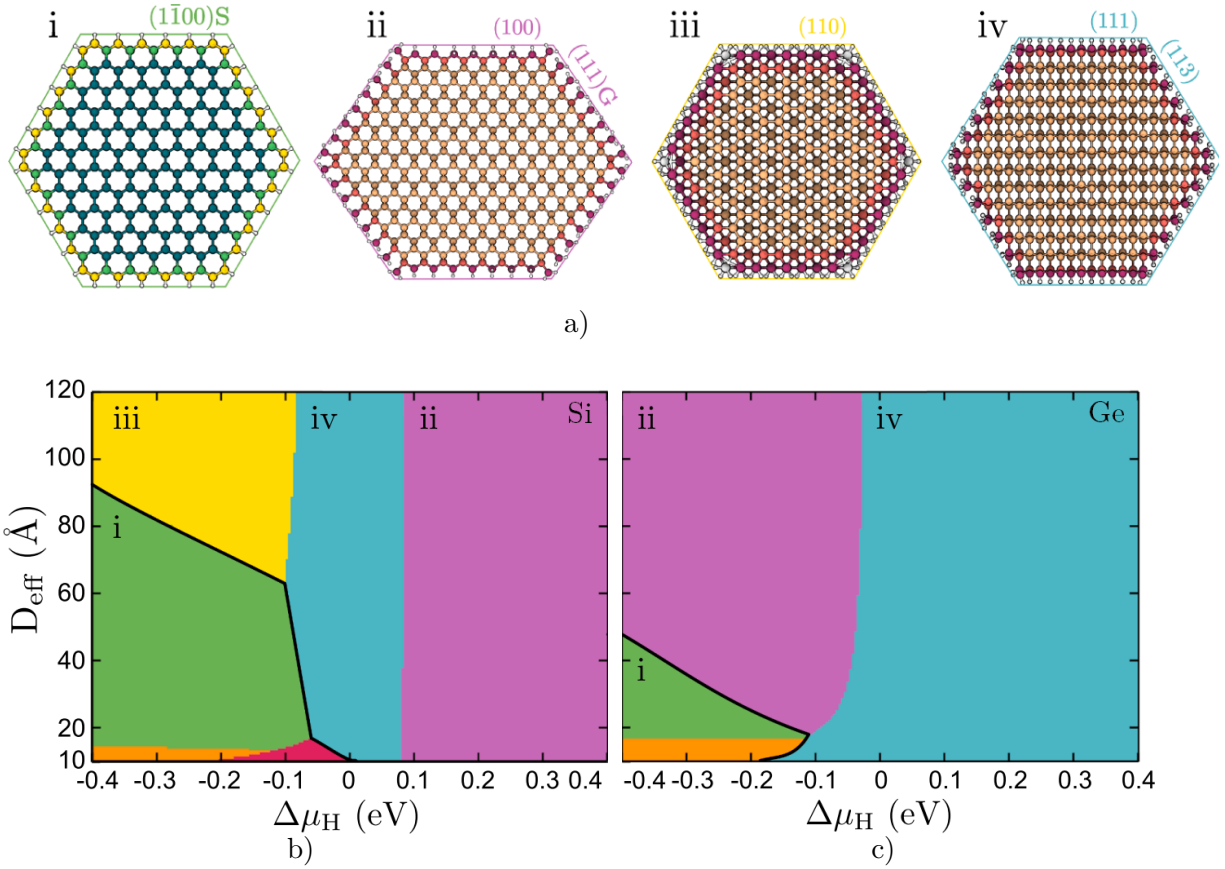

FIGURE 1.21: Diameter-H chemical potential phase diagrams for Si and GeNWs. a) Nanowire configurations. Atoms in white are H atoms, while the others are Si atoms. For them, the colors indicate how many nearest-neighbors they have. (i) Nanowire configuration with a 2H structure and [0001] growth direction, displaying {1$\bar{1}$00} lateral surfaces. (ii) 3C nanowire with a [110] growth direction with two different lateral surfaces: {100} and {111}. (iii) 3C nanowire with a [111] growth direction and {110} lateral surfaces. (iv) 3C nanowire with a [112] growth direction and two different lateral surfaces: {111} and {113}. b)-c) Phase diagram of Si and Ge. Each colored area corresponds to one most stable nanowire configurations indicated by the roman numeral. The numeral refers to the configuration in a). Modified from [140].

In an extensive study of both surfaces and edges in Si and Ge, Béjaud and Hardouin Duparc found that polytype 2H surfaces are overall less energetic than those displayed in 3C [140], except in the case of large area surface reconstructions. This and the larger bulk cohesive energy of 2H implies the existence of a critical diameter where the most favorable phase switches between 2H and 3C. Those authors tested multiple configurations of Si and GeNWs and calculated their total energy in order to confirm the existence of a critical diameter. From this, they estimated the critical diameter at 13 nm in Si. Thus, as suggested previously, size effects should impact the stability of 2H. In the case of Ge, the differences in energy between surfaces in 2H and those in 3C are not as large as in Si. Consequently, the critical diameter is predicted to be lower at 6 nm. These results are consistent with previous calculations in [135].

Let us now consider the chemical environment. In the VLS technique, Si and Ge atoms are usually supplied to the catalyst by the dissociation of Si_xH_{2x+2} or Ge_xH_{2x+2} molecules that are often mixed with H_2. The reactor therefore contains atomic hydrogen and partially dissociated silicon and germanium hydrides. H atoms are known to fix themselves to Si and Ge surfaces, by filling dangling bonds. Modifications of surface energies is the result of this change in the chemical environment. The effect of H atoms can be summarized in a single quantity: the chemical potential of H atoms $\Delta\mu_H$. There are therefore two degrees of freedom: the diameter D_{eff} and chemical potential of hydrogen $\Delta\mu_H$. A phase diagram was built [140] (Figure 1.21) which summarizes the most stable polytype as a function of those two quantities.

The phase diagrams show a clear trend. When H atoms are included in the calculations, the critical diameter, represented by a thick black line, decreases as the chemical potential of H increases. The effect is more pronounced for Ge. Also, we see that the 2H polytype has a clear tendency to prefer nanowires with a $[111]_C/[0001]_H$ growth direction and a hexagonal cross-section (configuration (i)). Experimental growth of 2H seems to support these simulation results [110]. These results provide valuable guidelines for our experiments. The authors have warned however, that interpreting the physical meaning of the chemical potential $\Delta\mu_H$ is not straightforward. Furthermore, the phase diagrams only indicate which phase is the equilibrium one at the temperature of 0 K, while the growth is clearly an out-of-equilibrium process involving high temperature and important physical and chemical effects such as diffusion and nucleation. Thus, more theoretical studies involving these aspects are necessary for getting the full picture at the typical experimental conditions.

1.5.3 Kinetic aspects and nucleation theory

The positions of atoms are chosen when new layers are grown. Which polytype is formed is then determined at the time of the growth. Careful considerations of the growth kinetics should thus complete the guidelines obtained from Section 1.5.2. While the temperature and pressure are generally constant during experiments, the total number of precursor atoms in the nanowire system is fluctuating since atoms are adsorbed from the vapor phase to the catalyst droplet, and atoms are leaving the droplet after they precipitate to form the nanowire. There can also be other channels such as diffusion of precursor atoms from the nanowire sidewalls to the catalyst, increasing the number of precursors in the droplet; or desorption from the catalyst to the vapor phase, which has an opposite effect (Figure 1.22). It is important to note that the effects described are temperature dependent, often following an Arrhenius law. DFT studies are unable to consider these kinetical aspects that affect how much precursor atoms are in the catalyst, which is the driving force for the growth of the nanowire [141].

Crystal growth generally involves the formation of small solid nuclei, obtained for example from the condensation of dissolved atoms in a liquid solution. A physical description of this process can be given through classical nucleation theory. In this theory, the chemical potentials of the old μ_d (dissolved) and new (solid) phase μ_s are considered. The difference between the two quantities $\Delta\mu = \mu_d - \mu_s$ is the driving force for the phase transition. A physical interpretation of this value could be the gain in free energy per atom associated with the phase change. Depending on its value, different situations arise. If the chemical potential difference is negative, the catalyst particle is undersaturated in precursor atoms, the natural trend will be to increase the concentration of precursor atoms in the catalyst, thus the formation of a solid precipitate is unfavorable while the dissolution of the solid phase is preferred. If the difference

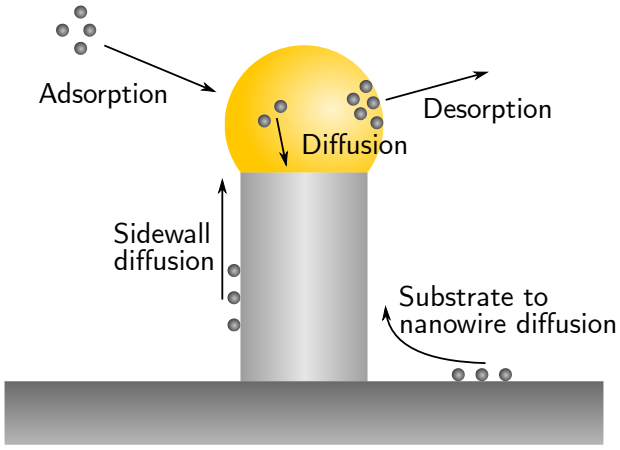

FIGURE 1.22: Example of temperature-activated phenomena during nanowire growth.

is zero, the catalyst is saturated, and a situation of equilibrium is reached. The formation of solid precipitates is stopped and so is dissolution. If the difference is positive, the growth is resumed. The latter is the situation that is of interest in the context of nanowire growth. The supersaturation s is the ratio between the current concentration of dissolved atoms in the liquid c and the equilibrium concentration in the liquid c_{eq}: $s = c/c_{eq}$. This quantity is linked to the difference of chemical potential between the two phases:

$$s = \exp\left(\frac{\mu_d - \mu_s}{k_B T}\right) \tag{1.9}$$

Suppose that a positive chemical potential difference is reached. In this case, the continuous formation of solid nuclei is still not guaranteed. Indeed, an energy barrier is associated with the creation of a new phase because an interface of energy σ per unit area between the dissolved phase and the solid phase is created, which adds up surface energy cost. Thus, depending on the typical nucleus size and the interfacial energy, precipitation only occurs once a threshold excess chemical potential is reached. The value of the threshold depends on whether the nucleation is said to be homogeneous, the nucleus is completely immersed in the catalyst, or heterogeneous, the nucleus is located at another interface in the catalyst. Homogeneous nucleation is in general a rarer process compared to heterogeneous nucleation as the supersaturation threshold is higher, more interfaces are created in the former case. A textbook example is the supercooling of water. In the absence of impurities, pure liquid water can be brought to temperature below 0 °C. Adding impurities at these temperatures will provide favorable nucleation sites for ice formation. In nanowires, heterogeneous nucleation is also preferred, as precipitation occurs at the catalyst-nanowire interface.

An important result derived from nucleation theory is that the growth rate of nanowires using the VLS technique depends on the growth conditions. It was shown by solving adatom diffusion equations that the growth rate $\mathrm{d}l/\mathrm{d}t$ depended on: the effective arrival flux of precursor atoms in the catalyst V, the temperature T, the nanowire radius R and the chemical nature of the catalyst through the excess chemical potential in the liquid $\Delta\mu_{LS}^{\infty}$ and the Gibbs-Thomson

radius R_{GT} [142]:

$$\frac{1}{V}\frac{\mathrm{d}l}{\mathrm{d}t} = \left[1 - \exp\left(\frac{\Delta\mu_{LS}^{\infty} - \Delta\mu_{AS}}{k_B T} + \frac{R_{GT}}{R}\right)\right] \times \left[\frac{1}{\sin^2\beta}\exp\left(\frac{\Delta\mu_{AS} - \Delta\mu_{VS}}{k_B T}\right) + \frac{2\lambda}{R}\frac{K_1(R/\lambda)}{K_0(R/\lambda)}\right] \tag{1.10}$$

with $R_{GT} = 2\gamma_{LV}\Omega_L \sin\beta/k_B T$ in which γ_{LV} is the liquid-vapor surface energy, Ω_L is the elementary volume in the liquid phase and β the contact angle. Decreasing nanowire diameter below R_{GT} induces lower growth rate because of the Gibbs-Thomson effect [143]. Other quantities in Equation (1.10) involve the adatom diffusion length λ and the chemical potential differences between the substrate (S), the adatoms (A) and the vapor (V). K_0 and K_1 are the modified Bessel function of the second kind of the zeroth and first order respectively.

1.5.4 Application of nucleation theory to III-V nanowires

The use of nucleation theory can also determine which phase is most likely to form. This is of special interest to us since we want to know under which conditions the different Si and Ge polytypes will arise. Unfortunately, no such study exists on Si and Ge NWs at the time of the writing of this thesis. This framework was however successful in explaining some experimental results in III-V nanowires, in particular why the wurtzite phase would form instead of the zinc blende phase. Indeed, there is a rule stating that the heavier the column-V elements, the more stable the zinc blende structure will be compared to wurtzite [144]. GaAs for instance is supposed to crystallize into the zinc blende structure. The difference in bulk cohesive energy between zinc blende and wurtzite is on the order of 24 meV per III-V atom pair [144]. Nevertheless, it was found that the wurtzite structure can be present in GaAs NWs of up to 50 nm in diameter [145]. This has to be compared with what is predicted for bulk Si and Ge (see Section 1.5.1) and the observations in SiNWs (see Section 1.3.4).

Thus, GaAs NWs are objects that, although they do not behave quite similarly to Si and Ge NWs, can give guidelines for the growth of the 2H polytype. Also, contrary to Si or Ge NWs, multiple experimental studies successfully synthesized the GaAs wurtzite structure using the VLS technique [146]. Although earlier studies showed wurtzite phase with a high density of stacking faults [147, 148, 149], more advanced experiments showed GaAs NWs with alternating wurtzite and zinc blende sections with controllable length. This is done by modifying growth conditions in real time, in particular the III/V gas or flux ratio [150, 151, 152]. Low ratios favor the formation of wurtzite sections while high ratios yield zinc blende sections. By stabilizing the ratio, long pure sections of wurtzite with a diameter of around 30 nm are synthesized [151, 152].

These observations can be understood in the framework of nucleation theory [153]. As described in Section 1.1.3, the growth of NWs by VLS occurs in a monolayer by monolayer fashion. A monolayer is created through the growth of a small nucleus. This nucleus is created by the III-V elements present in the catalyst particle in supersaturation. A critical point in the theory resides in the location where the nucleus appears. Indeed, depending on this location, the formation energy of the nucleus is not the same because of different involved interfaces. This is shown in Figure 1.23. When the nucleation site is fully contained in the catalyst particle, no nucleus-vapor interface is created. If the nucleation site is located at the edge of the nanowire on the triple phase boundary, one nucleus-catalyst interface is replaced by a nucleus-vapor one. In the latter case, wurtzite is nucleated while in the former, zinc blende is obtained.

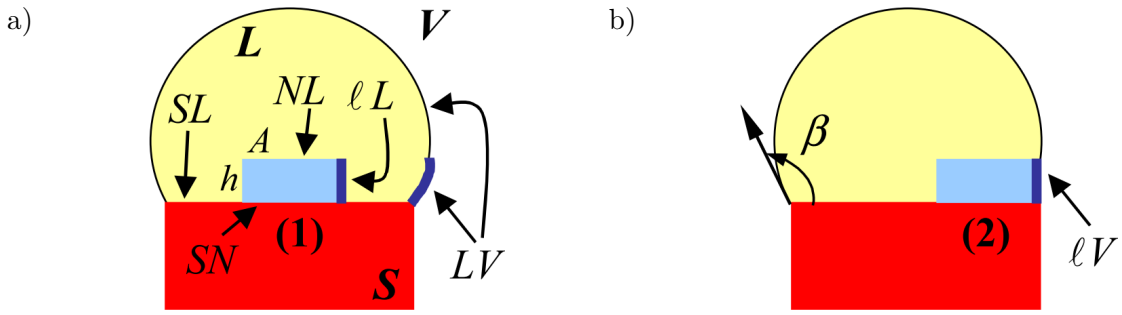

FIGURE 1.23: Interface created by the formation of a nucleus during a VLS growth in the case where: a) the nucleus is formed completely inside the catalyst particle; b) the nucleus is formed at the nanowire edge. β is the contact angle. Reproduced from [153].

The nucleation site in GaAs NWs can be selected by changing the shape of the catalyst particle, and in particular its contact angle. The latter is the angle defined by the catalyst-nanowire interface and the tangent to the catalyst particle. Indeed, the contact angle β is a quantity that appears in the equation governing the cost in energy of the formation of a nucleus ΔG_j [153]:

$$\begin{aligned}\Delta G_j = &- Ah\Delta\mu + A\gamma_{SN} \\ &+ Ph\left[(1-\alpha)\gamma_{\ell_L} + \alpha\left(\frac{\gamma_j}{\cos\theta_j} + (\gamma_{LS} + \gamma_{LV}\cos\beta)\sin\theta_j - \gamma_{LV}\sin\beta\right)\right]\end{aligned} \tag{1.11}$$

where the j index denotes whether the nucleus is wurtzite (W), zinc blende with Ga-terminated lateral edges (A) or zinc blende with As-terminated lateral edges (B). A is the area covered by the nucleus, h its height, P its perimeter. γ_{ij} are surface energies between phase i and j (see Figure 1.23), α is the fraction of the nucleus perimeter in contact with the vapor phase and θ_j is the angle between the wire sidewall and the catalyst-nanowire interface. By analyzing the equation, Glas *et al.* showed that, depending on the nucleation site: either at the triple phase boundary or inside the liquid droplet, the energy cost was different and depended on the contact angle and the nucleated polytype. In another study, Dubrovskii *et al.* [154] linked the contact angle and nanowire tapering with the formation of either the zinc blende or the wurtzite structure. High ($> 128°$) and low ($< 111°$) contact angles should favor zinc blende while intermediate values favor the wurtzite structure. Because As is more difficult to be absorbed by the catalyst particle than Ga, the growth of GaAs NWs is often limited by the amount of As in the catalyst particle. Therefore, if too much Ga is supplied to the catalyst, the excess Ga cannot be used to nucleate GaAs, thus increasing the catalyst volume, which in turn increases the contact angle and consequently the nucleus formation energy. This explains how a change in the III-V ratio can induce a phase transition.

While the formation of the metastable wurtzite structure in GaAs NWs is now well understood, the direct application of results derived from nucleation theory and experimental protocol to group-IV nanowires is not trivial for several reasons. First, Si and Ge are monoatomic compounds, so a similar technique involving a flow ratio between two compounds for synthesizing polytype 2H is not possible. Furthermore, the equations obtained from nucleation theory involve surface energies. However, the surfaces found in Si and GeNWs are different compared to those in GaAs NWs. Also, while this theory explained nicely these phenomena with both Au-catalyzed and Ga-self-catalyzed growth, it was not tested with a Sn catalyst, which was the catalyst used to grow 2H SiNWs in the first place. The few experimental studies for Si [110] suggest that (i)

stabilizing a 2H nucleus through the above-described mechanism does not occur, probably due to a different hierarchy in surface energies and (ii) a small diameter could stabilize the 2H phase. Due to the lack of experimental data and a complete theory tailored to group-IV nanowires, the consistent synthesis of the 2H phase in both Si and GeNWs remains a challenge at this point.

Conclusion of the chapter

In this chapter, we have seen that Si and Ge are indirect band gap semiconductors, which fundamentally limits their usefulness in terms of both electronic and optical properties. Theoretical investigations show that the indirect nature of the band gap could disappear when Si or Ge crystallize in the hexagonal diamond structure, or polytype 2H, with a wire-like shape, improving Si and Ge optical absorption properties. Several domains of applications could use the improved performance of Si and Ge 2H NWs such as optoelectronics or thermoelectricity. Obtaining the hexagonal diamond structure spontaneously in SiNWs and GeNWs is however challenging, which is problematic for synthesizing large quantities, necessary for these applications. Indeed, the established way involves either the application of shear stress or the epitaxial growth on a wurtzite template. The spontaneous formation of the 2H polytype in SiNWs was observed but the formation mechanisms are unclear. Furthermore, no complete theory involving both equilibrium and kinetical aspects yet exists.

In this context, the aim of this thesis is to get insights on what stabilizes polytype 2H in Si and GeNWs. We propose an experimental approach to this problem. Indeed, one of the biggest issues at this point is the lack of experimental data concerning the growth mechanism of polytype 2H. We propose to follow the evolution of the system in real time during our growth experiments. Ideally, we want to access pertinent physical quantities and to test the response of the system to changes in growth conditions in real time. The elaboration of an experimental protocol capable of coping with such requirements poses a unique challenge and will be developed in further details in the next chapter.

CHAPTER 2

Experimental setup for growth and observations

2.1 Why *in situ* transmission electron microscopy?

The goal of this thesis is to understand the mechanisms of formation of the metastable 2H phase in Si and GeNWs. Thus, we want to use an experimental apparatus that is able to synthesize this particular phase. The most obvious candidate for this task is the same piece of equipment with which this phase was first obtained [110]: the plasma-enhanced chemical vapor deposition (PECVD) reactor Plasfil. The growth technique and experimental conditions can be taken similar to those used in that study. However, while reproduction of that experiment should eventually give hexagonal diamond SiNWs, this will not provide more information on the growth itself than it is already explained in the previous work as the PECVD reactor lacks high-resolution imaging during growth. Indeed, since nanowire growth via the VLS method generally occurs in a monolayer by monolayer fashion (see Section 1.1.3), the ability to distinguish individual atoms in the growing nanowires provides the ultimate approach to differentiate between the 3C and the 2H phases. Furthermore, this investigation must be done in real time in order to understand the kinetics of the growth. Also, growth followed by *in situ* observations prevents the formation of an oxide shell around the nanowires, since there is no air exposure during the sample observation. This is not the case for PECVD growth, as the oxidation during the transfer of the sample to a characterization tool is unavoidable.

Very few characterization tools have atomic resolution. Among them, we can cite scanning tunneling microscopy (STM), atomic force microscopy (AFM) and transmission electron microscopy (TEM). The first two techniques are limited to surfaces only while also lacking sufficient time resolution for a real time study. Indeed, both techniques require the displacement in a scanning fashion of a sharp physical tip over a surface to gather information on the position of atoms. This scanning can take several seconds before an image is formed. To give an order of magnitude, the growth rate of the 2H SiNWs in the above-mentioned study [110] is in the order of $8.3\,\text{Å} \cdot \text{s}^{-1}$ or a little more than two atomic monolayers per second. Obviously, AFM is not adapted for the purpose of our experiments. There are however some research on high-speed AFM that brings the time resolution to below 100 ms but with impaired spatial resolution [155]. Thus, transmission electron microscopy is a better choice, with up to 0.08 nm spatial resolution and time resolution not limited by the scanning of a physical tip.

Conventional TEM was initially not designed for growth experiments. Indeed, to function properly, it requires high vacuum (less than 10^{-6} mbar). The development of differential pumping systems in TEM [156, 157] contributed to the elaboration of the environmental transmission electron microscopy (ETEM) technique, where a pressure up to a few mbar can be obtained in the specimen chamber. This is of relevance to us because the VLS technique involves the supply of precursor atoms to catalytic seeds via a vapor phase. Finally, adding a fast acquisition camera allows for the real time recording of the growth. The NanoMAX microscope, which has been developed by LPICM in partnership with the Centre de Nanoscience and Nanotechnologies (C2N) in the framework of the TEMPOS "Equipex", is equipped to fulfill all the previous requirements for such an operando system.

In situ TEM growth is therefore an appealing solution for the problems raised above, given that this technique has been successful in highlighting new phenomena [158, 159]. However, the conditions may differ between TEM and the PECVD growth done in the Plasfil reactor, such as the geometry, how the gas is injected and how reactive species generated in a remote plasma reach the substrate under the electron beam. Therefore, we will first test a specific growth condition in the PECVD reactor and then try to replicate the experiment in the NanoMAX TEM. The comparison between the two growth results may be very informative and will help identifying the dynamics and the most important conditions necessary for the growth of 2H NWs.

We have formulated the experimental needs in terms of resolution and growth, and concluded that only an *in situ* ETEM can achieve them. The rest of the chapter is focused on presenting the experimental techniques, equipment, and the preparation of samples for the growth.

2.2 Plasma-enhanced chemical vapor deposition growth

Plasma-enhanced chemical vapor deposition (PECVD) is a type of thin-film deposition technique which uses an electrical discharge to generate a plasma resulting from the dissociation of the gas precursor molecules [160]. In standard CVD, dissociation is done through high temperature conditions only. The use of plasma has several advantages. First, the growth can be carried out at lower temperature because the precursor dissociation process is due to collisions between the molecules and electrons. For instance, SiH_4 is known to dissociate rapidly above 500 °C [161], while SiNWs growth can start for temperature as low as 300 °C and thin film deposition at room temperature in PECVD processes. Low temperature processes are especially useful when dealing with thermally fragile substrates [162]. The film quality is comparable to that obtained in standard CVD [163].

The substrate is placed in the reactor chamber which is pumped down (between 3×10^{-6} mbar and 5×10^{-5} mbar) to prevent the incorporation of impurities (O, C and N) during the process. Precursor gases are introduced into the chamber through the inlet. Several gases are available in this equipment and are used for different purposes. Those which are of interest to us are SiH_4, GeH_4, H_2, and Ar. SiH_4 and GeH_4 will provide the necessary Si and Ge for the growth of nanowires. Note that while SiH_4 inside the gas cylinder is pure, it is not the case for GeH_4 which is diluted in 99 % H_2 due to its toxicity. There are mass flow controllers that can individually set the desired flow for each gas. The total pressure of the reactor is controlled by both the gas flow and the pumping speed. A butterfly valve located at the outlet with a controllable opening regulates the pumping rate. Typical pressures for nanowire growth are in the range of a few

mbar.

a)

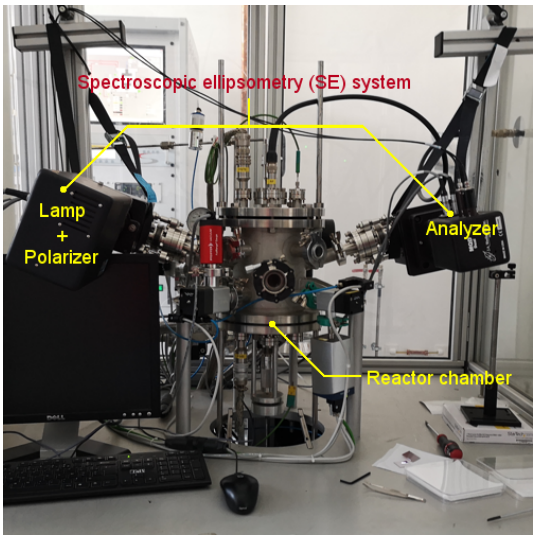

b)

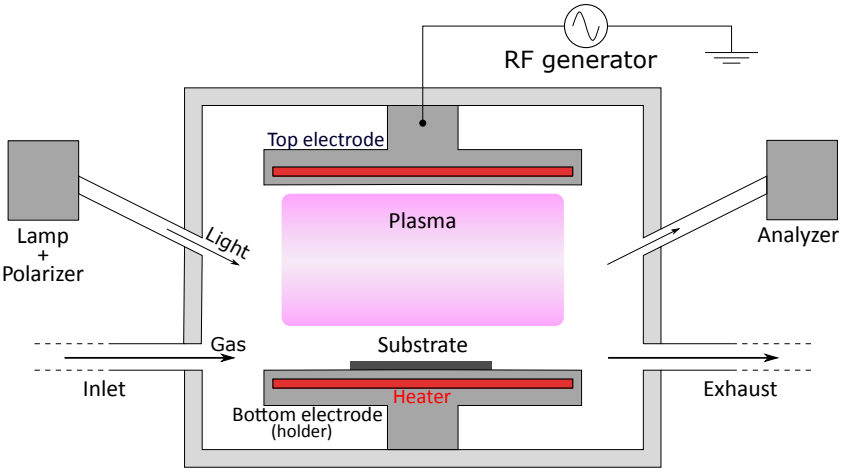

FIGURE 2.1: a) Photography of the Plasfil PECVD reactor. b) Schematic of the reactor.

There are two heating elements in the reactor, also doubling down as electrodes. They are located on the top and bottom of the chamber. The substrate is placed on the bottom one. While the top one can, for safety reasons, only be heated to 200 °C (nominal heater temperature), the bottom one is set for a maximum nominal temperature of 650 °C. Note that the substrate is not in the direct contact with the heating element, but with the bottom electrode, and therefore, the temperature provided by the heating element is not the real substrate temperature. To accurately assess the substrate temperature, a calibration has been performed with a probe placed on the substrate holder itself. Therefore, we are able to give the correct surface temperature as a function of the nominal temperature of the bottom heating element.

Plasfil is a capacitively-coupled plasma (CCP) reactor. It has two electrodes, the bottom one is grounded while the top one is connected to a 13.56 MHz radio-frequency generator. When the power is switched on, an electric field is created between the two electrodes which accelerates residual electrons alternatively towards the top and bottom electrodes. These initial electrons are produced from particles ionized by cosmic rays or existing photoelectrons. Electrons with sufficient kinetic energy may start to dissociate the gas molecules in the chamber. When

dissociation occurs, positively charged ions, radical species and electrons are generated. The newly generated electrons will in turn dissociate the gas molecules and a chain reaction begins. The plasma state is achieved, and a static electric field establishes itself. Positive ions are accelerated towards the substrate by the electric field, bombarding it. Due to the reactive nature of these species and the electrons high kinetic energy, we have an increased growth rate compared to CVD without plasma and film growth is possible even at room temperature [164, 165, 166].

An issue mentioned in previous subsection is the direct feedback during growth process. The Plasfil reactor is equipped with a spectrometric ellipsometer (SE) system providing data in real-time during nanowire growth [167]. This ellipsometer has two arms. On one arm, a lamp followed by a polarizer emits a polarized light directed towards the substrate. Part of the beam is reflected by the latter and travels to the second arm of the ellipsometer, where the detector and analyzer are located. When the light interacts with the sample, changes in its polarization occur. The detector is able to measure the change, and deduce various parameters related to the growth if an optical model of the substrate is provided. For example, thickness of deposited amorphous Si layer, the presence of nanowires, or catalyst transformation processes in real time. A limitation of this instrument is its macroscopic nature, allowing us to only see an averaged optical response from large sample area (up to tens of square millimeters).

In Plasfil, nanowires are usually grown on Si wafer. These can be directly transferred to a scanning electron microscope for observation. This is not the case for the transmission electron microscope where thin samples are a necessity as we will explain later. Thus, we must first transfer the nanowires from the Si wafer onto the amorphous carbon membrane of a carbon-coated Cu or Au TEM grid. We use the scratching technique to do so. Several droplets of isopropyl alcohol which will act as a solvent are poured on the nanowire-full face of the Si wafer. The Si wafer is then scratched repeatedly with a metallic tweezer to detach the nanowires from the wafer and join the aqueous phase to form a suspension. This solution is then transferred to the Cu grid with a micropipette. A sufficient number of nanowires on the grid is obtained when this process is repeated five to eight times.

2.3 Observing nanowires with electron microscopy

2.3.1 Principles of electron microscopy

2.3.1.1 The choice of electrons for the probe

To observe an object through an optical system requires the use of a light source. In every day's life, visible light is the most common choice. Since light is a wave, it will diffract on the structures we grow, which determines the spatial resolution at which they can be observed. Diffraction always occurs, but its effects are lower if the wavelength of the probe is below the size of the obstacles. Typically, the resolution power d of an optical system, which is the smallest distance between two points of the observed object that the system is able to distinguish, is given by:

$$d = \frac{0.61\lambda}{NA} \tag{2.1}$$

where NA is the numerical aperture, with $NA = n \sin \alpha$. n is the refractive index and α the aperture angle (the maximum angle from the optical axis a ray can enter the optical system). We see in this equation that λ, the wavelength of the probe intervenes. However, because visible light has a large wavelength compared to the typical dimensions of the nanoscale objects that we grow, it is a very ill-suited choice for the type of observations we want to carry out. Indeed, the wavelength of visible light ranges from 400 nm to 700 nm, while nanowires can have diameter from a few nm to a hundred nm. Also, we also want to precisely determine the position of atoms. Since the inter atomic distance is in the order of 0.1 nm, we thus prefer to use lower wavelength probes instead of visible light to have a good resolution that is to have a resolution that is not limited by diffraction.

X-Rays are a potential candidate because of their short wavelength. With them, structural analysis of samples is possible via the X-ray diffraction (XRD) technique [168]. However, they are not charged and as a result they weakly interact with matter. In order to have sufficient signal intensity, thick samples are necessary. This requirement is not compatible with the characterization of thin nanowires. Electrons interact more strongly with matter than X-Rays, so thin samples can be studied. Furthermore, they are easily produced by electron guns and can be manipulated by the application of a magnetic field. Therefore, electrons are the best choice.

Electrons are produced from an electron gun which comes in two types: thermionic or field emission [169]. When a material is heated, its electrons acquire thermal kinetic energy. Once a threshold temperature is reached, their kinetic energy becomes higher than the work function φ of the material and electrons are able to exit the material altogether. Value of φ is around a few eV which leads to the high operating temperature of thermionic guns. That is why thermionic guns are made of a W filament either raw or with a LaB_6 crystal welded to it. The W is chosen because of its very high melting point and relatively low cost. LaB_6 boast a higher lifetime than W tip and also have superior brightness, and its lower work function (2.4 eV) means that its operating temperature is also lower. It is generally present in most modern thermionic guns. Electrons are then accelerated by an electric field so that their resulting kinetic energy is from tens to hundreds of keV depending on the accelerating tension of the anode creating an electron beam. Field-emission guns (FEGs) extract electrons from a sharp tip by tunneling upon the application of an electric field. With this gun type, no heating is required at all so that the tip remains at room temperature. Such sources are called cold-field-emission (CFE) guns. There also exist FEGs that are heated for the purpose of having a more stable beam. These are called Schottky FEGs. The kinetic energy of the electrons determines their wavelength, which is then used in the calculation of the resolution of the microscope (Equation (2.1)). Given the velocity of the electrons accelerated by the strong electric field on the anode, they have to be considered as relativistic objects. The relation between the accelerating tension V and wavelength λ is given by:

$$\lambda = \frac{h}{\sqrt{2m_e eV\left(1 + \frac{eV}{2m_e c^2}\right)}} \tag{2.2}$$

where h is the Plank constant, m_e the electron rest mass, e the electron charge, V the acceleration voltage and c the speed of light. The obtained wavelength from Equation (2.2) can be injected into Equation (2.1) to obtain the theoretical resolution of the microscope as a function of the accelerating tension. For a typical 300 kV accelerating voltage and maximum angle α of 0.015 rad, an ideal resolution of 0.08 nm can be achieved, which is sufficient to distinguish atoms in a crystalline arrangement.

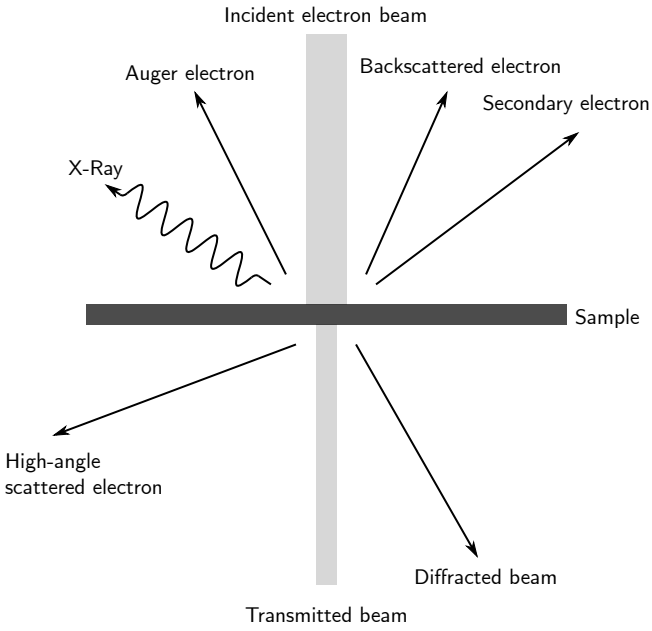

FIGURE 2.2: Schematic depicting the possible outcomes of an electron-matter interaction.

The focusing or defocusing of the electron beam is possible by using magnetic lenses. These consist of a cylindrical coil where a strong electrical current flows. A magnetic field is created inside the coil, modifying the electrons trajectory through the Lorentz force. Changing the current intensity induces variation of the magnetic field amplitude, which in turn changes the electron trajectories. Thus, contrary to typical optical lenses, the magnetic lenses focal length can be adjusted. Another difference between the two types of lenses is the angular aperture α. Magnetic lenses are more prone to optical abberations, so that α is limited to only tens of mrad, where optical lenses can be used for angles in tens of degree. Other aberrations may also decrease the real resolution, some of which are mentioned in Section 2.3.1.3. The high current in the lenses means that they require water cooling.

The sample, electron gun and beam are all placed in a closed vacuum enclosure. There are multiple reasons for this. The absence of air prevents the scattering of electrons due to collisions with the air molecules. In the gun, it also prevents the formation of electric arcs that would rapidly destroy the tip. Moreover, that vacuum must be ultra-high in the case of a cold field emitter, as the deposition of remaining atoms on the tip would rapidly disable the electron emission.

When the electron beam hits the sample, there is a multitude of electron-matter interactions [170], mainly scattering, which creates different kinds of radiations that can then be detected in order to characterize the sample or to create an image of it (see Figure 2.2). The nature of these interactions depends on the chemical composition of the sample and the incident electron energy. They can either be elastic or inelastic, the latter occur when the incident electron transfers a part of its kinetic energy to other particles. Different electron microscopy techniques detect different byproducts of these interactions. In the following sections, we will focus on scanning electron microscopy (SEM) and transmission electron microscopy (TEM) that are used in this thesis.

2.3.1.2 Scanning electron microscopy

In a scanning electron microscope, electrons are produced and focused into a very thin beam that rapidly scans the substrate surface. A possible result of high energy electrons hitting one of the sample atoms is the production of secondary electrons (SE). It is an inelastic interaction. The secondary electrons come from the ejection of valence electrons from their atomic orbitals. They typically have low energy and therefore, get often absorbed by the neighboring atoms. However, if the secondary electrons come from an atom that is close to the surface, it may escape the sample and thus be used for imaging purposes. Consequently, this technique is best suited for the study of the topography of a sample at nanoscale.

Another type of signal that can be exploited by a SEM is that of the backscattered electrons (BSE). Backscattered electrons are electrons from the incident beam which trajectories were deviated because of the sample atom nuclei. They have the same energy as the incident beam so that the interaction producing them is elastic. A very interesting property of this interaction is that its cross-section is Z sensitive. Thus, heavier nuclei are more likely to deviate incident electrons than lighter ones, which leads to a contrast between two chemically different areas of the sample. Methods based on the analysis of backscattered electrons offer basic localized chemical analysis.

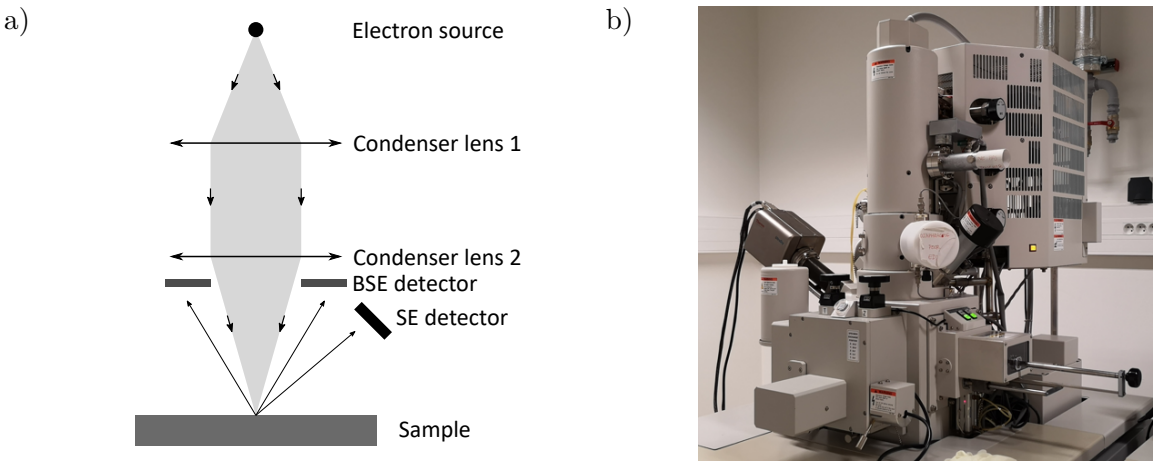

FIGURE 2.3: a) Simplified schematic of a SEM. b) Photography of the SEM used for our nanowire observations: the CFE Hitachi S-4700, which is also equipped with an energy dispersive X-Ray spectrometer, see Section 2.3.2.

The resolution of a SEM is generally limited by the size of the electron probe. Most SEMs have a resolution down to 5 nm with the accelerating voltage being from 5 kV to 40 kV. This means that a SEM is unable to distinguish individual atoms in the sample, as well as catalytic seeds with diameter below this 5 nm distance threshold. More specialized techniques such as electron channeling contrast imaging (ECCI) [171] or electron backscatter diffraction (EBSD) [172] can visualize defects and obtain some data on the crystal structure. These techniques require thick samples though, and thus the atomic structure in thin nanowires remains inaccessible. While this limits the usefulness of the technique, since we are interested in discriminating the hexagonal diamond phase from the cubic diamond, the SEM still holds unique advantages. For instance, the angle range of tilting in SEM is quite large, so that a sample can be viewed under several angles. Measuring nanowire length is therefore feasible even when they do not grow perpendicular to the substrate. The shape of nanowire cross-sections is also very acces-

sible, something that is more difficult in a TEM. Moreover, SEM allows one to observe thick substrates such as Si wafers, contrary to TEM. Finally, it is non-damaging, contrary to TEM.

2.3.1.3 Transmission electron microscopy

In SEM, we detect the byproducts of the interaction between the incident beam and the sample. In transmission electron microscopy (TEM), we are interested in the incident electron beam itself after it has gone through the sample. Due to this, information about the sample is no longer limited to its topology but rather its whole volume. To allow a significant portion of the beam to traverse the sample, the accelerating voltage of the electron gun (80 to 300 kV) is set much higher than in SEM and the sample must be thin enough (typically below 100 nm). For sufficiently thin substrates, the majority of the electrons from the incident beam are transmitted through the sample without any alterations on their kinetic energies or trajectory. Some electrons will be deviated.

a)

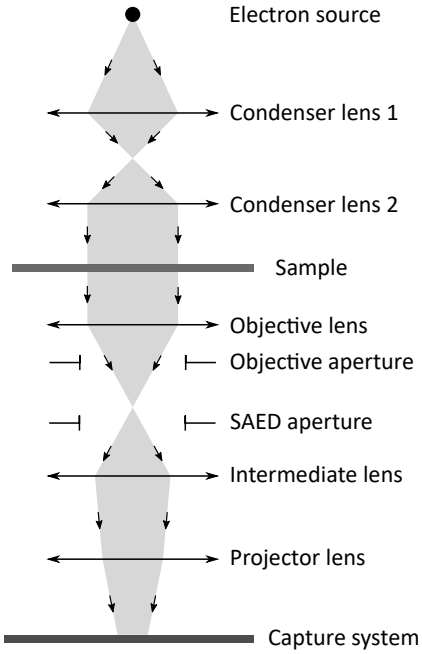

b)

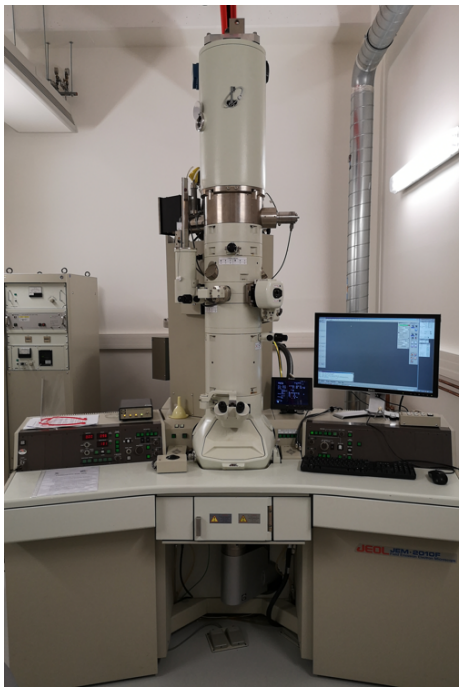

FIGURE 2.4: a) Simplified schematic of a TEM. b) Photography of the TEM used for our ex-situ nanowire observations: the Jeol 2010F equipped with a Schottky FEG.

The trajectory deviation experienced by the incident electrons depends on the arrangement of the atoms in the sample, it adopts the projected symmetry of the material. If the observed area of the sample is amorphous, the deviation presents a cylindrical symmetry related to the radial distribution function of the material. The latter represents the probability of finding an atom at a distance r from a reference one. Physically, it gives the average distance with first and higher order nearest neighbors. If the area is crystalline, then the action of atomic planes in the crystal is similar to a beam splitter where some electrons are transmitted and others reflected. Thus, for a given family of planes (hkl), the electrons are always reflected with the same angle (Figure 2.5). Bragg's law allows to derive the deviation angle:

$$\sin\theta = \frac{n\lambda}{2d_{hkl}} \tag{2.3}$$

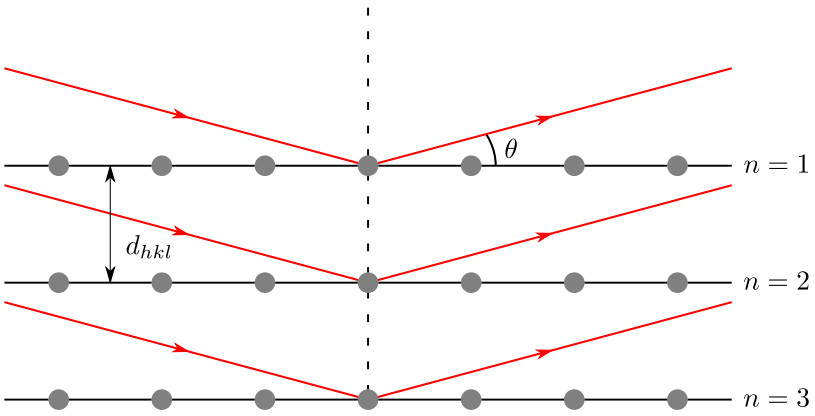

FIGURE 2.5: Electrons (in red) deviation by a set of (hkl) atomic planes according to Bragg's law.

where θ is the angle between the incident electron and the (hkl) planes, n is the diffraction order, λ the electron wavelength and d_{hkl} the interplanar distance of the (hkl) planes. The total deviation of the beam will be twice the angle θ. Suppose that the sample presents two areas with the same d_{hkl} spacing and the same thickness but oriented differently with respect to the electron beam, one in Bragg condition, the other not. Even though the deviation angle is the same, the diffraction patterns will be rotated to each other and the two areas will present different contrast even if they are structurally similar. This is called diffraction contrast.

We have seen that some directions are privileged in crystalline materials. In order to get a cartography of all these privileged directions, we need diffraction patterns. In TEM, we can modulate the strength of the intermediate lens: instead of projecting an image of the sample, we can rather expose the focal plane of the objective lens where there is an electron diffraction pattern. This will give a 2D image of the 3D reciprocal lattice of the sample perpendicular to the direction of observation. In orientations called zone axes (if the sample is crystalline), we will get a periodic set of spots. Adding a selected area electron diffraction (SAED) aperture allows to perform the diffraction operation on a chosen part of the sample. A second aperture, called the objective aperture, can select the central beam or a given diffracted beam in the pattern. In the latter case, going back to imaging mode with both apertures will yield a dark field image of the sample. Domains of the sample that contributed to the intensity of the selected diffraction spot will appear bright, while those which did not will appear dark. A popular use of this imaging mode is to clearly separate grains (domain with a unique structure).

To make the best use of the high resolution, aberrations in the optical system of the microscope should be kept at the minimum. There are mainly two types: chromatic (C_c) and spherical (C_s). Chromatic aberration rises from two contributions: the polychromatic nature of the beam and the inelastic scattering of the electrons in the sample. Electrons with different energies are focused differently by the magnetic lenses of the microscope, so that the image of a point in the sample is a circle. This results in a less sharp image. Spherical aberrations are due to electrons being focused differently the farther they are from the optical axis of the lenses. They are responsible for most of the resolution losses. Both aberration types can be corrected to some degree to acquire sharp images. An aberration corrector, which is present in most advanced tools, can remove most of the spherical aberration [173], while monochromators help alleviate the chromatic aberration [174].

2.3.2 Energy dispersive X-ray spectroscopy

When a high energy electron interacts with the core electrons of an atom, it may transfer its energy to a core electron, effectively ejecting it from its host atom. What is left for a short moment is a hole in the deep electronic layer of the atom. This state is not stable however, as this hole will be filled almost immediately by another electron transiting from the upper layers to the hole layer. When this occurs, the descending electron may liberate its excess energy in the form of an X-ray photon, as shown in Figure 2.6. In some cases, the descending electron may transfer its energy to another upper shell electron and eject it from its orbital: an Auger electron. The final outcome is random although the probability of either is known for each element. Higher Z elements have a higher probability of emitting an X-ray photon while lower Z elements will more often produce Auger electrons.

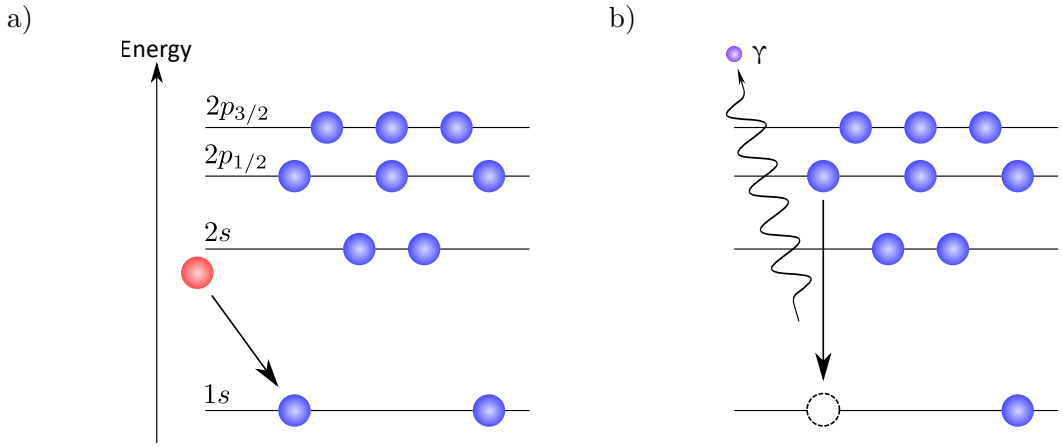

FIGURE 2.6: Schematics of X-ray photon emission by scattering of a high energy electron on a core electron. a) An electron with high kinetic energy (in red) interacts with a core electron. b) The core electron is ejected from the host atom, creating an excited state for the atom. It then relaxes by an upper shell electron filling the newly created hole. The transition creates an excess of energy, liberated as an X-ray photon (in purple).

For a given element, the energy levels of the electronic layers are discrete and well-known. Thus, the chemical nature of the element can be deduced from the energy of either the X-ray photon or the Auger electron. Energy dispersive X-ray spectroscopy (EDX) is focused towards detecting and measuring X-ray photons. For example, Si has a distinct X-ray line at 1.739 keV, called the Kα line. It corresponds to the transition from the electronic states 2p to 1s. Some lines from an element may overlap with lines from other elements, in particular if the energy resolution of the EDX detector is low. Confirming the presence of the other spectral lines for a given element is primordial to avoid misinterpretations.

In TEM, as seen in Figure 2.4a, a large area of the sample is bombarded. In scanning transmission electron microscopy (STEM), the beam is focused into a spot, then scanned along the sample, in a fashion similar to SEM. First, we acquire a high-angle annular dark-field (HAADF) image of a part of the sample that gives its topography. It allows one to select the analyzed area. Then, we slowly scan the sample in order to build a map of emitted X-ray photons: a full X-ray spectrum is recorded at each pixel. Coupling the EDX technique with STEM allows to acquire an EDX map with a very good resolution [175].

Although the technique is quite precise, it is limited by the very long exposure time required

to gather a statistically significant amount of photons. This is especially problematic for two reasons. On the one hand, the sample may drift due to thermal expansion or dilatation, on the other hand, long exposure to a high energy electron beam may induce severe irradiation damage. This can lead to change in morphology, composition or even destruction of the irradiated area.

2.3.3 Identification of the 2H phase

2.3.3.1 Image simulations

We presented the TEM technique whose resolution allows to distinguish the crystalline arrangement of atoms. At first glance, one could then assume that the simple observation of nanowires is enough to discriminate between polytype 3C and 2H. Indeed, they have different crystal structure. Despite this apparent simplicity, unfolding the polytype nature is not so straightforward. The reason comes from how TEM images are formed. They are 2D projections of a 3D structure along a specific axis. The imaging of crystals is especially dependent on the choice of this axis since they are anisotropic. Some axes will give more information than others due to their high symmetry. These are called zone axes and coincide with preferential directions in the crystal structure (see Section 1.2). Because we are interested in the crystal structure itself to discriminate between polytypes 3C and 2H, it is necessary to be in the right zone axis. When in relevant zone axis, an image can provide clear information about the observed crystal structure.

Thus, a TEM image needs to be interpreted before drawing any conclusions. In order to facilitate this part of the work, we can use computer simulated TEM images to compare between the experimental image and the calculated image of the hypothesized crystal structure. If the contrast patterns visible in both images are similar, we can then reliably conclude on the structure of the observed object. In the opposite case, the initial guess is most likely incorrect. In addition, electron diffraction pattern can be simulated to be directly compared with the measured one.

Electrons interact strongly with atoms, which means that the dynamic diffraction framework needs to be used as opposed to the kinematic one. In the former, a given electron can scatter multiple times over its course in the sample while the latter only considers one scattering event during the whole duration of the electron interaction with the crystal. The kinematic framework is generally less time-consuming in terms of computation but it does not work well with increasing thickness. Furthermore, it cannot explain double diffraction [176], a phenomenon where additional spots can appear on the diffraction pattern, even when they would not happen in an infinite crystal due to destructive interferences.

Algorithms that produce a TEM image of a crystal of thickness t have to take into account the scattering of electrons due to their interaction with matter. Therefore, they aim to solve the Schrodinger's equation in a periodic potential $V(\mathbf{r})$ to determine the amplitude and phase of the electronic wavefunction $\Psi(\mathbf{r})$ along directions given by the Bragg's law:

$$-\frac{\hbar^2}{2m}\Delta\Psi(\mathbf{r}) - eV(\mathbf{r})\Psi(\mathbf{r}) = E\Psi(\mathbf{r}) \tag{2.4}$$

Solving this equation is computationally demanding because of the very small wavelength of the incident high energy electrons. For example, 200 keV electrons have a wavelength of 0.025 Å. Thus, to accurately obtain variations of the wavefunction $\Psi(\mathbf{r})$ along the whole thickness of the

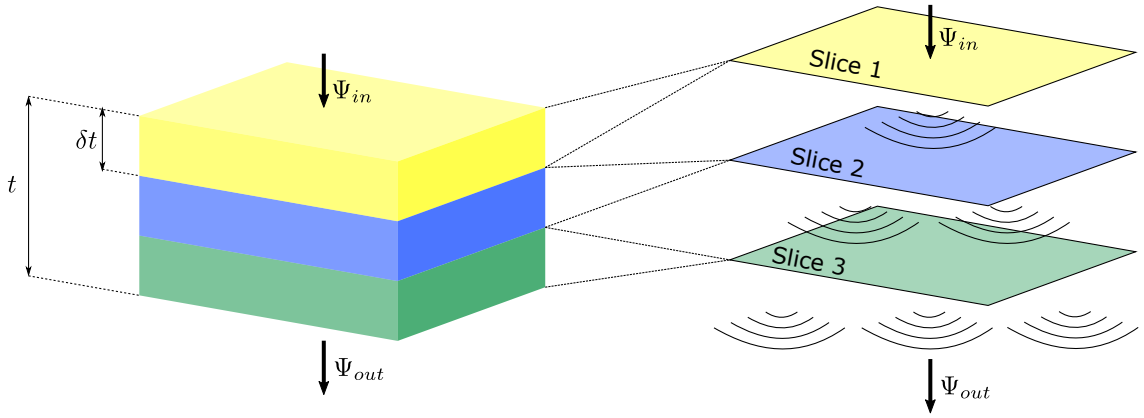

FIGURE 2.7: Schematics of the multislice algorithm for simulating TEM images. The left crystal is cut into three slices of equal thickness. The wavefunction of the incident beam is then transmitted and propagated through each slice and empty layer between them.

crystal, it is necessary to sample the crystal volume very finely. This leads to extremely high computer memory usage for crystals with only a moderate thickness ($\sim 10\,\text{Å}$). The multislice algorithm [177, 178] can provide a relatively fast way to find solutions by making two assumptions. The first one is that the wavefunction $\Psi(\mathbf{r})$ can be factored in two terms: one fast oscillating term due to the electron small wavelength and a slow varying one that accounts for scattering by the crystal:

$$\Psi(\mathbf{r}) = \Phi(\mathbf{r}) \exp(i\mathbf{k} \cdot \mathbf{r}) \tag{2.5}$$

with $|\mathbf{k}| = 2\pi/\lambda$ and $\Phi(\mathbf{r})$ the slow varying term. The slow variation of $\Phi(\mathbf{r})$ is guaranteed by the high electron energy, which should not change significantly on the scale of their wavelength. With this ansatz, we now solve Schrodinger's equation in $\Phi(\mathbf{r})$ and this does not require a space sampling as dense as before. The second assumption is that the crystal of thickness t is composed of multiple slices of equal thickness δt separated by empty layers (see Figure 2.7), which is where the multislice method derives its name from. The incident beam interacts with the projected potential of the first slice of thickness δt. The Schrodinger's equation is solved for this slice. Then, the solution is propagated to the second slice through Fresnel diffraction. This process is repeated for subsequent slices. The number of slices chosen depends on the thickness of the simulated crystal. Thicker samples require larger number for an accurate computation of the wave function.

Once the wavefunction at the exit of the crystal is acquired, its convolution with the contrast transfer function of the microscope will yield the desired simulated image. The contrast transfer function is unique to each microscope as it depends on parameters like the chromatic and spherical aberrations. It also depends on the defocus parameter $\delta f = f - f_0$, where f_0 is the distance between the sample and the front focal plane of the objective lens. For our simulations, we need to know the specificity of the used TEM in order to retrieve a reliable image directly comparable to a measured one. Fortunately, these are known, as they are provided by the manufacturer.

2.3.3.2 Relevant zone axes

Let us use the simulations previously described to calculate images and diffraction pattern of the 2H polytype. For that purpose, we use the JEMS package developed by P. Stadelmann [179] to carry out the necessary calculations. First, we build a supercell containing several unit cells of the 2H structure. The same is done for polytype 3C to make comparison between both polytypes possible. For convenience, both supercells have a cuboid shape with similar dimensions. The latter are chosen so that periodicity is preserved. In the following, the subscript indicates to which polytype the direction or plane belongs to. For example, $[111]_C$ designates the [111] direction in polytype 3C. As described in Section 1.2, the stacking direction of polytype 3C is $[111]_C$ and is $[0001]_H$ in polytype 2H. These two directions are parallel and we use the notation $[111]_C/[0001]_H$ in the following. Additionally, directions in the supercell coincide with high symmetry directions in both polytypes 2H and 3C. For example, the supercell **a** direction is parallel to the $[110]_C/[12\bar{1}0]_H$, **b** is parallel to $[112]_C/[10\bar{1}0]_H$ and **c** to $[111]_C/[0001]_H$.

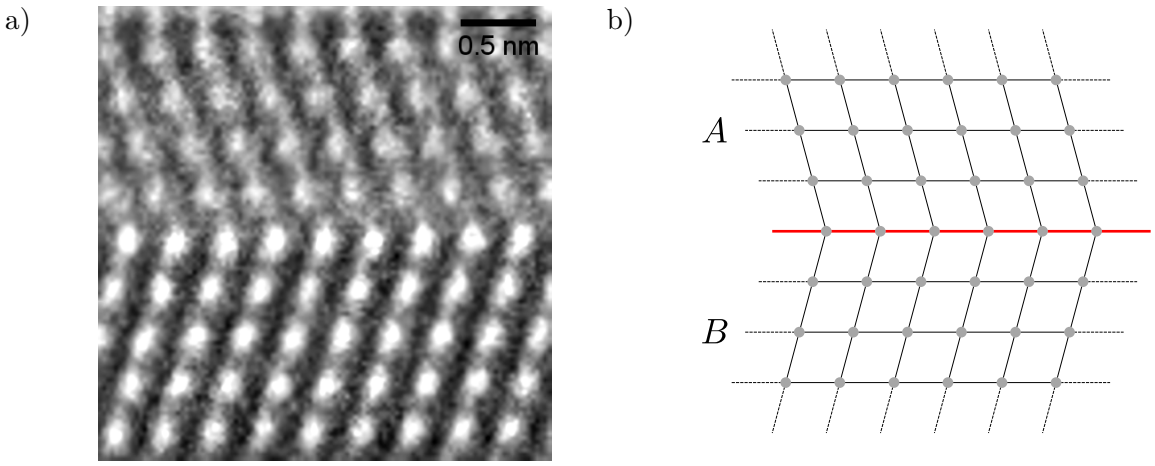

FIGURE 2.8: Twin defects occur frequently in group-IV crystals. A crystal grain is said to be in a twinning relationship with another grain when their orientations are related by a symmetry of the space group, but applied to the wrong axis or plane. In face centered cubic materials, natural twinning corresponds to a mirror symmetry about a $\{111\}_C$ plane ($\{111\}_C$ planes are no mirror planes in face centered cubic space groups). a) TEM image of two Si grains in a twinning relationship. b) Schematic of two grains A and B in a twinning relationship. The red line is a twin plane and also acts as a mirror plane.

We have carried out the dynamical diffraction calculations along the above-mentioned high symmetry directions. The diffraction patterns of both polytypes 3C and 2H in the $[112]_C/[10\bar{1}0]_H$ are shown in Figure 2.9a-b. We see that in both patterns, the spots are arranged in a similar rectangular lattice. It means that this specific zone axis does not allow for discrimination between polytype 3C and 2H. This is not particularly surprising as both polytypes have similar structure when viewed along this direction. Along the $[110]_C/[12\bar{1}0]_H$ direction (Figure 2.9d-e), the patterns widely differ. Polytype 3C exhibits a honeycomb arrangement, while polytype 2H is more rectangular like. Therefore, the $[110]_C/[12\bar{1}0]_H$ direction should allow distinction between the two polytypes. This is fortunate because since most Si and GeNWs grow in the $[111]_C$ or $[112]_C$ directions (see Chapter 3 and 4), the $[110]_C/[12\bar{1}0]_H$ zone axis will be perpendicular to the nanowires growth axis. In general, this is how we want to observe them. Finally, we consider the $[111]_C/[0001]_H$ direction (Figure 2.9g-h). This is a special case, as we clearly see a hexagonal symmetry in both diffraction patterns. However, the spacing between spots is different, 3C

having a $5.205\,\mathrm{nm}^{-1}$ spacing, while 2H is $3.015\,\mathrm{nm}^{-1}$. In theory, 3C and 2H are distinguishable in this zone axis. In practice, this is true only for defect free nanowires. Depending on the growth conditions, cubic Si and GeNWs can present twin planes that lie perpendicular to the $[111]_C$ direction. These defects break the order in the crystal and may change periodicity. This in turn can add additional spots in diffraction patterns. To test the previous statement, we can build a new supercell of 3C polytype with a twin plane (Figure 2.8) perpendicular to the c direction. Its dimensions are similar to the two previous ones. The diffraction patterns of the twinned structure are shown in Figure 2.9c, f, i. Along the $[112]_C$ direction, there are no major changes aside from a visible streaking between spots. Streaking due to twin planes is a very common occurrence. When viewed in the $[110]_C$ zone axis, streaking is again visible and we see some additional spots. However, we can still differentiate it from the 2H diffraction pattern. The real problem is with the $[111]_C$ direction, as the additional spots due to twinning coincide exactly with the new spots the 2H polytype has. Thus, when observation is done in this zone axis, the risk of confusion between twinned cubic and hexagonal diamond is very high. Consequently, the only common zone axis where differentiation between 2H and 3C is possible is the $[110]_C/[1210]_H$ direction. This has caused problem in previous literature, where claims have been made about the 2H polytype in SiNWs with $[111]_C/[0001]_H$ zone axis images. Cayron *et al.* [90] have warned about this risk and the same argument was used to doubt the existence of lonsdaleite [91]. In the next chapters, we will take great care to always be in the correct $[110]_C/[12\bar{1}0]_H$ zone axis to identify polytypes.

Let us verify the conclusions by simulating HRTEM images of the problematic $[111]_C/[0001]_H$ zone axis. To do so, we create several supercells of identical thickness set to 37.62 nm, which is equal to 40 times the unit cell length of polytype 3C along the $[111]_C$ direction or 60 times the unit cell length of polytype 2H along the $[0001]_H$ direction. In Figure 2.10a-b, we show the simulation result for a pure 3C and 2H supercell, respectively. While both images show hexagonal symmetry, they are still distinguishable from each other as the distance between bright spots is different between the two polytypes. Now, we add a twin plane perpendicular to the $[111]_C$ direction. Note that the position of the twin plane is carefully selected so that periodic boundary condition along the $[111]_C$ is still satisfied. We obtain the images shown in Figure 2.10c-f. While the position of the bright spots remains mostly the same, we start to see some change in the contrast. As more twin planes are added into the supercell, we observe more and more modifications in the simulated images. For a supercell containing six twin planes (Figure 2.10f), the exhibited spot configuration is now strikingly similar to the one displayed in the pure 2H supercell, which resembles a honeycomb. That means that there is a strong ambiguity of the $[111]_C/[0001]_H$ zone axis regarding the discrimination between polytype 2H and 3C when multiple twin planes are present. When there only are a few twin planes, discrimination may still be possible, although it is preferable to use another zone axis to unambiguously confirm the nature of the observed polytype.

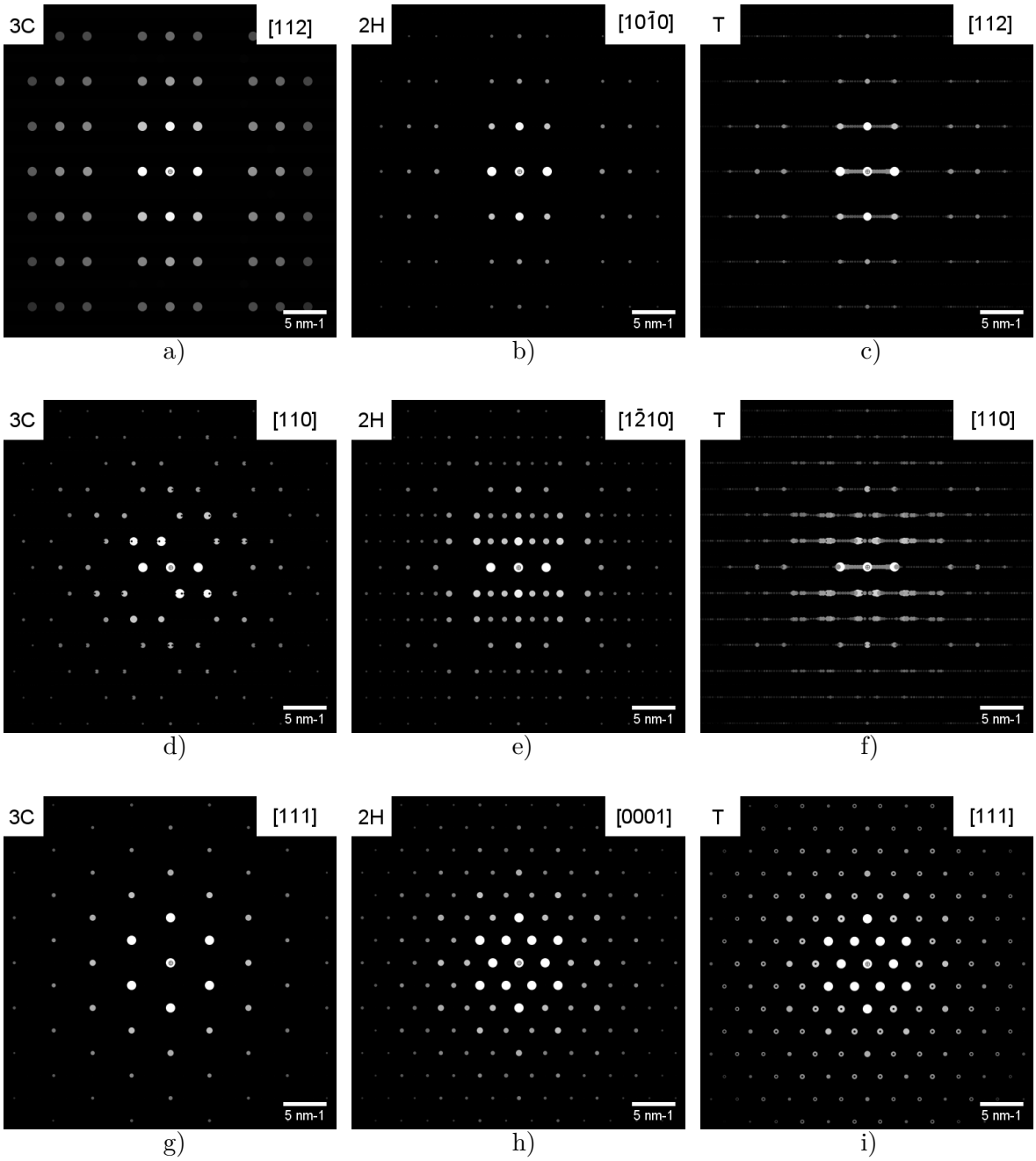

FIGURE 2.9: Simulated electron diffraction pattern of bulk Si for polytype 3C (a,d,g), 2H (b,e,h) and faulted 3C with several twin planes (c,f,i), noted T in the figures in three different zone axes: $[112]_C/[10\bar{1}0]_H$, $[110]_C/[12\bar{1}0]_H$ and $[111]_C/[0001]_H$.

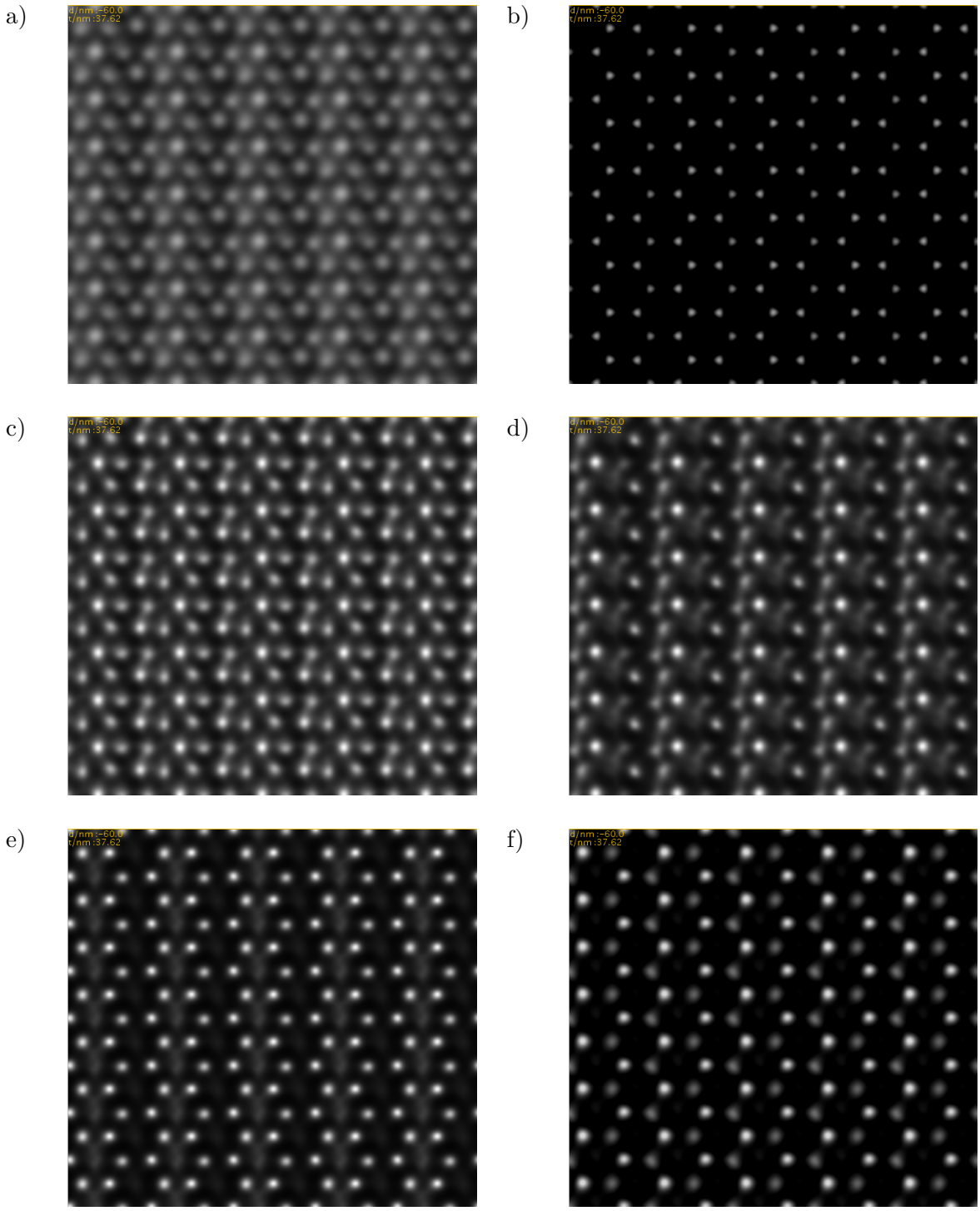

FIGURE 2.10: Simulated HRTEM images of polytype 3C, 2H and several twinned 3C structure in the $[111]_C/[0001]_H$ zone axis. The defocus is set to -60 nm for all simulated micrograph. a) Pure 3C. b) Pure 2H c) 3C supercell with one twin plane. d) With two twin planes. e) With four twin planes. f) With six twin planes.

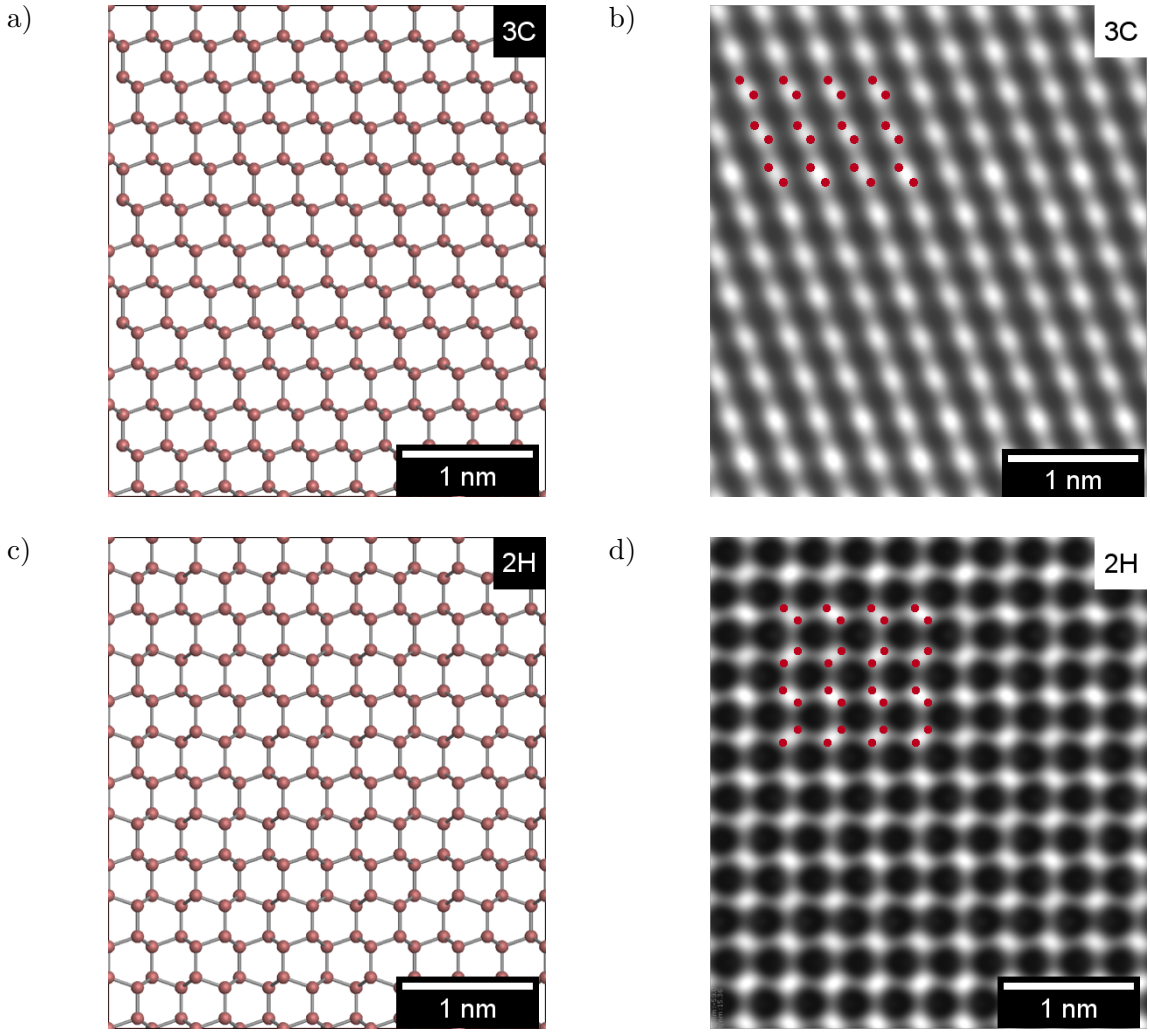

FIGURE 2.11: Simulated HRTEM images of polytype 3C and 2H in the $[110]_C/[12\bar{1}0]_H$ zone axis. The defocus is set to -59 nm. a)-b) 3C supercell and simulated image. The red dots in b) show the position of some atoms. c)-d) 2H supercell and simulated image.

Given the previous result, we now simulate what polytype 2H and 3C look like along the $[110]_C/[12\bar{1}0]_H$ direction. In this direction, the supercell thickness is 0.38 nm. Even a single slice is enough to accurately simulate a high resolution TEM image in this case. Using the characteristics of a Titan 80-300 TEM, we obtain the images shown in Figure 2.11. In both the 3C and 2H polytype, atoms are arranged in layers of dimers. When simulated, individual dimer yields a dumbbell-shaped contrast pattern. Thus, each bright spot in the HRTEM images corresponds to the contribution of a column of dimers. In the 3C polytype supercell (see Figure 2.11a), we can see that all dimers are oriented similarly and arranged in parallel diagonal lines. This is exactly why we also see diagonal stripes in the simulated image in Figure 2.11b. Ergo, the bright spots can be visualized in a diamond-shaped lattice where the angle between the diagonals is either (approximately) 110° or 70°. In the 2H polytype supercell, between each horizontal layer, the dimer orientation is flipped so that the diagonal arrangement of 3C vanishes (see Figure 2.11c). Subsequently, dimers in the HRTEM image belong to a square-shaped lattice as shown in Figure 2.11d. The clear difference between Figure 2.11b, d allows for the unambiguous differentiation between the 3C and 2H polytypes.

2.4 Growing nanowires *in situ*

We have presented the characterization techniques used for the purpose of this thesis. We now focus on the NanoMAX TEM used to grow Si and GeNWs *in situ*.

2.4.1 General characteristics of the NanoMAX microscope

NanoMAX is an environmental transmission electron microscope (ETEM) that we use to perform *in situ* growth of SiNWs. It is a modified Thermo Fisher Titan 80-300 microscope with a Schottky FEG and is equipped with an aberration corrector of the objective lens (Figure 2.12a). This grants a very high spatial resolution of 0.08 nm in TEM mode. Furthermore, the microscope is placed on a separated concrete slab to prevent external vibrations from disturbing the observations. For the same purpose, the microscope room is fitted with a magnetic field compensator, protecting it from electromagnetic perturbations. The microscope is equipped with an UltraScan 1000 camera thay is capable of recording *in situ* videos at a frame rate of 4 frames per second (fps) at a resolution of 1M pixels.

An EDX module is also fitted to the microscope, which, in combination with the STEM mode, allows to acquire detailed chemical maps. Additionally, a residual gas analyzer (RGA) allows to measure the concentration of gas species in the TEM column, provided that they can reach the detector. Detected gas molecules are classified depending on their molar masses.

a) b)

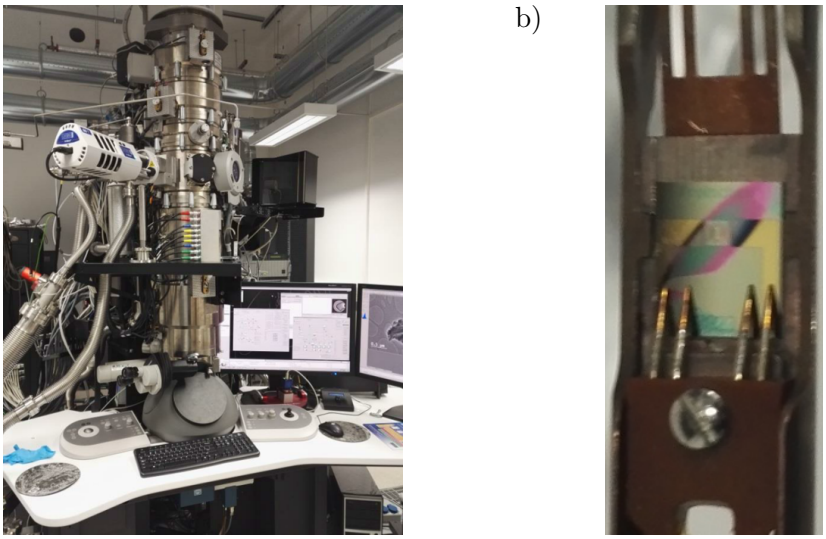

FIGURE 2.12: a) Photography of the NanoMAX microscope. b) Photography of the sample holder. Notice the four metallic tips in contact with the substrate.

Due to the special nature of the substrate used during our experiments, we also require a special TEM sample holder, shown in Figure 2.12b. It is provided by Protochips and contains an internal circuitry. It enables a connection to a power supply which can output an electrical current to the sample causing its heating. More details are provided in Section 2.4.4. The holder can be titled along two angles which is very useful for orienting the grown nanowires in a desired zone axis.

2.4.2 Atomic sources for growth

The originality of the NanoMAX microscope comes from the material sources that can be plugged into it to enable the growth of desired nanostructures. For that purpose, there are two ports on the side of the TEM column where such sources can be installed. These are located at the same height as the sample holder. In that way, the traveling distance of precursors inside the TEM is minimized (Figure 2.13a).

Sources in NanoMAX come in two types. The first type is Molecular Beam Epitaxy (MBE) sources (Figure 2.13b). This type of source relies on pure metallic pellets placed in a crucible, which is heated by the current flowing through W wiring around the crucible. By heating at a temperature above the evaporation point of the pellet, effusion of individual atom starts. The installation of a collimator directly in front of the source selects the emitted atoms with the correct trajectory. At the output of the MBE source, an atomic beam is created with the vapor pressure controlled by the temperature. A manually controlled shutter at the output of the source can stop the atomic beam whenever needed. Two MBE sources can be plugged to the microscope at the same time. Binary compounds can then be grown. For our experiments, we have used a Ge MBE source. No Si source was designed for the microscope due to the required high temperature (high Si melting point of 1414 °C), which could damage the O rings between the source and the microscope, compromising the structural integrity of the equipment.

The second type of sources used in NanoMAX is based on chemical vapor deposition (CVD). Such sources inject gaseous molecules into the TEM chamber. Mass flow controllers set up the desired flow for each gas type. Similar to PECVD growth, we use SiH_4 as the source for Si atoms. However, for GeNWs, the gas precursor was a mixture of 10 % Ge_2H_6 and 90 % H_2. The dilution in the gas cylinder is due to the high toxicity of germanium hydrides. Using higher order hydrides has some advantages: it requires less thermal energy to dissociate and for the same partial pressure of hydrides, the growth rate is significantly higher. H_2 acts in our experiments as the carrier gas. In some experiments, a specially developed gas injection is used (Figure 2.13c). Unlike in normal conditions, where gases are simply injected inside the column, it has a supplementary pipe which directly delivers the gas to the substrate. Therefore, in this configuration, molecules travel a shorter distance when compared to the simply filling the column. We find that this increases the pressure near the sample by a factor of 1.5.

Several gauges monitor the total pressure inside the TEM column in real time. The pressure values displayed tend to change slightly with time due to film deposition because of the cracking of the gases in the gauges themselves. Consequently, the total pressure values given are rather imprecise but should nevertheless give a good order of magnitude. For a given flux of SiH_4, the relative uncertainty on the pressure is around 20 %.

Having two types of sources is interesting from a chemical point of view. For GeNWs, MBE provides a source of pure Ge, while CVD sources deliver also H_2. Hydrogen is known to fill the dangling bonds on Si and Ge surfaces [180, 181], which leads to surface energy variations between MBE and CVD conditions. This will cause dramatic changes in the growth dynamics as we will see in Chapter 3.

To approach more closely the conditions in Plasfil reactor, where the 2H polytype has been previously demonstrated, an electron cyclotron resonance (ECR) plasma source was installed on the microscope. Electrons of charge $-e$, with mass m_e and velocity v in a stationary and homogeneous magnetic field of intensity B have their trajectories modified by the Lorentz force.

Their trajectories become a circle of radius r_c, called the cyclotron radius, with angular velocity ω_c:

$$r_c = \frac{m_e v}{eB}; \quad \omega_c = \frac{eB}{m_e} \tag{2.6}$$

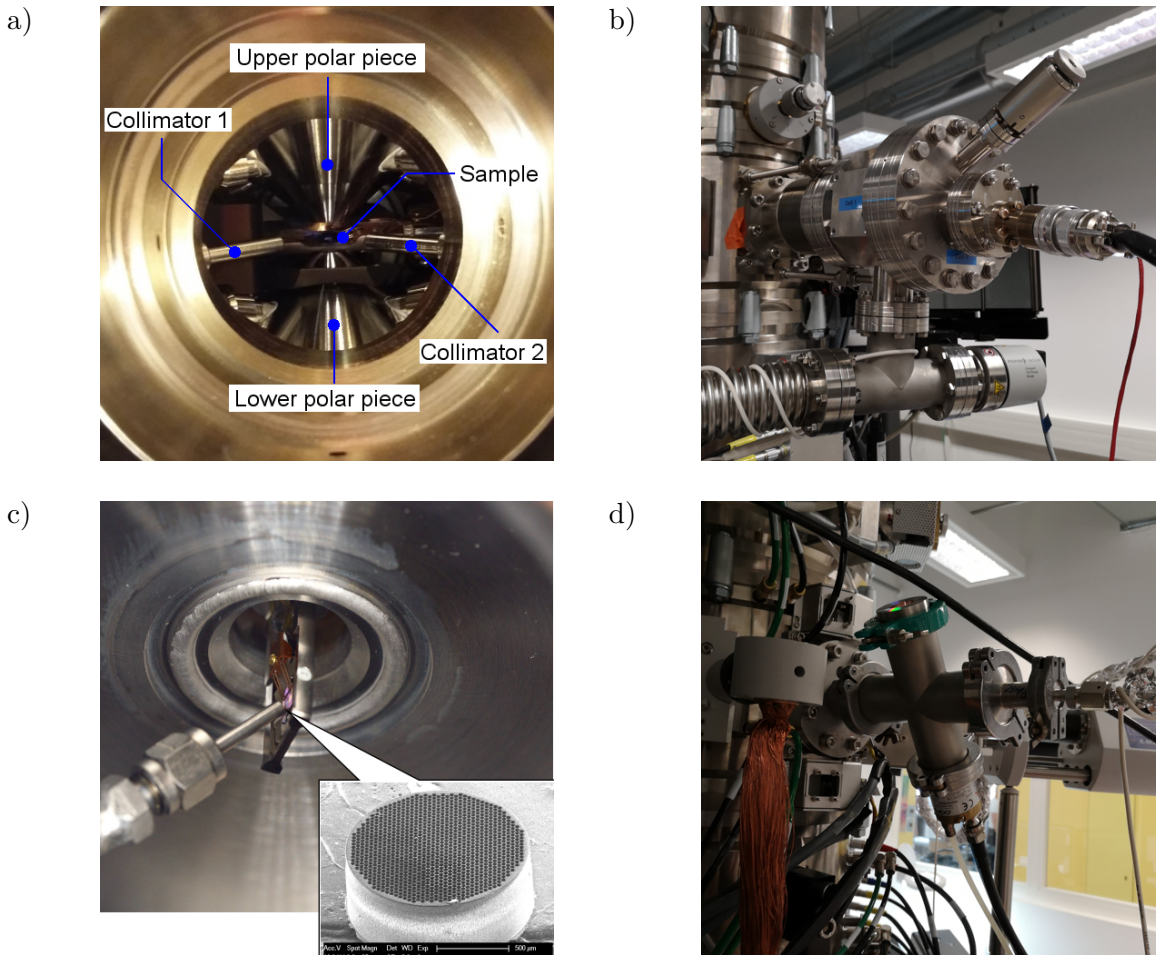

FIGURE 2.13: Showcase of the available sources in NanoMAX. a) Photography of the inside of the microscope through the EDX detector port. The upper and lower pole pieces are visible. The holder is located between the two pieces. Two pipes, next to the holder, deliver the precursors for the growth. b) Photography of the Ge MBE source. c) Photography of the special gas injection system fitted on a trial vacuum chamber (courtesy of Daniel Bouchier). Inset: SEM micrograph of the tip of the injector. d) Photography of the ECR plasma source. H_2 must go through it to join the TEM column.

When exposed to an electric field of exact frequency $f_c = \omega_c/2\pi$ with polarization perpendicular to the magnetic field, electrons are continuously accelerated in a spiral-like motion. This phenomenon is called electron cyclotron resonance and allows electrons to acquire great kinetic energy [182, 183]. Such electrons may then collide with the gas molecules, creating ions and radical species. In our case, the microwave generator has a frequency of 2.45 GHz and adjustable power up to 200 W. The plasma chamber is plugged in one of the side ports of the equipment and is connected to the H_2 CVD source (Figure 2.13d). Thus, the H_2 coming out of the gas cylinder goes through the plasma chamber where it partly cracks. It then arrives at the sample in the TEM column as a mixture of molecular and atomic hydrogen.

Compared to the Plasfil PECVD reactor, the plasma operated in NanoMAX is thought to generate atomic hydrogen more effectively. However, the plasma region is just above the substrate in Plasfil. In NanoMAX, the plasma is remote as it is not possible to have such a configuration for practical reasons. Indeed, the plasma may interfere with the electron beam of the microscope and disturb observations. Consequently, to reach the substrate in NanoMAX, radicals and ions must travel a much longer distance, close to 30 cm. This is especially problematic for hydrogen radicals which have low lifetime and may recombine before being able to modify surface chemistry. Even though the number of radicals should be higher in the ECR plasma source, we estimate the effective arrival rate of hydrogen radicals on the substrate to be much lower than in Plasfil. This can be eventually improved by improving the pumping efficiency in the column to make recombination less probable, or by creating a pressure difference between the remote plasma chamber and the TEM column. That solution also prevents gases such as SiH_4 or GeH_4 from depositing in the plasma chamber.

2.4.3 Effect of the electron beam on the sample

While *in situ* TEM allows the collection of data unobtainable by other means, it is important to remember that the high energy of the electrons used for imaging directly influences the experiment. The effects of the beam are already documented [184] and we summarize some of them here. We also show how they affect the growth and some means to counter them.

The most visible aspect of damage induced by the electron beam is atomic displacement and sputtering, also known as knock-on processes. High energy electrons can transfer energy to atoms they cross. If the energy transferred is above a so-called displacement energy E_d, then the atom may leave its equilibrium position in the crystal lattice and migrate to an interstitial site, creating a vacancy-interstitial atom pair, also known as a Frenkel defect. The energy required depends on the chemical element. For example, Si has a knock-on energy threshold of 18 eV. Thus, incident electrons must transfer more than 18 eV to successfully displace Si atoms. To transfer an amount E of energy expressed in eV to an atom of atomic weight A, electrons must have an incident energy V expressed in keV of [185]:

$$V[\text{keV}] = \left(\sqrt{1 + \frac{AE}{561[\text{eV}]}} - 1\right) \times 511[\text{keV}] \tag{2.7}$$

Thus, for $E = E_d$, we can deduce the incident threshold energy V_d at which displacement effect starts. Typical values for some elements are given in Table 2.1. TEMs are typically operated with an incident energy of 80, 200 or 300 keV. It is clear that transition metals are not affected by displacement. Elements C and Si (and light elements in general) are however, sensitive to the electron beam, so precautions must be taken. Note that previous calculations are valid for atoms in the bulk. For those close to the surface, sputtering may occur, which can eject atoms from the crystal altogether and break chemical bonds. The sputtering energy E_s is usually lower than the displacement one E_d. Using Equation (2.7) and setting $E = E_s$, a new sputtering threshold energy V_s can be defined. While heavy metals remain stable, C, Si, Ge and Cu become problematic. In the context of our experiment, we should consider sputtering physics when growing SiNWs, especially for those with low diameter.

If the beam is focused into a single spot for long enough, irradiation damage where the beam was focused may occur (see Figure 2.14). This is irreversible, so that the catalytic seeds are completely removed, killing the growth at this spot. Focusing the beam is necessary for

TABLE 2.1: Threshold incident electron energy V_d and V_s for some chemical elements in order to communicate E_d and E_s to displace or sputter atoms [186]. E_s can be estimated as 5/3 of the sublimation energy [185].

Element	A	V_d(keV)	E_d (eV)	V_s (keV)	E_s (eV)
C	12	293	69	67	13
Si	28	352	37	90	7.7
Cu	64	565	30	148	5.8
Ge	73	695	35	181	6.4
Sn	119	660	20	393	10
Au	197	1542	43	406	6.3

EDX to function properly, as we need to gather a statistically significant amount of X-rays to reliably confirm the presence of a chemical element. At the same time, we are also changing the chemical environment of the spot we want to observe. A compromise must be reached, between minimizing the irradiation damage and maximizing photon counts. Even when the beam is not focused, it is very likely that sputtering may still occur. Working in low dose by reducing spot size and screen current or minimizing the sample exposure time are solutions, but they reduce the quality of the gathered data. Low dose imaging implies a loss in image sharpness and contrast. Minimizing sample exposure means cutting off the electron beam, which of course completely stop any measurements.

The electron beam may also charge the sample. Nanowires in particular are susceptible to undergo this charging. When illuminated by the probe, they can start to bend or oscillate due to electrostatic charging. For long and thin wires, the oscillation amplitude can become high enough so that we lose information on the crystalline structure of the nanowire. Charging can also affect neighboring wires and the motion can become widespread for dense arrays, rendering observations difficult. We can alleviate this problem by growing low density nanowire arrays.

Radiolysis is a common problem when observing organic samples. In our case, it is actually favorable as atomic precursors produced by the dissociation of gas molecules can help with the catalytic growth. Electrons of the beam have sufficient energy to break the gas molecules and therefore, we can expect a surplus of radical species in the TEM column. Data for the cross section of interaction between electrons and H_2 [187], SiH_4 [188] and Ge_2H_6 [188] molecules are available and allow to predict the cross section by use of the binary encounter-Bethe (BEB) model [189]. For each molecular orbital, an ionization cross section σ_{MO} is determined as:

$$\sigma_{MO} = \frac{4\pi a_0^2 N \left(\frac{R}{B}\right)^2}{\frac{V}{B} + \frac{1+\frac{U}{B}}{n}} \left[\frac{Q \ln \frac{V}{B}}{2} \left(1 - \left(\frac{B}{V}\right)^2\right) + (2-Q)\left(1 - \frac{B}{V} - \frac{\ln \frac{V}{B}}{1+\frac{V}{B}}\right)\right] \tag{2.8}$$

where V is the incident electron energy, B the binding energy of the orbital, U the average kinetic energy of the orbital, N the electron occupation number of the orbital, Q the dipole constant of the orbital, $R = 13.60\,\text{eV}$. R is the Rydberg energy constant and $a_0 = 0.53\,\text{Å}$ the Bohr radius, and n is the scaling factor equal to either 1 or 2 depending on whether the molecule is composed of light or heavy atoms. The total cross section is the sum of individual molecular orbital ionization cross sections. For the H_2 molecule, the total cross section is $2 \times 10^{-3}\,\text{Å}^2$ for an incident electron energy of 300 keV [187]. For the more complex SiH_4 and Ge_2H_6 molecules [188], we have a cross section of $9 \times 10^{-3}\,\text{Å}^2$ and $1.9 \times 10^{-2}\,\text{Å}^2$, respectively. At an incident electron energy of 20 eV,

a) b)

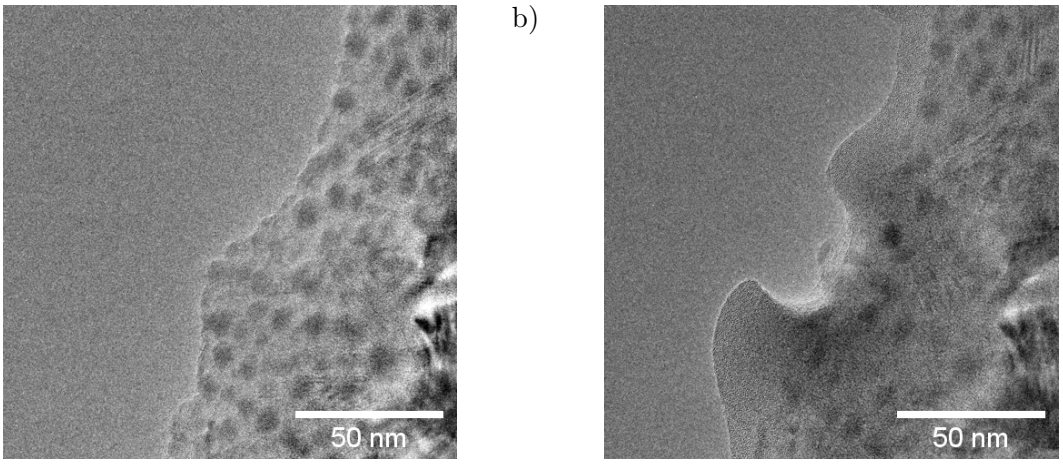

FIGURE 2.14: Illustration of beam induced damage. a) TEM micrograph of a SiC membrane with CuSn metallic catalytic seeds. b) TEM micrograph of the same area of the membrane after one minute exposure to a focused beam at 300 keV.

the three previously mentioned total cross section become $2.8 \times 10^{-1}\,\text{Å}^2$, $2.249\,\text{Å}^2$ and $2.516\,\text{Å}^2$ respectively. Given the small cross sections for 300 keV, the contribution of radiolysis to the generation of radical species can be neglected.

One last effect of the electron beam which is considered here is the local heating due to inelastic scattering. The incident electrons may transfer some energy to the sample atoms, which in consequence may increase the sample temperature. Since the temperature governs most of the dynamical aspects of the growth, it is critical to estimate the shift in temperature caused by the electron beam. It has been shown that the shift in temperature ΔT, neglecting radiative emission from the sample, is given by [184]:

$$\Delta T = \frac{I\langle E\rangle}{4\pi\kappa e\lambda}\left[0.58 + 2\ln\left(\frac{2R_0}{d}\right)\right] \tag{2.9}$$

where I is the beam current, $\langle E\rangle$ is the average energy lost by electrons after inelastic collision, κ the thermal conductivity of the material, e the elementary charge, λ the inelastic mean free path of electrons given by $\lambda[\text{nm}] = 143/V^2 + 0.054\sqrt{V}$ with V being the incident electron energy in eV, d the diameter of the electron beam, and R_0 is the electron range. Value of R_0 is defined as the distance an electron with energy V can travel through a given material before losing all of its kinetic energy. For electrons with energy greater than 50 keV, the range follows a power law [190]:

$$R_0(V) = bV^n\left[1 - \frac{1}{\left(1 + \frac{V}{Nm_ec^2}\right)^2}\right] \tag{2.10}$$

where we take into account relativistic corrections. Numbers b, n and N are fitting parameters. Let us now consider the maximum heating induced by the beam in Si. For Si, we have $b = 0.542\,\mu\text{m}\cdot\text{eV}^{-\text{n}}$, $n = 0.676$ and $N = 5$ and the beam current I is close to 5 nA [190]. The energy lost by the electron can be transferred to a phonon, plasmon or another electron in the electronic shell of an atom. The average energy lost by electrons due to inelastic scattering $\langle E\rangle$ depends on the material that is crossed. Let us assume that all the incident electrons transfer a part of their kinetic energy to other electrons promoting them to a higher energy level. In Si, the

maximum possible energy transfer recorded by electron energy loss spectroscopy (EELS) is 1839 eV which corresponds to a K transition [191]. The maximum heating can be estimated by taking $\langle E \rangle = 1839\,\mathrm{eV}$. The thermal conductivity κ of Si [127] is $150\,\mathrm{W \cdot m^{-1} \cdot K^{-1}}$. For an incident electron energy of 300 keV, the inelastic mean free path λ is 30 nm while the electron range R_0 is 544 μm. At our working magnification, sufficient to gather information on the nanowire crystalline structure, the probe diameter d is 70 nm. Putting these numbers into Equation (2.9) gives a maximum heating of 3 K. This value is most likely overestimated since we only considered one channel for incident electrons to transfer their kinetic energy. Other channels such as plasmon excitations result in a much lower energy loss, in the 50 eV range and have much higher cross-sections. The final conclusion is that the heating effect of the electron beam is not sufficient to significantly change the growth dynamics.

2.4.4 Preparation of samples

Growing nanowires in a TEM poses unique technical challenges. As we have seen in Section 1.1.3, VLS/VSS requires both sufficient heating and catalytic seeds. In this section, we present the two types of heating substrates we used for the growth and how we deposited the catalyst particles.

2.4.4.1 Two types of substrates

The substrates we used for the *in situ* growth in NanoMAX are of two different kinds. The first one is a commercial Protochips Fusion substrate. It consists in a Si chip of 8×6 mm in size, with a doped polycrystalline SiC membrane on the top (Figure 2.15a-b). The Si chip has been etched by the back side up to the SiC membrane over a square of 200×200 μm. Over this Si chip hole, the SiC membrane has an array of 3×3 holes of 7 μm diameter each. There are gold contacts from both sides of the Si chip hole array. Because of the Au contact deposition process by the manufacturer, there is some Au contamination on the SiC membranes which take the form of Au nanoparticles of average diameter of 15 nm.

The purpose of these gold contacts is to allow for the passing of an electrical current through the SiC membrane. This current will heat the substrate so that the temperature necessary for the growth is reached. The maximum temperature reachable by the chip is 1200 °C. The temperature can be tuned by changing the intensity of the electrical current through the manufacturer software. The calibration between current intensity and substrate temperature is provided by the chip manufacturer; this calibration is done by measuring the current intensity and the temperature by a pyrometer. It is vital to mention that the resistance of the chip can change during the preparation step, where we deposit catalytic seeds on top, and during the growth experiment. Indeed, as-deposited metallic particles may change the path of least resistance for electrons in the SiC membrane. Furthermore, during the growth, these metallic particles may change both size and chemical composition, again modifying the resistance value. We find that the resistance value could decrease from 5 % to 10 % between the growth beginning and the experiment end. Consequently, the temperature given by the software is only a nominal temperature and does not necessarily indicate the exact substrate temperature. This issue is even more complicated since other factors may further modify the real temperature, and no other *in situ* measurement of the substrate temperature is available in the TEM column.

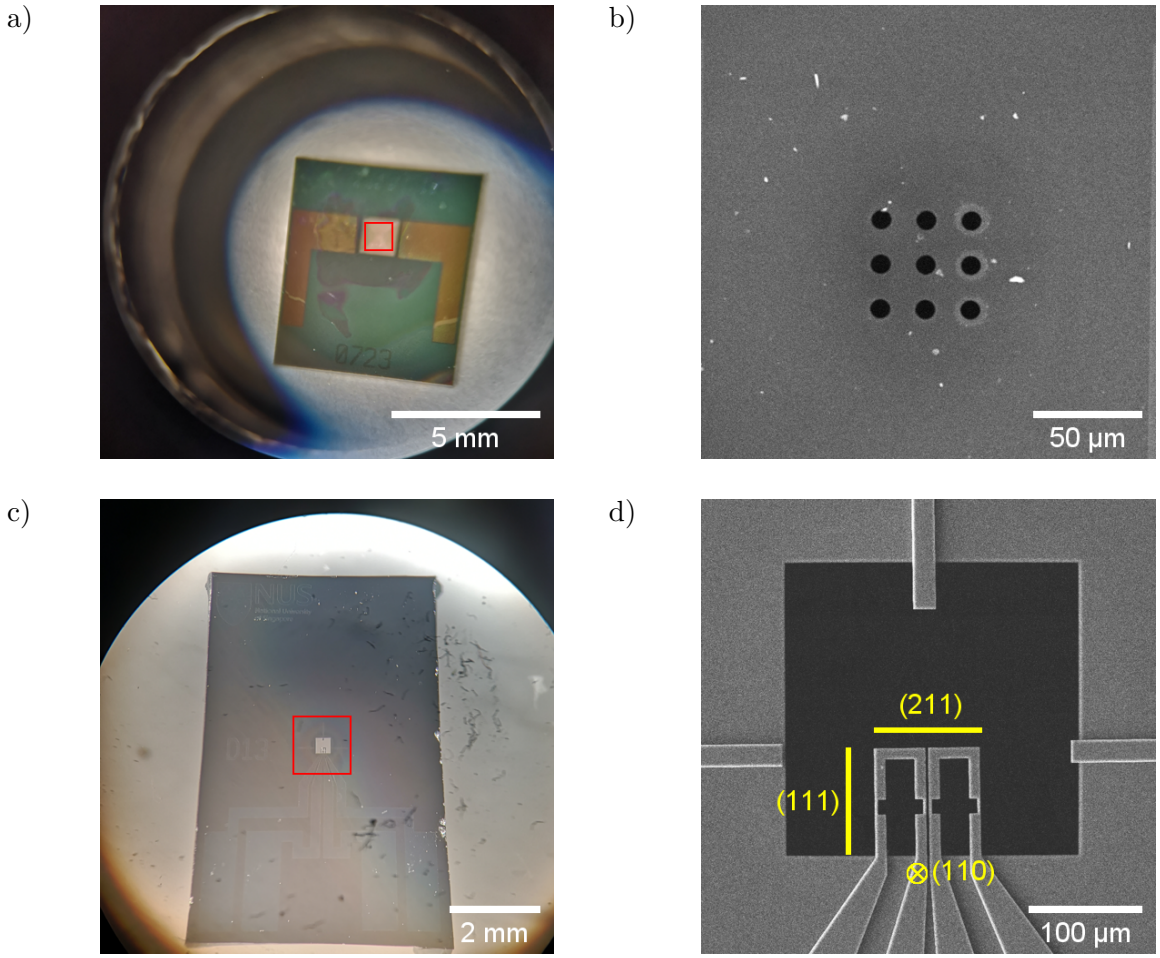

FIGURE 2.15: Showcase of the two different types of substrate used for our growth experiment. a) Optical microscope image of the commercial Protochips Fusion chip. b) SEM image of the red squared area in a). c) Optical microscope image of the Si cantilever. d) SEM image of the red squared area in c). The crystalline orientation of each surface is indicated.

We have observed the growth of nanowires on Protochips Fusion chip over one of the 9 holes. However, as the growth was not epitaxial, the obtained nanowires have random orientation. Due to this, nanowires will often not be in a favorable zone axis for their observation and the crystalline arrangement of Si atoms is not immediately visible. Therefore, a time-consuming tilting of the sample is usually necessary for every nanowire we want to observe. This was not always possible, especially for very thin wires of diameters below 10 nm. Putting a nanowire in the correct zone axis requires the production of an electron diffraction pattern, which for too thin nanowires may either give too weak and unusable signal or lead to a damage by the irradiation effect of the focused electron beam.

Therefore, we also used a second type of substrate, kindly provided by Federico Panciera (C2N) and fabricated at the National University of Singapore. It again consists of a Si chip that is pierced in its center, but instead of the SiC membrane on the top of the chip, the latter is etched in such a fashion that monocrystalline Si forms a cantilever geometry (Figure 2.15c-d). These Si contacts form two loops, so that an electrical current can flow through each to achieve heating as for the SiC membrane. Note that because the thickness of the loops is not uniform, a temperature gradient will form. This is convenient, as it will allow us to test different substrate

temperatures in a single process. Nanowires then grow directly on the Si loops. These two loops are etched out from monocrystalline Si arranged so that the lateral edges are Si (111) surfaces, the front edge is (112), while the top surface is (110). The loops are not connected in series, so that heating through only one loop is feasible. Thanks to this particular configuration, nanowires will grow epitaxially. In particular, wires growing on the lateral edges will be perpendicular to the electron beam and in the [110] zone axis. Therefore, significantly less time is spent tilting the sample to find the correct zone axis for observation.

There are unfortunately several downsides in using this substrate. To begin with, there is no calibrated relation between the current intensity and the substrate temperature. While the SiC membrane does not give the correct temperature, it still gives an order of magnitude in real time. With the Si cantilever, no such information is available. We have proposed two solutions but both of them come with their limitations. First, we could do the calibration at the end of the growth experiment thanks to a spatially-resolved IR camera or pyrometer. In this case, the spatial resolution is too low to precisely map the temperature gradient. The second solution involves using a known physical phenomenon to calibrate the substrate temperature. For example, the melting temperature of bulk Sn is known to be 232 °C. Thus, we can check at which current intensity we observe the melting of Sn nanoparticles, therefore providing an approximate calibration. This solution should provide a precise temperature measurement. The evolution of the temperature with the current intensity can be known by an extrapolation. Because of the temperature gradient, the temperature will be correct only for a small area of the loop. Note that for very small particles, nano-size effects may change the temperature value where physical phenomena take place. Bulk Au is known to melt at 1064 °C. However, for nanoparticles, as the size decreases, so does the melting temperature [192]. The change can be very dramatic, with the melting temperature going from approximately 1000 °C for 10 nm large particles to 500 °C for particles below 2 nm. Another technique that can be used is to measure the nanowire growth rate grown on specific parts of the cantilever substrate. As the growth rate is a function of temperature following an Arrhenius law, a point measurement of the cantilever temperature is obtained. Extrapolation to other parts of the cantilever is possible through finite-element modeling [193]. We did not perform any temperature calibrations, although order of magnitude for the temperature on the cantilever will be provided in the following.

The substrate choice will thus depend on what we want to achieve. If a somewhat accurate temperature measurement is a priority then the SiC membrane is arguably better. On the other hand, the Si cantilever will yield more of easily accessible data on the arrangement of atoms in SiNWs.

2.4.4.2 Thermal evaporation

Catalytic seeds are necessary for the VLS/VSS growth method to work properly. Prior to the growth, we use thermal evaporation to deposit a metallic thin film on the substrates. It is a type of physical vapor deposition (PVD) technique like sputtering for example. By melting a metallic ingot, placed on a W crucible, by an intense electrical current, a flux of metal atoms is emitted from the crucible. The substrate is fixed to a holder above the crucible, so that the metal atoms condense on it. High vacuum ($\sim 10^{-5}$ mbar) will prevent the contamination of the deposited film. It also prevents collisions between the evaporated atoms and the ambient air. The thickness deposited on the substrate is monitored by a quartz crystal microbalance. By providing the density of the metal we want to deposit, the microbalance can give the deposited

thickness in real time with a minimal step of 0.1 nm. When the ingot has melted, the atom flux is continuous and the deposition is ended by using a movable shutter when the desired thickness is obtained. The apparatus is a BocEdwards FL400 shown in Figure 2.16a-b.

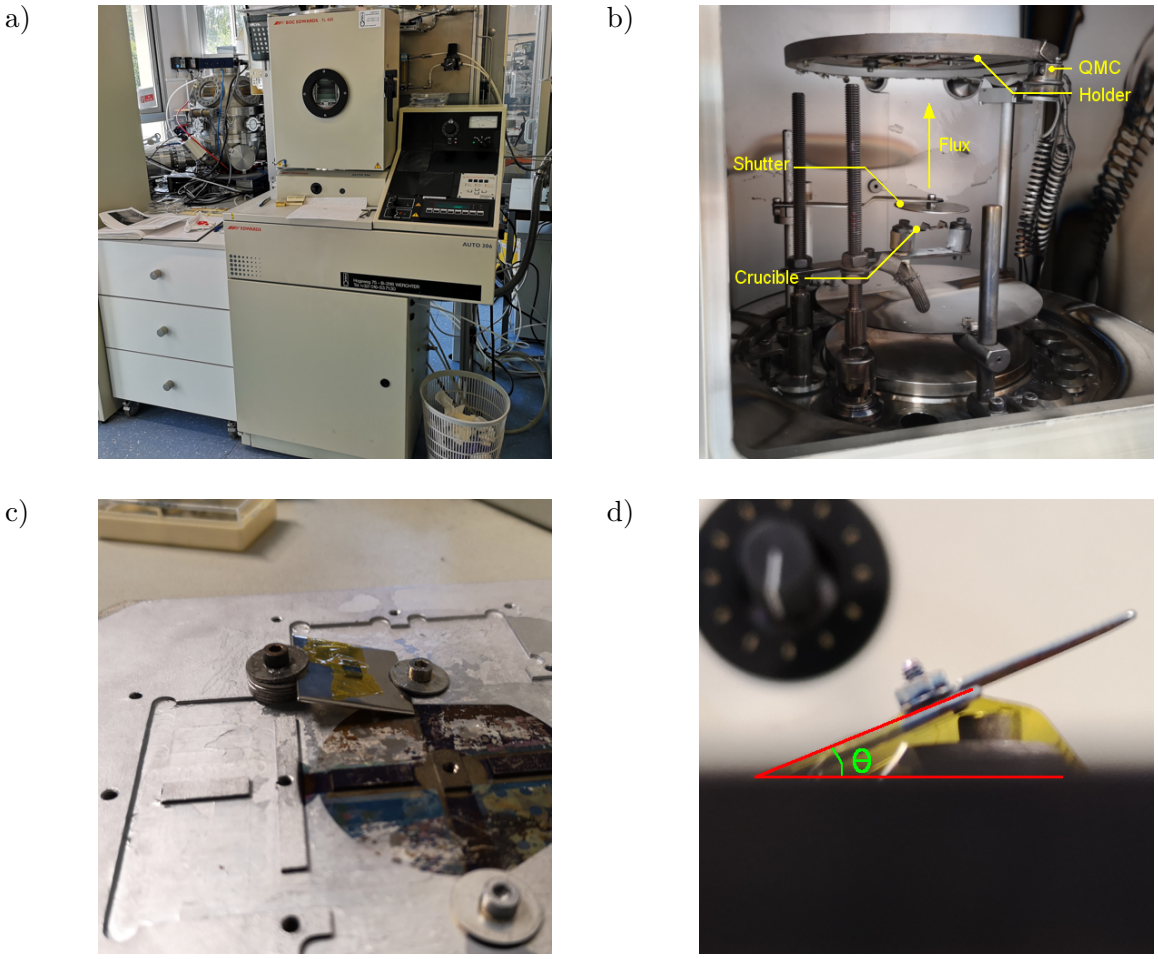

FIGURE 2.16: Experimental setup for the deposition of the catalytic seeds. a) Exterior of the thermal evaporator. b) Interior of the evaporator, the important parts are highlighted; QMC stands for quartz microbalance. c) Si cantilever placed on a tilted metallic plate on the sample holder. d) Angle between the metallic plate and the sample holder.

Metal evaporation on the SiC membrane does not pose a significant challenge. In general, we are not interested by the epitaxial growth on this kind of substrate. On the other hand, the epitaxial growth is the main reason for using the Si cantilever. Si is known to undergo rapid oxidation under ambient air and when left on a shelf, it naturally exhibits native oxide on its surface. This means that if the metallic particles are deposited without prior treatment, there will be a native oxide layer between the particles and the pure crystalline Si. That oxide is amorphous and prevents any epitaxial growth. Furthermore, there is a SiO_2 membrane hanging over the center hole, which must be stripped off before the cantilever can be used. For both reasons, it is necessary to remove all SiO_2, which can be done efficiently by exposing the cantilever to HF vapor. Four minutes exposure to 40 % concentrated HF vapor followed by dipping in deionized water and drying is sufficient to remove the oxide. It is preferable that both the sample preparation and the growth are done within a short period of time while the hydrogen atoms left from HF treatment are still passivating the Si surface bonds preventing an immediate oxide growth. Another difficulty arises due to the geometry of the cantilever. Indeed, we will often

want to observe SiNWs in the [110] zone axis, the only axis which allows for the unambiguous discrimination between the 3C and 2H phases. Given the configuration of the cantilever, it means that we have to deposit the seeds on the lateral edges of the loops. However, the lateral edges are parallel to the direction of the evaporated atoms flux. Thus, if the cantilever is simply fixed to the substrate holder, very little metal atoms will be deposited on the lateral edge. By tilting the Si cantilever as shown in Figure 2.16c-d, the lateral edge will receive a part of the evaporated flux. Kapton tape stuck to the cantilever will prevent it from falling. The effective thickness d_{eff} of metals on the lateral edge is given by:

$$d_{eff} = d_{meas} \sin\theta \tag{2.11}$$

where d_{meas} is the thickness measured by the quartz crystal microbalance and θ the angle between the plane of the Si cantilever and the substrate holder placed perpendicular to the beam of evaporated atoms.

Conclusion of the chapter

In this chapter, we have presented the experimental setup which will allow us to synthesize the 2H polytype in Si and GeNWs. We have seen that, in order to obtain and observe this phase in real time, we will need an equipment with a good time resolution and an extreme spatial resolution. After comparing multiple techniques, we have clearly identified *in situ* TEM as the best method that can yield the most complete set of data for giving insights on what stabilizes the 2H phase.

The principles of electron microscopy which will be the main characterization tool in this thesis have been introduced: when an incident electron beam interacts with a sample, various electrons and photons are generated. They can be detected for various purposes such as structural analysis at an atomic scale or local chemical analysis. In TEM, since the image is related to the electrons wavefunction, the action of the sample on the former can be numerically simulated in order to predict the image of a given crystalline structure. Using this property, we simulated the image of polytype 3C and 2H in three different zone axes. We found that an unambiguous discrimination between the two polytypes can only occur when they are observed along the $[110]_C/[12\bar{1}0]_H$ direction. There is no visual difference between the two polytypes in the $[112]_C/[10\bar{1}0]_H$ zone axis. As for the $[111]_C/[0001]_H$ direction, twin defects which are common in group-IV nanowires can make image interpretation difficult.

NanoMAX, an *in situ* ETEM, has all the atomic sources needed to grow a variety of nano-objects as well as a remote plasma produced by an ECR plasma source. Because there are important differences between the PECVD reactor Plasfil and NanoMAX, it is beneficial to use both growth methods in parallel. Examples of dissimilarities include having the sample directly exposed to the plasma in Plasfil and using a remote plasma source in NanoMAX and the additional effect of the electron beam. Finding and understanding differences in the obtained nanowire structure is critical to fully understand the growth dynamics in both Plasfil and NanoMAX. The geometry of the TEM forces the use of specially made substrates that come in two types: a SiC membrane and a monocrystalline Si cantilever. Both substrates can be connected to a power source that will drive the heating. The deposition of metallic catalytic seeds, necessary for the VLS growth, is done through thermal evaporation.

CHAPTER 3

Surface dynamics in the growth of germanium nanowires

In this chapter, we focus on the growth of GeNWs. Compared to Si, Ge is a heavier atom and will appear with more contrast in TEM images. It is also the only column-IV element for which both MBE and CVD sources are available in the NanoMAX microscope. The catalyst used for the growth was gold, deposited on a Protochips Fusion SiC membrane by thermal evaporation. We deposited an amount corresponding to a nominal layer thickness of 1 nm. This resulted in the particle distribution shown in Figure 3.1.

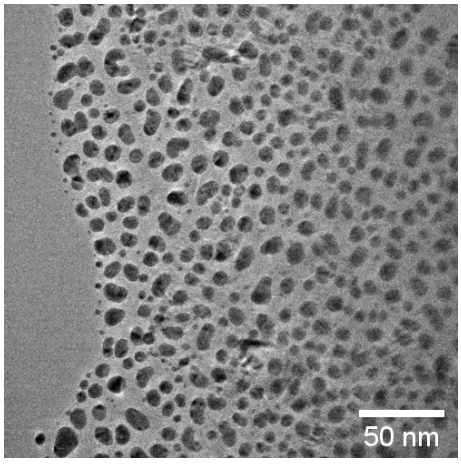

FIGURE 3.1: TEM micrograph of a Protochips Fusion SiC membrane with as-deposited Au particles corresponding to an evaporated layer of 1-nm nominal thickness. The area without particles on the left is one of the nine holes inside the membrane described in Section 2.4.4.1.

The shape of as-deposited solid seeds depends on their sizes. Small seeds are quasi-spherical while larger ones are elongated. The average particle length in the Figure is around 10 nm although some very small Au particles are also visible. In a single particle, the contrast is not homogeneous over its whole area. The main reason is that some areas are closer to Bragg's condition than others. This highlights that a given individual Au particle is not monocrystalline but is rather composed of several grains. In our experiments, the melting of Au nanoparticles (NPs) is achieved upon heating above the eutectic temperature of the Au-Ge system (361 °C) and increasing Ge concentration inside particles through the molecular beam issued by the

melting of a Ge pellet in the case of MBE or the supply provided by the cracking of germanium hydrides in the case of CVD. Unless specified otherwise, we set the temperature of the substrate to 400 °C.

3.1 *In situ* growth using a molecular beam epitaxy source

We use the substrates with evaporated Au particles with distribution as in Figure 3.1 to grow GeNWs using the molecular beam epitaxy source described in Section 2.4.2.

3.1.1 Flux estimation of the Ge atomic beam

The flux of Ge atoms delivered by the MBE source is a function of the source temperature. In order to get a constant flux over time, we have fixed the temperature of the source to 1200 °C. Note here that the substrate temperature differs from the MBE source temperature and they have no influence on each other. Let us make a rough estimate of the flux of Ge atoms impinging on the substrate. To do this, after heating the substrate to the desired 400 °C temperature, we have recorded the time evolution of the Au particles over a few minutes. From the video, we infer the volume V of a particle at two different moments separated by a time interval Δt by assuming that particles possess a spherical shape (Figure 3.2) and that the projected area of the droplet on the substrate S defines its cross-section. The assumption of a spherical particle is reasonable for small solid ones (Figure 3.1). In addition, when melting is achieved by reaching the eutectic concentration, faceting disappears and particles now display a curved shape. Knowing the elementary volume occupied by a Ge atom $\Omega = 2.26 \times 10^{-29}\,\mathrm{m}^3$, a flux J is calculated as:

$$J = \frac{V(t+\Delta t) - V(t)}{S(t+\Delta t)\Omega\Delta t} \tag{3.1}$$

Note that the flux J calculated by this way suffers from at least three sources of error. First, there is an underestimation of the flux due to the fact that not all Ge atoms impinging on the substrate will effectively contribute to the increase in volume of the investigated particle. Indeed, Ge atoms need to stick to the particle in the first place to be considered in Equation (3.1). Thus, a sticking coefficient α with value between 0 and 1 modulates the measured flux J. Therefore, J is more akin to an effective arrival rate rather than the real flux of the Ge MBE source. The second error source is due to the diffusion of Ge atoms on the substrate, which may contribute to the increase in volume of a given AuGe liquid particle. Since S is taken as the projected area of the AuGe particle, we overestimate the incoming flux by underestimating the total area of the substrate participating to the growth of the measured particle. To have a better picture, we would need to know the diffusion length of Ge atoms at the substrate temperature. Also, we have to measure the volume variation on a lonely particle, as neighbor particles may influence the collection of Ge atoms of the measured particle. The third error source is due to the assumption that the particles are spherical. While the three error sources prevent an accurate assessment of the Ge flux at a source temperature of 1200 °C, it does yield a good estimation of the order of magnitude.

Let us use the AuGe liquid particle marked by the arrow in Figure 3.2a to estimate the incoming flux. Images in Figure 3.2a-b were taken 343 s apart at the same spot during MBE growth. By measuring the diameter of the particle, we can infer both its volume and the

a) b)

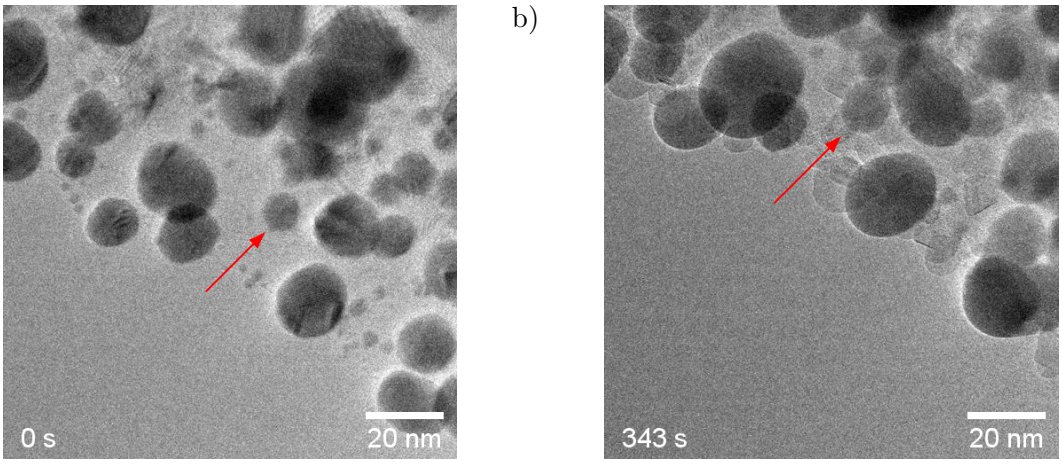

FIGURE 3.2: TEM micrograph of a random assembly of AuGe particles taken at a) the initial stage when the Ge beam is switched on and b) 343 s later at a temperature of 400 °C with the Ge MBE source heated at 1200 °C. The red arrow on both images shows the same particle at different times. Its position is different across both pictures because of image drift.

projected surface S. We take S as the surface of the liquid particle after 343 s. We find the flux J to be roughly 2.5×10^{-1} atoms $\cdot$ nm$^{-2} \cdot$ s^{-1} or 0.07 Ge (111) monolayer per second. Under these conditions, we expect a very slow growth rate for our GeNWs. This means that the growth dynamics is observable without using the fast camera. It is particularly important for observing the early stages of the growth.

3.1.2 Observing the growth

The substrate is heated from room temperature to 400 °C. On the Au-Ge phase diagram shown in Figure 3.3, this corresponds to the first vertical red arrow. When the flux of Ge atoms is turned on, the as-deposited solid Au particles start to increase in size. Particles may start to coalesce with time due to their proximity, which increases the particle average diameter, while also reducing the particle density. Ostwald ripening may also take place. At the same time, the concentration of Ge in the particles raises which gives a horizontal displacement towards the right-hand side of the diagram (second red arrow). As Ge atoms are continuously provided, a point is reached where the initially solid particles melt, leading to the disappearance of once visible lattice fringes and grain boundaries (Figure 3.4b). Also, rather than displaying facets, particles adopt a curved shape, becoming more spherical. At this stage, a eutectic melt of liquid AuGe is obtained. With more supplied Ge, saturation in Ge occurs and any additional atoms will provoke a state of supersaturation in AuGe liquid droplets. Precipitation of solid Ge nucleus follows when the supersaturation in Ge reaches a threshold. This is visible in the images by a clear change of contrast inside the AuGe liquid droplets (Figure 3.4e-f). The dark contrast is due to the heavier nucleus of Au atoms, which deflects electrons considerably more than Ge. Notice that the appearance of the nucleus is a very fast process, it took less than a second for it to precipitate. Once it is obtained, the nucleus can be used as a base for the growth of a GeNW, as more atomic planes are fabricated in a monolayer by monolayer fashion. There is a noticeable pause after a layer is formed before the next one starts its growth. This is due to the Au droplet being no longer supersaturated after the growth of a monolayer. Before starting a new one, the AuGe melt must first refill to reach supersaturation, a process that is not instantaneous. This

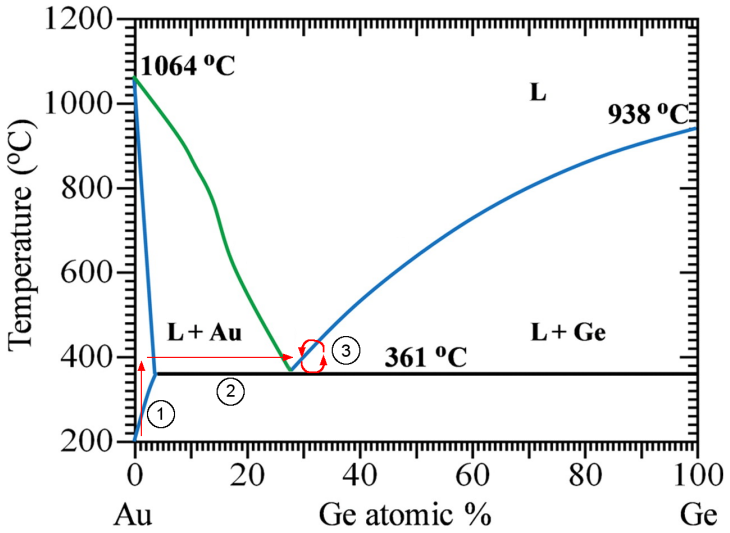

FIGURE 3.3: Au-Ge binary phase diagram (reproduced from [32]). The red arrows and the corresponding circled numbers indicate the trajectory taken by the system during the growth and their order, respectively.

process is cyclic [194], as shown by the double circling red arrows in Figure 3.3.

From the melting of the AuGe particles (Figure 3.4b) to the appearance of the Ge nucleus (Figure 3.4c), there is an incubation time of 231 s. However, after that, we see that the elongation of the newly formed nucleus occurs continuously (Figure 3.4d). The precipitation of the initial Ge nucleus shows a drastically different characteristic time compared to the monolayer by monolayer growth after the nucleation. Indeed, Ge atoms are absorbed for 362 s before a nucleation event takes place while completing a new monolayer only took a few tens of seconds. This can be understood by considering the energetics of both mechanisms and the size of the Au seeds. Creating a Ge nucleus involves the assembly of a given volume of Ge crystal and the apparition of multiple surfaces. This has a certain cost in energy. The excess energy is supplied by the supersaturation of Ge in the AuGe melt. When the Ge supersaturation reaches a threshold value, the Ge nucleation barrier can be overcome and a nucleus is formed. In contrast, adding a new monolayer to a GeNW is easier because it creates less new surfaces. Thus, it is clear that the energy barrier is smaller for creating a new monolayer compared to the precipitation of the initial Ge nucleus. Consequently, the amount of excess Ge needs not to be as high for the layer by layer growth and so the characteristic time for creating a new layer is also lower.

3.1.3 Morphology of grown nanowires

Most of the nanowires grown with our Ge MBE source show a peculiar morphology. Unlike the ones depicted in the literature [195], they present an asymmetrical trapezoidal shape with a notably thick bottom while the top part is narrower, giving a tapered aspect. One of such wires is shown in Figure 3.5a. Given the diameter of the liquid catalyst at the top, it is very unlikely that the thick bottom is the result of the layer by layer growth described before. Indeed, the liquid catalyst has a diameter of 18 nm. This value is consistent with the average diameter of AuGe melt at the start of the growth when the Ge beam is introduced. Consequently, it is not capable of growing such a large base. It is likely that it is the result of sidewall deposition with

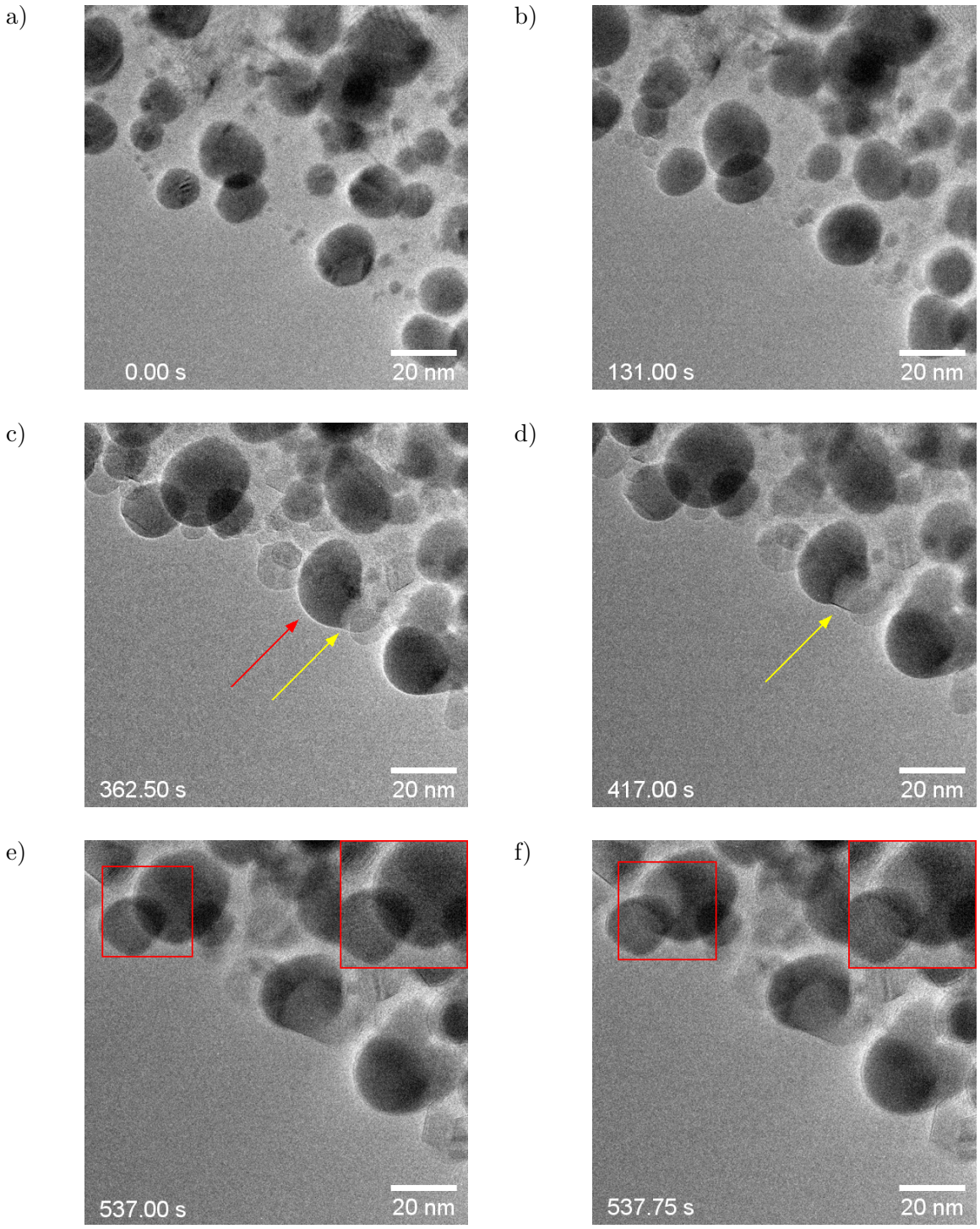

FIGURE 3.4: TEM micrographs of the early stages of the growth. a) As-deposited Au solid particles at 400 °C before any Ge flux. b) After 131 s of exposure to a Ge beam, the Au solid particles have melted and become AuGe liquid droplets. c) At 362 s, the droplet shown by the red arrow has precipitated a Ge nucleus indicated by the yellow arrow. d) From 362 s to 417 s, the Ge nucleus has continuously elongated to form a GeNW marked by the yellow arrow. e-f) Another AuGe liquid particle highlighted by the red squared area gave a Ge nucleus. This is indicated by the partial brightening of the particle. From the time stamp, we can see that the nucleation process took less than a second.

Ge atoms from the MBE flux which keep impinging on the sidewalls as observed in Figure 3.9. Note that some nanowires had a diameter that could reach 100 nm at the top. Catalysts that large are likely to be a result of the temperature-activated coalescence of smaller liquid AuGe droplets. All GeNWs grown with the MBE source have a cubic diamond structure. Furthermore, observed GeNWs have hexagonal cross-sections as shown in Figure 3.5c.

The sidewall facets of GeNWs grown by MBE appear to be uniquely of the {112} type, on average, with a slight departure due to tapering. Not surprisingly, due to the three-fold symmetry of the ⟨111⟩ growth axis, the faceting does not possess mirror-symmetry. From the perspective of the [110] zone axis, two different geometries of {112} sidewalls are visible in Figure 3.5b. On one side, the faceting shows a succession of two different surfaces: flat {111} and rough {113}, where {111} surfaces are longer overall than {113}. On the other, we have a very rough surface which is close to a {113} due to tapering but with irregularities in the form of atomic steps.

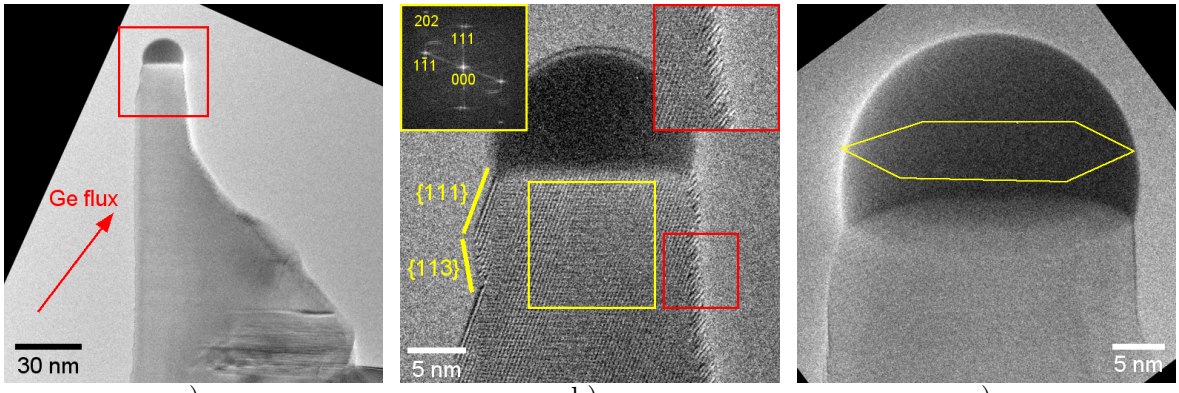

a) b) c)

FIGURE 3.5: TEM micrographs of GeNWs grown with the MBE source. a) Low magnification view. The arrow indicates Ge flux direction. b) Close-up view on the catalyst in a) close to the [110] zone axis. Inset: Fast Fourier Transform exhibiting the pattern of the [110] zone axis. Details of the right sidewall. c) Birds eye view of a GeNW, revealing its hexagonal cross-section and the exclusively {112} mean orientation of its sidewalls.

Due to the coalescence of the catalyst particles during the early stages of the growth, we have found that the distribution of GeNW diameters was very broad, from 20 nm to 100 nm at most at the tip. With this diameter distribution, GeNWs were found to grow mostly, if not only, along a ⟨111⟩ direction. Quite often, the interface between nanowires and liquid AuGe catalysts is not a single plane, but it is rather composed of a main plane perpendicular to the growth axis and a secondary smaller plane rotated 35° with respect to the main part (see Figure 3.6). This geometry is known as a truncation and has been reported for both Si and Ge NWs, regardless of the source type, CVD or MBE. It plays a role during the growth as the volume of the truncation fluctuates following the successive formation of new monolayers. The exact angle value should also fluctuate with time. Gamalski *et al.* [194] showed that the area of the truncation is at its lowest just before the nucleation of a new monolayer. Conversely, the area is the smallest just after the completion of a monolayer. After this, the area increases steadily again until a new nucleation takes place, which gives a sawtooth like variation. The truncation is thought to act as a small Ge reservoir for the growth of a layer [194].

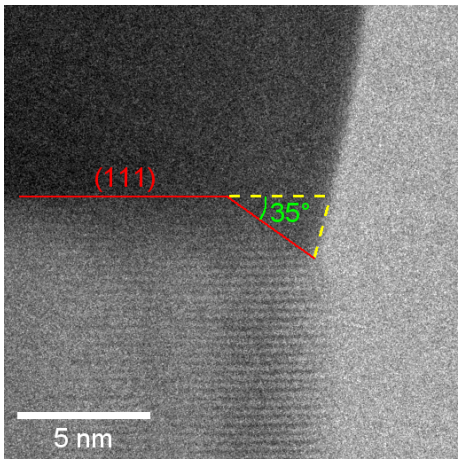

FIGURE 3.6: TEM micrographs of a GeNW with a truncated facet. The red solid line delimits the nanowire-catalyst interface. The yellow line delimits the truncated area.

3.1.4 Nanowire retraction

The very low Ge flux of 0.07 Ge (111) monolayers per second mentioned in Section 3.1.1 allows us to observe interesting dynamics. To better visualize this, we can monitor the length of a given nanowire for several minutes. This process can be automatized and performed by a written code. We used the position of the interface at the origin time as the reference. This allows us to trace the nanowire length as a function of time as shown in Figure 3.7.

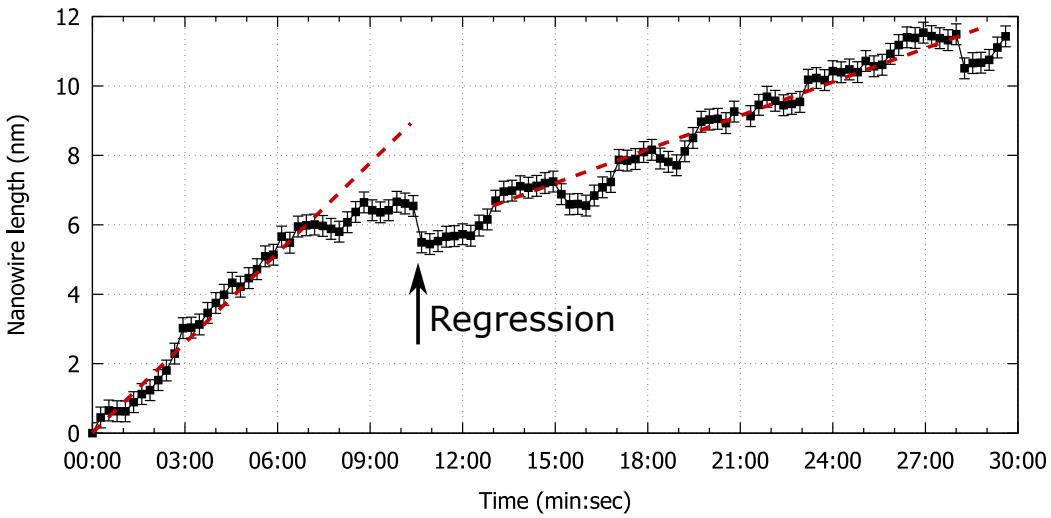

FIGURE 3.7: Time evolution of the length of the nanowire shown in Figure 3.5a-b.

Over the 30-minute recording, the average growth rate is $7.4 \times 10^{-3}\,\mathrm{nm \cdot s^{-1}}$ or 0.02 Ge (111) monolayers per second. The length evolution shows two interesting features. First, it is quite clear that the growth at low Ge flux is not linear. As indicated by the two dotted lines in Figure 3.7, there are actually two different growth speed of $1.6 \times 10^{-2}\,\mathrm{nm \cdot s^{-1}}$ and $5.5 \times 10^{-3}\,\mathrm{nm \cdot s^{-1}}$. Second, after 10.5 minutes, a significant drop in the nanowire length can be observed. This suggests that the nanowire has regressed at this instant and lost approximately three Ge (111) monolayers while the Ge flux from the MBE source did not change. Therefore, it seems that

a)

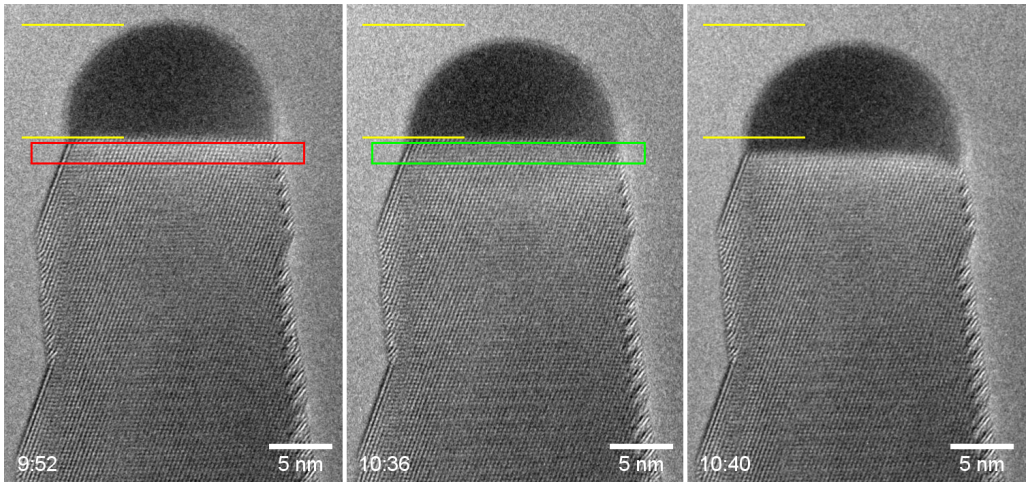

b)

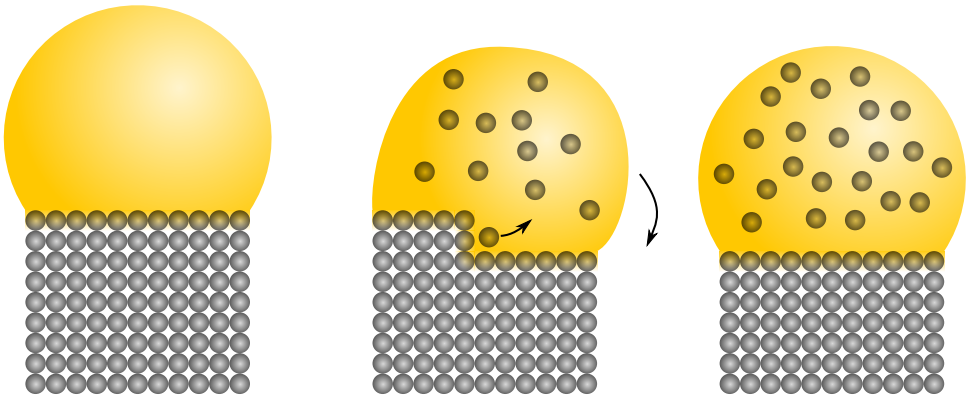

c)

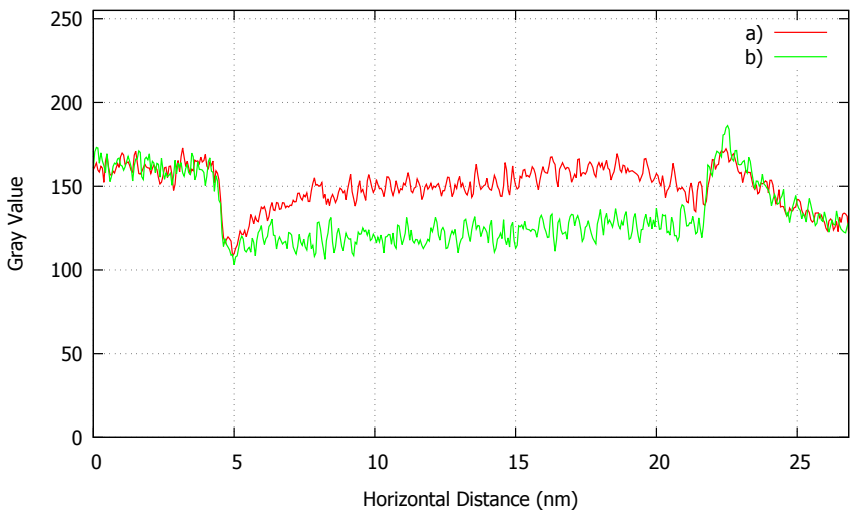

FIGURE 3.8: Regression of the GeNW of Figure 3.5a-b. a) TEM micrographs of the GeNW undergoing regression at three different moments. Yellow lines are always placed at the same pixel coordinates (after drift correction) and serve as guides for the eyes. Red and green rectangles show the area for which the plot profiles are calculated. b) Side view schematic of a regressing nanowire. c) Gray average value profiles of the red and green area as a function of the horizontal coordinate in nanometers. Gray levels are normalized.

the AuGe liquid catalyst became undersaturated in Ge at this moment of the growth which points towards a Ge leakage. Following this, the growth rate decreases. Leaking of Ge atoms from the catalyst may indicate some form of desorption processes, possibly accelerated by the electron beam. However, the vapor pressure of Ge at 400 °C is vanishingly small and rules out this possibility [196]. Instead, we propose that Ge atoms diffuse out of the catalyst. Given the low flux of Ge, the Ge atoms lost are not replaced fast enough to counterbalance the diffusion. Ge atoms from the nanowire are then extracted to refill the catalyst, leading to the regression of the nanowire. The decreased growth rate may originate from an increased out-of-catalyst diffusion rate.

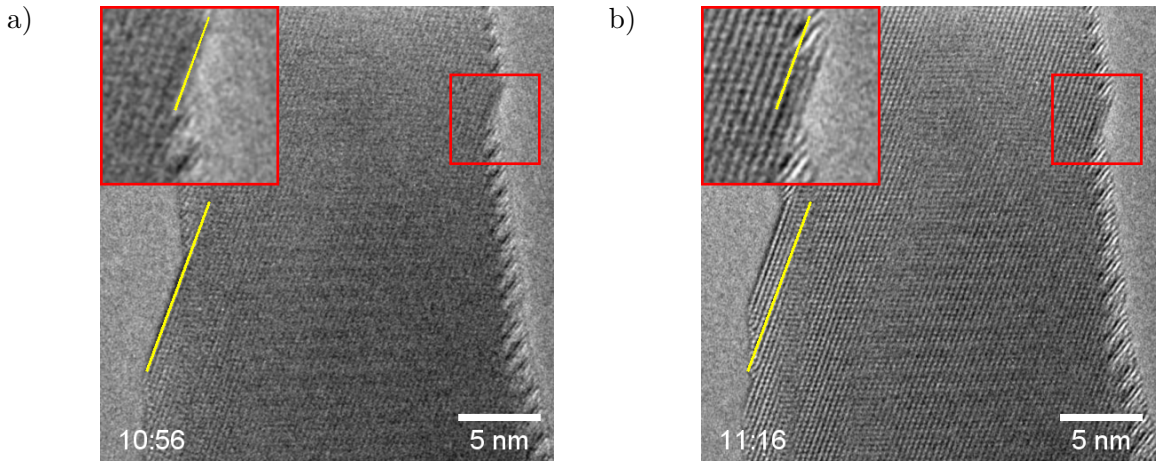

FIGURE 3.9: Lateral deposition on the GeNW of Figure 3.5a-b following the instant when regression occurred. The timestamps are the same as in Figure 3.8. Yellow lines are always placed at the same pixel coordinates and serve as guides for the eyes.

Let us examine in more detail the nanowire regression. The state of the nanowire prior to the regression is shown in Figure 3.8a which consists of three images taken at timestamps 9:52, 10:36 and 10:40. We have drawn yellow lines on the images to serve as reference to better highlight changes. The time stamps shown in the bottom left corner are consistent with those in Figure 3.7. We can see that from 9:52 to 10:36, the height of the catalyst droplet has decreased while no additional monolayers were added. On the contrary, it is apparent that the catalyst-nanowire interface was also displaced towards the nanowire base by a few Ge (111) planes which is consistent with the idea of a regression. Its mechanism can be understood by analyzing the interface evolution. There is a noticeable darkening of the area just below the catalyst-nanowire interface at 10:36 compared to the same interface at 9:52. To establish this, we can draw a plot profile at 9:52 of the gray value of the image and compare it to another plot profile done on 10:36 in the same area. Both rectangles are 30 pixels wide in order to use average gray values from all 30 pixels. The red and green rectangle in both figures display where the plot profile is done. Gray level profiles of images 9:52 and 10:36 are shown in Figure 3.8c. Note that there were no changes in observation conditions between the two images: the defocus of the objective lens was kept constant and so the gray level values can be directly exploited after the background level is normalized in both images. The plot profiles clearly show a contrast difference below the interface between moments 9:52 and 10:36. The darkening of the area just below the interface demonstrates that the catalyst has leaned towards the back side of the nanowire as shown by Figure 3.8b. This darkening is due to the increased electron scattering property of Au thanks to its higher nucleus mass compared to Ge. Because of the leaning of the catalyst towards the backside of the nanowire, it is very likely that the consumption of the nanowire starts at the triple phase boundary, where the liquid catalyst takes the place of the dissolved monolayers. The

inner parts are dissolved next, followed by the opposite edge. Thus, "degrowing" seems to occur in a step-flow like fashion, similar to what has been observed in nanowire growth [197, 198, 199]. The "degrowth" mechanism shown here helps to achieve Ge saturation in the droplet no matter the incoming flux of Ge and the eventual diffusion of Ge atoms out of the catalyst. Before growth can restart, there is an incubation time where Ge from the incoming flux continues to fill the catalyst after which sufficient supersaturation is attained again. This is shown by a plateau in the nanowire length after the regression in Figure 3.7.

Following the regression, an important restructuration of the left sidewall occurs, reducing the length of {113} facets and increasing {111} and {112} ones. Figure 3.9 shows this restructuration that occurs from 16 seconds to 36 seconds after the retraction. It is worth noting that before the regression took place, there is little lateral deposition. It is only after we observed an increase in the deposition rate on the sidewall. Consequently, we believe that this important influx of Ge atoms filling the sidewalls comes from the catalyst and explains the difference between the effective Ge flux and the nanowire growth rate. This creates a shortage of Ge atoms in the AuGe catalyst. The shortage creates a Ge undersaturation that is then compensated by the GeNW regression. Once the restructuration is over, "degrowth" will stop and normal growth of the nanowire resumes. In the next section, we describe why this phenomenon occurs.

3.1.5 Surface restructuration

It is expected that nanowires thicken during the growth, as sidewalls receive a continuous flow of Ge from the Ge beam. Some Ge atoms can also come from the catalyst itself. This can lead to a restructuration of the surfaces displayed by the sidewalls. A nanowire undergoing such a restructuration is shown in Figure 3.10. Over the course of several seconds, we can see the addition of two {111} layers to the GeNW surface plane on the left (yellow arrows). They originate from the {113} surfaces shown by the yellow arrow in Figure 3.10a and then propagate along the sidewall towards the nanowire base in a step-flow fashion. The step propagation front is not a single plane. Because of this surface restructuration on sidewalls by propagation of additional {111} layers, the system will tend to extend existing {111} surfaces, push {113} surfaces to fuse together and reduce the number of edges on the sidewall. By reducing this number, the system minimizes the energy of the left sidewall.

{113} surfaces have an energy of $0.066\,\mathrm{eV}\cdot\mathrm{Å}^{-2}$. {111} surfaces have a slightly greater energy at $0.069\,\mathrm{eV}\cdot\mathrm{Å}^{-2}$ while {112} have the lowest energy of the three, at $0.060\,\mathrm{eV}\cdot\mathrm{Å}^{-2}$ [200]. Given that the sidewalls are made of {111} instead of {112}, it is likely that the {111} surfaces are reconstructed which lowers their energy below the {112} one. It is therefore surprising that {113} surfaces are created in the first place. This can be explained by considering the two following aspects:

- The diameter of the GeNW near the catalyst-nanowire interface is constrained by the diameter of the liquid catalyst.
- {111} sidewalls which have the lowest energy are not parallel to the nanowire growth axis.

In Figure 3.10, if the catalyst would continue growing the GeNW by prolonging the flat {111} sidewall on the left, it would lead to the shrinking of the catalyst-nanowire interface. Knowing that the liquid catalyst is pinned on the edge of the nanowire and assuming it preserves its

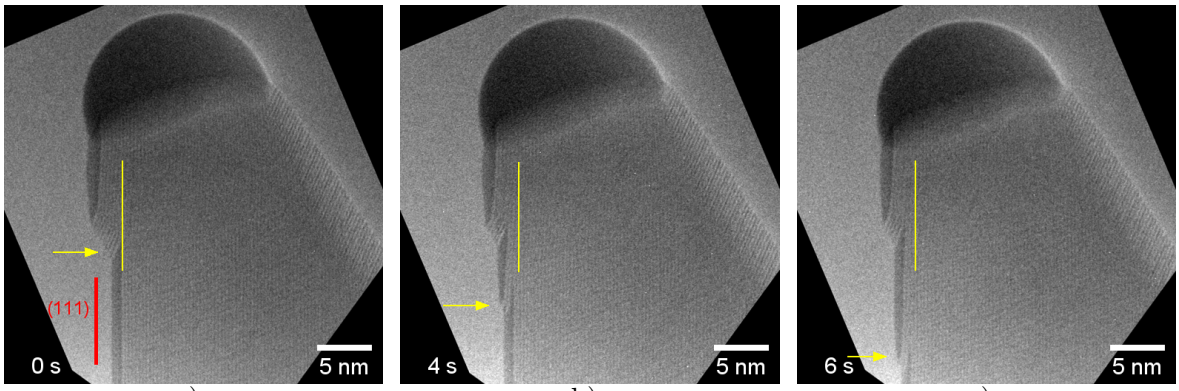

a) b) c)

FIGURE 3.10: TEM micrographs of a GeNW undergoing surface restructuration. The yellow arrow shows the position of a step flow. The red line in a) indicates the orientation of {111} planes; the yellow lines, parallel to it, are guides to the eye to show the thickening of the nanowire.

volume, we see that the decline in the total area of the interface would result in the deformation of the droplet. Thus, the system would endure a geometric frustration. This is similar to what occurs in SiNWs when catalyzed by Au [201]. To reduce the frustration, the catalyst will alternatively create low energy {111} and higher energy {113} surfaces to maintain a roughly constant diameter of the catalyst. Therefore, it is the step-bunching of the newly created {111} planes that creates {113} facets. Alternating {111} and {112} would still lead to the size reduction of the catalyst-nanowire interface and to a droplet deformation. That is because {112} surfaces are perpendicular to the interface. In the GeNW of Figure 3.5, the right-hand sidewall also undergoes significant restructuration. At first, we see a succession of {111} and {113} surfaces due to the geometrical frustration. However, while the {111} surface at the top remains stable during the growth, it is different for the other {111} and {113} surfaces below. Indeed, we observe a gradual transition from two types of surface to a single one thanks to the sidewall deposition: the incoming Ge atoms preferentially deposit at the top edges of {111} surfaces. This filling has the following consequences: {113} rough surfaces gradually disappear and a single and longer {111} is established. Also, atomic steps in other {113} are filled to become a rough {112}. Overall, we have a replacement of {113} by lower energy {112} ($0.071\,\mathrm{eV}\cdot\mathrm{\AA}^{-2}$) followed by a reduction in the number of edges on the sidewall. Sidewall deposition thus constitutes a path towards controlling faceting after the growth of GeNWs which are growing along the ⟨111⟩ direction.

Because the surface restructuration is dependent on the diffusion of Ge atoms towards the step, we conjecture that it can be controlled by varying the substrate temperature. To that effect, we image another sidewall and observe a change in behavior when we change the surface temperature. At 360 °C, Ge atoms seem to preferentially deposit on the rough part of the walls, composed of facets oriented close to {113} (Figure 3.11a-b). When we reduce the temperature to 200 °C, rather than reducing the wall roughness on the right side of the image, Ge atoms diffuse towards existing monoatomic steps (Figure 3.11c-d). This results in the propagation of the said steps and the creation of multiple small {111} surfaces. The distance between the steps provides a lower bound of around 10 nm for the Ge atoms diffusion length at 200 °C. At room temperature, Ge atoms are unable to diffuse and this leads to the formation of an amorphous layer of Ge at the surface. We then see that temperature is a key factor for surface restructuration and also influences the step bunching. Lower temperatures favor their spreading

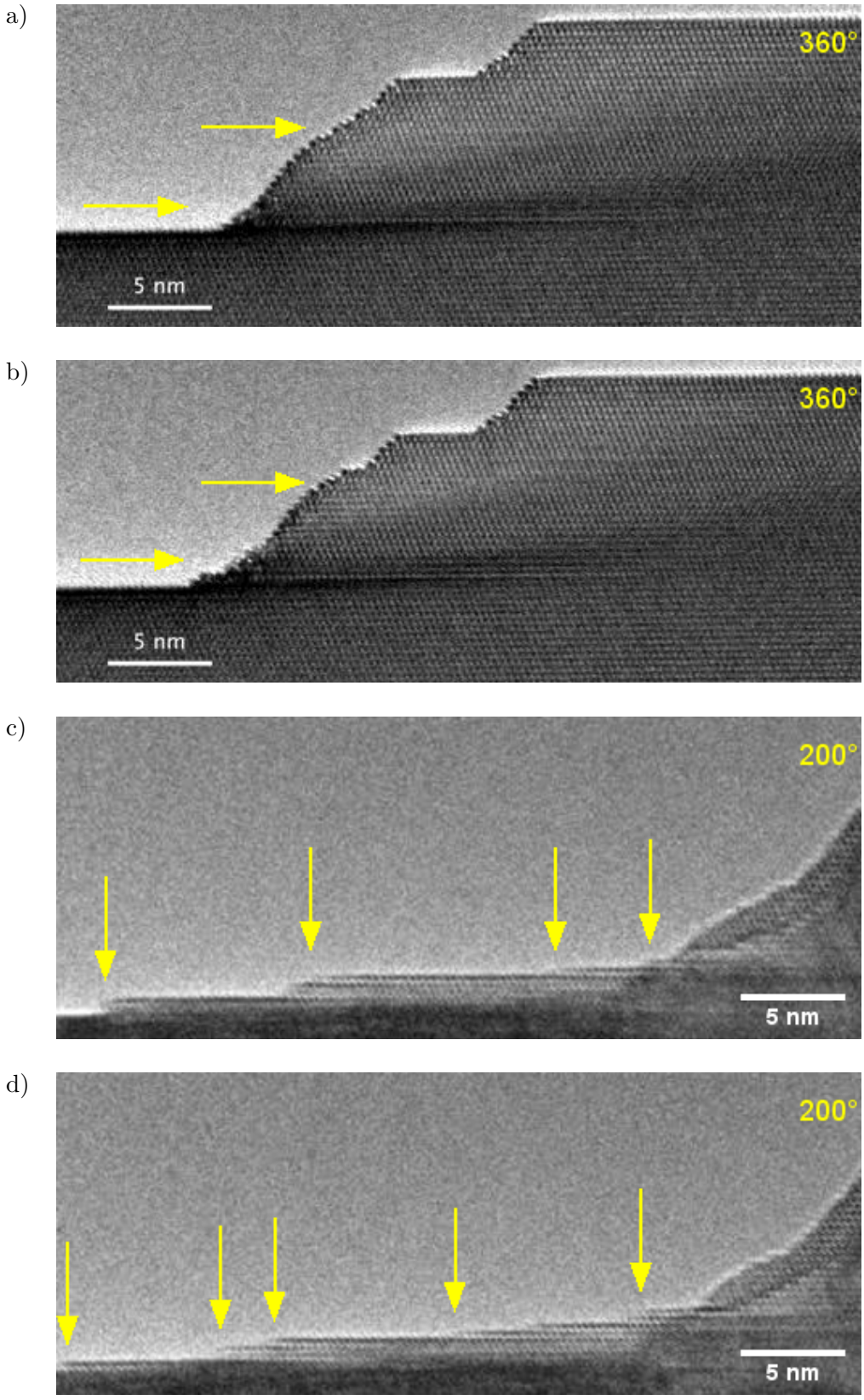

FIGURE 3.11: Effect of temperature on the surface restructuration. Images taken at temperatures of 360 °C for a) and b) and 200 °C for c) and d), respectively. Images at the same temperature are taken 100 s apart. The yellow arrows indicate area of interest between images taken at the same temperature.

while high temperatures stabilize their bunching. Consequently, carefully changing temperature during growth allows for a fine control on the morphology of GeNW sidewalls.

3.1.6 Unpinning of the catalyst

Under steady growth conditions, the catalyst droplet is pinned at the top edge of the nanowire thanks to the balance of the forces associated with surface tensions (Figure 3.13). On some occasions however, it is possible for the liquid catalyst to unpin from the top of the nanowire and slide along the sidewalls. The nanowire in Figure 3.12, growing along the ⟨111⟩ direction, has its catalyst unpinning from the top {111} and sliding along the atomically rough {122} before joining the flat {111} sidewall. In the initial stage, the nanowire was cooled at 352 °C, which solidified the catalyst. The presence of periodic lattice fringes in the catalyst in Figure 3.12a is an evidence of the solidification. The spacing measured is 0.36(5) nm. The high uncertainty is due to the small visible number of fringes in the catalyst. However, the measured spacing is visibly larger than the Ge (111) spacing (0.326 nm) and any interplanar distances in Au. It is possible that the observed solid phase is actually a metastable compound of Au and Ge, which was already reported for GeNW growth [202]. Also, there is a contrast in the catalyst particle. This suggests a phase separation between the Ge-rich and the Au-rich part.

We then heat the substrate to 450 °C, after which the melting and unpinning of the catalyst is observed. After that, the propagation of atomic steps, as seen in Section 3.1.5, allows the catalyst droplet to slide back and forth (Figure 3.12b). At the same time, the droplet is visibly shrinking during its erratic movement, showing not only a loss of Ge atoms but also Au. After a few seconds, the liquid droplet has stopped moving while the sidewall continuous supply of Ge leads to the growth of a new branch on the existing nanowire (Figure 3.12c). Finally, the catalyst completely vanishes (Figure 3.12d). Note that the unpinning was also observed at constant temperature.

Let us investigate what made the catalyst unpin in the first place. Thermodynamics dictates that for a droplet to undergo movement while resting on a solid surface, the sum of forces exercised on the triple phase boundary between the vapor phase, the liquid droplet and the solid surface should be non-zero. The balance of forces at the edge of a droplet resting on a flat surface is given by the well-known Young's relation:

$$\gamma_{LV} \cos\beta + \gamma_{SL} = \gamma_{SV} \tag{3.2}$$

where γ_{LV}, γ_{SV} and γ_{SL} are the liquid-vapor, solid-vapor and solid-liquid interfacial energies respectively. β is the wetting angle of the droplet. When the relation is true, the droplet remains static. This relation must be modified due to the specific geometry of a nanowire into the form:

$$\gamma_{LV} \cos\beta + \gamma_{SL} = \gamma_{SV} \sin\theta \tag{3.3}$$

where θ is the angle between the normal to the catalyst-nanowire interface and the adjacent sidewall (Figure 3.13), also called tapering angle.

Because the droplet was initially pinned at the top, it is safe to assume that either change in the wetting angle, tapering angle or interfacial energies could account for its shift in behavior. These changes have different implications. The wetting angle is directly linked to the volume of the liquid droplet and nanowire diameter. We already established that the catalyst could lose part of its Ge content when we discussed the regression event. It is also possible that Au

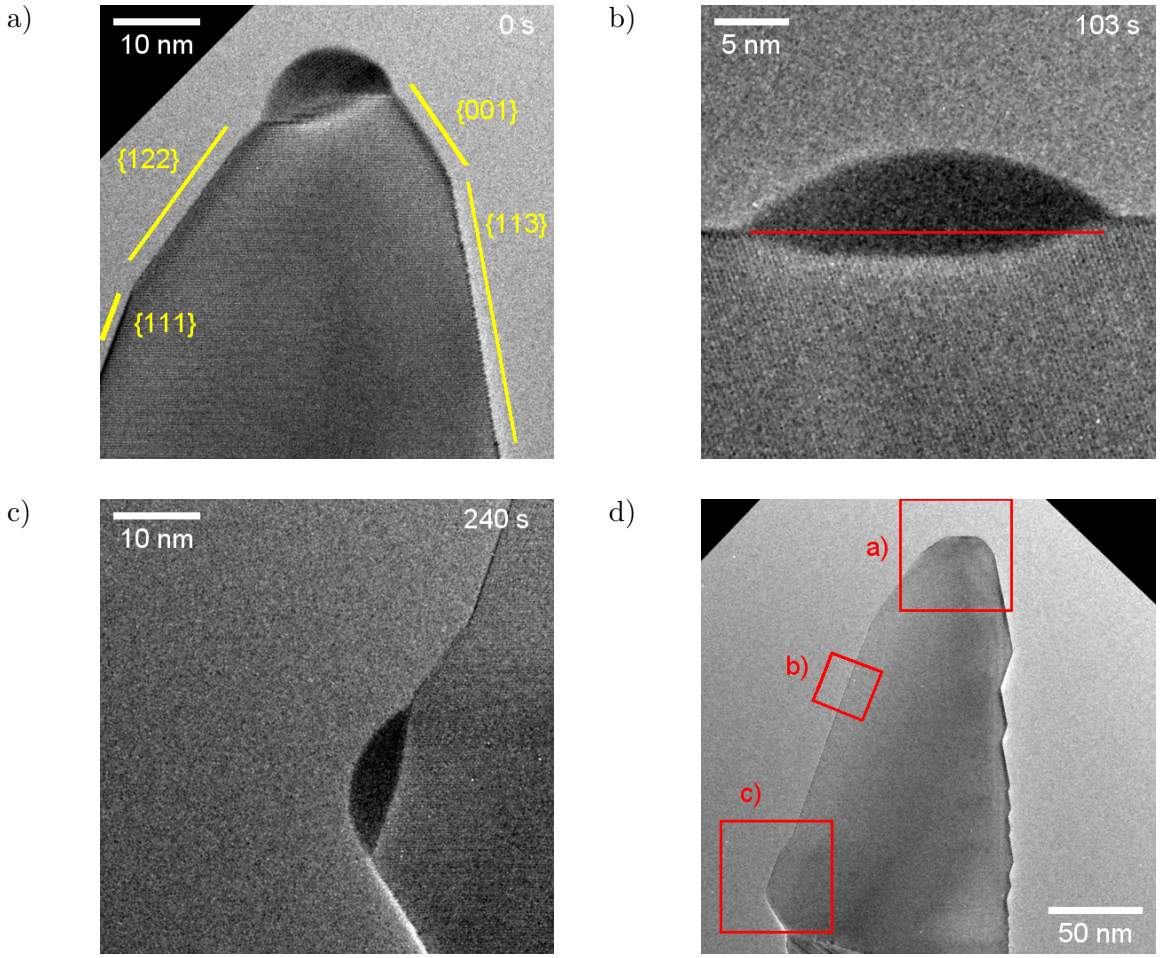

FIGURE 3.12: Unpinning of the catalyst from the top of a GeNW. a) The solid catalyst at 352 °C is initially on top of the nanowire. b) 103 s after heating at 450 °C, the catalyst has unpinned and is sliding back and forth on a flat 111 surface. The red line shows that the droplet rests on an atomic step. The image is rotated to better highlight the step. c) After 240 s, the catalyst has come to a rest and is growing a new branch. d) Low magnification view of the nanowire showing where the sliding catalyst has been imaged.

atoms leak out of the catalyst as we will see later in Section 3.3.2. A possible explanation for the unpinning is that the leakage is significant enough so that it disturbs the balance of forces at one region of the triple phase line. The second option implies that one solid-vapor interfacial energy abruptly changes during the growth. This can happen in the case when the surface is restructured prior to the unpinning. This is also a very likely possibility given the observations of Section 3.1.5. Modifications of the surface type will have repercussions on the tapering angle θ. A good illustration is the nanowire of Figure 3.12a: the surfaces adjacent to the catalyst are different as the left sidewall is a {122} surface while the right one is a {001} type. Both will give different values of θ (-36° for {122} and 33° for {001}). In conclusion, it is probable that the droplet unpinning is due to a combination of both a volume variation and changes in surface energy during the growth.

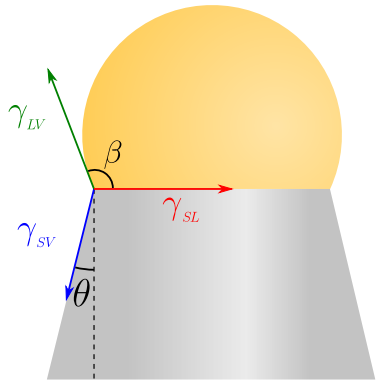

FIGURE 3.13: Schematic of forces at the triple phase boundary.

3.2 Chemical vapor deposition growth of GeNWs

In this section, CVD sources are used to grow Au-catalyzed GeNWs. In the *in situ* microscope NanoMAX, a gas cylinder containing a mixture of digermane Ge_2H_6 diluted in 90 % H_2 provides the Ge required for the growth. In the plasma-enhanced chemical vapor deposition (PECVD) Plasfil reactor (see Section 2.2), a bottle of germane GeH_4 diluted in 99 % H_2 is used. Using both pieces of equipment to grow GeNWs may grant additional insights on the dynamics, specifically on the effect of the plasma environment.

3.2.1 Nucleation and growth

Prior to the injection of the 10:90 Ge_2H_6/H_2 mixture, we heat the SiC membrane to 300 °C. 0.3 sccm of the mixture are introduced into the microscope, which gives a total pressure of 2×10^{-2} mbar or a Ge_2H_6 partial pressure of roughly 2×10^{-3} mbar. Upon arrival in the vicinity of the heated substrate, the combined action of the electron beam and the temperature easily cracks the digermane molecule. This is immediately visible by comparing Figure 3.14a-b. Both figures are separated by a time interval of 26 s. We see that the Au catalyst has expanded. Just after that, the Au particle has been melted and became a liquid alloy of AuGe. At 41 seconds, a solid Ge nucleus appears and starts to grow into a GeNW. Following the nucleation, the elongation of the GeNW occurs in a similar fashion as what we described with the MBE source. The subsequent growth of Ge (111) crystal takes place in a layer by layer fashion.

While the Au catalyst in the images has grown in size due to the absorption of Ge atoms, spherical Ge crystals begin to form at a rapid rate at the SiC surface. It is also another demonstration of the influence of the temperature on the atom diffusion. At 300 °C, the thermal energy is insufficient to drive most Ge atoms directly towards the Au catalyst. The impinging Ge atoms remain close to their landing location, condensing to grow these three-dimensional structures. With the MBE growth where the temperature was set to 400 °C, no such crystals were observed, even well after the first formation of a solid Ge nucleus. After 70 seconds of exposure to the gas mixture, the once-spherical Ge crystals have grown large enough to form a film on the substrate. This Ge film is problematic if one wants to obtain small diameter GeNWs. Indeed, the growth of this Ge film occurs at a much faster rate than the absorption of Ge and

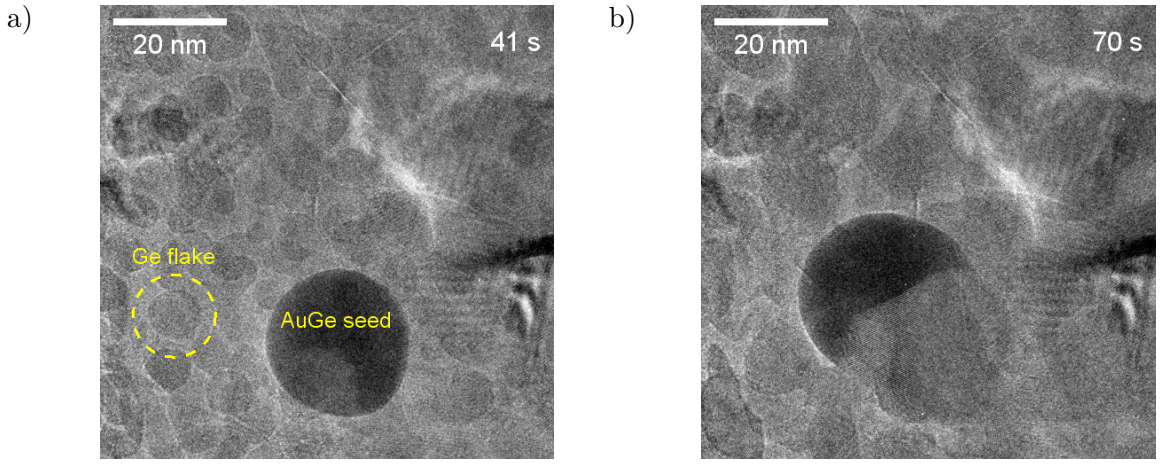

FIGURE 3.14: TEM micrographs taken during the early stages of the growth in NanoMAX using the CVD source on the heated SiC substrate at 300 °C. Ge flakes are seen growing while a GeNW is forming. At 0 second, the Ge_2H_6/H_2 mixture is injected in the TEM for a total pressure of 2×10^{-2} mbar.

subsequent nucleation in small Au droplets. Thus, before a GeNW can appear, some of the small catalysts have been buried under the Ge thin film (Figure 3.15). This does not occur for larger catalysts (10 nm or more) such as the one shown in Figure 3.14. This phenomenon favors the growth of large diameter GeNWs.

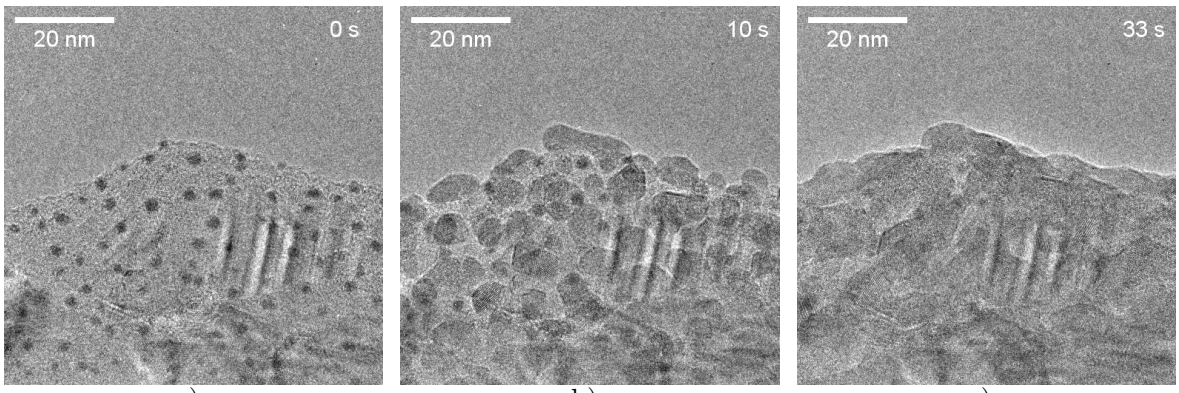

FIGURE 3.15: Burying of small Au catalysts ($\leqslant$ 5-nm diameter, darker contrast) at a substrate temperature of 300 °C. At 0 second, the 10:90 Ge_2H_6/H_2 mixture is injected in the TEM for a total pressure of 2×10^{-2} mbar.

For the growth in the Plasfil reactor, we use Au solid particles evaporated on Si (111) with a native oxide. Thus, we do not expect epitaxy nor any preferential growth direction. We first increase the temperature of the substrate holder to the growth temperature of 300°C at 0.8 mbar pressure of pure H_2. When the growth temperature is reached, the H_2 is purged from the reactor. We then introduce the 1:99 GeH_4/H_2 gas mixture at a pressure of 0.9 mbar and ignite the radiofrequency plasma with power of 10 W. This gives a GeH_4 partial pressure of 9×10^{-3} mbar. At this moment, the germane molecules start to dissociate and the growth process starts. The growth finishes by switching off the plasma and replace the gas mixture of GeH_4/H_2 with pure H_2. The electrodes are then slowly cooled to room temperature after which the sample is retrieved. We have then loaded the wafer inside an SEM and transferred some

of the grown GeNWs onto a carbon-coated TEM grid using the scratching technique shown in Section 2.2.

3.2.2 Nanowire morphology

Similar to the MBE growth, most wires produced in NanoMAX were found to grow in the ⟨111⟩ direction. For a growth experiment at a temperature of 300 °C, the GeNW diameter at the tip ranges from 7 nm to 86 nm with the average and median value at 35 nm and a standard deviation of 20 nm (measured on 65 wires). For the PECVD growth in Plasfil at 330 °C, the diameter at the tip ranges from 14 nm to 60 nm with the average at 31 nm and a lower standard deviation of 8 nm (measured on 68 wires). The main growth direction is also ⟨111⟩. Compared to the 10-nm average Au particles diameter in Figure 3.1, we see that most of the GeNWs have superior diameter. This is due to temperature-activated Au-particle coalescence. In the following, we will detail the differences between wires grown by CVD or PECVD.

3.2.2.1 Nanowire-catalyst interface

In GeNWs grown in NanoMAX by CVD, we again observe the presence of a truncated facet near the triple phase boundary (Figure 3.16). The angle between the main (111) interface and the truncated facet is similar to that found with MBE. This suggests that this facet has the same function as in MBE despite a superior growth rate for CVD ($5.4 \times 10^{-1}\,\mathrm{nm \cdot s^{-1}}$). In the PECVD Plasfil reactor, the interface is missing as all catalysts on top of GeNWs have vanished after retrieval of the sample and its loading into the SEM. We suggest two possibilities. First, the catalyst was consumed completely during the growth. We have already observed a similar event in Section 3.1.6. The other hypothesis is that the liquid catalyst was destabilized at the end of the growth when we stopped the plasma and cooled the sample back to the room temperature. This would mean that the plasma must have an effect on the surface energies, which may lead to unpinning the droplet after it is off.

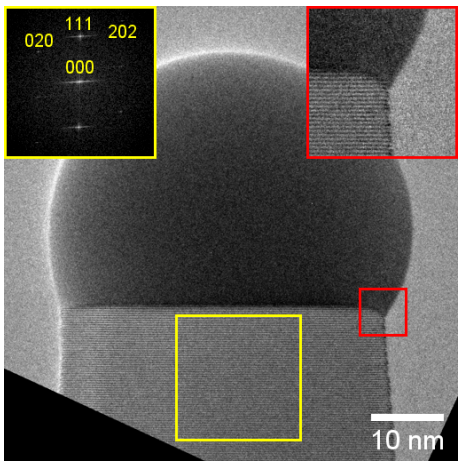

FIGURE 3.16: TEM image of a CVD-grown ⟨111⟩ GeNW in NanoMAX. Inset: FFT of the yellow squared area. Close-up view of the truncated facet in the red squared area.

To decide which hypothesis is correct, we grew GeNWs for different growth times. The results for 10-, 17- and 60-minute growths are shown in Figure 3.17. For any growth duration,

no catalysts are found on top of GeNWs. Also, wires grown for 60 minutes are noticeably longer than those growing for 10 or 17 minutes. It is then clear that the catalyst can stay on top for at least longer than the latter duration. Thus, it rules out the possibility that the catalyst be completely consumed during the growth. Furthermore, all the GeNW tips have more or less the same diameter regardless of the time. This also disqualifies the droplet consumption possibility and only leaves a potential unpinning due to the plasma shutdown that occurs at the end of the growth when we stop the plasma and cool down to room temperature to retrieve the sample for later observations.

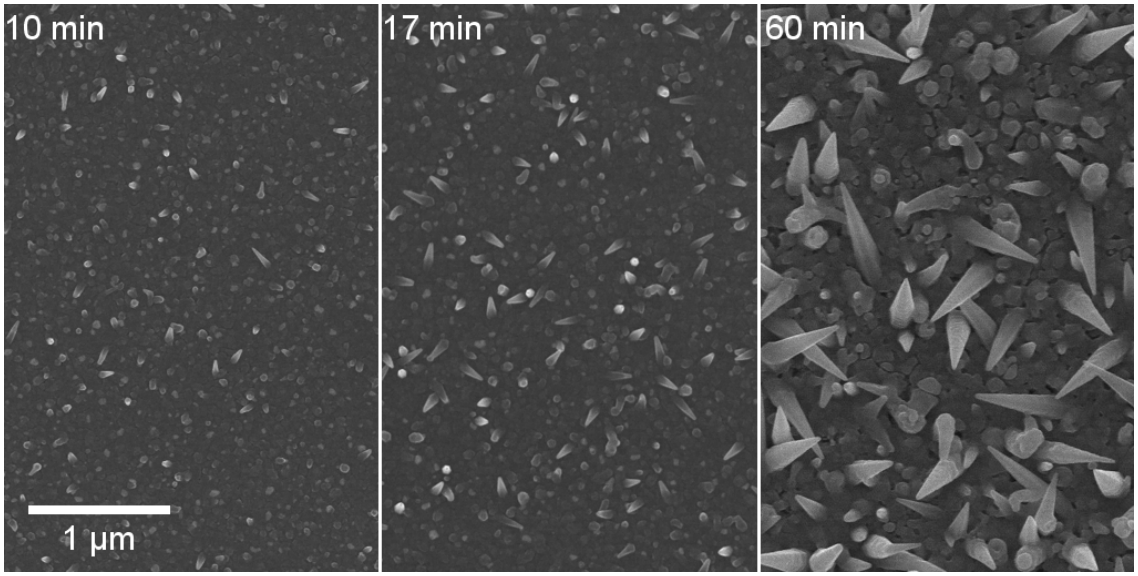

FIGURE 3.17: SEM images of GeNWs grown in Plasfil for different growth times on Si (111) at 330 °C. The scale is the same in all images. White dots in the 10- and 17- minute growths are GeNWs that grew almost perpendicularly to the substrate.

3.2.2.2 Tapering angle

By measuring two diameters on the same nanowire: one at the top and one far from it, we can define a tapering angle. An angle of 0° means that the GeNW is perfectly cylindrical. For GeNWs grown in NanoMAX, we find the tapering angle to be around 1° (Figure 3.18a). In the PECVD Plasfil reactor with a 9×10^{-3} mbar GeH_4 partial pressure at a temperature of 330°C, the tapering angle is more pronounced with a value of 12° (Figure 3.18b). The tip diameter is around 15 nm for most wires. Such a disparity has to be related to the differences of growth conditions between the two setups. Regarding Plasfil, we have already found that a potential consumption of the Au catalyst droplet during the growth is unlikely. Thus, the tapering in our GeNWs grown in Plasfil is not due to a gradual decrease of the catalyst diameter. Rather, sidewall deposition is a more reasonable candidate. Lateral walls near the base of a GeNW are exposed for a longer time to GeH_x than the top, which gives the tapered shape. More specifically, it is the ratio between axial and radial growth rate that drives the tapering angle. When the radial growth rate is no longer negligible compared to the axial one, an increase in the angle is expected.

The growth rates in NanoMAX and Plasfil both depend on the amount of cracked germanium hydride molecules that impinge on the growing GeNW, which is related to the cracking

efficiency and the partial pressure of the hydrides. In Plasfil, the cracking is done by the plasma environment. Thus, the reactor is filled with radical species issued by cracked germane. Both the lateral walls and the catalyst receive a similar amount of the latter. Thus, the lateral and axial growth rate are comparable and this leads to the high tapering angle. In NanoMAX, we have not used the plasma source for the growth. The cracking of Ge_2H_6 is essentially done by the contact between the molecules and the heated Au catalysts. Thus, there should be cracked species on the Au catalysts and negligible amount on the walls. This gives a high axial over radial growth ratio and maintains a very small tapering angle.

If the axial over radial growth rate favors tapering in Plasfil, it could also be due to the inability of Ge atoms which arrive on the sidewalls to reach the catalyst. This deprives the catalyst of Ge atoms and hinders the axial growth rate. A diffusion length for Ge atoms on the walls that is very inferior to the nanowire length can favor sidewall growth as was shown in Section 3.1.5.

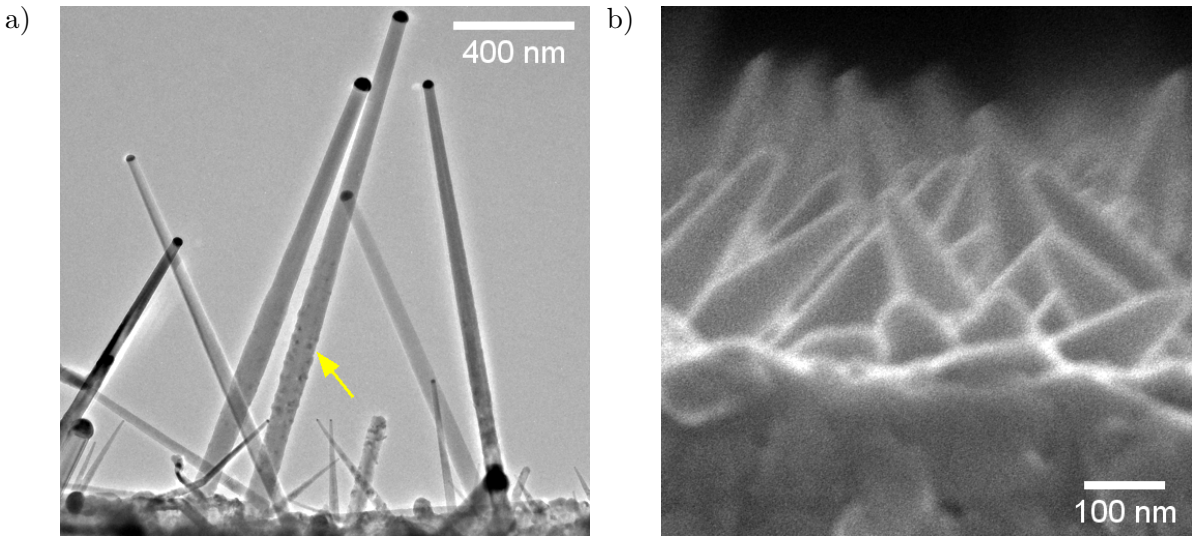

FIGURE 3.18: Difference of tapering angle between GeNWs grown in NanoMAX and Plasfil. a) TEM micrograph of GeNWs grown in NanoMAX on the heated SiC substrate. Some Au precipitates are found at the GeNW base (yellow arrow). These are formed after Ge_2H_6 purging and cooling down at room temperature. b) SEM micrograph of GeNWs grown in Plasfil on a Si (111) wafer.

3.2.2.3 Sawtooth faceting

In MBE, we have found the faceting to be asymmetrical when observed in the [110] zone axis. In CVD, since the general shape of GeNWs is different, we also expect a different faceting. An important difference is the symmetrical nature of the faceting, as both the left and right sidewall show a succession of similar family of planes. Figure 3.19a clearly demonstrates that both sidewalls are only made of small {111} planes arranged in a saw-tooth fashion with different oxide layer thicknesses. GeNWs grown in NanoMAX for example have a series of 3 (double-) atomic column creating a small tilted {111} plane ended on both side by a small step which is a two-atom wide {100} plane. This succession of small facets is ultimately what gives the GeNW a smooth appearance, contrasting with GeNWs grown with MBE.

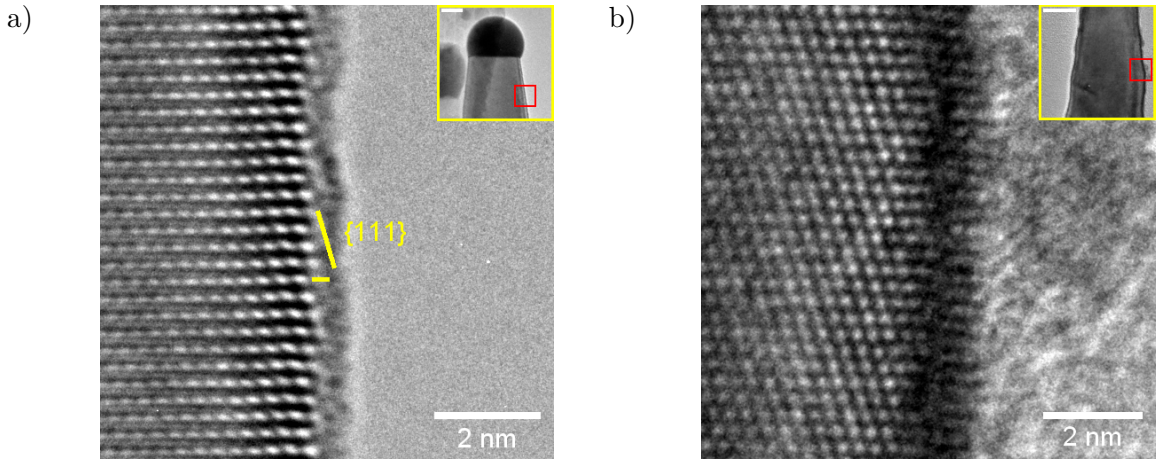

FIGURE 3.19: Difference of sidewall faceting between GeNWs grown in NanoMAX by CVD and Plasfil by PECVD. a) TEM micrograph of the red squared area in the inset. Inset: low magnification view of a GeNW grown in NanoMAX, scale: 20 nm. b) TEM micrograph of the red squared area in the inset. Inset: low magnification view of a GeNW grown in Plasfil transferred on a TEM Cu grid using the scratching technique, scale: 20 nm.

The faceting of GeNWs grown in Plasfil is more difficult to observe properly. The substrate transfer from the reactor to TEM implies the GeNWs exposure to ambient air. An oxide layer inevitably forms around the sidewalls and hinders observation. Figure 3.19b shows a similar structure of the sidewall with a saw-tooth faceting based on small {111} planes. The major difference with NanoMAX is associated with the fact that the faceting in Plasfil has to accommodate the much higher tapering angle. It can be seen that the small tilted {111} planes are not always three atomic column-long but sometimes four or more before encountering a horizontal {111} step. By modulating the length of the tilted surfaces, different tapering angle can be obtained.

3.2.3 Temperature influence on the growth of GeNWs

Nucleation in NanoMAX was done at a temperature of 300 °C. After we obtained GeNWs with sufficient length, we varied the temperature in a range from 230 °C to 300°C under a 2×10^{-3} mbar Ge_2H_6 partial pressure. We find that the growth rate is independent of the temperature in the 250-300°C range at 5.4×10^{-1} nm $\cdot$ s^{-1}. In a given GeNW, we have not observed any visible differences between parts that were grown at different temperatures. Faceting and tapering remain the same while catalysts retain their spherical shape.

The latter observation is surprising given that the eutectic temperature of the Au-Ge binary system is 361 °C. This means that along the whole temperature range where we grew GeNWs, we should have a solid catalyst containing a mixture of diamond cubic Ge and face centered cubic Au. Thus, we should have a catalyst with clearly defined facets. However, as Figure 3.18a shows, all catalysts have a spherical shape and this is evidence that they are liquid. Thus, we manage to have a VLS growth mode, and not VSS, even below the eutectic temperature. The liquid catalyst is then a metastable supercooled melt. Kodambaka *et al.* and Gamalski *et al.* have reported a similar behavior for the AuGe binary melt [32, 203]. Theses authors found liquid AuGe droplet for temperatures as low as 240°C where the gas precursor for germanium

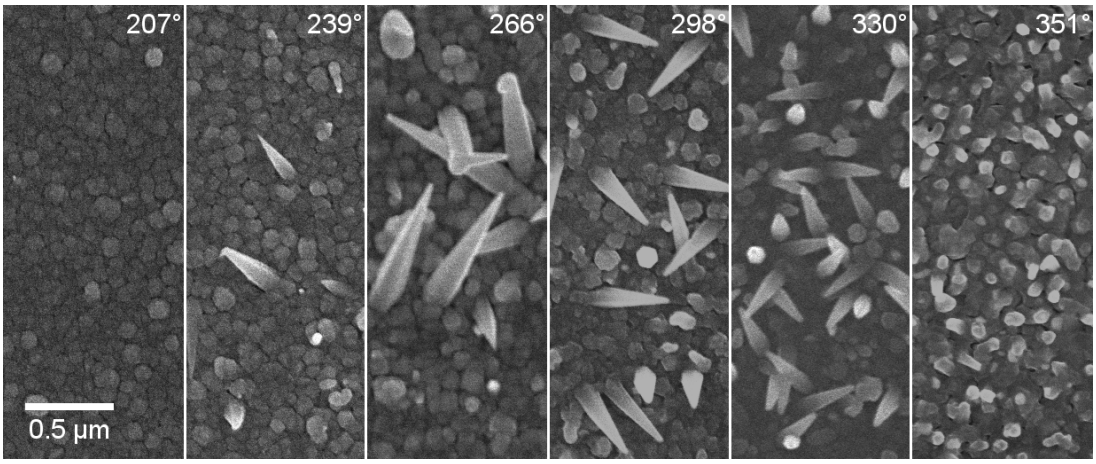

FIGURE 3.20: SEM micrograph of GeNWs grown in Plasfil for 60 minutes at different temperatures.

was also Ge_2H_6. While it is possible, thanks to size effects, to partially stabilize the supercooled droplet [192], it is more likely that the catalyst remains liquid due to the high nucleation barrier for the formation of solid face-centered cubic Au. High supersaturation in Ge inside the catalyst decreases the chemical potential of Au atoms. In contrast, a decrease in Ge concentration should allow the Au chemical potential to overcome the barrier and solidify the droplet. As temperature further decreases, it becomes harder to retain a high level of Ge supersaturation as dissociation of the Ge_2H_6 is more difficult. We later discuss how a high supersaturation is possible.

In the Plasfil reactor, we went for a broader temperature range from 207 °C to 400 °C. Figure 3.20 shows SEM low magnification views of typical GeNWs obtained at the indicated temperatures for the same growth time of 60 min. The growth of GeNWs starts at 239 °C. The nanowires are short and far away from each other. An increase in temperature to 266 °C yields a higher density array of GeNWs and longer ones. When the temperature is further increased to 298 °C, an even higher density is reached but the GeNW average length seems to decrease, in contrast to to NanoMAX where no measurable change in growth rate was observed over the 250-300 °C range. The measured growth rate in Plasfil is $1.6 \times 10^{-1}\,\mathrm{nm \cdot s^{-1}}$. From 351 °C onward, the nanowire shape changes drastically. Dense and short wires become the norm.

3.3 Divergence in surface dynamics with growth conditions

In the previous sections, we have described the growth and highlighted some structural differences in GeNWs for three fundamentally different growth conditions:

- *In situ* growth in NanoMAX in a high vacuum environment where Ge atoms were supplied by an MBE source giving a slow growth rate of $7.4 \times 10^{-3}\,\mathrm{nm \cdot s^{-1}}$.
- *In situ* CVD growth in NanoMAX with a vapor phase containing Ge_2H_6 molecules and H_2 at a rate of $5.4 \times 10^{-1}\,\mathrm{nm \cdot s^{-1}}$.
- PECVD growth in the Plasfil reactor using a mixture of GeH_4 and H_2 as a precursor at a rate of $1.6 \times 10^{-1}\,\mathrm{nm \cdot s^{-1}}$.

In this section, we now discuss physical consequences of these different environments on surface dynamics.

3.3.1 Influence of surface hydrogenation

Apart from the wide disparity in the observed growth rates, the most obvious repercussion of using different types of sources is the chemical composition of the vapor phase surrounding the growing nanowires. In MBE, pure Ge atoms are sent towards the sample to grow GeNWs while CVD necessarily involves the presence of hydrogen atoms coming from the cracking of germanium hydride molecules. Upon cracking, radical species, such as atomic hydrogen, are produced which may impinge on the nanowire lateral walls and be adsorbed, filling existing dangling bonds. In Plasfil, due to the plasma environment, hydrogen atoms are present in a much greater quantity. Large scale hydrogen adsorption may create a passivation layer around the nanowire, greatly influencing surface dynamics by lowering surface energies [204, 205]. It was also suggested that a hydrogen layer reduces Ge surface self-diffusion [206]. At the same time, some hydrogen atoms may desorb from the GeNWs sidewalls [207] especially at high temperature. This can reduce the hydrogen passivation layer quality and lead to further modifications in surface energies.

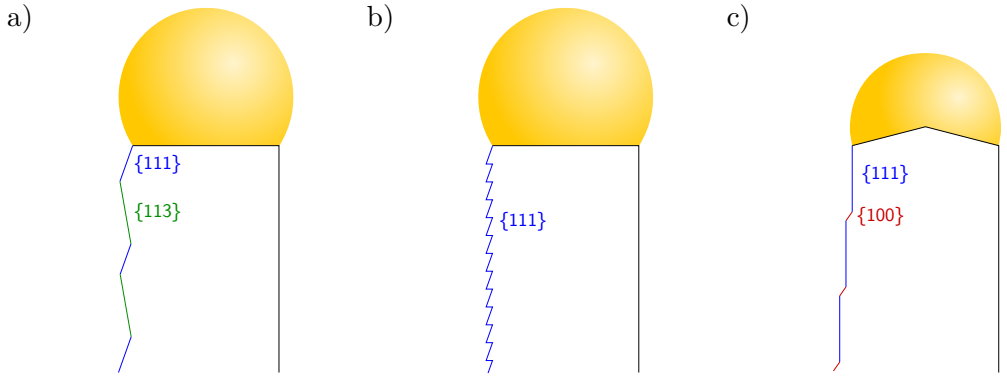

FIGURE 3.21: GeNW sidewall configuration depending on their coverage by adsorbed hydrogen atoms. a) Hydrogen-free surface configuration (MBE). b) Hydrogen-filled surface configuration (CVD) at a H_2 partial pressure of around 10^{-1} mbar. c) Hydrogen-filled surface configuration (PECVD) at a H_2 partial pressure of around 3 mbar; notice that, in this case, the GeNW is growing along the $\langle 110 \rangle$ direction.

Changes in surface energies generally have an impact on the equilibrium shape of a given crystal. It is also the case for nanowires, particularly with the sidewall faceting. Comparing what was obtained with MBE and CVD growths, it is clear that adsorbed hydrogen plays a major role. Hydrogen-free MBE growth favors large facets, alternating {111} and {113} orientations (Figure 3.21a) while CVD with the presence of hydrogen shows very short tilted and horizontal {111} sidewalls (Figure 3.21b). We have established that the coexistence of at least two different surface types in the nanowire sidewalls is due to geometrical frustration: {111} surfaces are the lowest energy surfaces but they are not parallel to the growth axis. If the catalyst droplet continues to grow {111}, it would reduce the size of the interface and lead to deformations in the droplet (Figure 3.13). Therefore, the catalyst needs to create another surface to preserve the diameter of the interface. If hydrogen is not considered, alternating {111} and {113} minimizes the total energy of the system as well as keeping an overall constant nanowire diameter and the number of surface edges, which cost energy, is minimized. If a significant amount of hydrogen

is covering the walls, we see that the reduction of surface energy is so high that it now becomes more favorable to only grow low energy hydrogen-filled {111} [208] facets with more surface edges. If coverage becomes insufficient, then newly nucleated layers revert back to the {111} and {113} double surface type configuration [206].

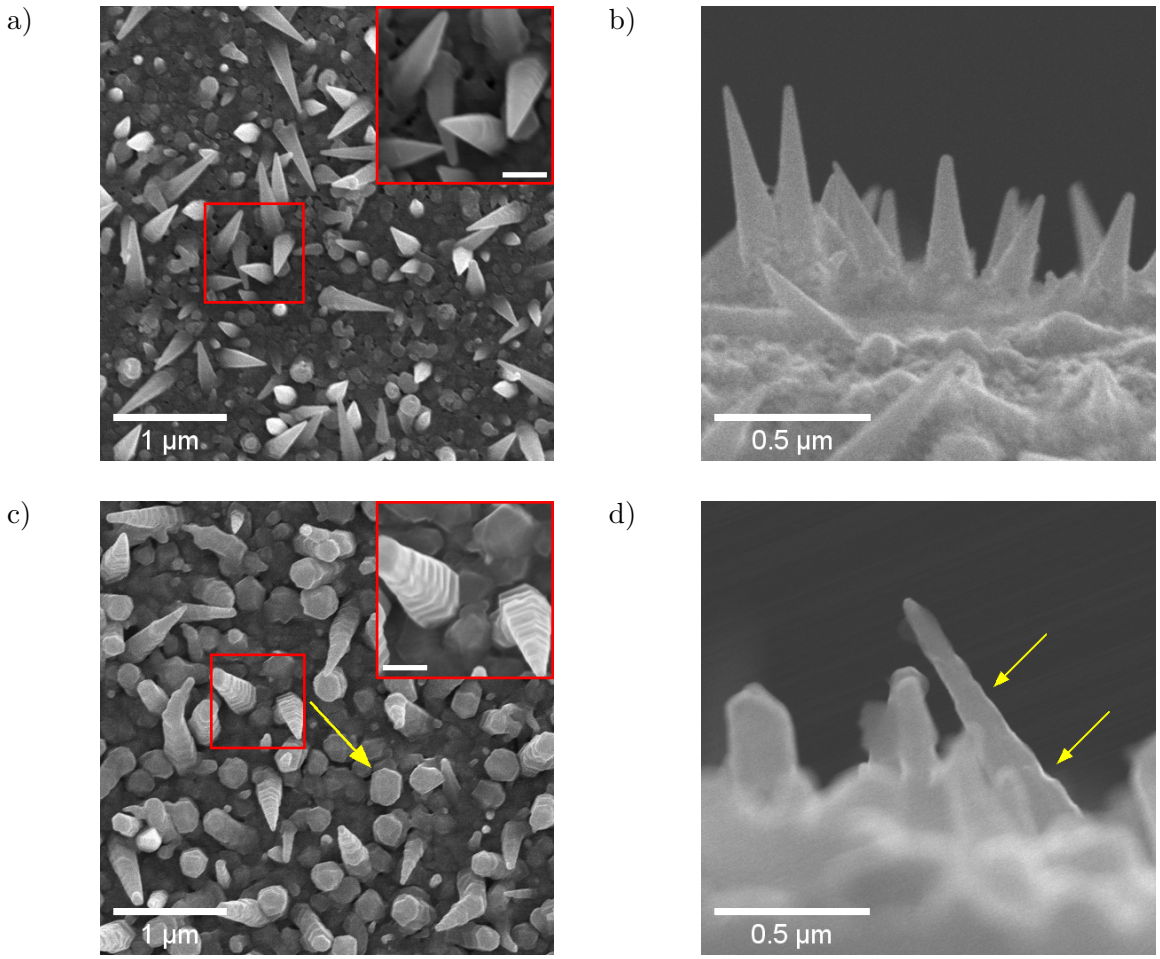

FIGURE 3.22: Effect of hydrogen partial pressure on the 60-minute growth of GeNWs in Plasfil at 330 °C on a Si (111) wafer. a-b) Top and side view SEM micrographs of sample prepared at 8.9×10^{-1} mbar H_2 partial pressure. Inset: Close-up view, scale bar: 200 nm. c-d) Top and side view SEM micrographs of nanowires grown at 2.9 mbar H_2 partial pressure. The yellow arrow in c) shows a nanowire lacking a tip. Yellow arrows in d) indicate terraces in a GeNW. Inset: Close-up view, scale bar: 200 nm.

The hydrogen layer also affects the liquid catalyst droplet, and is a determining factor for its stability. Thanks to the experiments in the Plasfil reactor, we have shown indeed that upon plasma shutdown, the liquid catalyst is no longer pinned to the tip of the nanowire. Figure 3.17 clearly demonstrates this where no catalysts are visible at the nanowire tips regardless of the growth duration. Let us try to explain this mechanism. The plasma environment is responsible for the efficient cracking of GeH_4 into GeH_x radicals. Furthermore, H_2 is also dissociated into atomic hydrogen. When the plasma is off, these chemical species are no longer produced so that additional atomic hydrogen no longer impinges onto the sidewalls. The quality of the hydrogen passivation layer then starts to degrade in coverage because the hydrogen atoms desorbing from the nanowire surface are not replaced. Next, sidewall surfaces become bare and their energy rise back to their initial value. This gradual increase in surface energy, exacerbated by the high

tapering angle of the grown GeNWs, changes the equilibrium wetting angle at the triple point and destabilizes the liquid catalyst droplet on top. Finally, a critical point is reached when the droplet wets the nanowire it sits on, ultimately leading to the unpinning of the catalyst. Notice that this explanation only rests on the presence of hydrogen radicals and not on the plasma conditions. Thus, in the NanoMAX growth, if Ge_2H_6 present in the column is completely purged or significantly reduced, it should give the same result as a plasma switch off in Plasfil. Such an experiment was reported in the literature [206] and a destabilization of the catalyst was indeed observed.

Desorption is a thermally activated process. As temperature is increased, the rate of desorption should accelerate in an exponential way which depends on its activation energy. Thus, for a constant partial pressure of H_2 and germanium hydride, if the environment becomes hotter, there should exist a point where the amount of desorbed hydrogen per unit time exceeds the amount of hydrogen atoms adsorbed by the sidewalls. In the Plasfil reactor, for a H_2 partial pressure of 0.9 mbar, it seems that the threshold is reached around 351 °C where the GeNWs shape undergoes a transition as seen in Figure 3.20. A similar result was also described elsewhere [207] along with the observation that the transition temperature shifts with the pressure of H_2.

Because a change in surface energies affects the stability of the catalyst droplet, the nanowire growth direction can be influenced by the presence of hydrogen atoms. Figure 3.22 shows two growth experiments with two different H_2 partial pressures, one at 8.9×10^{-1} mbar and the other at 2.9 mbar. The GeH_4 partial pressure was fixed at 9×10^{-3} mbar in both cases. Nanowires grown with a high H_2 partial pressure (Figure 3.22c-d) have faceted sidewalls, contrary to those grown with a low amount of hydrogen (Figure 3.22a-b). We can clearly see the presence of terraces on the inset of Figure 3.22c. This is confirmed by the yellow arrows in Figure 3.22d. Furthermore, in this higher H_2-pressure sample, there is a higher proportion of wires where catalysts were unpinned. Such wires are identified by their top part, that do not present a thin tip. A few GeNWs presenting this particular shape were also observed in NanoMAX, see Figure 3.23. Analysis of the planes shows that their growth direction is ⟨110⟩ instead of the usual ⟨111⟩ [209] where the sidewalls are flat {111} or {100} surfaces, see Figure 3.21c. This is further confirmed by the inverse V-shape of the catalyst-nanowire interface, as this is a recurring feature in those wires [209]. Lateral growth is responsible for the formation of the observed terraces akin to the diffusion-induced propagation of atomic steps observed in Figure 3.11.

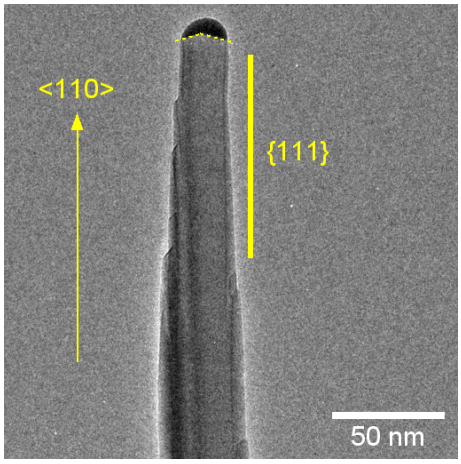

FIGURE 3.23: TEM micrograph of a ⟨110⟩ GeNW with flat {111} walls and terraces.

3.3.2 Existence of a wetting layer

In the previous section, we established that a plasma shutdown leads to the unpinning of the liquid catalyst, and that the adsorbed hydrogen affects the stability of the droplet. Also, in MBE growth, we have observed that the catalyst could unpin from the tip of the nanowire, and start sliding along flat {111} surfaces before finally vanishing. Thus, an interesting question arises about the nature of the mechanism responsible for these observations, and in particular how the catalyst can lose Ge and Au atoms during the growth. We propose that the formation of an AuGe wetting layer, originating from the AuGe catalyst, can explain our results. A similar phenomenon was observed during the growth of Au-catalyzed [210, 211, 212, 213] or Sn-catalyzed SiNWs [28].

Evidence for this wetting layer can be found in the *in situ* data. Because liquids tend to wet flat high energy surfaces rather than low energy ones, bare Ge (111) surfaces are good candidates for the search. A TEM image simulation, like the one used to simulate the 2H structure in Section 2.3.3.2, can help with the identification of the Au liquid layer. Using the structure depicted in Figure 3.24a consisting of the bare Ge (111) surface and a layer of randomly placed Au with one atom wide thickness, we obtain in a ⟨110⟩ zone the simulated image as in Figure 3.24b. The random position of the Au atoms should represent the liquid nature of the layer. The average distance between Au atoms is chosen so that the known liquid Au density of $17.31\,\mathrm{g}\cdot\mathrm{cm}^{-3}$ is achieved. The image obtained presents a very dark fringe on the Ge (111) surface. A very interesting characteristic of this dark fringe is that a change in the defocus of the TEM objective lens does not change its dark contrast. Thus, this dark fringe is clearly distinguishable from a Fresnel fringe that occurs on an object border, which can become dark or white depending on the defocus. The dark contrast is due to the high interaction cross section between incident electrons and the heavy Au nuclei as electrons are heavily deviated from their original path.

The GeNW grown by MBE (see Section 3.1.6) and shown in Figure 3.24c presents a long {111} section that does have a noticeably dark fringe while the upper rough {122} does not. This should be indicative on the presence of a continuous wetting layer. It provides a channel for the leaking of the catalyst droplet: the latter depletes its content in order to cover a portion of the {111} surfaces present in the GeNW. The fact that high energy rough surfaces such as {122} are not concerned by the wetting also explains how the AuGe liquid catalyst is stable in the first place. Rough planes serve as walls in the leaking process, while the Au catalyst extends a monolayer film over {111} planes. This limits the total area the catalyst can wet and allows for the droplet to stay on the top without sliding down.

Other evidence of the wetting layer in MBE grown GeNWs can be found after the growth. Upon cooling down, the liquid layer breaks down and forms small Au solid particles along the initially covered surface plane. This is best seen in Figure 3.25a-b. Clusters of dark aggregates can be seen on the edge of the GeNW. Some particles, like the one in the inset of Figure 3.25a are correctly oriented with respect to the electron beam and this enables to reveal their internal periodic structure. The nature of the dark aggregates is confirmed by EDX analysis of a dark spot in Figure 3.25a, which is shown in Figure 3.25d with peaks corresponding to Au. Clearly, they segregate on specific areas of the walls. This supports the hypothesis that the Au wetting layer can only exist on specific surfaces. Since the crystal structure and the surface energy hierarchy are similar between Si and Ge [140], based on studies on which Si surfaces are wetted, we believe that wetting only occurs on {111} surfaces [214].

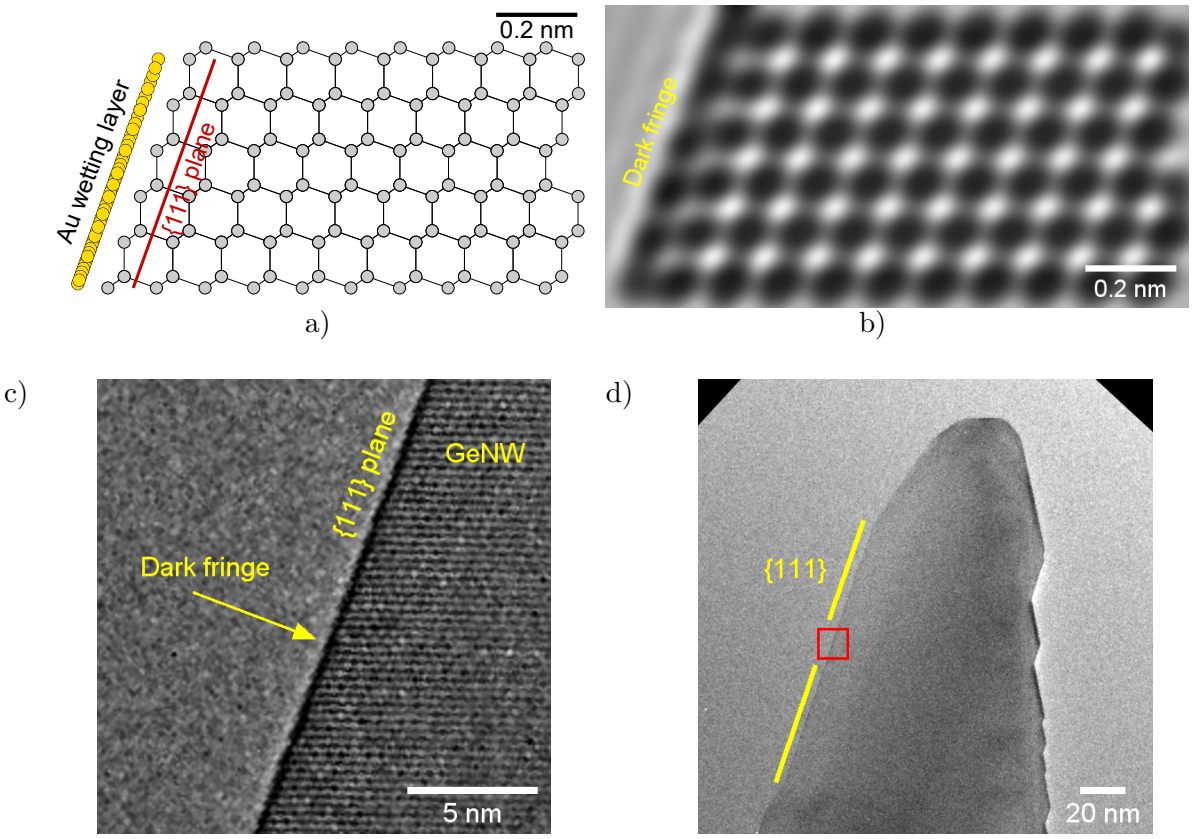

FIGURE 3.24: HRTEM image of the Au wetting layer. a) Side view of the supercell used for the TEM image simulation. Ge atoms are in gray while Au atoms are yellow. b) Result of the simulation done with a defocus value of 50 nm, notice the dark fringe on the left side. c, d) Experimental images of the nanowire discussed in Section 3.1.6 (Figure 3.12d). c) Close-up view of the red squared area in d), showing a flat {111} surface presenting a dark fringe.

Wires grown in NanoMAX under CVD conditions do not show such wetting layer. No dark fringes that are invariant on defocus were found, including on the tilted {111} surfaces. The hydrogen passivation layer seems to prevent the formation of the Au wetting layer. This is understandable as wetting is less probable (the exact probability should depend on the surface hydrogenation) when in presence of a low energy surface and we know that adsorbed hydrogen atoms usually lower surface energies [140]. In Plasfil, due to the destabilization of the catalyst following the plasma shut down, we expect to see those particles after the growth close to the top. Figure 3.25c shows that it is indeed the case. Observation far from the top of nanowires shows the absence of Au particles on any walls.

The existence of an Au wetting layer in MBE growth has several consequences. First, the GeNW growth is in principle limited in time because of the leaking of the catalyst. Next, the catalyst particle may not act as a sink anymore for Ge atoms impinging on the walls: instead of diffusing towards the liquid droplet, these atoms may attach themselves directly to the Ge crystal on Au-covered {111} surfaces. For a given flux of Ge atoms, the growth rate of the nanowire may slow down with that decrease of the arrival rate at the catalyst droplet. The lateral growth rate in the presence of the wetting layer is expected to increase accordingly. In the droplet, germanium supersaturation should be reached more easily due to the smaller amount of liquid Au. Surface restructuration which reduces the number of edges, observed in Figure 3.10, may

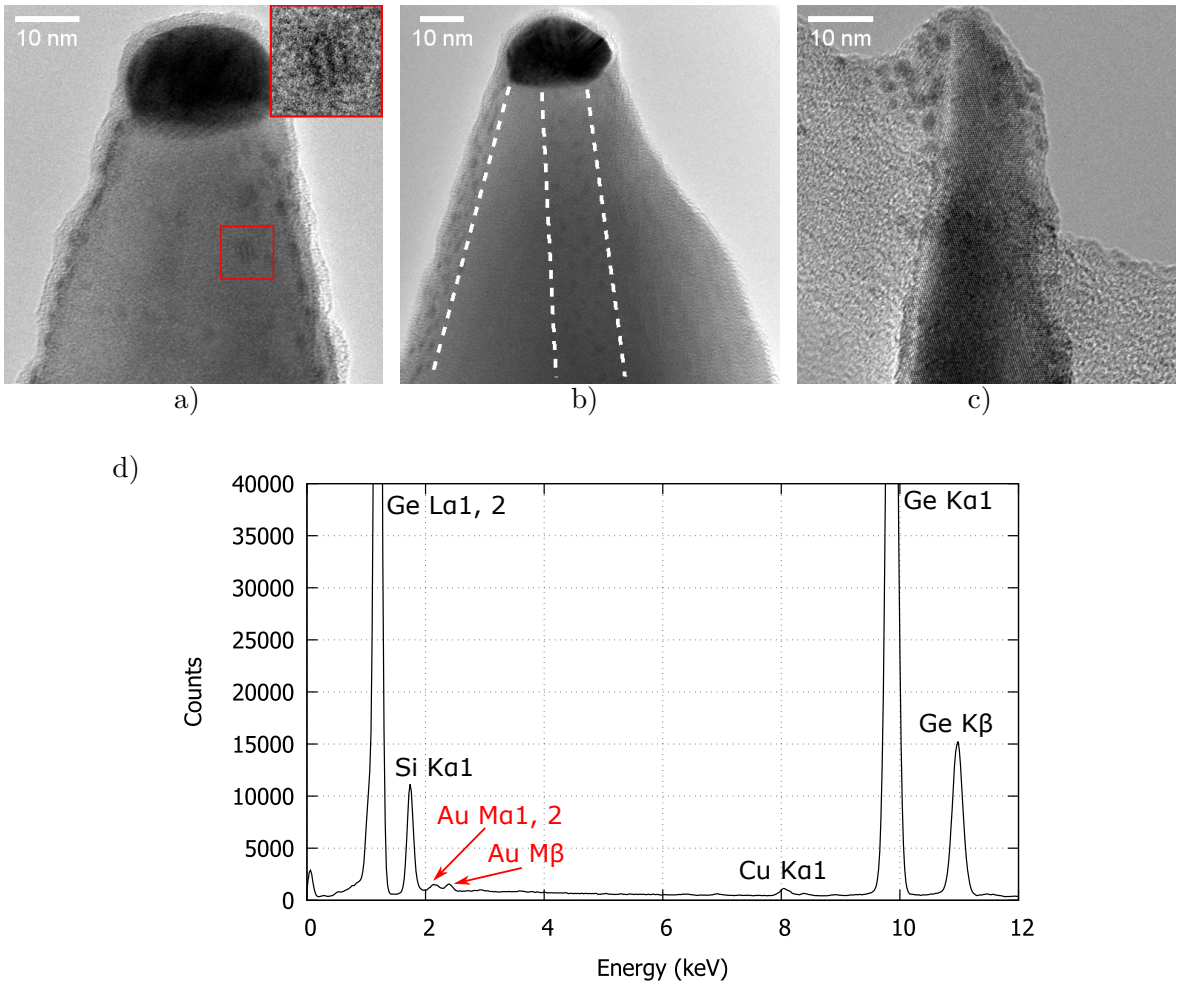

FIGURE 3.25: Images of GeNWs in the presence of the wetting layer. a) Post-growth TEM micrograph of a GeNW grown by MBE in NanoMAX. Inset: Close up view of a dark aggregate. b) Post-growth TEM micrograph of a GeNW grown by MBE in NanoMAX showing spatial segregation of the aggregates. c) Post-growth TEM micrograph of a GeNW grown by PECVD in Plasfil transferred on a TEM Cu grid with a C membrane, showing similar aggregates. d) EDX spectrum done on a dark particle of a).

be a consequence of this wetting layer as Au may improve transport of Ge atoms. Furthermore, we observed little surface reorganization in CVD in NanoMAX where there should be no Au wetting layer during the growth. At the end of the growth after purging of Ge_2H_6, a Au wetting layer can form. While the Au wetting layer may complicate the growth process, it can sometimes be advantageous as the decoration of GeNW sidewalls is sometimes useful, e.g. for catalytic and sensing applications [215].

3.3.3 Diffusion of Ge atoms during CVD and MBE growth

The existence of a hydrogen passivation layer or the Au wetting layer on the nanowire surfaces should affect the diffusion of Ge atoms on the sidewalls. During the MBE growth, significant sidewall reorganization occurs after the nanowire retraction. Between Figure 3.9a-b, there is a clear influx of Ge atoms that extends the {111} surfaces and reduces the number of edges on

the left sidewall. We have previously shown that this influx of Ge atoms was coming from the catalyst droplet after it dissolved three Ge (111) planes. Assuming that the large influx of Ge atoms filling the lateral {111} planes comes from the catalyst droplet, an order of magnitude for the required Ge adatom diffusion coefficient can be estimated. About 20 nm separate the catalyst and the {111} gathering spot in the nanowire of Figure 3.8a and the first Ge atoms arrive 30 seconds after the retraction event. This gives an average minimum diffusion coefficient $D = L^2/t$ of $10^{-13}\,\mathrm{cm}^2 \cdot \mathrm{s}^{-1}$ through a flat {111} and a rough {113}. Experimental measurements on self-diffusion on Ge (111) surface by Scanning Tunneling Microscopy (STM) [216] give a value of $9.7 \times 10^{-17}\,\mathrm{cm}^2 \cdot \mathrm{s}^{-1}$ at room temperature. Given the activation energy of 0.83 eV, the diffusion coefficient at 400 °C should be $3 \times 10^{-9}\,\mathrm{cm}^2 \cdot \mathrm{s}^{-1}$. The precise value of self-diffusion on {113} surfaces are not known precisely but should be lower because of its roughness. Thus, the motion of Ge atoms diffusing towards the sidewalls driving the reconstruction is a possibility.

In contrast, we did not observe any kind of sidewall reorganization on CVD-grown GeNWs. This indicates that, during CVD growth, the sidewalls allow limited diffusion-driven dynamics. The lack of diffusion from the catalyst is further confirmed by the stability of the catalyst droplet and the observation by Dubrovskii *et al.* that the diffusion length of adatoms in MBE is superior to the one in CVD [217]. Adatoms in MBE typically have diffusion length in the order of a few μm. Surface hydrogenation is likely responsible for the reduced diffusion length of Ge in CVD, as we already established that its presence during the growth prevents the existence of the wetting layer. It can also explain why the catalyst particle is liquid below the AuGe eutectic temperature. Because Ge diffusion is blocked, high Ge supersaturation is preserved in the catalyst and the nucleation barrier for solid Au will remain high.

Conclusion of the chapter

In conclusion, we have studied the growth of GeNWs by the VLS technique, both in the NanoMAX *in situ* TEM and in the PECVD Plasfil reactor. During the in-situ experiments in NanoMAX, we have used both MBE and CVD sources for supplying Ge precursors to Au catalyst droplets. GeNWs of different morphologies were obtained. While the majority of wires grew in the ⟨111⟩ direction, a certain number of differences were noted depending on the type of source and equipment used, substrate temperature and the presence of hydrogen in the vapor phase.

Table 3.1: Summary of the growth conditions of Au-catalyzed GeNWs in three different environments and the resulting nanowire characteristics.

Process type	MBE	CVD	PECVD
Equipment	NanoMAX	NanoMAX	Plasfil
Ge source	Atomic Ge	Ge_2H_6/H_2	GeH_4/H_2
Ge flux/pressure	$0.2\,\mathrm{Ge(111)} \cdot \mathrm{s}^{-1}$	2×10^{-3} mbar	9×10^{-3} mbar
Temperature (°C)	300-400	230-300	240-330
Growth rate ($\mathrm{nm} \cdot \mathrm{s}^{-1}$)	7.4×10^{-3}	5.4×10^{-1}	1.6×10^{-1}
Hydrogen	No	Yes	Yes
Wetting layer	Yes	No	Only when plasma off
Tapering	High	Low	High
Sidewall faceting	{111}/{113}	{111}	{111}
Growth direction	⟨111⟩	⟨111⟩/⟨110⟩ H_2 high	⟨111⟩/⟨110⟩ H_2 high

The in-situ MBE growth gave faceted, tapered and extremely slow growing wires. The growth was observed in real time. We found that the growth operates in a layer by layer fashion. The catalyst-nanowire interface is not planar as a truncated facet is present at the triple phase boundary. These observations are consistent with the literature. Significant sidewall restructuration was observed with {111} surfaces being prolongated and the number of edges reduced. This was accompanied with a nanowire regression where some Ge atomic planes are dissolved back by the AuGe catalyst. Along with this, some catalyst droplets could unpin from a nanowire tip. Such catalyst can then slide along the flat {111} sidewalls, sticking to propagating atomic steps.

In contrast, nanowires grown by CVD and PECVD with a gaseous mixture of Ge_2H_6/GeH_4 and H_2 grew much more steadily, with a stable catalyst droplet and small facets of a few-atom length that appear smooth when viewed at low magnification. The nanowire-catalyst interface is similar to that during MBE growth, as a truncated facet is also present in CVD conditions. Tapering can still occur, especially when GeNWs are obtained in a plasma environment.

Many of the structural differences can be attributed to the chemical composition of the vapor phase. While the cracking of germanium hydride molecules is critical to the growth of GeNWs by CVD, it also creates a large amount of atomic hydrogen, which highly influences surface energies by creating a passivation layer. This layer stabilizes the catalyst droplet by preventing it from wetting the sidewalls and suppressing the formation of an eventual Au wetting layer on the sidewall. In MBE growth, only pure Ge is supplied to the growing nanowires. A Au wetting layer can then form, which can facilitate Ge atom transport and provoke surface restructuration. The dynamics described above clearly demonstrate how critical an understanding of surface dynamics can be for predicting the morphology and growth of a GeNW.

CHAPTER 4

In situ growth of Au-catalyzed silicon nanowires

In this chapter, we grow Au-catalyzed SiNWs by conventional CVD. Only one gaseous precursor in the form of silane SiH_4 is available in the microscope. Since this growth has been extensively studied during the past two decades, it can serve as a benchmark to validate further studies. By obtaining similar results, we can verify the experimental equivalence of the growth in NanoMAX microscope with that achieved in deposition systems used by other authors. The substrate used for this growth is the resistively heated SiC membrane with a thin Au layer of 1 nm deposited by thermal evaporation. The resulting Au particle distribution was shown in Figure 3.1. The substrate is heated in a temperature range between 420 °C and 450 °C. For comparison, the Au-Si eutectic temperature is very close to the Au-Ge one of 363 °C. The higher growth temperature compared to germanium is required by the higher dissociation energy of SiH_4 compared to Ge_2H_6. After reaching the growth temperature, SiH_4 and H_2 are introduced in the chamber at a flow of 1.5 sccm each to reach a total pressure of 7×10^{-3} mbar.

4.1 Morphology of wires

A summary of the structures obtained with such SiNWs is proposed here. All wires presented the cubic diamond structure. Due to the coalescence of AuSi liquid particles on the SiC membrane, the SiNWs' diameter distribution ranges from 20 nm to 200 nm. For such values of diameters, wires are expected to mainly grow along the $\langle 111 \rangle$ growth direction [31]. This is indeed what we observe in our growth experiments. In this configuration, the growth interface is not exactly a single atomic plane but is composed of a large $\{111\}$ surface, perpendicular to the growth axis, and very small truncated facets in the vicinity of the triple phase boundary line. These truncated facets play a similar role as in GeNWs: that of a Si reservoir. These facets also fluctuate [218] during the growth. As new layers are formed, the volume of these truncated facets will fluctuate periodically. We also found wires growing along the $\langle 112 \rangle$ direction albeit in smaller proportions. Such wires can be separated into two classes depending on the growth interface structure. The first type has a $\{111\}$ growth interface that is tilted with respect to the growth direction. Truncated facets appear again at the edges of the nanowire. The second type has a complex growth interface made of the juxtaposition of several planes. This is shown in the inset of Figure 4.1c, where the interface is clearly not planar. Often, $\{111\}$ twin planes that

cross the entire wire are present inside.

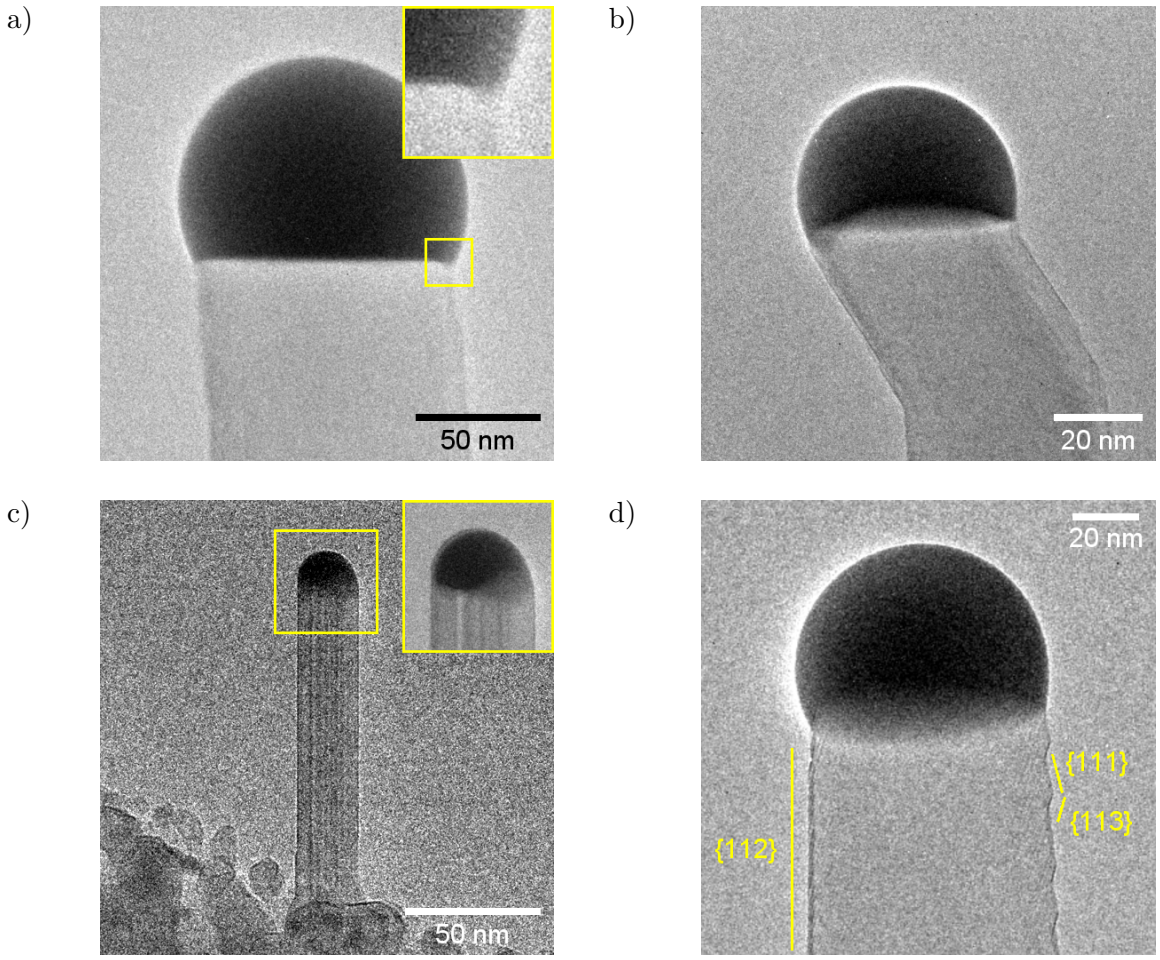

FIGURE 4.1: TEM micrographs of SiNWs grown in NanoMAX. a) ⟨111⟩-grown SiNW. Inset: Close-up view of a truncated facet. b) ⟨112⟩-grown SiNW with a tilted interface with respect to the growth axis. c) ⟨112⟩-grown SiNW with a complex growth interface. Inset: Close-up view of the interface. d) Sawtooth faceting in a ⟨111⟩ SiNW.

Figure 4.1 summarizes the different morphologies observed. No ⟨110⟩ wires were found over the course of our experiments. Given the size distribution of our SiNWs, this is an expected result as Au-catalyzed ⟨110⟩ wires are mostly predominant when the diameter is below 20 nm [31].

The faceting of the sidewalls differs between those three categories of wires. ⟨111⟩-grown SiNWs have a quite complex one. It shows a distinct sawtooth faceting with an alternation of {111} and {113} surfaces (Figure 4.1d), as reported in a previous *in situ* TEM work [219]. On low magnification images, the combination of {111} and {113} facets gives the appearance of a smooth {112} surface. The respective length of each type of surface can be controlled by the volume of the liquid catalyst. If the catalyst is shrinking, the nanowire will taper by creating longer {111} and shorter {113} surfaces. The ratio between the two lengths will depend on the leakage intensity [201]. If the catalyst is leaking Au at a fast rate, {111} surfaces will be longer and {113} shorter compared to a growth regime where the catalyst is stable. Contrary to GeNWs, the faceting is not symmetric as the opposite sidewall shows an almost flat {112} surface which could be a succession of very short {111} and {110} surfaces. For tilted ⟨112⟩

wires, the faceting features flat {111} surfaces mainly. If tapering happens, introducing small {113} facets helps accommodating changes in the catalyst diameter. As for straight ⟨112⟩ wires, having flat walls perpendicular to the interface, suggests that these are {111} surfaces.

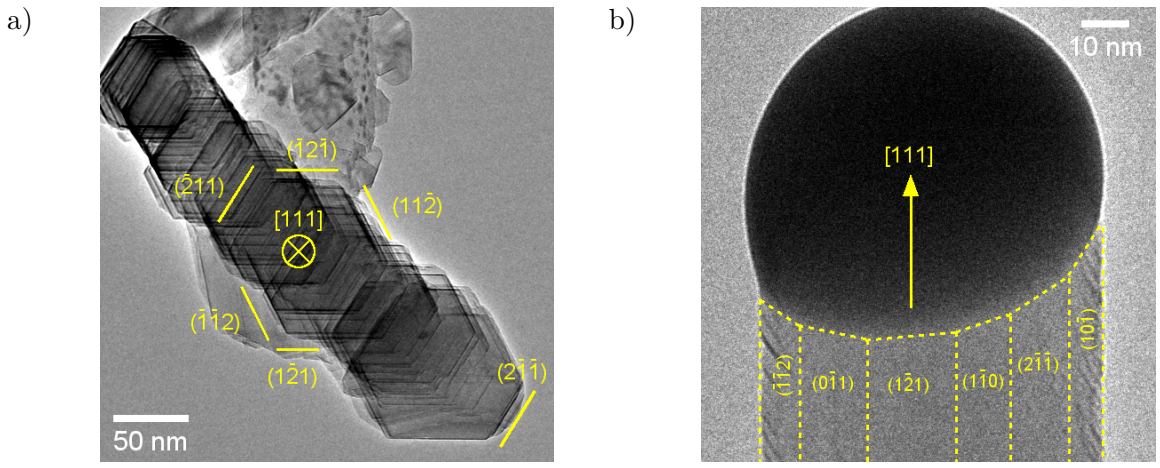

FIGURE 4.2: TEM micrograph of SiNWs cross-sections. a) Hexagonal section. b) Dodecagonal section.

The cross-section of a SiNW is observable through a bird's eye view perspective. Tilting of the sample reveals either a hexagonal or dodecagonal section for straight ⟨111⟩ and tilted ⟨112⟩ wires. During the experiments, one wire has tilted so that its growth direction became almost parallel to the electron beam. This allowed for the direct observation of its hexagonal cross-section in TEM. The shape is irregular with two sets of planes with different lengths as shown in Figure 4.2a. Given the three-fold geometry and the faceting observed, the edges are likely all {112} surfaces [220, 214]. We did not observe a dodecagonal SiNW in such a view angle. However, by delimiting the boundary between the catalyst and the nanowire in bird's eye view, one can deduce the dodecagonal section, see Figure 4.2b. Indeed, six different surfaces are visible from the front. Notably, the left {112} sidewall clearly shows a saw-tooth faceting composed of upward-pointing {111} and downward-pointing {113}. The new facets appearing between two {112} planes are {110} surfaces. Transitions between a hexagonal section and a dodecagonal one is possible in a nanowire. Oehler *et al.* [139] suggested that this transition is due to the radial growth of {110} surfaces. They observed that the wire base had a hexagonal section while the top part was dodecagonal. Because the wire base were exposed longer to the SiH_4, {110} radial growth went on for a longer time at the base. In the work of those authors, the {110} surfaces eventually merged with {112}, resulting in the hexagonal section. By adding HCl into the reactor, the authors could prevent radial growth and preserve the original dodecagonal section.

4.2 Au spreading on nanowire sidewalls

During SiNW growth, it is possible for the Au catalyst to leak out, which causes it to decrease its volume over time. Figure 4.3 taken at a temperature of 450 °C, shows a growing ⟨112⟩ SiNW with the liquid catalyst forming a smaller droplet attached to the wall. At 33 seconds, the droplet has possibly attached itself onto a defect on the left sidewall, therefore anchoring the droplet to it. As the wire continues growing for 30 more seconds, the catalyst starts to deform and building strain. At some point, the strain becomes so high and the deformation becomes so

great that the liquid catalyst splits into two parts. The main part remains on top of the SiNW and continues to catalyze growth as usual. The much smaller second part shown by the yellow arrow is stuck to the initial defect on the sidewall. It has a diameter of around 5 nm. After some time however, it is able to start sliding along the wall in a back and forth motion, similar to what we observed in Ge (Figure 3.12).

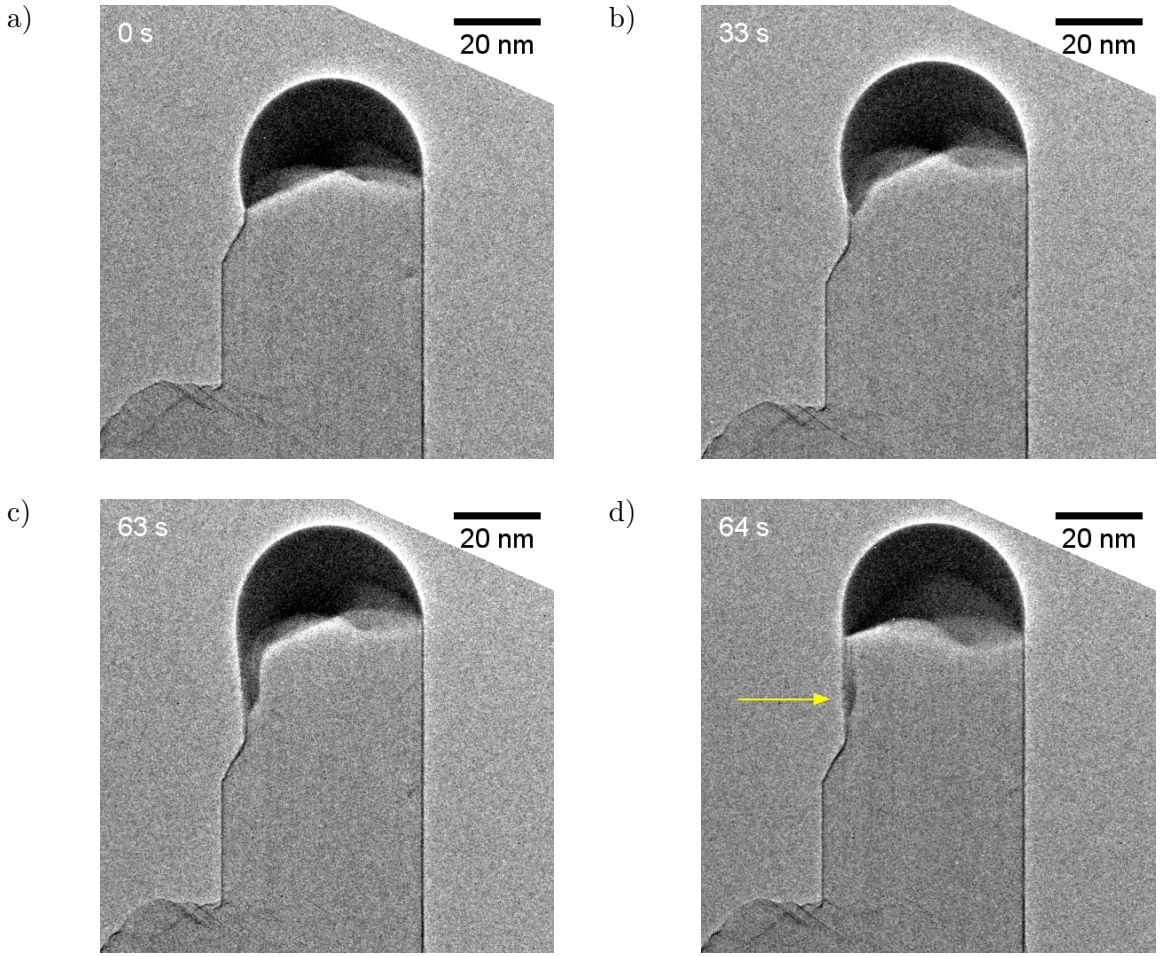

FIGURE 4.3: TEM micrographs of a growing ⟨211⟩ SiNW with a complex growth interface, extracted from a movie recording, showing the evolution of the catalyst at the time indicated after the movie start. A small AuSi liquid droplet is created on the left sidewall indicated by a yellow arrow in d).

This is one of the mechanisms which allow for the spreading of liquid AuSi on a nanowire sidewall. Another one often cited in the literature is the presence of an AuSi wetting layer along the walls. Reports of solid Au-decorated walls are numerous in the literature [212, 213, 211, 210]. Such precipitates originate from the dewetting of a liquid layer sticking to the nanowire sidewalls upon cooling. Whether this layer forms or not will depend on the growth conditions. It was found that diameter of the nanowire, temperature and partial pressure in silicon precursors have an impact on the stability of this wetting layer [212, 211, 210]. Hence, it should modify the observed density of Au particles on the walls after the growth. The pressure parameter seems to be critical as den Hertog *et al.* suggested that silane molecules adsorbed by the walls can block AuSi diffusion. This is not unlike what has been suggested for GeNWs in Section 3.3.2. Temperature influences the desorption rate and will change the minimum pressure required to achieve the Si coverage of the walls that will effectively block diffusion. Madras *et al.* found a

SiH_4 partial pressure threshold of 0.13 mbar at 500 °C, above which the Au coverage decreases significantly [212]. Our growth experiments were done at a SiH_4 pressure of 7×10^{-3} mbar so it is expected that the sidewalls are filled with Au solid particles upon cooling. This is indeed what we observe as shown in Figure 4.4a, as dark spots are present along the section shown. The average particle size is 3 nm. It would mean that sufficient adsorption of either SiH_4 or other molecules produced by SiH_4 dissociation lowers the sidewall surface energy, preventing its wetting by liquid Au and hence the formation of the observed Au particles.

Interestingly, AuSi particles on Figure 4.4a are randomly dispersed on the sidewall. Indeed, the surface density of AuSi particles seems to be homogeneous along the width of the nanowire. This is surprising when compared to the faceting of the ⟨111⟩ SiNW described above. {110}, {111}, {112} and {113} all have different surface energies. One would then expect a given surface to host the wetting layer, like in our GeNW growth. On the contrary, every sidewall facet is concerned. This result was obtained before by Dailey *et al.* [211] who explained that this only occurs near the tip of the nanowire due to the solidification of a liquid layer that follows the catalyst as the growth progresses. Further away from the tip, spatial segregation occurs where only some facets present AuSi particles. Several studies pointed out that the preferred facets are {112} with the saw-tooth faceting [220, 214]. In particular, upward tilted {111} are most likely to host those particles.

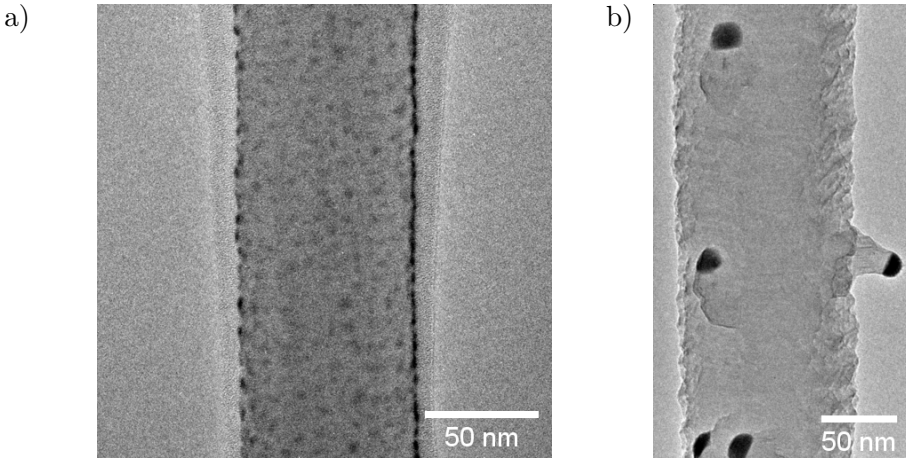

FIGURE 4.4: Spreading of AuSi liquid on the sidewalls of SiNW. a) Solidified Au particles after cooling down to room temperature. b) Growth of branches on a SiNW with small AuSi liquid droplets on the walls.

A consequence of this wetting layer is that these AuSi particles on the wall, upon receiving SiH_4 gas at high temperature, can begin the growth of a new branch of the initial SiNW. An example is shown in Figure 4.4b. If no oxide layer has formed prior to this regrowth, it is possible for the new branch to be in an epitaxial relationship with the main part of the nanowire. If grown for long enough and with a high density of Au particles on the wall, the final result gives a tree-like structure [213, 211, 221] in which a single SiNW can have multiple smaller branches. An out-of-control leaking may also significantly shorten the lifespan of a growing SiNW. The wetting could also influence the growth direction of NWs. A general observation of ⟨112⟩ complex interface wires make it clear that their sidewalls are not wetted. It seems then that sidewall wetting by liquid Au promotes ⟨111⟩ growth while pristine walls favor the growth along the ⟨112⟩ direction [222]. Madras *et al.* suggested that the wetting layer changes the surface energies in play so that ⟨111⟩ growth becomes favorable.

4.3 Kinking mechanism in silicon nanowires

Instances where a given SiNW switches to another direction are a common occurrence in our growth conditions. This is known as kinking. We have recorded a SiNW growing in the ⟨111⟩ direction which kinked towards ⟨112⟩ direction with a tilted {111} growth front over the course of 160 seconds in Figure 4.5. The kinking angle is therefore 90°. Using this recording, the mechanism leading to the formation of a kink is made clear. At first, one can only see a single {111} plane. As the kinking starts, the right-hand side triple phase boundary line sticks to one position of the right sidewall. Because the growth continues, the main {111} (in red) front rises and this creates a new small {111} plane (in blue) that is immerged in the liquid droplet. An intermediate plane is also created (in yellow). Characterizing this new surface is not straightforward because the angle between it and the two adjacent {111} surfaces fluctuates as the kinking progresses. {110} would be the closest match. As new monolayers are added thanks to the progression of the main {111} growth front, the new {111} does not change position. Consequently, the length ratio between the two fronts shifts in favor of the blue one. To accommodate this, the catalyst droplet begins leaning towards the right side. Finally, the previously main growth front disappears, simply becoming a {111} wall, as the growth continues towards the ⟨112⟩ direction.

The fact that a sidewall needs to be partially covered by the catalyst droplet shows that the kinking probability from ⟨111⟩ to tilted ⟨112⟩ depends on the growth conditions. This also highlights the importance of surface energetics. Indeed, we have seen in the previous section that wetting can only occur if the pressure in silicon precursor is below a certain threshold that depends on the growth temperature. Higher temperature will increase this threshold pressure. Thus, low pressure should favor this type of kink. This was reported by Madras *et al.* [222] who showed that SiNWs grown on a Si (111) wafer would preferably kink in that manner for a temperature of 400 °C and a Si_2H_6 partial pressure of 2.7×10^{-4} mbar. However, upon increasing the pressure of silicon precursor, kinking starts to occur preferentially towards ⟨112⟩ but with a complex growth interface.

4.4 Effect of temperature and pressure on the growth rate

As temperature influences most of the processes that govern the nanowire growth, such as Si atoms diffusion in the liquid catalyst and the SiH_4 dissociation rate, it is expected that the growth rate of Au-catalyzed SiNWs will depend on temperature following an Arrhenius law (Equation (1.1)). To verify this, we choose a given SiNW which presents a ⟨111⟩ growth direction, a diameter of 90 nm, growing under a 5×10^{-3} mbar SiH_4 pressure. Then, for a value of temperature, a video of the said wire is recorded for a duration of nine minutes. After this time period has elapsed, the temperature is increased by a step of 30 °C and we begin a new recording of nine minutes. The growth rate is measured for four different values of temperature and is plotted in Figure 4.6.

By fitting the growth rate plot with the above described law, we find that the activation energy of the growth E_a is 0.35(4) eV. This value is inferior to the one found by Kodambaka *et al.* [223] of 0.5 eV. They also used an *in situ* TEM and grew their Au-catalyzed SiNWs on P-doped Si (111) wafer with Si_2H_6 as the gaseous precursor. The difference in the activation energy can be attributed to a different method of measuring this activation energy. In our case, a single

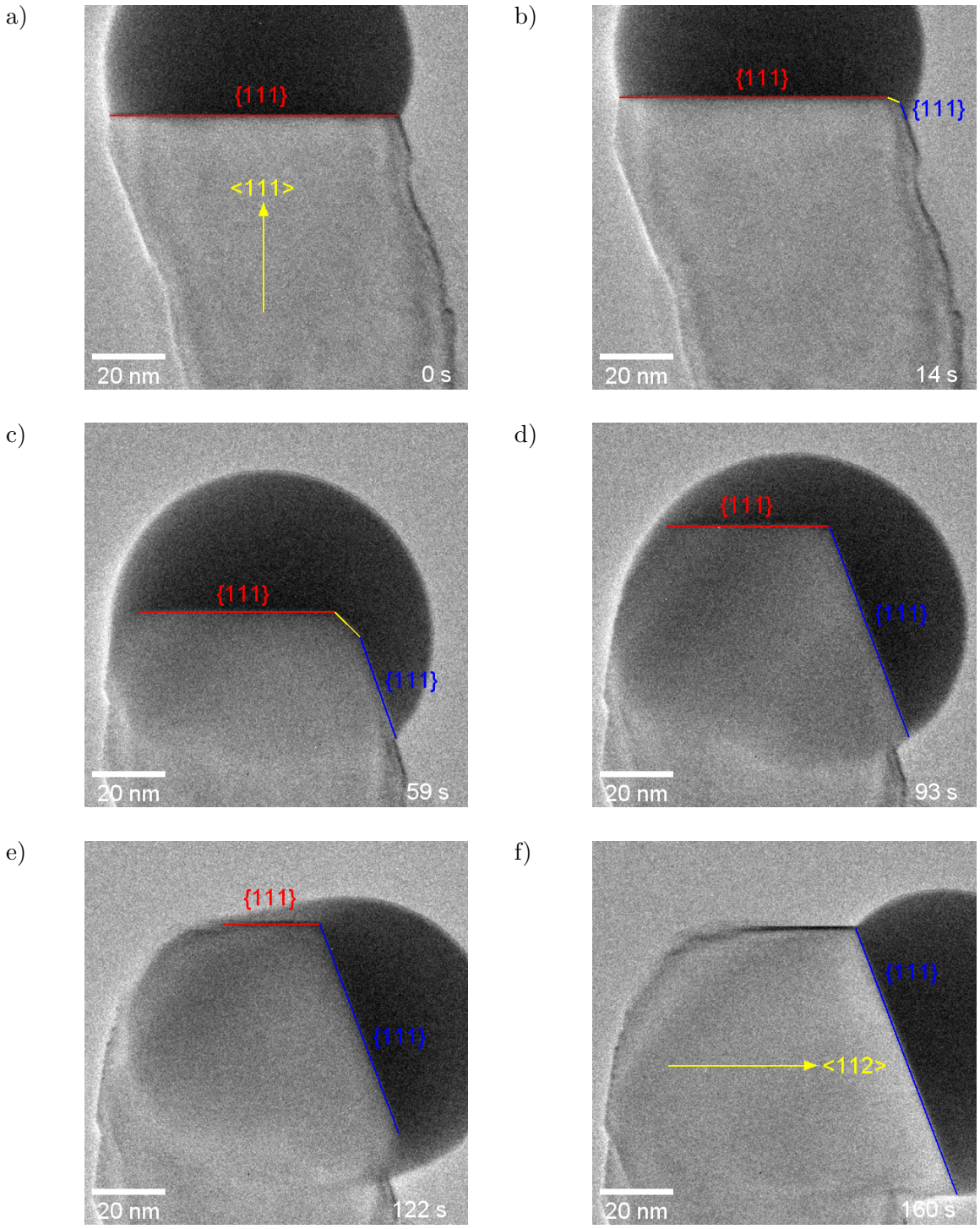

FIGURE 4.5: TEM micrographs, extracted from a recording of 160 seconds, showing the kinking mechanism of a ⟨111⟩ SiNW towards a tilted ⟨112⟩ growth direction. Colored lines show the growth front during kinking while individual colors denote a given plane.

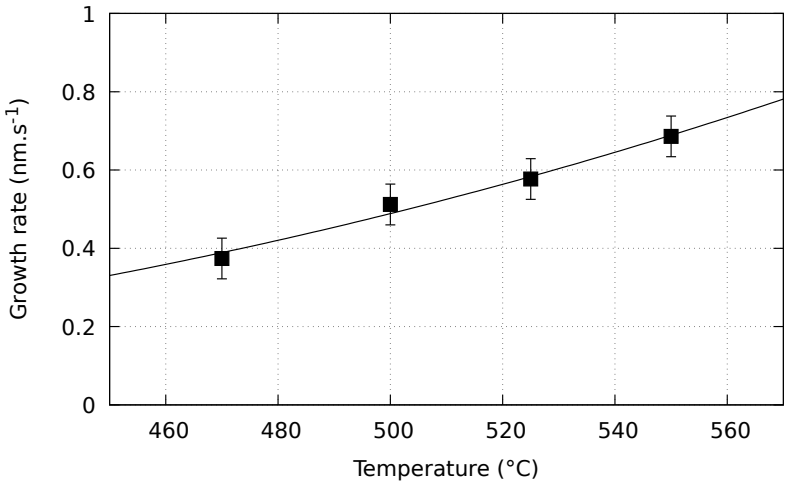

FIGURE 4.6: Temperature dependence of the growth rate of an Au-catalyzed SiNW. The line corresponds to the fit using Equation (1.1).

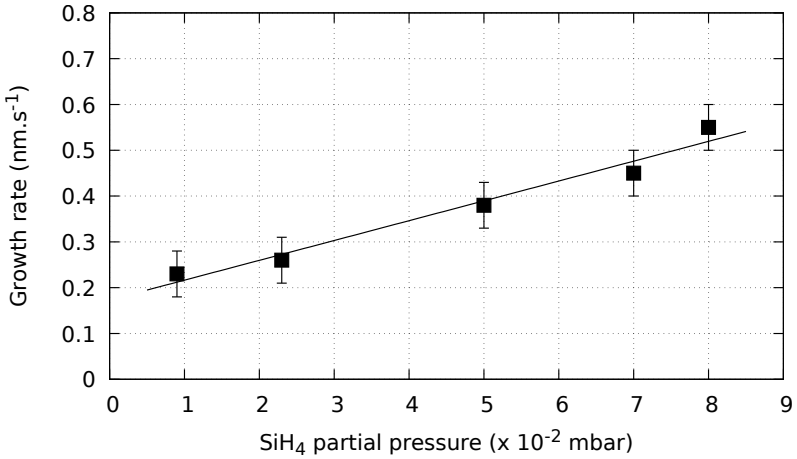

FIGURE 4.7: SiH_4 pressure dependence of the growth rate for an Au-catalyzed SiNW at 470 °C. The line is a linear fit of the data points.

wire was followed while the authors performed the measurements on a group of wires. Thus, their activation energy had averaged local fluctuations in temperature, pressure and Si arrival rate. They also worked at a considerably lower pressure, below 10^{-5} mbar. Their high SiNWs density could also have influenced the estimation. It is worth noting that the base pressure of their TEM column is around 10^{-9} mbar, which is two orders of magnitude below NanoMAX base pressure. As a result, they are less affected by eventual contaminants that could affect the dissociation rate of silicon hydrides by the Au catalysts. Another study using SiH_4 as the precursor reveals a similar activation energy of 0.5 eV [224].

Instead of varying the growth temperature, the SiH_4 pressure can be changed to study its influence on the growth rate. Using the same protocol as above, the same SiNW is followed and its growth rate measured at a fixed temperature of 470 °C. The SiH_4 pressure is varied from 9×10^{-4} mbar to 8×10^{-3} mbar. The results are shown in Figure 4.7. We find that the growth rate is linearly dependent on the SiH_4 pressure in the tested range with a slope

of $43(5)\,\mathrm{nm}\cdot\mathrm{s}^{-1}\cdot\mathrm{mbar}^{-1}$, in agreement with the study of Kodambaka. This suggests that in this pressure range, the growth rate is only limited by the arrival rate of SiH_4 molecules. For lower pressures, it is unlikely that this linear trend is retained. For a SiNW to grow, the Si supersaturation state must be reached. A too high Si desorption rate compared to the adsorption rate can prevent this, which is favored by low partial pressures. As such, we expect that there is a SiH_4 partial pressure threshold above which precipitation of a solid SiNW becomes possible.

Conclusion of the chapter

In summary, we have demonstrated the coherency of the SiNW growth experiments carried in the NanoMAX microscope. Indeed, we have compared our results with those reported in the literature and found that both share similar findings. This includes the general morphology of the wires, the propensity to kink at low partial pressure in silicon precursors which is linked to the wetting of sidewalls by the AuSi catalyst droplet. Measurements of growth rate in different temperature and pressure conditions were made. From these, we extracted an activation energy of 0.35 eV for the growth. This value is close to those obtained in past experiments by other authors, which further confirms the experimental coherency of the growth setup.

CHAPTER 5

The Cu-Sn system for growing silicon nanowires

In this chapter, we study the growth of SiNWs using CuSn catalysts, thanks to *in situ* observation in the NanoMAX microscope. We recall that the rationale for carrying growth with these types of catalysts is that Sn was the catalyst used to obtain PECVD-grown 2H SiNWs in the first place [110]. Furthermore, in that study, there was a high chance that Sn particles suffered Cu contamination from the TEM Cu grid substrate. Thus, we decided to vary the Cu over Sn ratio in order to reproduce the results described in the above-mentioned study. Also, both pure Cu and Sn catalysts were tried to assess their individual properties. For the purpose of mimicking PECVD conditions, the electron cyclotron resonance plasma source is switched on. It is then expected that radical species are present inside the TEM column. Cu and Sn are known to form compounds and this can have an effect on the catalyst structure which will then influence the growth.

We used both the SiC membrane and the (111) oriented Si cantilever as supporting substrates. The {111} surfaces of the Si cantilevers were HF-treated and smoothed using the method described in Section 2.4.4. On the SiC membrane, a layer of amorphous Si with a 5 nm thickness was deposited in the Plasfil PECVD reactor, where the layer thickness is monitored thanks to the mounted ellipsometer. The purpose of this layer is to decrease the surface energy of the SiC membrane. Indeed, pure Sn-catalyzed growth would not occur on bare SiC inside the Plasfil reactor, due to Sn high diffusivity. Because the generation of radical species is less efficient in NanoMAX, one can expect a similar outcome where no SiNWs are obtained. With this 5 nm amorphous layer on top, pure Sn growth becomes possible. Cu and Sn were then successively thermally evaporated which resulted in CuSn islands. For the sake of convenience, we separate the different tested compositions into four categories: pure Cu, majority Cu, majority Sn and pure Sn. Table 5.1 displays the tested compositions. The total deposited thickness of metals was varied from 0.5 nm to 0.7 nm. Thicker deposits will generally lead to higher SiNW diameters.

Upon insertion of the sample inside NanoMAX, we systematically carry out an EDX analysis of the deposited CuSn islands to verify if the deposition went on correctly. The substrate is then annealed to approximately 200 °C for 20 minutes to allow for the degassing of water molecules and other contaminants. H_2 is then introduced in the chamber at a flow rate of 30 sccm, yielding a total pressure of 3×10^{-2} mbar and the substrate is heated to 250 °C. Activation of

TABLE 5.1: Summary of the tested catalyst compositions in atomic and weight percent.

Thickness	Cu at. %	Sn at. %	Cu m. %	Sn m. %	Type
0.5 nm Cu	100		100		Pure Cu
0.4 nm Cu/0.2 nm Sn	82	18	71	29	Majority-Cu
0.2 nm Cu/0.2 nm Sn	69	31	55	45	Majority-Cu
0.3 nm Cu/0.4 nm Sn	65	35	48	52	Majority-Sn
0.2 nm Cu/0.5 nm Sn	48	52	33	67	Majority-Sn
0.5 nm Sn		100		100	Pure Sn

the ECR source at a constant microwave power of 50 W follows. This marks the beginning of the 10 minutes hydrogen radical-assisted annealing. This treatment purpose is to dewet the CuSn islands and obtain CuSn particles with a roughly spherical shape. It is also able to partially remove the oxide layer which covers the CuSn islands. This oxide layer is formed when the sample is transferred from the thermal evaporator to the TEM. We found that this step is critical, as this layer can inhibit catalysts. It is preferable to perform the evaporation and other treatments just before insertion inside the TEM to limit the oxide layer thickness. Note that there is no clear indication of temperature on the Si cantilever substrate. Temperature is gradually increased until the dewetting of the islands is achieved.

5.1 Pure catalyst growth

In this section, we briefly describe the main characteristics of growth with pure Cu or pure Sn catalysts.

5.1.1 Sn-catalyzed growth

Using pure Sn as catalyst presents some advantages as it has a low melting point of 232 °C, which combines well with the fact that PECVD growth allows to lower the growth temperature. Si is also vanishingly soluble in Sn and consequently supersaturation in Sn is reached very quickly compared to other metal catalysts. Sn is also in the same column as Si so that there is no concern over a possible doping of the nanowire. Another peculiar property of Sn is its very low surface tension which gives it the tendency to wet surfaces. This is especially problematic for SiNWs growth where the liquid Sn droplet fails to stay on top of the wire, terminating its continuous growth. This is made obvious by the complete lack of any reported growth by standard CVD conditions. *Ergo*, Sn-catalyzed growth is an excellent choice to quantify the efficiency of the ECR plasma source.

Following the hydrogen radical treatment, the substrate is heated up to 400 °C and exposed to a gas mixture of 1.5 sccm SiH_4 and 30 sccm of plasma exposed H_2 which results in a total pressure of 2×10^{-2} mbar. Nucleation of solid Si in Sn droplets starts immediately after gas injection. Both in-plane and out-of-plane SiNWs as well as Si crystals grow. Growth directions include mainly $\langle 111 \rangle$ and a few $\langle 112 \rangle$. Coalescence of Sn droplets as SiH_4 is introduced is limited compared to Au catalyst. As a result, the diameter distribution measured from 12 wires is narrow, ranging from 3.8 nm to 6.5 nm with an average at 5 nm. For such small SiNWs, the growth rate is a slow $3.5 \times 10^{-2}\,\mathrm{nm \cdot s^{-1}}$. It is understood that the Gibbs-Thomson effect would

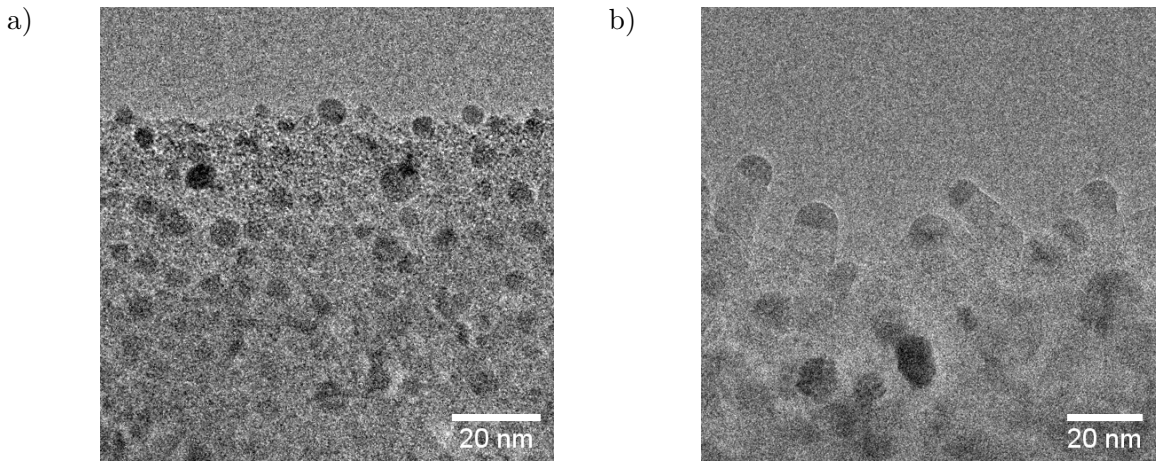

FIGURE 5.1: Sn-catalyzed growth in NanoMAX. a) Sn liquid droplet after dewetting by the radical-assisted hydrogen treatment. b) Array of Sn-catalyzed SiNWs.

slow down the growth rate of small diameter SiNWs due to the high curvature of small liquid catalyst. In these conditions, we observed no twin planes at all, in either of the ⟨111⟩ or ⟨112⟩ NWs.

A clear demonstration of the effect of the plasma can be made by deactivating the plasma during the growth. Figure 5.2 shows some images extracted from a recording of a SiNW in which we have deactivated the plasma. From 0 s to 86 s, the SiNW grows with the plasma on. At 87 s, the plasma power is switched off. Until 104 s, nothing visibly occurs. After this, the Sn droplet is abruptly destabilized from the tip of the nanowire. It starts to wet the left sidewall as it starts to display a dark contrast, before completely unpinning. At 111 s, the Sn droplet has created a small {111} facet on the left and flowed to the substrate. The catalyst unpinning described can be reproduced by not switching off the plasma, but by simply reducing the plasma power. In another experiment where the power is reduced from 50 W to 20 W, the time taken for the catalyst to unpin is 243 seconds, counting from the moment when the power is decreased. These two experiments are evidence that it is not the presence of plasma that is responsible for the stability of the catalyst. Rather, it is the adsorption of radical species by the sidewalls which creates a hydrogen passivation layer. A sufficient layer coverage allows for a stable liquid catalyst. Inversely, a too sparse coverage leads to a unpinning. The coverage value will depend on the influx of radical and the desorption rate which increases with higher temperature [207, 205]. There is a direct correlation between the influx of radical species and the plasma power which dictates the efficiency of the cracking process. When the plasma is switched off, the influx of radical species becomes zero and the coverage gradually degrades until the destabilization threshold is reached. For a plasma power of 20 W, it is apparent that the influx cannot compensate for the desorption rate at 400 °C. The destabilization threshold is reached much later since radicals are still generated. The two previous results are valid for all SiNWs grown on a sample. It shows that the generation of radicals affects the whole sample. Furthermore, the depinning is reproducible as we have tested it on three different samples. Consequently, the installed ECR plasma source gives us access to radical-assisted growth.

Although we clearly demonstrated the working principle of the plasma source, the efficiency of the radical generation process is not known. It should be noted that liquid Sn can still leak from the catalyst droplet during the growth with the plasma on. By comparing the catalyst between Figure 5.2a and b, it is estimated that the catalyst lose volume at a rate of $1.8\,\mathrm{nm}^3 \cdot \mathrm{s}^{-1}$,

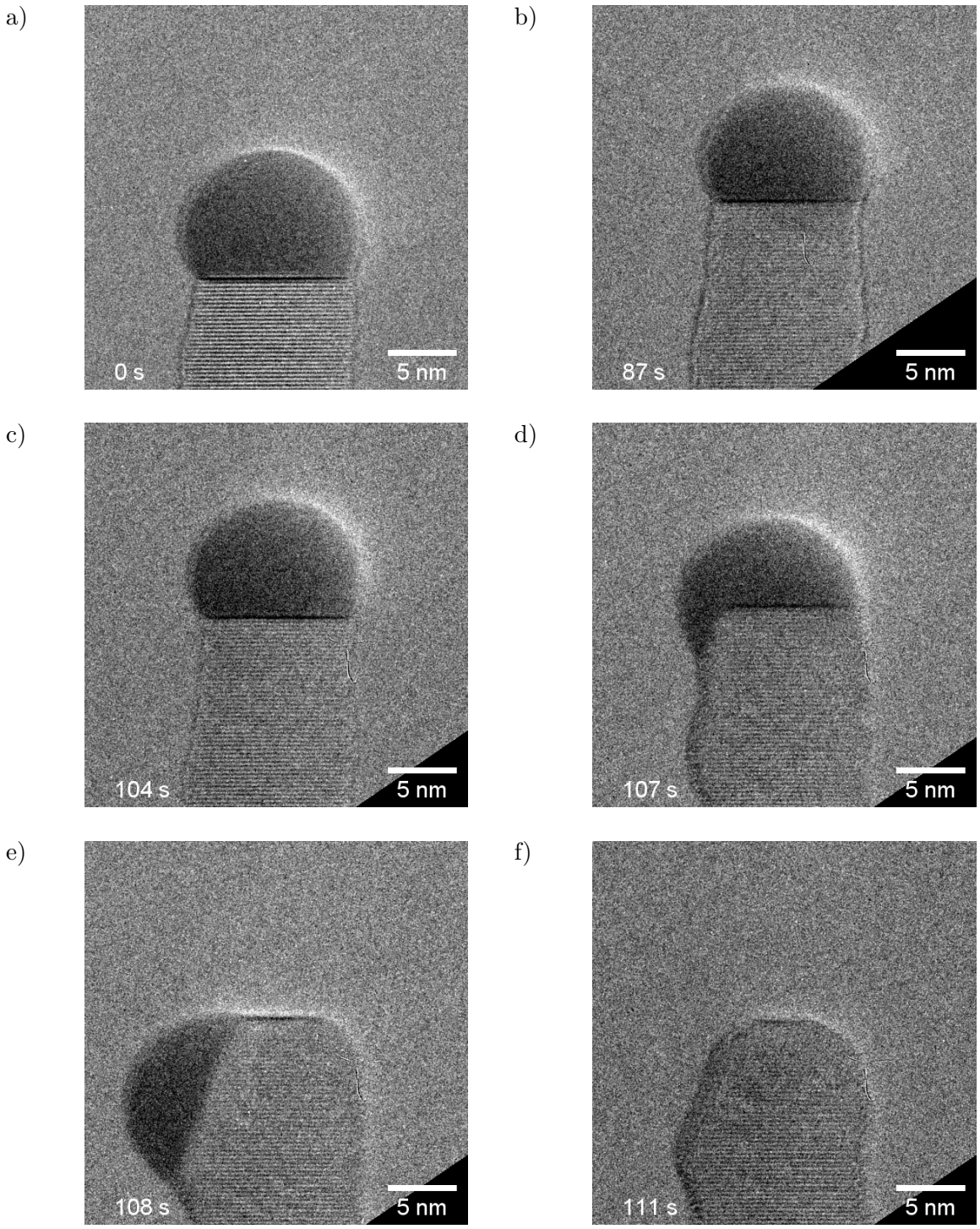

FIGURE 5.2: Effect of the plasma during the growth of a Sn-catalyzed SiNW. Frames extracted from a recording of a plasma effect demonstration. At 87 s, the plasma is switched off.

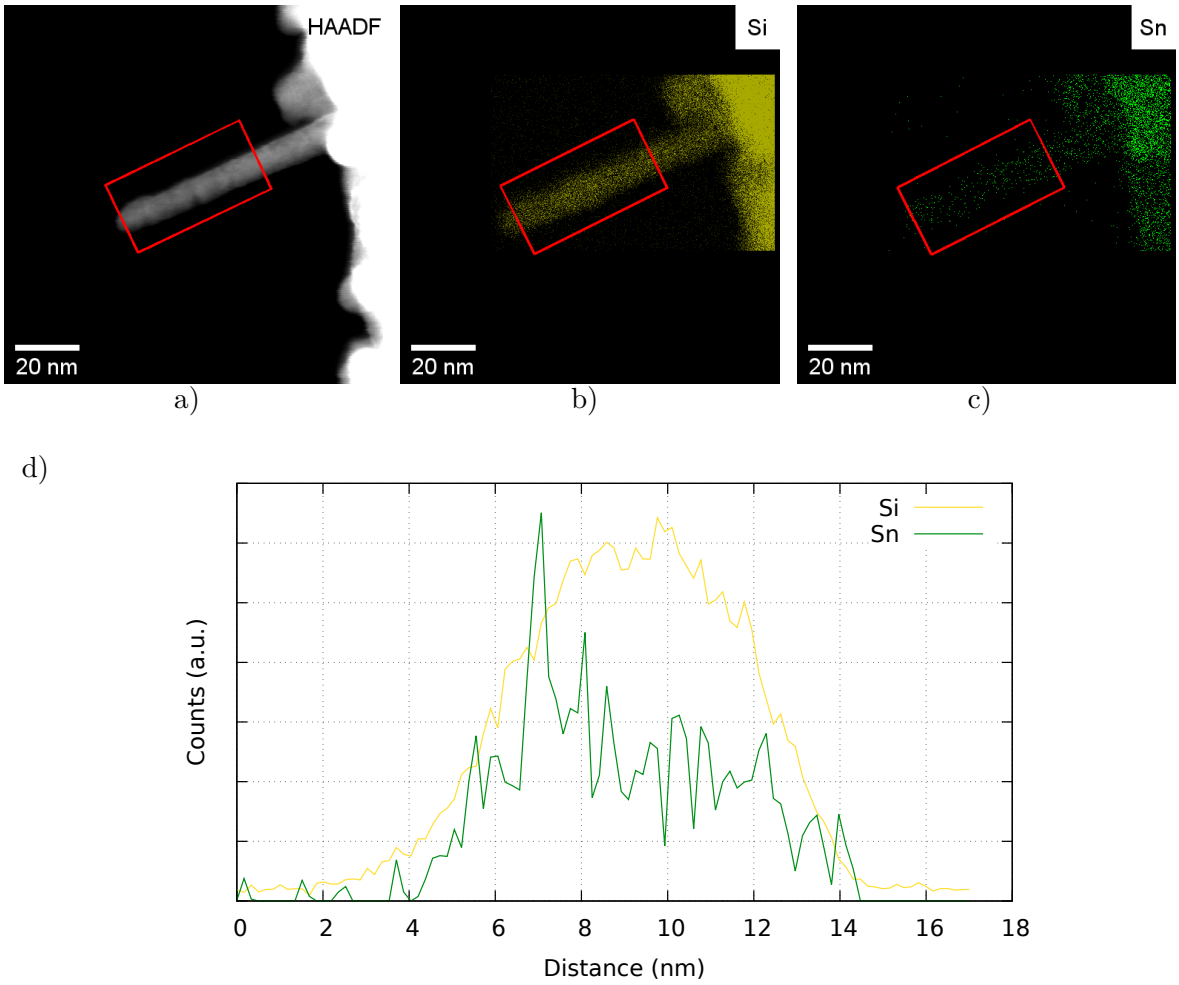

FIGURE 5.3: Evidence of a Sn wetting layer on a SiNW that has lost its catalyst. Images are taken after plasmas shutdown. a) HAADF image of the SiNW. b) Si chemical map. c) Sn chemical map. d) EDX plot profile for Si and Sn along the red rectangle in b) and c).

even with the plasma on. The density of liquid Sn [225] at 400 °C is $6.92\,\mathrm{g}\cdot\mathrm{cm}^{-3}$. This translates into a loss of 63 Sn atoms per second, assuming that the catalyst is almost exclusively Sn due to the low solubility of Si in Sn. Volumes are calculated by assuming that the Sn catalyst has a spherical shape. The volume loss could indicate that (i) we do not generate enough radicals per unit time to fully stop Sn diffusion or (ii) Sn-catalyzed growth is fundamentally unstable over long periods of time. As some wires were grown for a few hours, the first mechanism would be more significant. In Section 2.4.2, we have discussed that while the 50 W ECR plasma source should overall be more efficient than capacitively-coupled plasma source such as Plasfil in generating radicals, the distance between the source and the sample will significantly reduce the incoming flux. Furthermore, the H_2 partial pressure is reduced compared to Plasfil. Reports concerning the existence of a Sn wetting layer in PECVD-grown Sn-catalyzed SiNWs suggests that (ii) is also true [226]. If this wetting layer must subsist for the growth to occur, then it is understandable that the liquid catalyst will inevitably run out of Sn after a few hours of growth.

Figure 5.3a is a high angle annular dark field (HAADF) image of a SiNW that has lost its Sn catalyst due to leakage. Combining HAADF imagery and EDX analysis, we obtain the chemical maps for Sn atoms. Despite the absence of the Sn catalyst droplet at the top of the nanowire, a

significant quantity of Sn is present on the SiNW sidewalls. The EDX plot profile of Figure 5.3d shows that the amount of Si and Sn do not follow the same evolution along the width of the nanowire. In particular, there is a Sn peak on one edge of the nanowire. This result supports the hypothesis of the existence of a wetting layer that is responsible for the Sn leakage.

5.1.2 Cu-catalyzed growth

The Cu-catalyzed growth does not require the presence of a plasma environment to effectively work [33, 227, 228, 44]. This is due to the higher surface tension of Cu compared to Sn. Compared to other catalysts, Cu forms a eutectic with Si at 802 °C. Due to this high temperature, VLS growth is problematic in our experiments as reaching this value causes thermal vibrations which reduce the resolution of the microscope. In addition, it is expected high growth temperature promotes a fast diffusion of Cu atoms which results in the vanishing of the catalyst [44]. Also, to compare the results obtained with Sn, we want to stay at a temperature value around 400 °C. Thus, the growth mode will be VSS with a solid catalyst which contains Cu and Si. Deposition of 0.5 nm thick Cu layer is done through thermal evaporation. As-deposited catalysts have an average diameter of 3 nm. The hydrogen treatment described previously is applied to the Cu particles. Next, 400 °C heating is applied to the SiC membrane. At this temperature, no SiNWs grow. There is however growth of Si crystals around the small Cu particles which may cause them to get buried and inhibit SiNW growth.

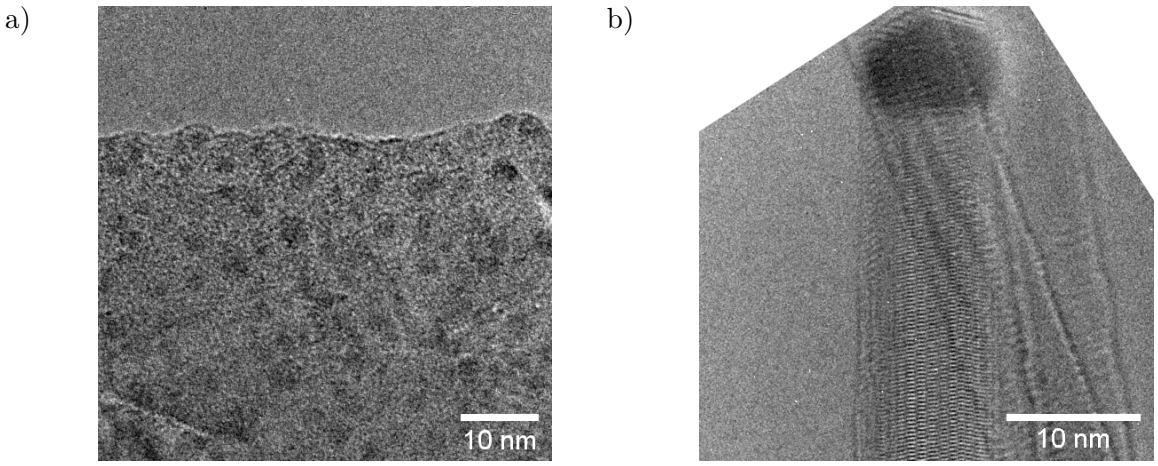

FIGURE 5.4: Cu-catalyzed SiNWs growth in NanoMAX. a) Cu solid particles after the hydrogen treatment. b) Cu-catalyzed SiNW growing along the ⟨112⟩ direction.

Growth was only observed after increasing the substrate temperature to 500 °C. The obtained distribution of Cu-catalyzed SiNWs are characterized by their very low density: only a small number of Cu catalysts manage to give birth to a nanowire. This is most likely due to most catalysts being buried. The average wire diameter is 8 nm, with the minimum diameter at 5 nm and the largest being 10 nm. One can see that the coalescence process still occurs despite the solid state of the Cu particles. Such catalysts heavily favor ⟨112⟩ SiNWs as this is the only growth direction noticed. Focusing the electron beam on a Cu catalyst promotes out-of-catalyst atomic diffusion. As such, growth rate measurements for more than a few minutes lead to the growth termination. Consequently, we measured a growth rate of $5 \times 10^{-2}\,\mathrm{nm \cdot s^{-1}}$ with a limited precision however, because of the continuous shrinking and limited life-time of the catalyst under the beam. Notwithstanding the small diameter, most SiNWs have a {111}

twin plane parallel to the growth axis. Cu catalysts on top do not have a spherical shape but rather show a very clear faceting. Thus, they must have a crystalline structure. Through electron diffraction, Wen *et al.* found a Cu_3Si compound [44] belonging to the trigonal crystalline system. The crystal shapes and lattice fringes in the present micrographs are similar to those we found with the majority Cu Cu-Sn system (see below, Section 5.3.3). We shall see in our detailed study of the latter, where the catalyst phase here is similar, that the catalyst structure here is most likely the same as that found by Wen *et al.*

5.2 Morphology of the nanowires grown by double element catalysts

So far, we have compared the growth of pure Cu-catalyzed and pure-Sn catalyzed SiNWs. The focus is now on using both Cu and Sn metallic particles in order to grow CuSn-catalyzed SiNWs. For the sake of clarity, samples where more Cu is deposited than Sn and ones where more Sn is deposited than Cu are treated separately. They are called majority-Cu and majority-Sn catalysts respectively. When Cu then Sn are deposited successively by thermal evaporation, with the thicknesses indicated in Table 5.1, metallic solid particles are obtained. Following the hydrogen treatment, they dewet and form spherical droplets with an average diameter of 5 nm. Coalescence is observed. According to the Cu-Sn phase diagram, Cu and Sn should mix to form alloys. To verify if this is the case in our small particles, we performed local EDX analysis on single dewetted particles (Figure 5.5a). The EDX spectrum in Figure 5.5b, obtained on the single particle circled in Figure 5.5a, clearly shows signals of both Cu and Sn. Thus, the sequential evaporation, followed by annealing at 250 °C in hydrogen radicals allows for the mixing of Cu and Sn in a single particle.

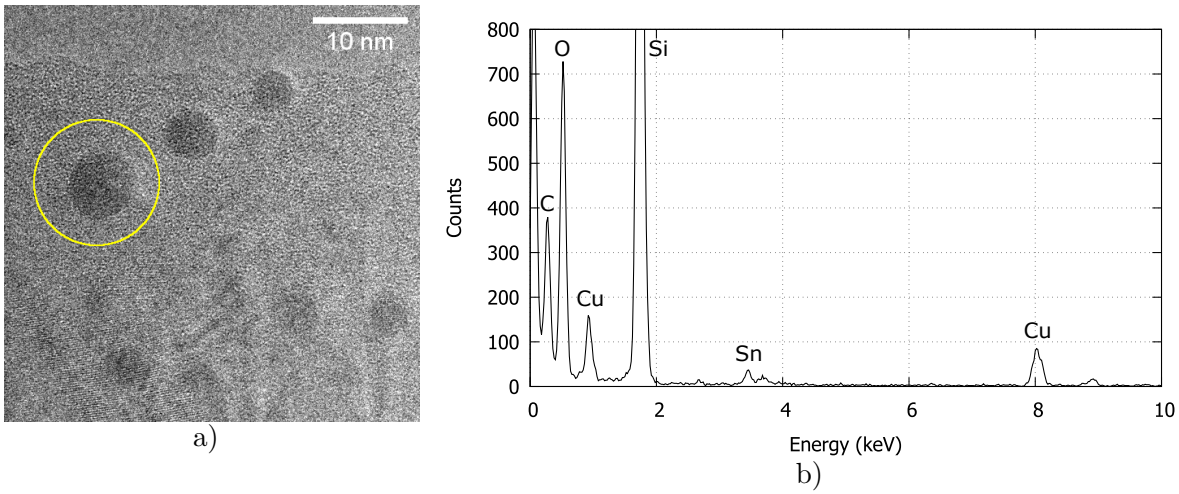

FIGURE 5.5: Chemical analysis of the as-deposited CuSn particles. a) TEM image of CuSn particles. b) EDX spectrum of the highlighted CuSn particle in a). The Si, C and O peaks essentially come from the oxidized, a-Si covered, SiC substrate.

There is an important observation on the CuSn dewetted particle shape. As described above, they have a spherical shape, independently of the tested composition. Purely solid metallic particles should present well defined facets. According to the Cu-Sn binary phase diagram, it is possible that a liquid and a solid phase coexist at 250 °C. If the diagram is correct for particles of such size, it is expected that particles like the ones shown in Figure 5.5a have both a liquid and a solid phase. From this, we can expect that CuSn particles have a core-shell structure: a

solid core that is partially or completely immerged in a liquid melt.

5.2.1 Temperature dependence of nanowire diameter

As described in Section 2.4.4, the Si cantilever substrate is made of two loops. On each loop, there are two regions where the loops section is smaller. These smaller sections determine how much the cantilever is heated when an electrical current is applied. Some areas of the cantilever will then be hotter than others, creating a temperature gradient. We are then able to observe on the same sample low and high temperature growth.

For majority-Cu catalysts on a (111) oriented Si cantilever and a constant current intensity, we find that the obtained SiNWs have different morphologies depending on where they grow on the cantilever (see Figure 5.6). In this figure, the images are taken at the end of the experiments with all gases off and at room temperature. All regions had an equal growth time of 2 hours and the same growth conditions except for the temperature variation caused by the cantilever geometry.

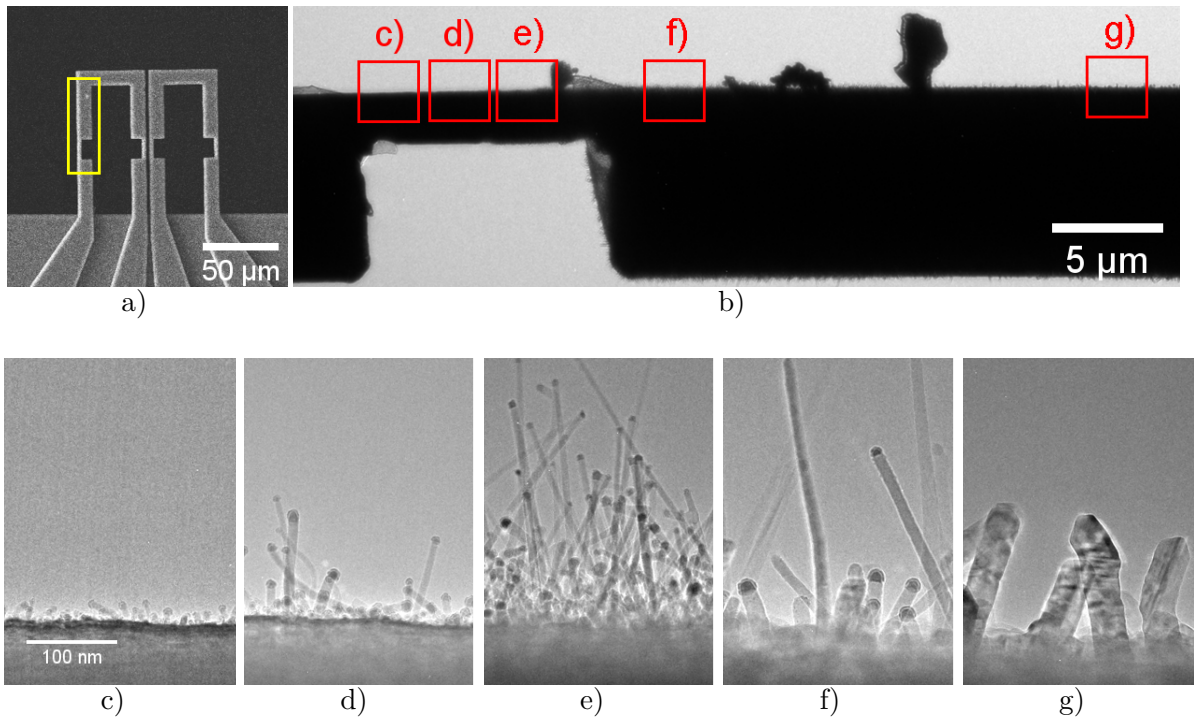

FIGURE 5.6: Temperature dependence of the morphology of majority Cu-catalyzed SiNWs. a) SEM view of the cantilever. b) TEM image of the yellow rectangle area in a). The red squares shows where image c) to g) are taken. Temperature increases from left (∼250 °C) to right (∼800 °C) but the precise value is unknown.

On the coldest part of the cantilever, no SiNWs were observed (Figure 5.6c). Either dissociation of the SiH_4 molecules or diffusion of Si inside the CuSn islands is not achieved. As we go towards warmer part, we start to see SiNWs, although very short ones and with a relatively small density (Figure 5.6d). At these temperatures, the growth is so slow that some CuSn catalysts have yet to nucleate Si. It is also possible that some of the CuSn particles were buried by a Si layer, leading to the termination of the growth process. The longest SiNW were about 100

nm long while the average length is closer to 40 nm. The average diameter was 9 nm (measured on 62 nanowires). Moving to the places with higher local substrate temperatures gave roughly the same average nanowire diameter but has shown an increased density and nanowire length above 100 nm (Figure 5.6e). The increase in growth rate is expected, as Si diffusion becomes more efficient. When the temperature is further increased, we can see a sudden change in the dynamics. The nanowire density is reduced, but the average diameter increases, being closer to 20 nm (Figure 5.6f). Larger diameter nanowires emerge because the initial CuSn particles were also larger. Coupled with a lower nanowire density, this means that some CuSn droplets have coalesced together, forming larger droplets (Figure 5.20). Even hotter temperatures exacerbate this coalescence, resulting in increase in nanowire average diameter to 30 nm (Figure 5.6g). Their catalysts have vanished at some point during the experiment, terminating the growth. We did not observe the vanishing but we assume that it probably happened when we tried to increase the current intensity to further increase the temperature. Indeed, on the hottest part of the cantilever, no SiNWs were observed. A temperature that is too high promotes the diffusion of Cu in Si which will terminate the solid Cu catalysts [44].

For majority Sn catalyst, the temperature evolution is very similar to that observed with majority Cu catalyst, see Figure 5.7. Low temperature yields low density arrays of short and thin nanowires (Figure 5.7a). With increasing temperature, wires become longer (Figure 5.7b). Furthermore, we can observe the formation of a large catalyst that is probably due to particle coalescence (Figure 5.7c). These big catalysts finally provide large diameter nanowires upon a further increase in temperature. The result is a wide distribution of nanowire diameters in regions of the cantilever with similar temperature. "Small diameters" range from 3 nm to 8 nm with an average at 6.3 nm measured on 36 wires. Nanowires with diameter larger than 15 nm coexist with this small diameter distribution. This shows that, for a given deposited thickness, Sn particles are more likely to coalesce than Cu ones. Liquid Sn should be more mobile than solid Cu. Notice that, as with majority Cu catalyst and for the same reason, an increase in temperature translates into an increased growth rates on thin wires.

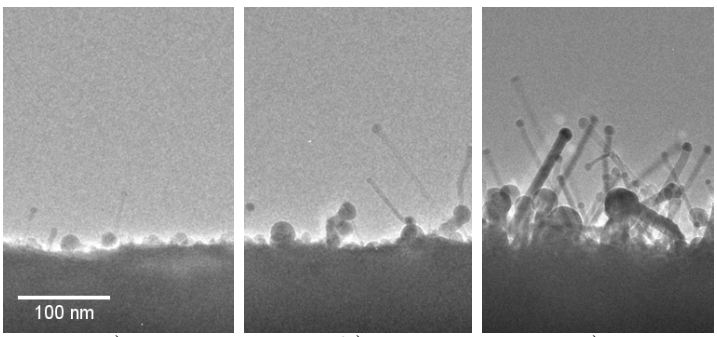

FIGURE 5.7: Temperature dependence of the morphology of majority Sn-catalyzed SiNWs. Temperature increases from left to right starting at around 250 °C. Precise value is unknown.

5.2.2 Small diameter nanowires

In the following, we will focus on nanowires grown at lower temperature with small diameter ($<$ 15 nm) on either the SiC membrane (380 °C) or on the Si cantilever at lower temperature. For majority Cu catalysts, SiNWs are found to grow on two different directions: $\langle 111 \rangle$ and $\langle 112 \rangle$.

- Some wires grew in the ⟨111⟩ direction and show good crystalline quality with very few defects (see Figure 5.8b). Occasionally, some twin planes perpendicular to the growth axis were observed. All the observed ⟨111⟩ wires also have some level of tapering, which indicates that the catalyst particle is losing volume. The sidewalls are very rough, with a series of longer {111} and shorter {113} surfaces. A very noticeable feature of these SiNWs is the absence of the truncated facet at the catalyst-nanowire interface, which was common in Au-catalyzed SiNWs [218] as was shown in Chapter 4.
- Wires predominantly grow in the ⟨112⟩ direction and there is usually one or more twin planes parallel to the growth axis, see Figure 5.8c. Sidewalls are usually very smooth and have vertical {111} surfaces. Other walls include {113} surfaces. Wires show very little sign of tapering. As for the catalyst particles, they do not possess the spherical shape that is expected for a liquid droplet. This is especially visible in Figure 5.8b, which presents a left part with fringes and a right part with none. This hints at a complex structure inside the catalyst.

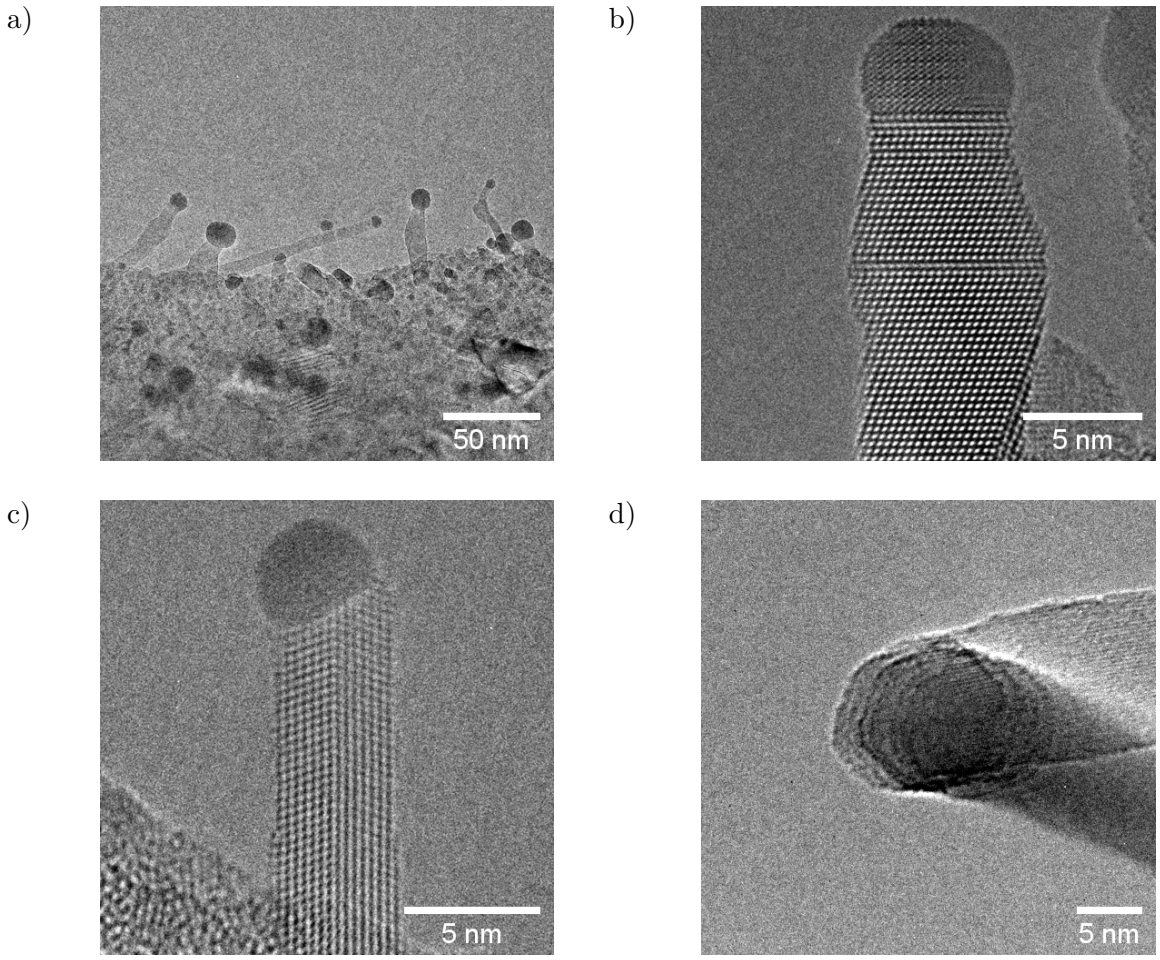

FIGURE 5.8: TEM micrographs of small diameter SiNWs grown with majority-Cu catalyst on the SiC membrane at 380 °C. a) Low magnification view. b) High resolution view of a ⟨111⟩ SiNW. c) High resolution view of a ⟨112⟩ SiNW. d) View of a SiNW that kinked, revealing its hexagonal section.

During the growth, one nanowire was found to be kinked toward a direction nearly parallel to the electron beam, revealing its hexagonal cross-section. This is shown in Figure 5.8d. The

hexagonal section has been reported before in the large diameter Au-catalyzed ⟨111⟩ SiNWs [229, 139]. We already established in Chapter 4 that these walls are most likely {112} surfaces.

In majority Sn-catalyzed growth, small diameter nanowires also exist. As before, both ⟨111⟩ and ⟨112⟩ wires are present in our samples although ⟨111⟩ wires are predominant. For the 0.2 nm/0.5 nm Cu/Sn composition, only 2 wires presented the ⟨112⟩ growth direction out of 16 where the growth direction could be clearly distinguished, totaling a 12 % probability. The others grew along ⟨111⟩. On the latter wires, see Figure 5.9a, the saw-tooth faceting alternating short {111} and {110} surfaces presented in Chapter 4 is visible. The SiNWs tapering is limited in this instance as wires longer than 100 nm can maintain their diameter. ⟨112⟩ wires have essentially similar characteristics as in majority-Cu growth. Twin parallel to the growth axis can also be found.

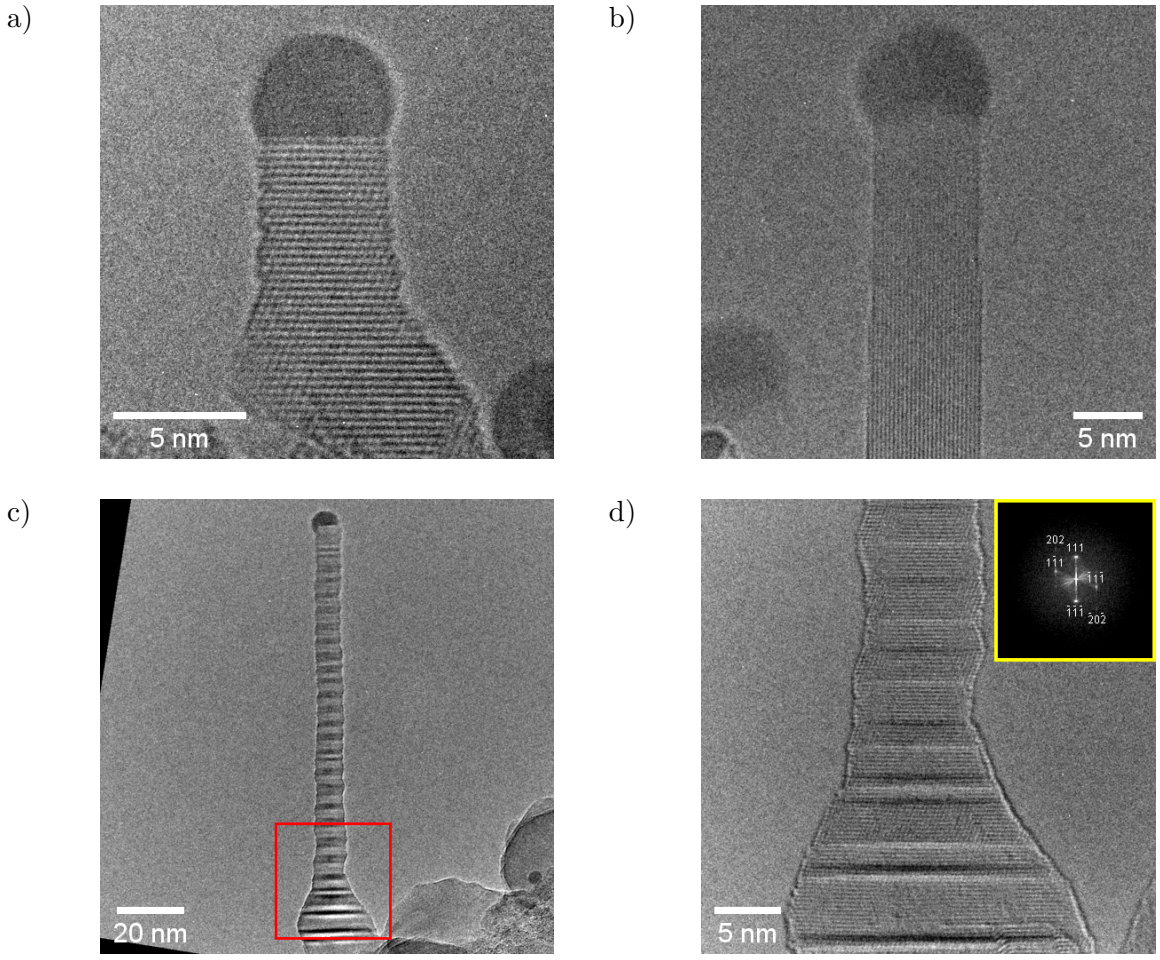

FIGURE 5.9: TEM micrographs of small diameter SiNWs grown with majority-Sn catalyst on the SiC membrane. a) High resolution view of a ⟨111⟩ SiNW. b) High magnification view of a ⟨112⟩ SiNW. c) Low magnification view of a ⟨111⟩ SiNW featuring repeated twinning. d) High resolution view of the red squared area in c). Inset: FFT of d).

A close investigation on majority-Sn catalysts shows again a deviation from a spherical shape. In particular, the catalyst in Figure 5.9a is asymmetric with a right side that displays a curvature and a left side that is reminiscent of faceting. It is apparent that the alloying of both Cu and Sn creates complex catalytic seeds with both a solid and a liquid part. This is consistent with our analysis on the dewetted particles after the hydrogen treatment. The proportion of deposited

Cu and Sn during the thermal evaporation will determine the respective size of the solid and liquid parts. If Cu is predominant, then we will have catalysts such as the one in Figure 5.8b, with a larger solid part than liquid. If Sn is the main element, a typical catalyst will look like the one in Figure 5.9a with a larger volume liquid part.

On low magnification view of some ⟨111⟩ wires, there is an alternating pattern of areas with a bright and dark contrast, see Figure 5.9c. This is common as out of the 14 ⟨111⟩ wires observed with the same majority-Sn catalyst, 10 had this characteristic, giving a ratio of 70 %. Upon closer inspection, the boundary between bright and dark areas is equivalent to a mirror plane or twin plane. They are perpendicular to the growth axis. The visible streaking in the FFT inset of Figure 5.9d is a characteristic of this type of planar defect. There does not seem to be any kind of periodicity in the spacing of the twin planes. The number of {111} monolayer between successive twin planes ranges from 3 to 10 planes with an average at 6.6. This means that for a SiNW section of length 100 nm, there will be in average 49 twin planes. Consecutive sections with equal number of monolayers before a twin plane are sometimes found. For instance, some SiNWs include small portions of 6H or 8H polytype. The occurrence of these polytypes is most likely due to chance given the twinning aperiodicity.

While twinning is a common defect in SiNWs, to observe this dense regular twinning is uncommon in SiNWs grown with either Au, Cu or Sn catalyst. The *in situ* growth in NanoMAX with pure Au, Cu and Sn did not yield such wires either. This high-density twinning can be found in other compounds like GaAs NWs for example [150]. Only In catalysts provide this twin density in SiNWs [230]. It is important to stress that there were no changes in growth temperature nor gas pressure during the experiment. Therefore, it seems that this morphology is a characteristic of majority Sn growth and that both Cu and Sn conspire together to create such wires.

5.2.3 Large diameter nanowires

Nanowires with larger diameter (above 15 nm) were found mostly on the Si cantilever on the high temperature area, regardless of catalyst composition. For majority-Cu growth, all the large diameter wires grew epitaxially from the Si (111) surfaces of the cantilever as shown in Figure 5.10a. Most of the wires were tilted with the same angle with respect to the Si cantilever surface, corresponding to the ⟨112⟩ growth direction. The remaining wires that grew perpendicularly to the substrate had the ⟨111⟩ growth direction. All of them had a diamond cubic structure. For wires in the ⟨111⟩ growth direction (Figure 5.10b), the maximum diameter observed was 60 nm, with an average at 25 nm. Twin planes perpendicular to the growth axis were a common occurrence on this part of the cantilever. Tilted twin planes also started to appear, sometimes intersecting with the perpendicular ones, creating complex linear defects such as the one shown in Figure 5.10d. Surprisingly, on ⟨111⟩ wires, no truncated facets were observed in any of the nanowires again, which suggests growth dynamics that are very different than the ones observed with Au. For wires in the ⟨112⟩ growth direction (Figure 5.10c), the diameter could be as large as 32 nm. Twin planes parallel to the growth axis are again very abundant, with some wires having multiple twins. The faceting is similar to those in small ⟨112⟩ wires, with rough {113} and very smooth {111} surfaces.

For all wires, it seems that majority-Cu catalysts have a much higher tendency to create defects, unlike Au or Sn catalyst; a trend that was also observed in another study with the Cu catalyst [231]. Furthermore, catalyst particles do not display a spherical shape in any of the

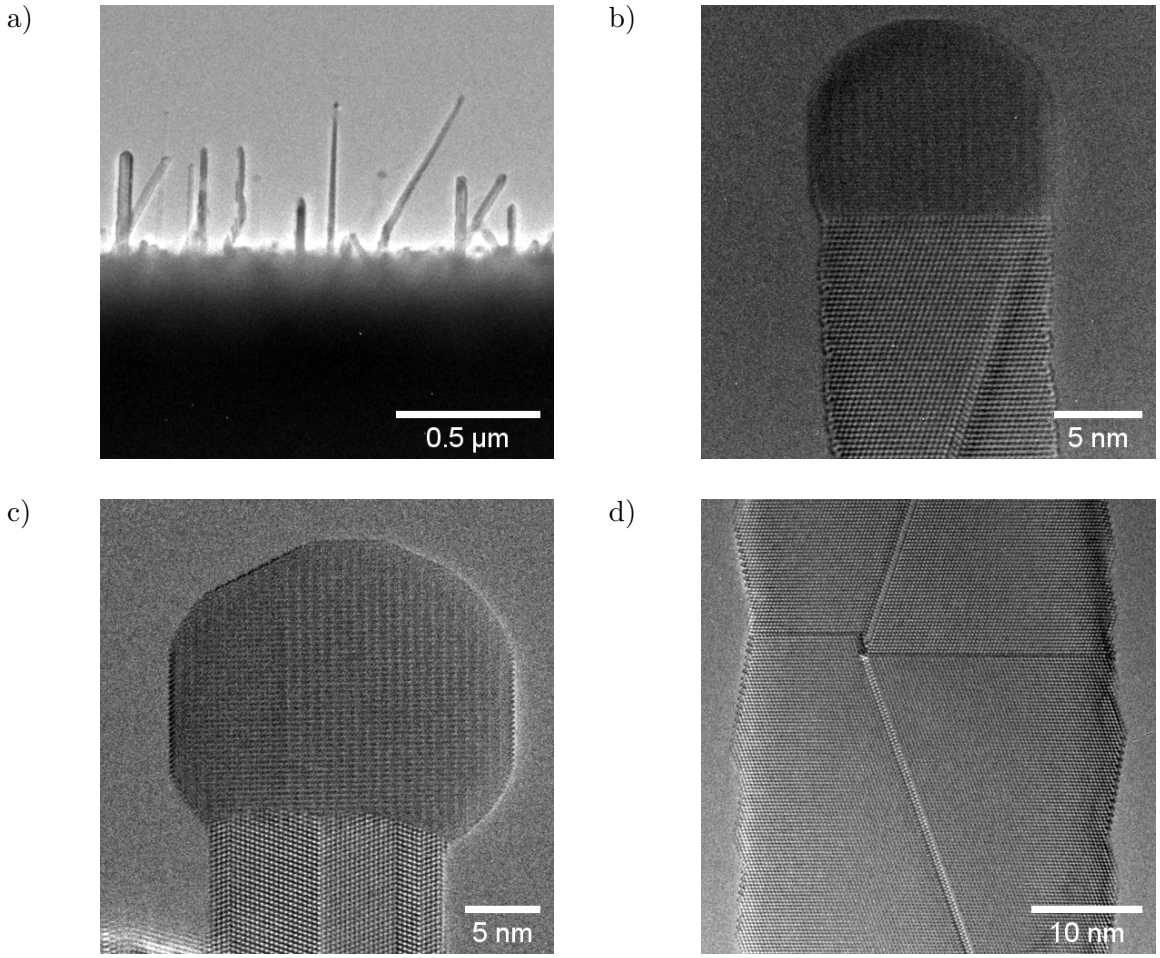

FIGURE 5.10: TEM images of large diameter SiNWs grown with majority-Cu catalysts on the Si cantilever. a) Low magnification view. b) High resolution view of a ⟨111⟩ SiNW. c) High resolution micrograph of a ⟨112⟩ SiNW. d) Complex defect due to several twin planes intersecting in a ⟨111⟩ SiNW.

nanowires. Unlike in small diameter SiNWs, there is not a visible phase separation between a liquid and a solid phase. Instead, catalytic seeds appear completely solid.

In the case of majority-Sn catalysts, SiNWs with diameter larger than 15 nm were also observed on the hot part of the Si cantilever. All large diameter SiNWs grew along the ⟨111⟩ direction, see Figure 5.11a. Some of them have kinked during the growth as shown in Figure 5.11b but they retained their original {111} growth interface. Compared to majority-Cu growth, twinning is rarer and the twin planes are exclusively perpendicular to the growth axis. The complexity of the catalytic seeds structure that was hinted in small diameter SiNWs is now made obvious by their larger size. They display a clearly defined boundary between solid and liquid phases. The former is easily identifiable by its faceting while the latter has a curved boundary with the vapor phase. Although the shape of the solid phase can change from wire to wire, on tens of observed SiNWs, both the solid and the liquid parts were found to be in contact with the growth interface at all times. Therefore, on the plane of the growth interface, there exists a line where solid Si, liquid and solid catalyst meet.

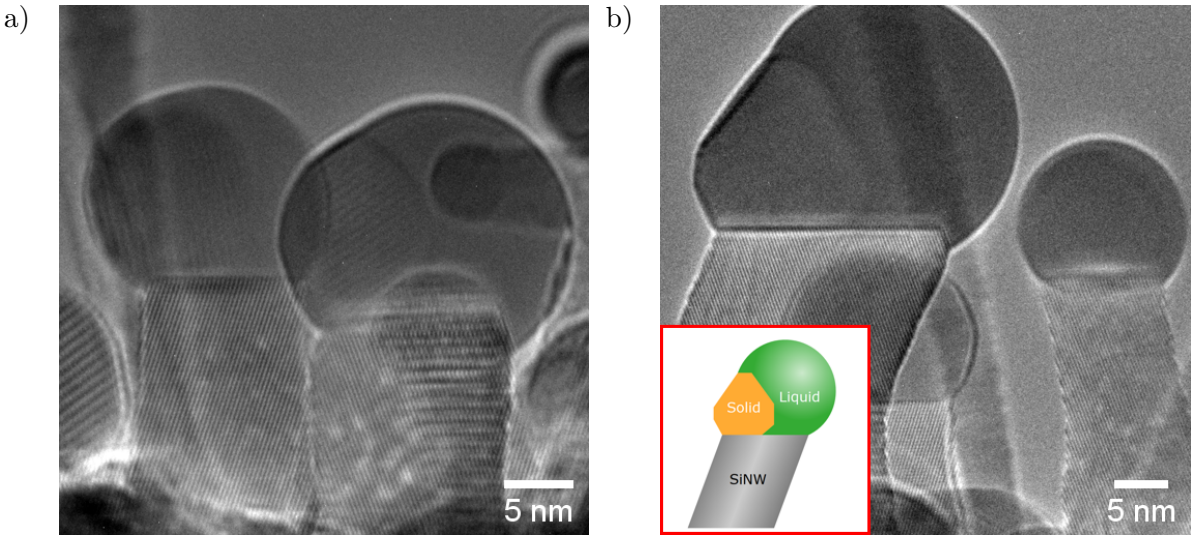

FIGURE 5.11: TEM images of large diameter SiNWs grown with majority-Sn catalysts on the Si cantilever. a-b) High resolution images of ⟨111⟩ SiNWs. In these images, majority-Sn catalysts are clearly biphasic. Inset: Schematic of the catalyst structure.

5.3 Nature of the catalyst

A striking feature of the CuSn-catalyzed growth is the appearance of facets on catalyst surfaces. Indeed, contrary to the Au-catalyzed and Sn-catalyzed growth, the catalyst does not have a hemispherical shape with a smooth spherical surface. Rather, it presents facets typical of its partly crystalline character. Under a favorable orientation, it is possible to observe its lattice planes. On the other hand, there are volumes in the catalyst that resemble a liquid phase. This means that with CuSn as catalyst, the growth operates under either the vapor-solid-solid (VSS) mode, the vapor-liquid-solid (VLS) mode or both at the same time.

Noticeably, the solid nature of the catalyst is observed for both low diameter (below 10 nm) and large diameter (above 10 nm and below 50 nm) SiNWs. In particular, large diameter SiNWs catalyzed by majority-Cu catalysts lack a visible liquid part. This is an unexpected observation as Sn is known for its low melting point. Furthermore, large diameter SiNWs are generally obtained in high temperature regions of the Si cantilever. This hints towards an evolution of the catalyst composition as the growth experiments progress. Because nucleation of each nanowire new plane takes place at the catalyst interface, understanding the effect of the catalyst composition and structure should provide insights on the growth mechanisms. The following section will focus on this.

5.3.1 Catalyst chemical composition analysis

The EDX spectrum of Figure 5.5 established that both Cu and Sn can be deposited in order to form single particles. By performing the EDX analysis again on grown SiNWs, we can uncover the catalyst composition evolution during the growth. In the SiNW with a diameter below 10 nm, shown in Figure 5.12a grown at 380 °C on the SiC membrane with majority-Cu catalyst, STEM-EDX technique was used to obtain chemical maps of Si, Cu and Sn, respectively Figure 5.12b-d. This particular wire has grown for around one hour after the first nucleation. The

chemical maps indicate that the nanowire itself is made almost exclusively of Si. As for the catalyst, Si and Cu were detected with a ratio of 40:60. A few counts of Sn were also found but the amount of Sn in the catalyst is too low for quantitative analysis by EDX.

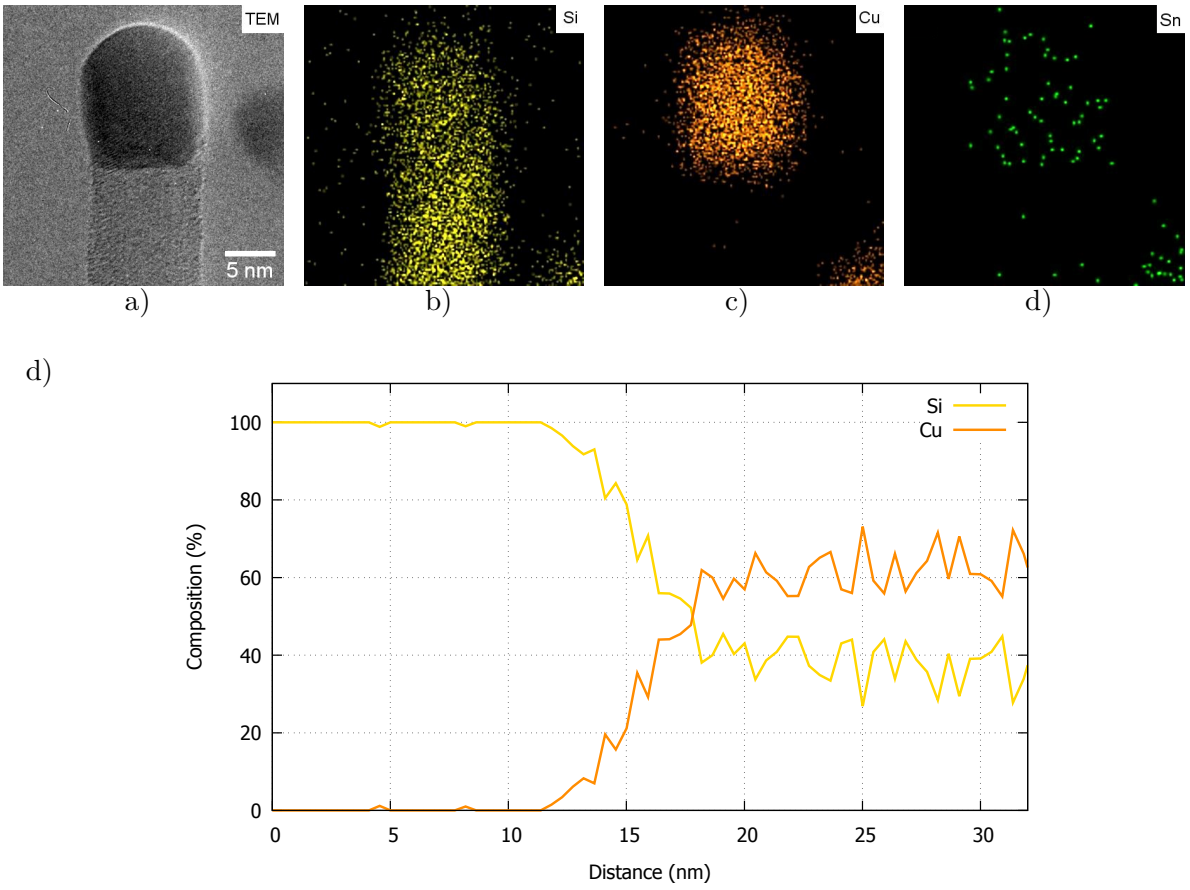

FIGURE 5.12: EDX chemical maps of a majority-Cu catalyzed SiNW. a) SiNW TEM image. b) Si chemical map. c) Cu chemical map. d) Sn chemical map. e) Line plot of Si and Cu concentration along the nanowire axis in a).

While the analysis was carried out on small diameter SiNWs and given the catalyst shape in larger diameter ones, one can conclude that SiNWs grown by majority-Cu seeds are almost exclusively catalyzed by Cu. Indeed, large SiNWs seeds are well faceted with no apparent curvature. Therefore, the growth mode for SiNWs catalyzed by majority-Cu seeds is the vapor-solid-solid (VSS) mode.

The same analysis can be carried out on SiNWs grown with majority-Sn catalyst. Let us remind that such nanowires present a catalyst that has both a solid and a liquid part. For that purpose, consider the nanowire shown in Figure 5.13a with a diameter of around 50 nm. This wire has grown for a few hours. We perform EDX analysis on specific parts of the catalyst. To do so, the electron beam is focused into either the S1 or the S2 spot. S1 is the curved liquid part while S2 is the faceted solid part. The resulting spectra are summarized in Figure 5.13b. An intense Si signal is present in both catalyst parts, essentially coming from the environment. Cu and Sn are also found in S1 and S2. However, the quantitative analysis yields different ratio of Cu and Sn for in either of the EDX spots. Excluding Si, the S1 liquid part is Sn-rich at 63 at. % and 37 at. % Cu content. On the other hand, the S2 solid part is Cu-rich at 84 at. % and 16 at. % Sn content. Thus, we see that Cu and Sn do not segregate completely from each

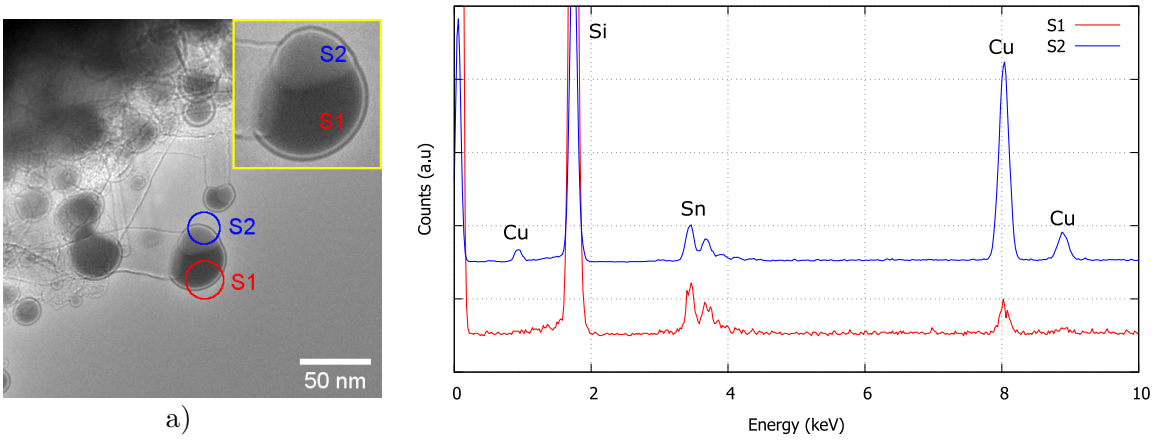

FIGURE 5.13: EDX analysis of majority-Sn catalyst. a) TEM image of the analyzed SiNW. S1 and S2 designate measured areas. Inset: close-up view of the catalyst. b) EDX spectrum of the S1 (red) and S2 (blue) spots.

other but can be incorporated in either the Cu-rich or the Sn-rich part. We have not done the analysis on small diameter SiNWs. However, if we consider the catalyst shape in wires such as the one in Figure 5.9a, we could expect similar results.

The coexistence of both a solid and a liquid part inside a single catalyst raises interesting questions. In particular, the question on the growth mode of majority-Sn catalyst becomes more complicated to answer. It becomes unclear whether the growth operates in the VLS or VSS mode. To decide between the two will require a careful examination of a growth interface as a nanowire is growing. This will be done later in the chapter.

5.3.2 Sn depletion in the catalyst

In majority-Cu growth, the EDX analysis proved that Sn is no longer present in significant amount inside the catalyst after the start of the growth. We suggest that during the incubation time before growth starts, Sn gradually diffuses out of the catalyst in a mechanism similar to that described before: through the formation of a Sn wetting layer, this time on the substrate. We already described this in Section 5.1.1. Other mechanisms can be proposed such as the evaporation of Sn or its incorporation in the SiNWs. However, they fail to explain the relatively fast Sn loss rate, where it takes no more than 30 min to completely empty the Sn content of the initially majority-Cu catalyst. Indeed, the vapor pressure p_v of liquid Sn as a function of temperature, which can be used to derive the evaporation flux of Sn, is given by [232]:

$$\log p_v(T) = A + \frac{B}{T} \tag{5.1}$$

with $p_v(T)$ the vapor pressure expressed in atm, T the temperature in K, and $A = 5.262$, $B = -15332$ two constants. At 380 °C, this gives a vapor pressure of 6.22×10^{-14} Pa. We can then input this value into Hertz-Knudsen evaporation equation to deduce the evaporation flux φ:

$$\varphi = (p_v - p)\sqrt{\frac{1}{2\pi m k_B T}} \tag{5.2}$$

with p the Sn partial pressure in the TEM column, $m = 1.97 \times 10^{-25}\,\mathrm{kg}$ the mass of a Sn atom and k_B the Boltzmann constant. Assuming that there is no Sn vapor inside the TEM column, we obtain a flux $\varphi = 5.89 \times 10^{8}\,\mathrm{atoms \cdot m^{-2} \cdot s^{-1}}$. Let us assume that evaporation takes place in spherical Sn liquid particles of radii 2.5 nm. This should yield an evaporation rate of $1.2 \times 10^{-8}\,\mathrm{atoms \cdot s^{-1}}$. Given the small interface area of the CuSn particles and the time frame of our growth experiments, it is clear that evaporation cannot account for the observed fast depletion of Sn.

As for the diffusion of Sn in Si, Akasaka *et al.* have measured it using Rutherford backscattering analysis. They found a diffusion coefficient D [233] expressed in $\mathrm{cm^2 \cdot s^{-1}}$:

$$D = 0.054 \exp\left(-\frac{E_a}{k_B T}\right) \tag{5.3}$$

where E_a is the diffusion activation energy with value 3.5 eV. At 380 °C, this gives $D = 5.3 \times 10^{-29}\,\mathrm{cm^2 \cdot s^{-1}}$, which makes diffusion negligible on the timeframe of an experiment. Furthermore, we have to consider the solubility of Sn atoms inside a Si crystal. It is estimated at $1019\,\mathrm{atoms \cdot cm^{-3}}$ at 380 °C or 1 Sn atom for every 5000 Si atoms [234]. This leaves the only presented option of surface diffusion meditated through the Sn wetting layer on the top of the SiNW. If the main mechanism of leakage is the formation of a wetting layer, then the amount of atomic hydrogen filling the dangling bonds on the SiNW sidewalls is primordial. We have discussed this issue in Section 5.1.1.

Sn depletion in majority-Sn catalyst seems to be less of a concern however. Indeed, the plasma source deactivation has no major effect on those catalyst, contrary to pure Sn ones. In the pure Sn case, depinning of the catalyst is achieved in around 50 seconds. For the majority-Sn catalyst of Figure 5.13a, we have not observed any appreciable volume change in the Sn-rich part over the course of two minutes. Observations 20 minutes later on other nanowires reveal that they still retain their Sn-rich liquid part. If Sn depletion still occurs in majority-Sn growth, the timescale of this phenomena is different between the pure growth and the double catalyst growth and varies between the two by two order of magnitude in time. Therefore, the number of generated radicals by the plasma source is not a determining factor for the Sn stability in majority-Sn growth. This is confirmed by an experiment where we switched off the plasma. Instead of leaking out like in Figure 5.2, the liquid Sn stays on top of the nanowire. Thus, the presence of a solid Cu_3Si stabilizes the liquid part. This would imply that some of the surfaces present in Cu_3Si have a sufficiently high energy so that the Sn would wet them.

5.3.3 Structure determination of the Cu catalyst

We have previously assumed that Cu_3Si is the state of the catalyst in Cu-catalyzed growth. Previous *in situ* experiments have shown through electron diffraction that it is specifically η'-Cu_3Si at temperature between 470 °C and 550 °C for SiNWs with diameter above 50 nm [44]. Considering our growth temperature and the previously shown EDX data for majority-Cu growth, we can use the Cu-Si phase diagram [235, 236] to get an idea of the catalysts state (Figure 5.14). At temperatures between 380 °C for the SiC membrane substrate up to 1000 °C for the Si cantilever, this gives three possibilities: η-Cu_3Si, η'-Cu_3Si and η''-Cu_3Si. If the Cu content is below 74 %, Si should precipitate in the Cu_3Si, which is precisely what is needed for nanowire growth. Thus, we should have the same catalyst as in previous studies.

η-Cu_3Si is the bulk equilibrium phase at high temperature. Its crystalline structure is known

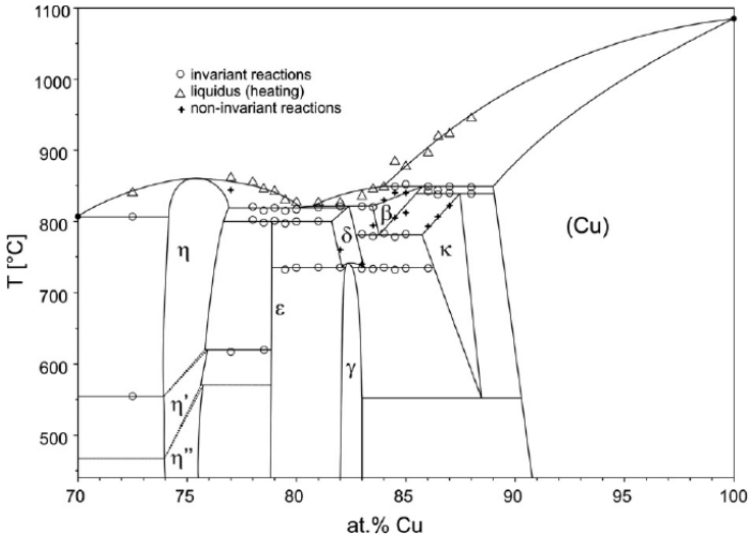

FIGURE 5.14: Cu-Si system phase diagram, reproduced from [236].

TABLE 5.2: Atomic positions in the η-Cu_3Si unit cell.

Atoms	Wyckoff Sites	Atomic Positions
Cu1	1a	(0, 0, 0)
Cu2	2c	(0, 0, 1/3)
Cu3	2d	(1/3, 2/3, 1/6)
Cu4	2d	(1/3, 2/3, 5/6)
Si1	2d	(1/3, 2/3, 1/2)

[237]. It has a rhombohedral unit cell with space group $P\bar{3}m1$ with lattice parameters $a = 4.06\,\text{Å}$ and $c = 7.33\,\text{Å}$. For this crystalline family, one uses the hexagonal four-index notation for planes. The atomic positions of Cu and Si atoms are given in Table 5.2 and projections of the unit cell are given in Figure 5.15. Notice that the stoichiometry of the unit cell is not exactly 3 Cu atoms for 1 Si atom because the occupancy of Cu sites is not 100 %.

Both η'-Cu_3Si and η''-Cu_3Si are superlattices of η-Cu_3Si and they are respectively the bulk equilibrium phase at intermediate and low temperature. Their crystal structures are both incommensurately modulated [238, 239]. Modulated crystals [240] are structures that are derived from a base unit cell of base vectors $\mathbf{a}$, $\mathbf{b}$ and $\mathbf{c}$. Atoms are displaced from their base cell theoretical positions in a direction and magnitude that are given by a periodic wave function $\boldsymbol{\delta}$. For a given atom at position $\mathbf{x}$, the displacement $\boldsymbol{\delta}$ is given by:

$$\boldsymbol{\delta}(\varphi, \mathbf{k}, \mathbf{x}) = \delta_x(\varphi, \mathbf{k}, \mathbf{x})\mathbf{a} + \delta_y(\varphi, \mathbf{k}, \mathbf{x})\mathbf{b} + \delta_z(\varphi, \mathbf{k}, \mathbf{x})\mathbf{c} \tag{5.4}$$

where φ is the phase of the wave, $\mathbf{k}$ the modulation vector and $\delta_\mu(\mu = x, y, z)$ are the given displacements along the base vector directions. Because $\boldsymbol{\delta}$ is periodic, the δ_μ should also all be periodic; they can hence be written as a Fourier series:

$$\delta_\mu(\varphi, \mathbf{k}, \mathbf{x}) = \sum_{n=0}^{+\infty} A_{\mu,n} \sin[2\pi n(\varphi + \mathbf{k}\cdot\mathbf{x})] + B_{\mu,n} \cos[2\pi n(\varphi + \mathbf{k}\cdot\mathbf{x})] \tag{5.5}$$

with the condition that $A_{\mu,n}$ and $B_{\mu,n}$ coefficients result in a displacement δ_μ that is finite and below the typical distance between atoms. The modulation vector $\mathbf{k}$ is given by:

$$\mathbf{k} = \alpha\mathbf{a}^* + \beta\mathbf{b}^* + \gamma\mathbf{c}^* \tag{5.6}$$

TABLE 5.3: Parameters for the incommensurately modulated η' and η'' phase.

Phase	Base group	Base lattice parameters	Modulation vectors	Ref.
η'	$P\bar{3}m1$	$a = 4.1084\,\text{Å}$ $c = 22.228\,\text{Å}$	$\mathbf{k}_1 = (0.244, 0.244, 0)$ $\mathbf{k}_2 = (-0.488, 0.244, 0)$	[238]
η''	$P\bar{3}1c$	$a = 4.07\,\text{Å}$ $c = 14.685\,\text{Å}$	$\mathbf{k}_1 = (0.2509, 0.2509, 1/3)$ $\mathbf{k}_2 = (-0.5018, 0.2509, 1/3)$	[239]

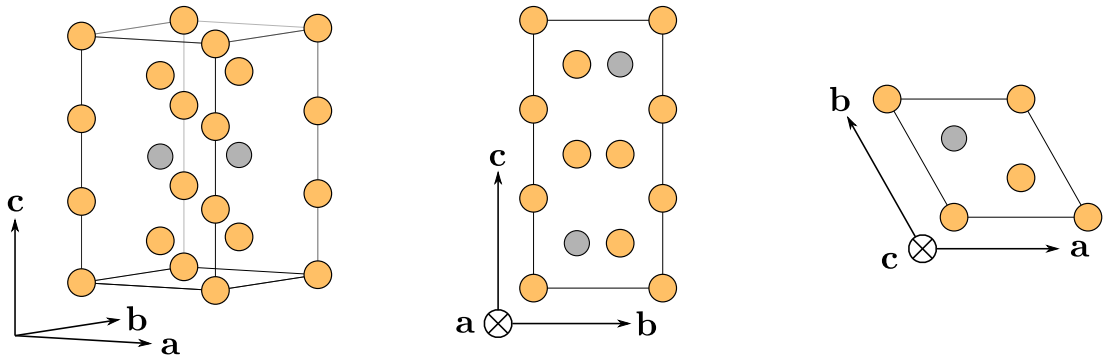

FIGURE 5.15: Unit cell of η-Cu_3Si, Cu atoms are orange, Si atoms are grey. a) 3D view. b) $[10\bar{1}0]$ view. c) [0001] view.

with $\mathbf{a}^*$, $\mathbf{b}^*$ and $\mathbf{c}^*$ the reciprocal unit vectors. It represents the wave vector of the displacement wave $\boldsymbol{\delta}$. If α, β and γ are all rational numbers, then the crystal structure is said to be commensurately modulated and the lattice parameters of the new unit cell are multiple of the lattice parameters of the base cell. If either α, β or γ is irrational, then the crystal structure is said to be incommensurately modulated and is now aperiodic. The lattice parameters of the new unit cell for the direction with irrational coefficients becomes infinite. This process can be generalized to two or more wavefunctions $\boldsymbol{\delta}_i$ with two or more modulation vector $\mathbf{k}_i$:

$$\boldsymbol{\delta} = \sum_i \boldsymbol{\delta}_i(\varphi_i, \mathbf{k}_i, \mathbf{x}) \tag{5.7}$$

with:

$$\boldsymbol{\delta}_i(\varphi_i, \mathbf{k}_i, \mathbf{x}) = \delta_{x,i}(\varphi_i, \mathbf{k}_i, \mathbf{x})\mathbf{a} + \delta_{y,i}(\varphi_i, \mathbf{k}_i, \mathbf{x})\mathbf{b} + \delta_{z,i}(\varphi_i, \mathbf{k}_i, \mathbf{x})\mathbf{c} \tag{5.8}$$

As such, incommensurately modulated crystals are defined by the space group of the base unit cell, its lattice parameters and one or more modulation vectors. The parameters for the η' and η'' are given in Table 5.3. Incommensurately modulated crystals change the constructive interference conditions compared to the base cells. This results in additional spots in the electron diffraction.

Since the atomic positions are known, it is possible to simulate an electron diffraction pattern using a dynamical framework. To that effect, we use the JEMS package [179], which was utilized to generate the HRTEM images presented in Section 2.3.3. Figure 5.16b shows the results of the simulation in the $[\bar{1}2\bar{1}0]$ zone axis. The results of the diffraction simulation can now be compared to an experimental diffraction pattern obtained on a catalyst particle. However, because the catalysts on top of SiNWs are generally unstable under a focused electron beam, we decided to perform the electron diffraction on a catalyst in the early stage of growth, see Figure 5.16a. To confirm that Cu_3Si is also the majority-Cu catalyst on big and small diameter SiNWs (grown at

380 °C), we instead did FFTs of the HRTEM images of the catalyst of Figure 5.10c and Figure 5.8b and compared the positions of the spots to the experimental diffraction pattern. We see a consistent pattern between the electron diffraction and the simulated diffraction of η-Cu_3Si without any additional spots that would correspond to an incommensurately modulated phase. Furthermore, the FFTs also display the same pattern as the electron diffraction. This proves that η-Cu_3Si is the state of the majority-Cu catalysts for both large diameter (high temperature) and small diameter (temperatures around 400 °C) nanowires.

At first glance, finding the η phase for small (low temperature 380 °C) nanowires is unexpected. However, given the size of the catalyst compared to the base lattice parameters of the η' and η'', it is appropriate to state that the catalyst is too small to contain enough displacement defects for the diffraction pattern to display additional spots and all η phases become indistinguishable. For large diameter SiNWs, if the catalyst is η-Cu_3Si, it is possible to give a range of temperature for the growth. According to the Cu-Si system phase diagram, the substrate temperature for big diameter SiNWs is between 550 °C and 850 °C.

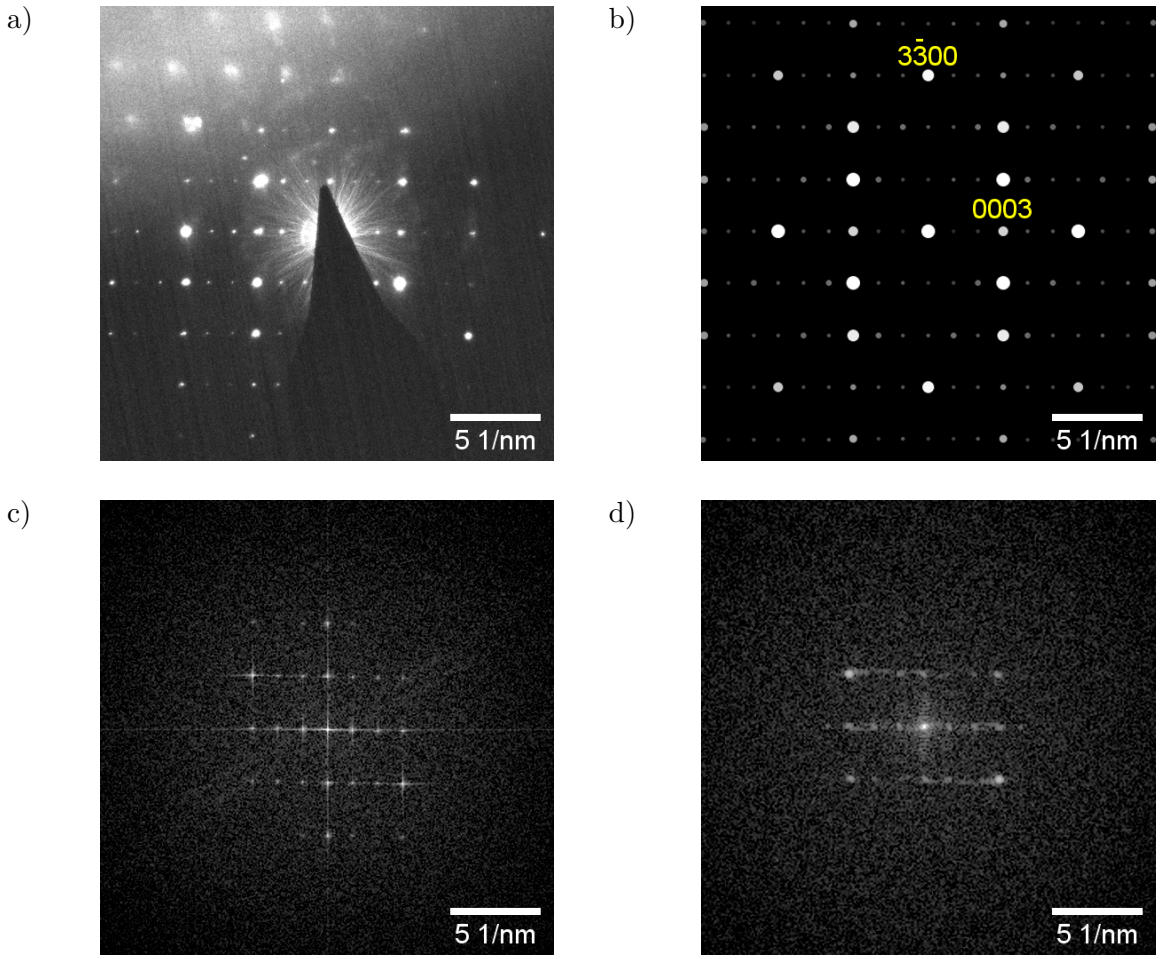

FIGURE 5.16: Diffraction and Fast Fourier Transform of the majority-Cu catalyst. a) Experimental diffraction pattern. b) Simulated diffraction pattern in the $[\bar{1}2\bar{1}0]$ zone axis of η-Cu3Si. c) FFT of the catalyst of the big diameter SiNW of Figure 5.10c. d) FFT of the catalyst of the small diameter SiNW of Figure 5.8b.

The lattice fringes or spacing in the Cu-rich part of the majority-Sn catalyst is similar to the one in majority-Cu part. Therefore, the Cu-rich part has the same crystalline structure as

η-Cu_3Si. There is however a non-negligeable amount of Sn inside given the EDX analysis of Figure 5.13. It is unknown if the Sn is dissolved, substituting Cu in the η-Cu_3Si matrix or if if it makes pure Sn precipitates in η-Cu_3Si. In the following, although it includes some Sn, we refer to it simply as Cu_3Si, the η phase of the Cu_3Si compound.

5.3.4 Cu and Sn respective roles in nanowire growth

From these observations, we can conclude that the growth of majority-Cu SiNWs is catalyzed essentially by Cu with Sn playing only supporting role. The exact role of Sn during the growth needs to be determined. Growth experiments done in a PECVD reactor reported in the literature with pure Cu catalyst have shown that SiNWs can only be obtained in a narrow range of temperature [227] from 500 °C to 650 °C. Below 500 °C, no SiNWs have been observed to emerge from the Cu particles. In that study, the 500 °C lower temperature bound is attributed to the high activation energy of Si diffusion in Cu (0.98 eV). Consequently, the time constant for Si diffusion from the vapor-solid interface of the Cu particle to its solid-substrate interface is long. Eventually, a shell of solid Si will form around the Cu particle before the nucleation of Cu_3Si, which is thought to be the catalyst for the growth. Thus, the catalytic activity of the deposited Cu particles is deactivated. In Section 5.1.2, we reproduced the same result in NanoMAX where SiNWs would not grow with pure-Cu below 500 °C.

In another study of Cu-catalyzed growth of SiNWs, other authors obtained growth at temperature as low as 400 °C in a standard CVD reactor by adding oxygen [228]. The inclusion of oxygen in the reactor oxidized the Cu particle into CuO_2, identified by peaks in X-ray diffraction. SiH_4 would then react with the copper oxide in the following reduction reaction:

$$2SiH_4 + 3CuO_2 \longrightarrow 2Cu_3Si + 3H_20 + H_2 \tag{5.9}$$

with a standard Gibbs free energy of formation $\Delta G = -43.8\,\mathrm{kJ \cdot mol^{-1}}$. There, the nucleation of Cu_3Si is induced chemically.

In our experiments, SiNWs are still obtained at 380 °C, regardless of the exposure of the CuSn islands to heating effect of the electron beam. In majority-Cu growth, we propose that there exists a pocket of liquid Sn so that nucleation of solid Si first occurs in liquid Sn. Then, Si would slowly diffuse into the pure Cu to form Cu_3Si. Once Cu_3Si is formed, the growth will proceed with Cu and Sn as catalysts. The described phenomena can be of interest when Cu is used as the catalyst if a low temperature growth is required, for instance where SiNWs are grown on thermally sensitive substrates.

In majority-Sn growth, Sn should also facilitate the nucleation of Cu_3Si although it is not expected to be a requirement for the growth to start. The larger volume of liquid Sn provides an avenue for the first nucleation of a Si crystal. Furthermore, before Cu_3Si is nucleated, the interface between the Sn liquid and the initial solid Cu may act as another channel for the inclusion of Si in Cu. The formation of a solid Si shell around Cu which can deactivate the catalytic activity of Cu is inhibited due to the vanishingly small solubility of Si in liquid Sn.

Cu and Sn have opposite effects on the apparition of twin planes in SiNWs. The study on pure-Cu and pure-Sn growth revealed that Cu leads to the formation of numerous twin planes. On the other hand, twins are almost non-existent in Sn growth. Inclusion of Cu in pure-Sn to create CuSn catalyst has led to twin planes appearing. With Sn, the favored growth direction is $\langle 111 \rangle$. Therefore, twin planes are perpendicular to the growth axis. As more Cu is added in

the mix, the main growth direction changes to ⟨112⟩. In this configuration, twin planes are now parallel to the growth axis. Pure-Cu SiNWs grow almost exclusively along the ⟨112⟩ direction. In order to fully understand why the growth direction can change, getting more insight on the catalyst structure is required.

5.4 Catalyst-nanowire epitaxial relationship

A solid catalyst opens up the question about the existence of the crystalline relationships between the catalyst and the nanowire itself. In large diameter nanowires, the fringes inside the Cu_3Si particle deliver precious information on the orientation of the catalyst with respect to the nanowire. Indeed, a Fast Fourier Transform performed on the fringes yield a spot pattern which can be compared to a simulated electron diffraction. Indexing the (hkl) spots in the diffraction pattern provides the orientation of the Cu_3Si and the epitaxial relationship.

5.4.1 ⟨112⟩ epitaxy

In the case of ⟨112⟩ SiNWs which is mainly grown with majority-Cu catalysts, we found that all the Cu_3Si catalysts analyzed display the same surfaces and the same fringes when viewed in the [110] Si zone axis (Figure 5.17). Thus, catalysts always have the same orientation with respect to the nanowire. The long lateral surfaces with a tooth-like structure are {0001} surfaces while the top short surface is a $\{1\bar{1}00\}$ surface. We note this relationship as $\langle 112\rangle_{Si}||\langle 1\bar{1}00\rangle_{Cu_3Si}$. In between the two, there are {1011} and {1013} intermediate surfaces that are also short.

This tendency must be related to the preferential development of certain crystal facets. Assuming that the Cu_3Si crystals are close to thermodynamic equilibrium, one may also assume that their shapes will obey the Wulff theorem. The latter can be described as follows. Given, the energy of $\{hkl\}$-oriented crystal surfaces, let us draw vectors, originating from the center of the crystal, normal to the $\{hkl\}$ planes and with intensities proportional to the surface energies γ_{hkl}. Planes normal to all existing and situated at their extremity are also drawn. The inner volume defined by the intersections of all planes is the equilibrium shape of the crystal. In this method, the absolute values of all surface energies are not relevant. It is only the ratios between all the different surface energies involved that matter.

By using the Wulff construction on the catalyst of Figure 5.17a, we can determine that since {0001} has the largest area as seen in the TEM images, it should be the surface with the lowest energy among the four previously cited. It is not possible to know its absolute value through this method. However, we can use the {0001} surface energy as the reference. Let us take the surface energy of {0001} as unity. Then, $\{10\bar{1}3\}$, $\{10\bar{1}1\}$ and $\{1\bar{1}00\}$ have a surface energy of respectively 1.29, 1.34 and 1.4. These values are extracted from growing SiNWs under a constant stream of gaseous and radical species at high temperature. Thus, it is possible that the equilibrium shape of the Cu_3Si catalyst might be different as ones predicted by DFT studies done at 0 K. To our knowledge, no such studies exist currently. Because the lowest energy surface is {0001} in our conditions, the catalyst will orient itself so that this surface is the most exposed to the vapor. In this configuration, the growth of ⟨112⟩ SiNWs is favored.

The catalyst-nanowire interface is quite unique because on the one hand, it is not perpendicular to the nanowire ⟨112⟩ growth axis, and on the other hand, the interface is not planar.

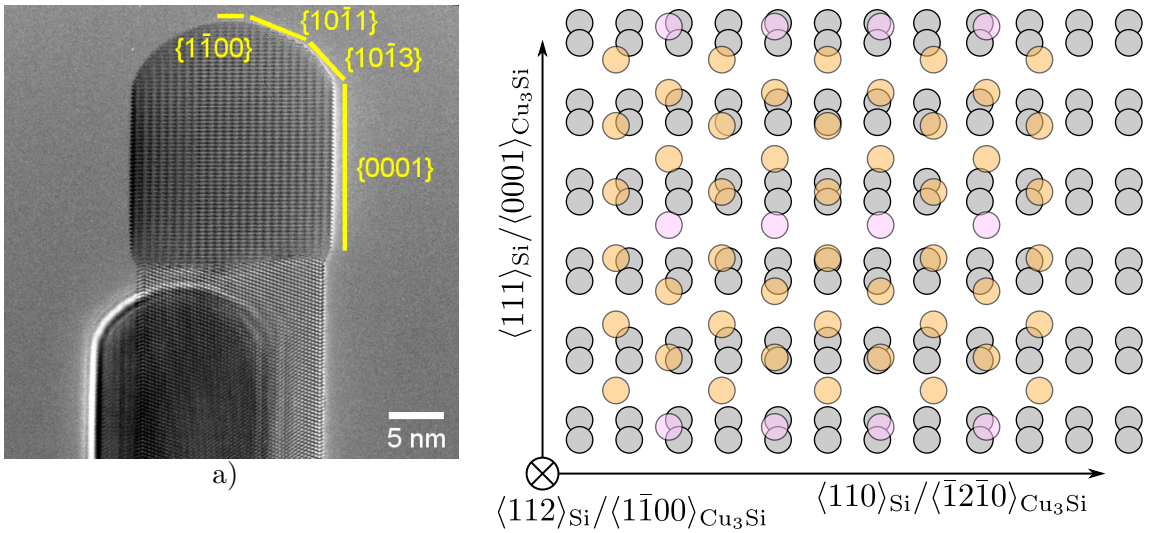

FIGURE 5.17: Orientation of the Cu_3Si catalyst in $\langle 112\rangle$ SiNWs. a) Side-view TEM image of the catalyst-nanowire interface of a $\langle 112\rangle$ SiNWs grown with majority-Cu catalyst. Two twin planes are located next to the left and right $\{111\}$ sidewalls. Surfaces in Cu_3Si are annotated. b) Top-view schematic of the interface depicting how the first two layers in a Si and Cu_3Si crystal interface stack together with the $\langle 112\rangle_{Si}||\langle 1\bar{1}00\rangle_{Cu_3Si}$ epitaxial relationship. Gray atoms are Si atoms in the Si crystal. Orange and pink atoms are respectively Cu and Si atoms in the Cu_3Si crystal.

The angle between one part of the interface and the plane perpendicular to the growth axis is 19°. This corresponds to a $\{111\}$ plane in Si. In Cu_3Si, it does not correspond to a specific plane, hence the lattice seems distorted in the catalyst. Furthermore, the contrast transition between the catalyst and the nanowire is not abrupt, suggesting that the interface has a 3D shape. In this case, the epitaxial relationship is not trivial. Because of this, we expect that this catalyst-nanowire interface should have a relatively high energy. We can also examine how the different layers in Si and Cu_3Si stack together. This is shown in Figure 5.17b. In the $\langle 112\rangle$ zone axis, the Si layers are made of Si dimers arranged in a rectangular lattice with a two-fold symmetry. For the $\langle 1\bar{1}00\rangle$ zone axis in Cu_3Si, Si and Cu atoms form a hexagonal arrangement also with a two-fold symmetry. The discrepancy between the two arrangements adds another level of complexity to this epitaxial relationship. It is possible that such a discrepancy is the reason why twin planes parallel to the growth axis in $\langle 112\rangle$ nanowires are so common. In fact, $\langle 112\rangle$ nanowires with an above 6 nm diameter systematically present one or more twin planes. On some occasions, $\{0001\}$ twin planes parallel to the nanowire growth axis could also be observed in Cu_3Si catalyst. They are not found to extend beyond the catalyst into the nanowire. Therefore, it is not very clear if they have a specific role in favoring the formation of twin planes in the wire.

5.4.2 $\langle 111\rangle$ epitaxy

For $\langle 111\rangle$ SiNWs which are grown with both majority-Cu and majority-Sn catalysts, there is more diversity in catalyst shape. We clearly identified two epitaxial relationships: $\langle 111\rangle_{Si}||\langle 0001\rangle_{Cu_3Si}$, $\langle 111\rangle_{Si}||\langle 1\bar{2}10\rangle_{Cu_3Si}$. An example of the first relationship is shown in Figure 5.18a-b. The top

surface in the Cu_3Si catalyst is a $\{0001\}$ surface. Other surfaces include $\{10\bar{1}1\}$ and $\{10\bar{1}3\}$ which were already present in $\langle 112\rangle$ epitaxy. Consider the stacking between the first layer of Si and Cu_3Si at the planar catalyst-nanowire interface. Both the $\{111\}_{Si}$ and the $\{0001\}_{Cu_3Si}$ present an hexagonal arrangement of atoms but with dissimilar parameters. Due to the positions of Si and Cu atoms in the Cu_3Si matrix, the symmetry of $\{0001\}_{Cu_3Si}$ is only three-fold for Si atoms, contrary to $\{111\}_{Si}$ which has a six-fold symmetry. There is also a mismatch between the two lattices. The hexagons sides for Si are 3.84 Å long while those for Cu_3Si are 4.06 Å, yielding a 5.4 % lattice misfit. No visible dislocations were observed at the interface in a nanowire with a diameter of 20 nm, which means that either the catalyst or the nanowire prefers to be strained, or that the stress is relaxed. Both majority-Cu and majority-Sn grown SiNWs can present this epitaxial relationship. In the case of majority-Sn, it is the only relationship that was observed.

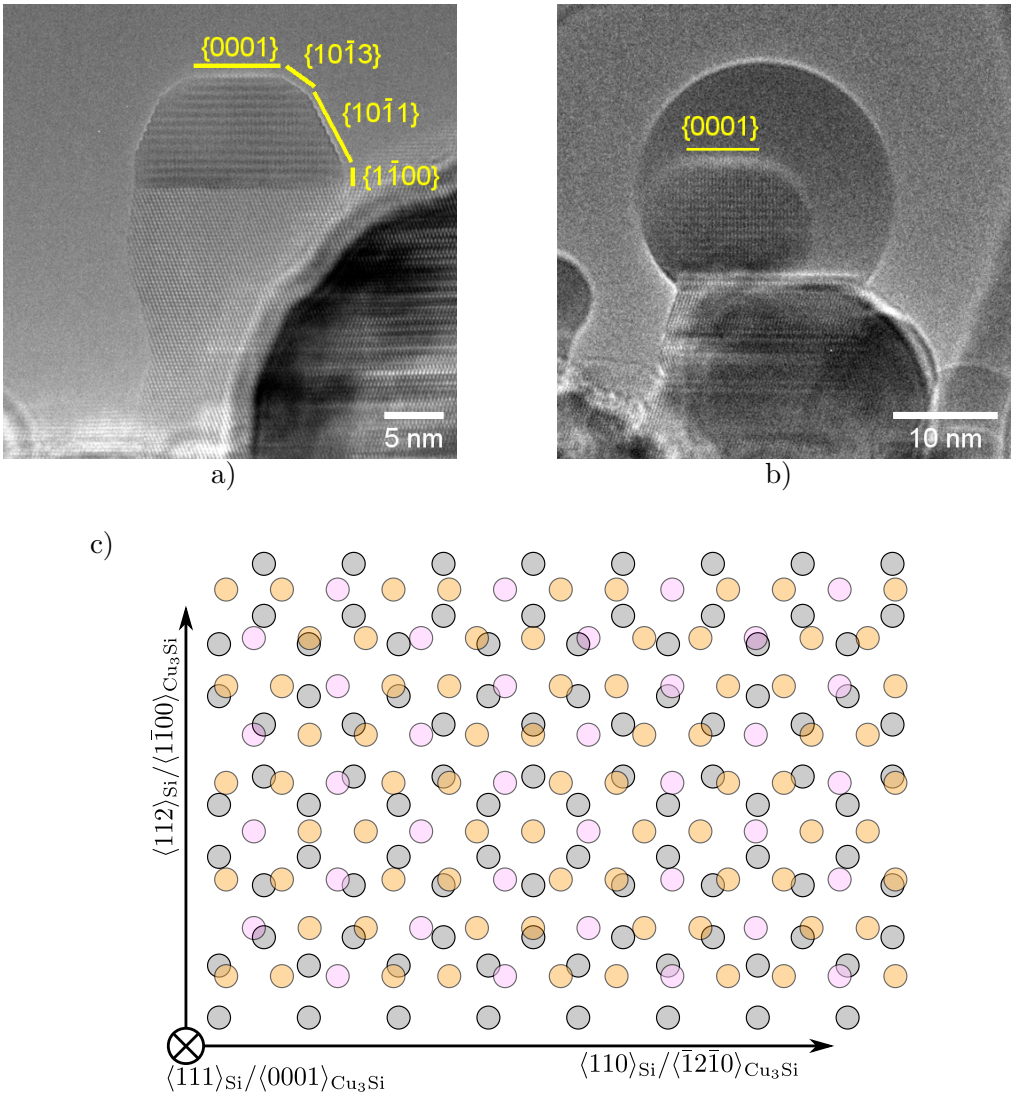

FIGURE 5.18: Orientation of the Cu_3Si catalyst in the $\langle 111\rangle_{Si}||\langle 0001\rangle_{Cu3Si}$ epitaxial relationship. a) Side-view TEM image of the catalyst-nanowire interface in a majority-Cu catalyst in this orientation. b) Side-view TEM image of a majority-Sn SiNW where the Cu_3Si core is in this orientation. c) Top-view schematic of the interface depicting how the first two layers in a Si and Cu_3Si crystal interface stack together with the $\langle 111\rangle_{Si}||\langle 0001\rangle_{Cu_3Si}$ epitaxial relationship. Colors are described in Figure 5.17b.

For the $\langle 111\rangle_{Si}||\langle \bar{1}2\bar{1}0\rangle_{Cu_3Si}$ relationship which is only found in majority-Cu (Figure 5.19a), the catalyst displays lateral longer $\{0001\}$ surfaces and a shorter top $\{\bar{1}2\bar{1}0\}$ surface. The catalyst-nanowire interface is also planar. In between the two, there is a smoothly curved surface that is probably made of a succession of few atoms long short intermediate surfaces between $\{0001\}$ and $\{\bar{1}2\bar{1}0\}$ with similar surface energies. If one observes how the first planes in Si and Cu_3Si stack in this relationship, it is apparent that both $\{111\}_{Si}$ and $\{\bar{1}2\bar{1}0\}_{Cu_3Si}$ layers again have an hexagonal arrangement. However, for the one in the $\{\bar{1}2\bar{1}0\}_{Cu_3Si}$ layer, the hexagons are not regular. Therefore, this epitaxial relationship should create greater strain in the catalyst-nanowire system. This may explain why we very rarely observe this orientation. Interestingly, while the lateral surfaces are $\{0001\}$, we found that catalysts with such an orientation have no $\{0001\}$ twin planes inside. It seems then that the occurrence of twin planes in the $\langle 112\rangle_{Si}||\langle 1\bar{1}00\rangle_{Cu_3Si}$ epitaxial relationship is linked to the complex geometry of the interface. Because the three studied relationship leads to nanowire with different appearances, immediate identification of growth direction and epitaxy type is possible.

At least one other epitaxial relationship was also found on $\langle 111\rangle$ wires grown with majority-Cu although we were unable to identify them as the spacing in the displayed lattice fringes does not match any known distance in Cu_3Si. A possible reason for this can be because these fringes are the results of moiré interference. One of the unknown relationships occurs mainly in nanowires with diameter larger than 30 nm.

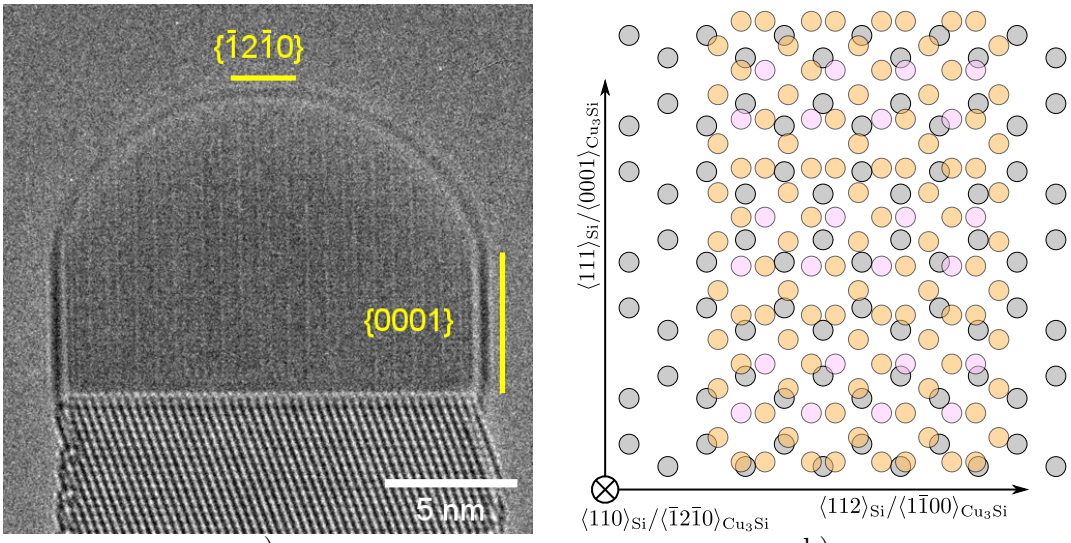

a) b)

FIGURE 5.19: Orientation of the Cu_3Si catalyst in the $\langle 111\rangle_{Si}||\langle \bar{1}2\bar{1}0\rangle_{Cu_3Si}$ epitaxial relationship. a) Side-view TEM image of the catalyst-nanowire interface in a $\langle 111\rangle$ SiNW with a majority-Cu catalyst in this orientation. b) Top-view schematic of the interface depicting how the first two layers in a Si and Cu_3Si crystal interface stack together with the $\langle 111\rangle_{Si}||\langle \bar{1}2\bar{1}0\rangle_{Cu_3Si}$ epitaxial relationship. Colors are described in Figure 5.17b.

5.4.3 Catalyst orientation selection

We have presented the different orientations that the Cu_3Si catalyst could take with respect to the nanowire. In this section, we try to understand how and when the epitaxial relationship is selected. There is no evidence that the solid catalyst can change orientation during nanowire

growth. Indeed, all the recorded solid catalysts display unchanging lattice fringes during growth. Moreover, this remains true even when we deliberately change parameters such as temperature or plasma power. Leakage of either Cu or Si atoms, leading to the shrinking of the catalyst, is also unable to change the catalyst orientation. It seems then that changing the interface orientation is a process which requires a considerable amount of energy and cannot be achieved in steady growth. Consequently, the relationship has to be chosen from the growth start or nucleation of the first Cu_3Si crystal.

The observation of early-formed catalyst can provide some insights in that matter. Figure 5.20 shows both majority-Cu and majority-Sn catalysts on a (111) crystalline surface of the Si cantilever that have not yet precipitated a SiNW. The TEM images were taken after the introduction of the SiH_4/H_2 gas mixture with the plasma activated. In Figure 5.20a, one can immediately recognize the characteristic shape of a $\langle 112\rangle_{Si}||\langle 1\bar{1}00\rangle_{Cu_3Si}$ catalyst. This is quite surprising as the (111) surface of the Si cantilever was HF-treated. Thus, we would have expected the other two $\langle 111\rangle$ possible epitaxy relationship. The fact that it is not the case means that in the case of those two catalysts in the TEM image, the $\langle 111\rangle$ epitaxy is forbidden, or unfavorable at the very least. A likely reason is because the cantilever surface is not atomically flat at the scale of the average catalyst size. Instead, it is particularly rough as it has not been etched by a KOH treatment. The interface in $\langle 112\rangle$ SiNWs is also not planar and that may favor this relationship in rough crystalline substrates.

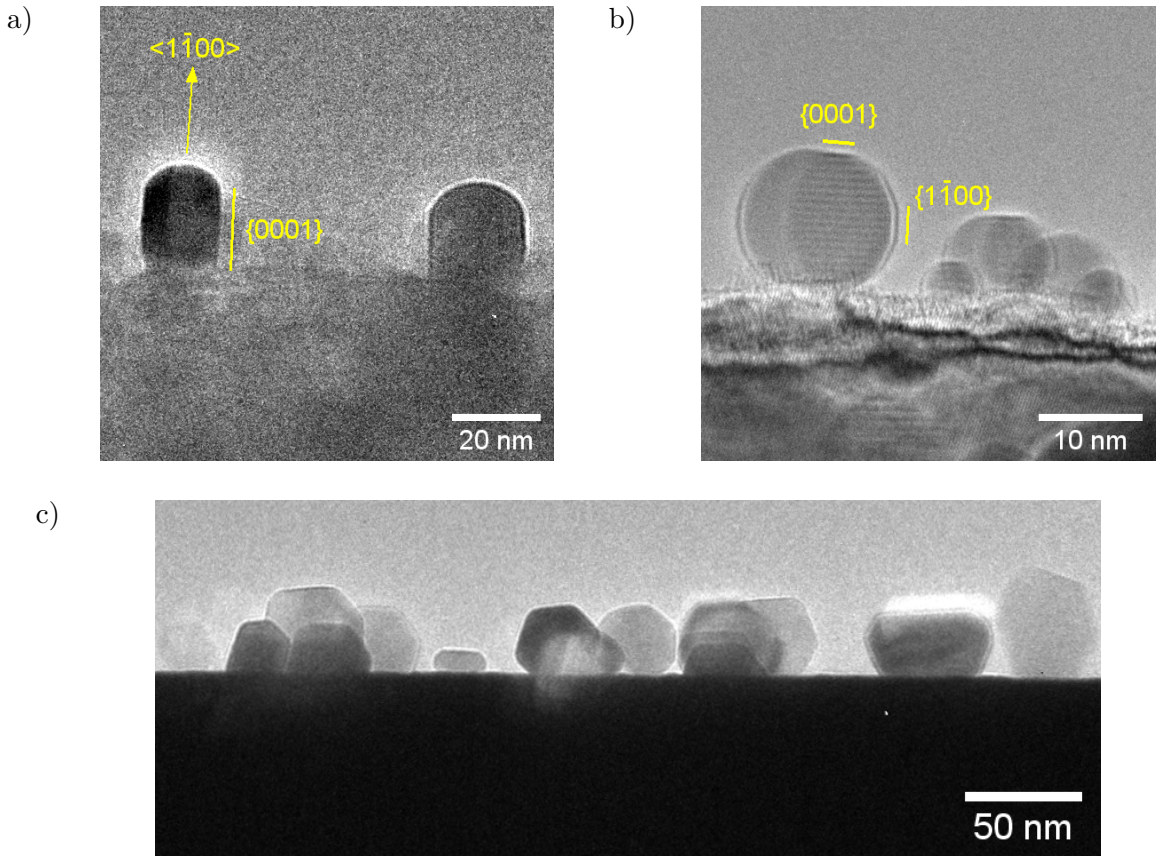

FIGURE 5.20: Orientation of catalysts after the nucleation of Cu_3Si on the Si cantilever (111) surface. a) TEM image of newly formed majority-Cu catalysts on a rough (111) surface. b) TEM image of majority-Sn catalysts. c) TEM image of majority-Cu catalysts lying on a smoothened (111) surface.

This hypothesis is supported by another experiment on the Si cantilever. By applying a current in the loops that raises substrate temperature to a value starting to melt the Si cantilever at its hottest points (> 1400 °C), adding the SiH_4/H_2 gas mixture and activating the plasma source, we smooth out the roughness of the cantilever substrate. After an HF treatment, we thermally evaporate the Cu and Sn metallic layers in a ratio that creates majority-Cu catalysts. The treated cantilever substrate is introduced in the TEM column. We then observe how Cu_3Si nucleation occurs. Figure 5.20c showcases Cu_3Si catalyst typical shapes on a smoothed (111) surface. It is immediately apparent that most of the catalysts on the flat substrate do not present the shape shown in Figure 5.20a that produces ⟨112⟩ SiNWs. Rather, most Cu_3Si catalysts choose to lie flat on the substrate which will yield ⟨111⟩ wires. Consequently, the abundance of ⟨112⟩ wires or $\langle 112\rangle_{Si}||\langle 1\bar{1}00\rangle_{Cu_3Si}$ epitaxy relationship on a (111) surface can be attributed to its roughness. On the polycrystalline and rough SiC membrane, ⟨112⟩ wires form again the majority.

Let us now observe the formation of majority-Sn catalysts just after Cu_3Si nucleation. Typical ones are shown in Figure 5.20b. No thermal treatment for the smoothening of the Si cantilever was carried out. The majority-Sn catalyst biphasic nature is obvious at this point. One can immediately observe both a solid and a liquid part. The lattice fringes inside the Cu-rich part allows for the catalyst orientation identification by means of a FFT analysis. It is determined that solid Cu_3Si prefers to sit in a direction where both the $\{0001\}_{Cu_3Si}$ and $\{111\}_{Si}$ are aligned despite the substrate roughness, consistent with previous observations that all SiNWs grown with majority-Sn catalyst grow along the ⟨111⟩ direction. This confirms that Sn does influence the eventual epitaxial relationship between catalyst and nanowire, and thus the growth direction. In Figure 5.20b, the liquid Sn seems to preferentially wet specific Cu_3Si surfaces such as $\{1\bar{1}00\}$, $\{10\bar{1}1\}$ and $\{10\bar{1}3\}$. In catalysts where the Cu/Sn ratio is heavily biased towards Sn, even more so than ones in Figure 5.20, we observe that the top {0001} surface will also get wet by Sn. These observations are not surprising considering the Cu_3Si surface energy hierarchy established in Section 5.4.1: {0001} has the lowest surface energy. The preferential wetting of the higher energy surfaces is likely the cause of the different orientations of the majority-Sn catalyst compared to majority-Cu ones. That ultimately exclusively yields ⟨111⟩ wires.

5.5 Step-flow growth and geometry

5.5.1 Vapor-Solid-Solid mode in SiNWs grown with majority-Cu

In situ data show that the majority-Cu growth happens in a way similar to the monolayer by monolayer growth observed in Au-catalyzed SiNWs. More information on the growth kinetics can be gathered in this case. Since majority-Cu SiNWs grow by the VSS method, the growth rate is lower and hence the dynamics of the monolayer by monolayer process is more easily observed. The use of an ultrafast camera was therefore not necessary here.

The evolution of the interface during the time lapse of a growing monolayer is shown in Figure 5.21. This ⟨111⟩ SiNW was grown on the SiC membrane at 380 °C. The epitaxial relationship displayed should be $\langle 111\rangle_{Si}||\langle 0001\rangle_{Cu_3Si}$ judging from the catalyst shape. In this series of TEM micrographs, one can clearly see that the growth of a monolayer starts from the edge of the catalyst-nanowire interface, creating an atomic step. As Si atoms are incorporated into the forming layer, the position of the step changes from one edge of the nanowire to the other.

When the step has reached the other edge, the monolayer is completely formed, and the cycle restarts. Similar dynamics were observed in Si [44, 197], Ge [194] and III-V nanowires [151, 199]. Multiple steps can also be seen growing at once, as visible in Figure 5.21b. Wen *et al.* have shown that this behavior was due to the incorporation rate of Si in the nanowire being smaller than the incoming flux of Si [197].

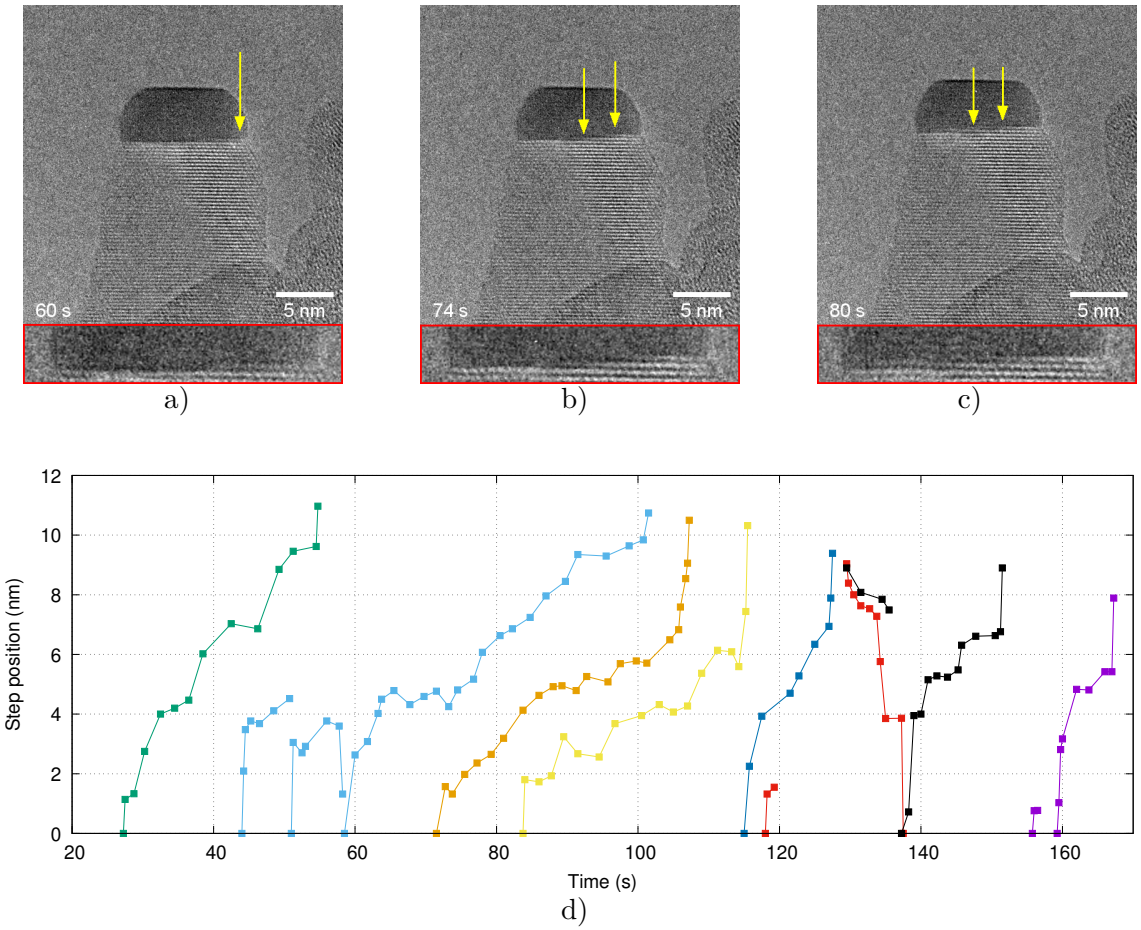

FIGURE 5.21: Several monolayers nucleating and traveling in a ⟨111⟩ SiNW. The yellow arrows show the position of the step. a) The nucleation starts at the edge of the catalyst-nanowire interface. b) Two monolayers are seen nucleating at once. c) The two monolayers of b) are propagating. Insets: close-up view of the interface. d) Evolution of the step position with time. Each color represents a single layer. Step position origin is taken at the right triple phase boundary. The time origin is the same in the graph and in the images.

Following the projected position over time of several steps allows us to gather more information on the step-flow process. This is shown in Figure 5.21d. For a given step, its position evolution follows a trend where the first and last nanometers are crossed rapidly while the propagation appears slower in the middle of the interface. In this figure, the tapering and subsequent diameter reduction of the SiNW is also visible as the maximum step position retreats with each successive propagation event. Interestingly, it was also observed that some steps could regress and vanish after propagating a certain distance. The second nucleated step in Figure 5.21d clearly presents this behavior twice. We believe that, at this point, there are not enough Si atoms in the Cu_3Si catalyst for it to be in equilibrium with the SiNW, let alone sustain the step growth. Since no variation in the Si arrival flux was detected, it is possible that the catalyst is also losing Si in another way, presumably through desorption of Si atoms being knocked-off

because of the electron beam or through an eventual Sn wetting layer. In addition, the plot shows that successive steps generally propagate in the same direction, from right to left as it happens. This can be understood by the fact that nucleation of a new layer requires more Si atoms than simply extending one across the interface. The side from which the layer started has more time to accumulate Si than the opposite side in where the layer was completed. Only once did the situation reverse and the reasons for it are unclear (red line in Figure 5.21d). It could be due to the shrinking of the majority-Cu catalyst acting as a supplementary Si atoms source.

Under a certain angle between the nanowire axis and the observation axis, it is possible to observe the catalyst-nanowire interface from the top, in a "bird's eye view", granting access to the geometry of the step flow [199]. We present such a view in Figure 5.22 which has a 10° tilt from the ⟨111⟩ nanowire growth direction. The SiNW was grown on the Si cantilever at high temperature. While the capture rate of the camera is insufficient to observe how the Si solid nucleus appears, it is clear that the nucleation occurs at the intersection of three interfaces, or triple-phase line: the solid catalyst-nanowire interface, the nanowire-vapor phase interface and the solid catalyst-vapor phase interface.

With this viewing axis, the propagation and the geometry of the atomic step can be seen in 3D with a clear view on the hexagonal cross-section of the nanowire. The tapering of the wire, coupled with the geometrical shape of the catalyst particle, indicates that the growth direction of this wire is ⟨111⟩ indeed. Thus, it is very likely that each nanowire plane has ⟨110⟩ edges, which would produce {112} sidewalls were the nanowire not tapered [219]. Knowing this, the identification of the nucleating step orientation is feasible, and the result of the analysis from the video are shown in Figure 5.22. The nucleation happens on the edge of two of the nanowire sidewalls, creating one {110} and one {112} step edges inside the catalyst. It was shown that nucleation occurs preferentially at the triple-phase line since less interfaces would be created [153]. As the coverage increases, one additional {112} edge is created before the {110} edge disappears for a {112} edge. When the monolayer is almost complete, three {112} step edges are present. The prominence of {112} edges in this process can be simply understood by the fact that {112} surfaces are less energetic than {110} surfaces.

We now follow the step-flow dynamics in the course of several monolayer growths of the nanowire shown in Figure 5.22a-d. To that effect, a measurement of the time evolution of the area coverage of the newly nucleated layer was done. The result is presented in Figure 5.22e. Ten nucleation events were followed in the course of 90 seconds. It can be seen from this plot that after a layer is completed, there is a waiting time before the new layer is started. It corresponds to the time needed for the Cu catalyst to reach Si supersaturation again. It depends on both the adsorbed Si arrival flux and the diffusion rate of Si in Cu_3Si. The latter varies with temperature. The time taken for a full monolayer to be completed seems regular over the course of the 10 nucleated layers, taking between 3 and 5 seconds in our growth conditions. There are two instances where it takes more than 10 seconds to fully complete a layer, they are represented in red in Figure 5.22e. Upon closer inspection, the lower step velocity is associated with the fact that there are two monolayers nucleating and growing simultaneously. Nucleating two monolayers at once requires more Si atoms. Because the Si arrival flux is constant, the step propagation velocity will adjust accordingly. A relation for the step velocity v has been previously proposed in [197] where v is proportional to $\Delta\mu_{Si}$ which is the difference of chemical potential of Si atoms between the Cu_3Si catalyst particle and the SiNW.

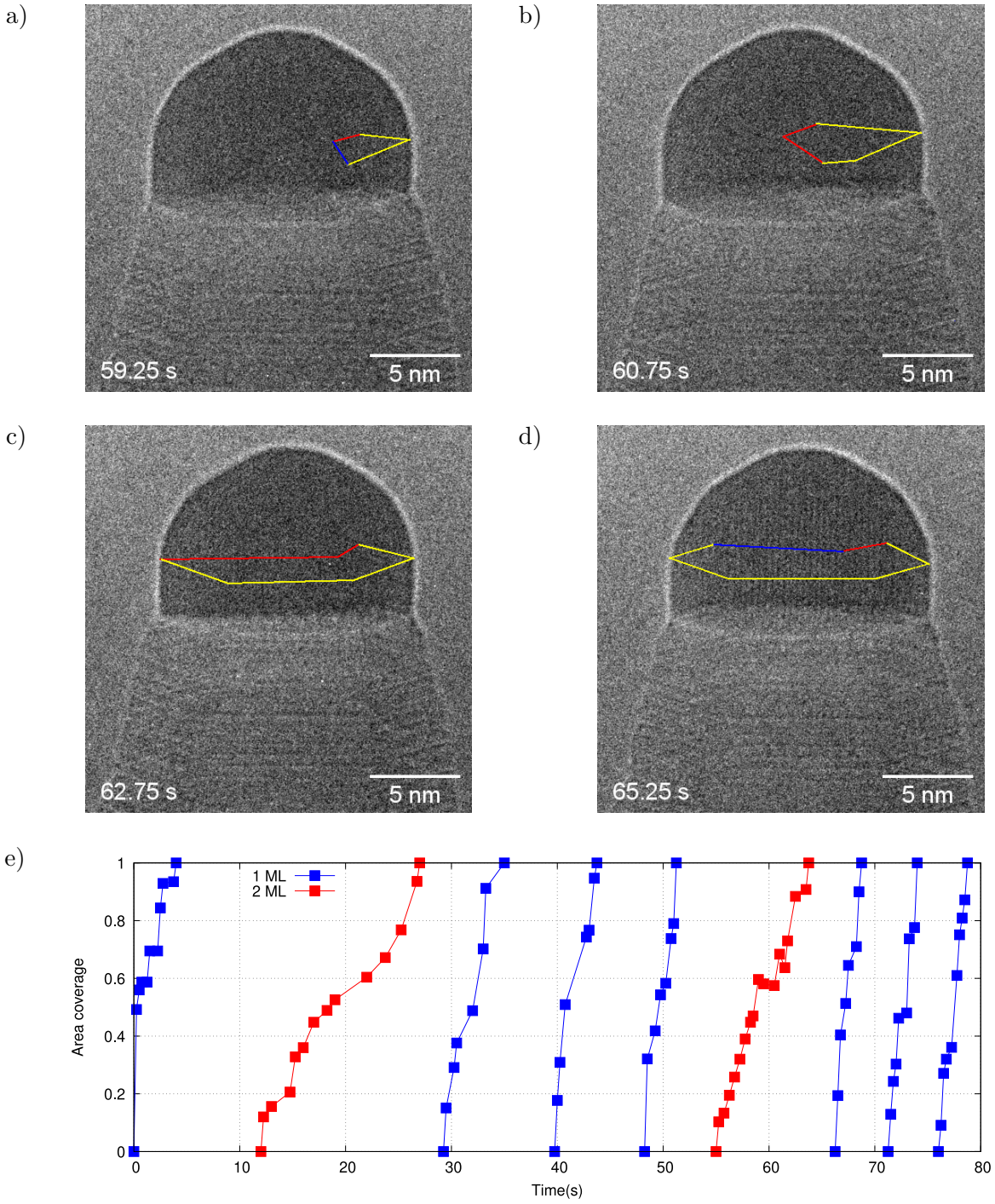

FIGURE 5.22: a)-d) Bird's eyes view of a ⟨111⟩ SiNW during the growth of a double monolayer. Yellow lines indicate the SiNW sidewalls and are shifted upwards for clarity. Red lines are ⟨110⟩ segments parallel to {112} surfaces; blue lines are ⟨112⟩ segments parallel to {110} surfaces. e) Evolution of the area coverage of a step for 10 nucleation events. The measured area coverage of a given layer is divided by the area of that layer when completed. The indicated time is synchronized with the images.

5.5.2 The hybrid growth mode of majority-Sn catalysts

In majority-Sn growth, the biphasic nature of the catalyst complexifies the growth mode determination. To that effect, we record the growth of a SiNW on the Si cantilever and carry out the same analysis on the step propagation. This is done on the nanowire of Figure 5.23. It grows along the $\langle 111 \rangle$ direction and the faceting of the Cu_3Si clearly indicates a $\langle 111 \rangle_{Si} || \langle 0001 \rangle_{Cu_3Si}$ epitaxy. A step-flow mechanism emerges from this series of TEM images. The step propagation extends from the left side with the liquid Sn to the right side with the solid Cu_3Si as shown by the yellow arrows. Therefore, both phases of the majority-Sn catalyst contribute to the growth. This hybrid growth mode is a mixture of VLS and VSS.

More characteristics of this hybrid growth can be derived by measuring the step position evolution with time. This is done in Figure 5.23d for seven successive (111) layers. The plots are noticeably different from those obtained on majority-Cu growth. Nucleation of a new layer always begins on the liquid Sn side. Furthermore, the propagation of the step in liquid Sn is not visible as the step velocity is much higher than the one frame per second framerate of the video. After the step has reached the interface between Sn and Cu_3Si, it undergoes a waiting time which is probably due to an insufficient Si concentration in the solid phase. This waiting time at the interface can last up to 20 seconds in our growth conditions. For the first created layer, the wait time is long enough so that a second step could be nucleated in liquid Sn and propagate to reach the Sn-Cu_3Si interface. Once a sufficient amount of Si atoms is gathered, the step may proceed in the solid phase at a much slower velocity. The step position evolves in a similar shape as in VSS.

While the step at the Sn-Cu_3Si interface can be more than one (111) monolayer high due to the step wait time at the interface, it is interesting to notice that the step height cannot be much larger. Indeed, tens of $\langle 111 \rangle$ SiNWs were observed and not a single one displayed a step more than five layers high. If we consider the two phases of a majority-Sn catalyst as independents catalysts, one expects the nanowire side under the Sn side to grow faster than the opposite side under the solid Cu_3Si. The low Si solubility should favor low incubation time. Figure 5.23d shows that the smallest waiting time observed between successive nucleation event is around 8 seconds. Also, both SiH_4 and H_2 are introduced inside the TEM column at a steady rate. This should yield SiNWs that have a jagged shape. None presented this hypothetical shape however. Instead, it seems as if the Sn catalyst would fail to grow as fast as it could but would wait instead for one or more layers to complete in the Cu_3Si side. All appears as if both liquid Sn and solid Cu_3Si would conspire together to slow the overall nanowire growth rate. Consequently, we believe that there must be some form of Si atoms transport across the Sn-Cu_3Si interface which should partially compensate for the slow Si incorporation rate in the forming layer in the Cu side compared to the Sn side.

This growth mode thus combines some properties of both VLS and VSS: the small incubation time and fast Si incorporation rate of VLS on the one hand and the relatively smaller diffusion rate and slower growth rate of VSS on the other. Such hybrid mode should occur when two metallic catalyst with widely different eutectic temperatures are used together.

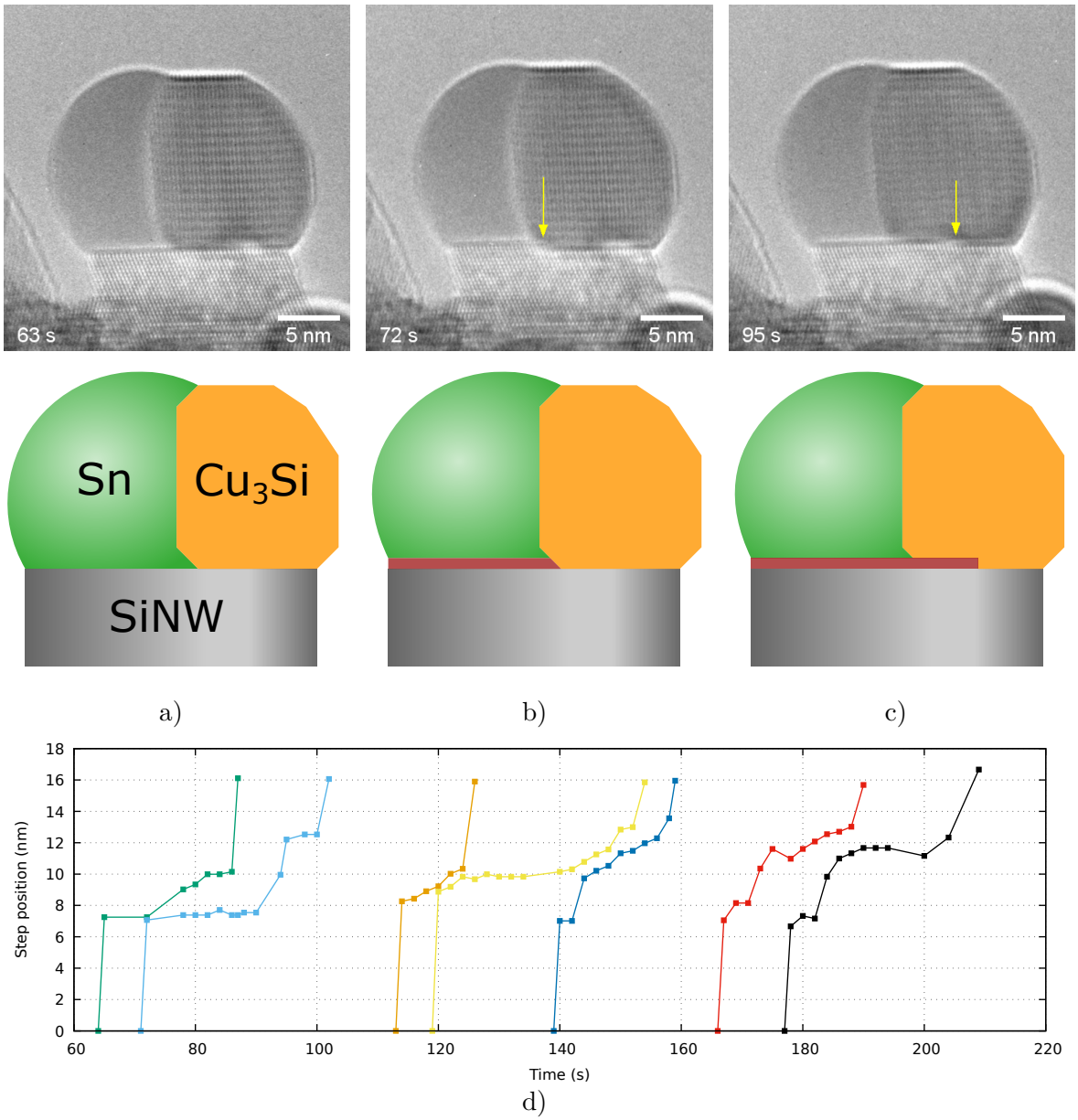

FIGURE 5.23: Step-flow growth in a biphasic majority-Sn catalyst. a)-c) TEM images of the two (111)-step propagation. The yellow arrows indicate the step positions. The red rectangle in the schematics represents the growing layer. d) Step position as a function of time. Each color represents a specific monolayer. The time origin is the same as the images. The origin of the step position is taken as the left triple phase boundary. The measured step position is divided by the total length of the catalyst-nanowire interface.

Conclusion of the chapter

In this chapter, we used metallic catalysts formed from the mixing of Cu and Sn to grow SiNWs on both SiC membranes and oriented Si cantilevers with the help of an ECR plasma source. Initially, growth with pure catalysts was attempted. Pure-Sn growth is known to require some form of plasma to occur. With our setup at 400 °C, SiNWs were indeed obtained which is a

measure of the efficiency of the ECR source to generate atomic hydrogen in a TEM. Pure-Cu growth is more difficult, as fewer wires were obtained overall coupled with a necessary substrate temperature increase to 500 °C. Afterwards, different ratio of Cu and Sn were experimented. They could be separated into two categories that we have called majority-Cu and majority-Sn catalysts. Nanowires could grow at a temperature as low as 380 °C. We characterize the influence of substrate temperature on the SiNWs diameter. A high temperature will favor the growth of larger diameter nanowire thanks to a catalyst coalescence process.

The chemical compositions of both types of catalysts were analyzed by EDX. It was found that majority-Cu catalysts are made almost exclusively of Cu as Sn tended to leak out. In majority-Sn ones, the catalysts presented a biphasic nature with a liquid Sn-rich shell and a solid Cu-rich core. The structural characterization of the Cu part revealed that its crystalline structure is that of η-Cu_3Si, be it in majority or minority Cu catalysts, a compound that is also found in pure-Cu catalysts. These experiments prove that Sn has a major role in the growth by enabling the nucleation of the first Cu_3Si crystal at a lower temperature.

Since the catalyst is at least partially solid, it will influence the growth direction of nanowires by forcing a specific epitaxial relationship. If the usually high energy surfaces are wet by liquid Sn, such as in majority-Sn catalysts, then the growing nanowire will adopt the $\langle 111 \rangle$ growth direction. Inversely, in majority-Cu catalysts, nanowires will prefer growing in the $\langle 112 \rangle$ direction. Other parameters like surface roughness may also change the preferred growth direction.

By observing the catalyst-nanowire interface during the growth, we were able to determine that new layers are created thanks to a step-flow mechanism. A Si nucleus is first formed, creating a step. Then, through Si atoms incorporation, the step will propagate across the whole interface until the layer is completed. The growth mode of SiNWs depend on the chemical composition of the catalyst. In the case of majority-Cu catalysts, the growth mode will be VSS which properties include a relatively slow step velocity and a long incubation time. Several monolayers can be seen nucleating at once. When majority-Sn catalysts are considered, the growth mode becomes a hybrid between VSS and VLS. Short waiting time and high step velocity are the norm in the Sn part while the solid part slows down the overall growth rate, presumably due to an exchange of Si atoms between both catalyst phases.

CHAPTER 6

Growth of polytype 2H in column-IV nanowires

The growth of Si and GeNWs with catalysts of varying chemical composition was described in the previous chapters. We now focus on the crystalline phase presented by these SiNWs.

6.1 Occurrence of the 2H phase in nanowires

6.1.1 Polytype 2H in GeNWs

The 2H phase is known to be less stable in bulk Ge compared to bulk Si [135]. We also observed a similar trend as none of the *in situ* grown GeNWs in NanoMAX presented the 2H phase. In fact, while the PECVD growth of Si nanowires with 2H regions, described in [110], was reproduced multiple times in the Plasfil reactor, the synthesis of GeNWs with Plasfil essentially yielded the equilibrium 3C phase. Using the conditions described in Section 3.2 however, a small section of a 60-nm diameter GeNW exhibited 8 {0002} planes having the 2H stacking (Figure 6.1). The rest of the GeNW presented the expected cubic diamond structure. However, it is not clear if these hexagonal planes grew spontaneously or if they appeared due to another process, as this is a post-growth image. *Ab initio* calculations predict that the 2H phase would only grow in nanowires with much smaller diameters [140]. From here, let us discuss some possible explanations below.

A first possibility is that of a shear deformation during sample handling. This specific GeNW was grown on a (111) Si wafer and then transferred to a TEM Cu grid for observation. The transfer is done through the scratching technique mentioned in Section 2.2. Scratching may lead to the nanowires breaking in several pieces due to the applied pressure of the tweezers. Let us note that the 2H part is located at the bottom of the GeNW, which could actually be a fracture crack due to scratching. The crack seems to follow a more or less a horizontal (111) plane. It is then possible that the 2H phase occurred during the scratching procedure by the application of an uncontrolled shear stress. Shear stress is known to produce ribbons of 2H phase in both bulk Ge [86] and GeNWs [103]. However, inducing a phase transition through shear stress alone seems to be unlikely. On the one hand, the Vickers indentation technique used in [86] is coupled

with a heating of the Ge samples at a temperature between 330 °C and 360 °C, while we handle samples at room temperature here. On the other hand, Vincent *et al.* [103] molded VLS-grown Au-catalyzed GeNWs in a hydrogen silesquioxane (HSQ) matrix and thermally baked the whole sample at a temperature range from room temperature to 500 °C. A threshold temperature of around 350 °C was found for the transition from cubic to hexagonal phase to occur. Another study involving the indentation technique at room temperature failed to reproduce an eventual phase transition to bulk 2H Ge [241]; the indentation only resulted in the formation of several twin planes. In conclusion, it seems that only shear stress coupled with high temperature can lead to a phase transition.

Shear stress at room temperature may thus manifest itself by multiple twinning. Figure 6.1a shows several twin planes perpendicular to the growth axis. Figure 6.1b exhibits a faulted cubic section which also displays twinning. GeNWs grown by CVD and catalyzed by Au do not usually present twinning when they were grown in NanoMAX. Only a few wires grown in Plasfil and then transferred to a Cu TEM grid by scratching displayed this kind of stacking faults. It is possible that these defects are the result of a cohesive displacement of Ge atoms. This is supported by the relative proximity of twin planes with the fracture plane created by the scratching. Dahmen *et al.* [94] proposed that polytype 2H could appear when multiple twin planes intersect each other. The resulting strain is accommodated by a martensitic phase transition from cubic to hexagonal. This explanation was used to describe how polytype 2H could appear in Si ingots following indentation [93]. In our nanowires, this is unlikely as all the TEM observed twin planes are parallel to each other.

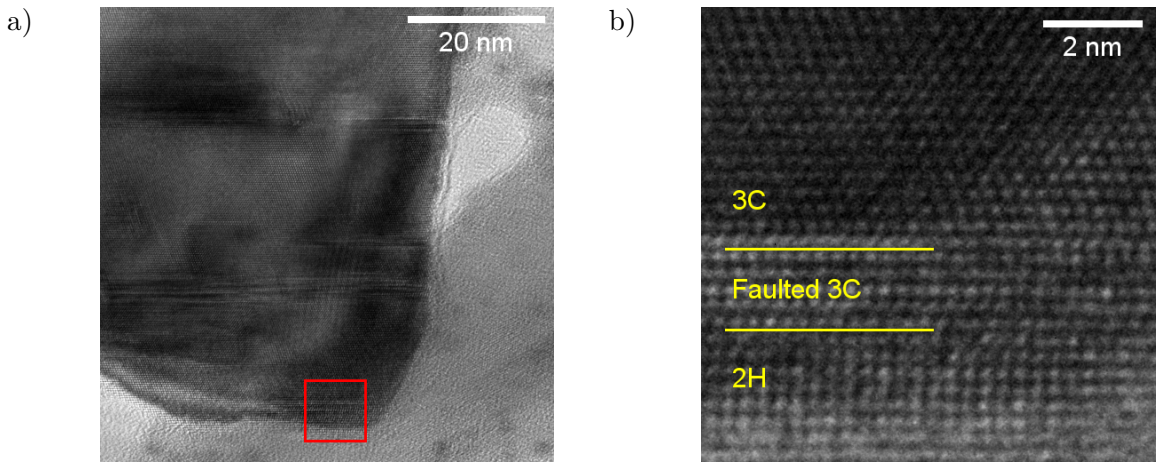

FIGURE 6.1: Realization of a GeNW presenting a 2H-phase region. a) Low magnification view. b) Close-up view of the red squared area.

In addition, if the 2H section was produced by any of the above-mentioned shear-based mechanisms, we do not expect that the boundary between the hexagonal and cubic domains be a simple $\{111\}_C/\{0001\}_H$ surface but rather a $\{115\}$ surface as found in several other studies [86, 103, 93, 104]. Thus, we can rule out the 2H phase produced by scratching-induced shear stress hypothesis.

The 2H section at the bottom of the GeNW of Figure 6.1 could have appeared during the PECVD growth. If this would be the case, this would show that the *ab initio* calculations, which state that polytype 2H becomes the energetically favored phase for GeNWs when the diameter is below 2 nm [242], could be incomplete or some hypothesis were unverified. When the effect of hydrogen atoms is considered in the calculations, the critical diameter jumps to 5 nm. The

visible 2H section of the GeNW of Figure 6.1 is more than 15-nm large in diameter. Thus, it seems that there exists an additional parameter excluding surface energies and hydrogen atoms effect that would increase the critical diameter to more than 15 nm. It remains unclear what this parameter could be. Furthermore, we have been unable to reproduce this result.

6.1.2 *In situ* synthesis of the 2H phase in SiNWs

Polytype 2H is more easily obtainable in SiNWs as we successfully grew them in both the *in situ* TEM NanoMAX and the Plasfil reactor. In this section, we will describe some of the characteristics of these SiNWs.

Some of the SiNWs which were in the $[110]_C/[12\bar{1}0]_H$ zone axis had the 2H phase. It seems that the $\langle 0001\rangle_H$ growth direction is the most favorable as all observed 2H SiNWs had this orientation. An example of a 2H SiNW of diameter around 5 nm grown with a majority-Cu catalyst is shown in Figure 6.2a. It was grown at 380 °C, at a SiH_4 partial pressure of 2×10^{-2} mbar, a H_2 partial pressure of 5×10^{-2} mbar and a plasma power of 50 W. The shape of the catalyst in the inset shows that the epitaxial relationship between the nanowire and the catalyst is most likely $\langle 0001\rangle_{Si} || \langle 0001\rangle_{Cu_3Si}$. The longest non-faulted 2H section spans 40 $\{0002\}_H$ planes. On the base of the nanowire, some cubic sections can be observed which means that the wire has gone through several phase transitions over the course of its growth. The Fast Fourier Transform (FFT) of the 2H section has a pattern consistent with the simulated electron diffraction of 2H Si (shown in Figure 2.9e, in Chapter 2), giving an unambiguous proof of the presence of this metastable phase in our nanowires (Figure 6.2b).

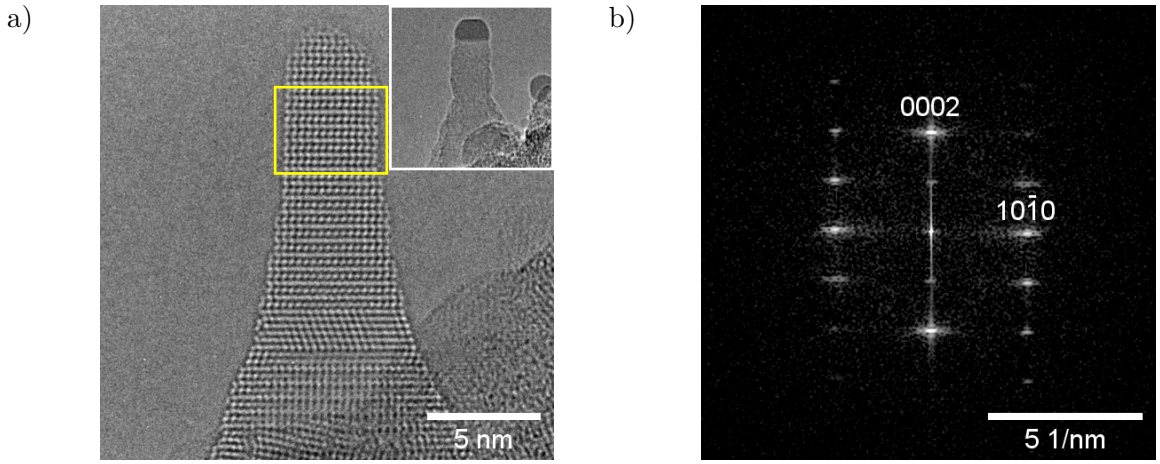

FIGURE 6.2: Diamond hexagonal SiNWs with a majority-Cu catalyst grown on the SiC membrane. a) HRTEM image of a 2H SiNW. Inset shows the same NW before it lost its catalyst. b) FFT of the highlighted area in a).

An interesting characteristic of the top 2H section is that the diameter of the nanowire is nearly constant, with very little tapering. This contrasts with the 3C sections, or other 3C nanowires that grew in the $\langle 111\rangle_C$ direction with majority-Cu catalysts where tapering always occurs. As discussed previously in majority-Cu catalysts, tapering is most likely due to electron-beam-activated Cu migration. Tapering in $\langle 111\rangle_C$ cubic nanowires is an easy evolution because of the sawtooth faceting of sidewalls which consist in alternating $\{111\}_C$ and $\{113\}_C$ surfaces [219]. Depending on the catalyst leakage rate, the length ratio between $\{111\}_C$ and $\{113\}_C$ will

vary. For sufficiently high rate, $\{113\}_C$ no longer appears only leaving $\{111\}_C$ surfaces. It can clearly be seen near the top 2H section of the nanowire (Figure 6.2a) that tapering proceeds by the introduction of individual atomic steps, as opposed to lateral $\{111\}_C$ facets in the 3C case. Considering that the angle between the top and lateral $\{111\}_C$ is 109°, we find that the 2H surface closest to make an angle of 109° with the top $\{0001\}_H$ is the $\{\bar{2}111\}_H$ surface. Contrary to the flat lateral $\{111\}_C$, this surface is atomically rough which may explain why tapering occurs in a different fashion between the two structures as surfaces with this characteristic generally have a higher energy.

From the HRTEM image of Figure 6.2a, we can extract information on the cross-section of a 2H SiNWs. Figure 6.3a is a close-up view of the yellow rectangle in Figure 6.2a. In this image, more details on the atomic positions can be obtained. What is of particular interest is the evolution of the contrast of each atomic column across the nanowire width. This should depend on the thickness of the nanowire at that point and some dynamical effects due to possible multiple interactions between the electrons of the incident beam and the nanowire itself. By using HRTEM image simulations that were first presented in Section 2.3.3, we can propose different nanowire cross-sections, simulate their corresponding image, and compare them with the experimental image. We start with a nanowire that has a hexagonal cross-section with six $\{10\bar{1}0\}_H$ lateral facets as shown in Figure 6.3d. A simulated HRTEM image is proposed in Figure 6.3b. The simulated image resembles the experimental HRTEM one of the 2H nanowire. Both images show the characteristic square-like lattice of polytype 2H when viewed along the $[11\bar{2}0]_H$ zone axis. Notably, the Si dimers are imaged as dumbbells as shown in Figure 2.11. The second proposed structure is shown in Figure 6.3e. It is a nanowire that has an octagonal section with six $\{10\bar{1}0\}_H$ and two $\{11\bar{2}0\}_H$ facets. Its simulated image is shown in Figure 6.3c. Aside from the different faceting, the two proposed configurations differ in the evolution of the thickness along the nanowire width. On the one hand, the hexagonal configuration has a thickness that first increases until the middle of the wire and then decreases. On the other, the octagonal one has a homogeneous thickness. From the experimental and the two simulated images, we can compare the gray level profile along the nanowire. This is shown in Figure 6.3f. We see that the hexagonal profile diverges from the experimental one in the wire middle while the octagonal profile follows it more closely. The dip in gray level is due to the increased thickness in the middle. Consequently, it is very likely that the observed wire in Figure 6.2 has a constant thickness and an octagonal section.

The fact that an octagonal cross-section is chosen is very surprising. Indeed, we have shown earlier the surface hierarchy for the 2H polytype. $\{10\bar{1}0\}$ has the lowest energy so one would expect that the cross-section be hexagonal with only $\{10\bar{1}0\}$ surfaces. Instead, the simulation suggests that there are both $\{10\bar{1}0\}$ and $\{11\bar{2}0\}$ surfaces in this 2H SiNW. This discrepancy can be explained by considering that there is atomic hydrogen on the SiNW sidewalls. The surface energies shown in Table 6.1 are only valid for bare surfaces. We have shown previously that the presence of hydrogen adatom can modify surface energies. If the modifications in surface energies reduce the energy difference or even invert the hierarchy between the $\{10\bar{1}0\}$ and $\{11\bar{2}0\}$ surfaces, it can become more favorable to display those two surfaces in an octagonal cross-section. DFT calculations on hydrogen saturated surfaces shows that this is the case [140], with $\gamma_{10\bar{1}0} = 0.0043\,\text{eV}\cdot\text{Å}^{-2}$ and $\gamma_{11\bar{2}0} = 0.0041\,\text{eV}\cdot\text{Å}^{-2}$.

Given that all SiNWs that presented the polytype 2H grew along the $\langle 111\rangle_C/\langle 0001\rangle_H$ direction, it should be the direction that minimizes overall energy under the chosen conditions. It should be noted that in the surface hierarchy of the hexagonal diamond structure, the $\{0001\}$ surfaces have the lowest energy, see Table 6.1. We expect that if a hypothetical 2H wire is

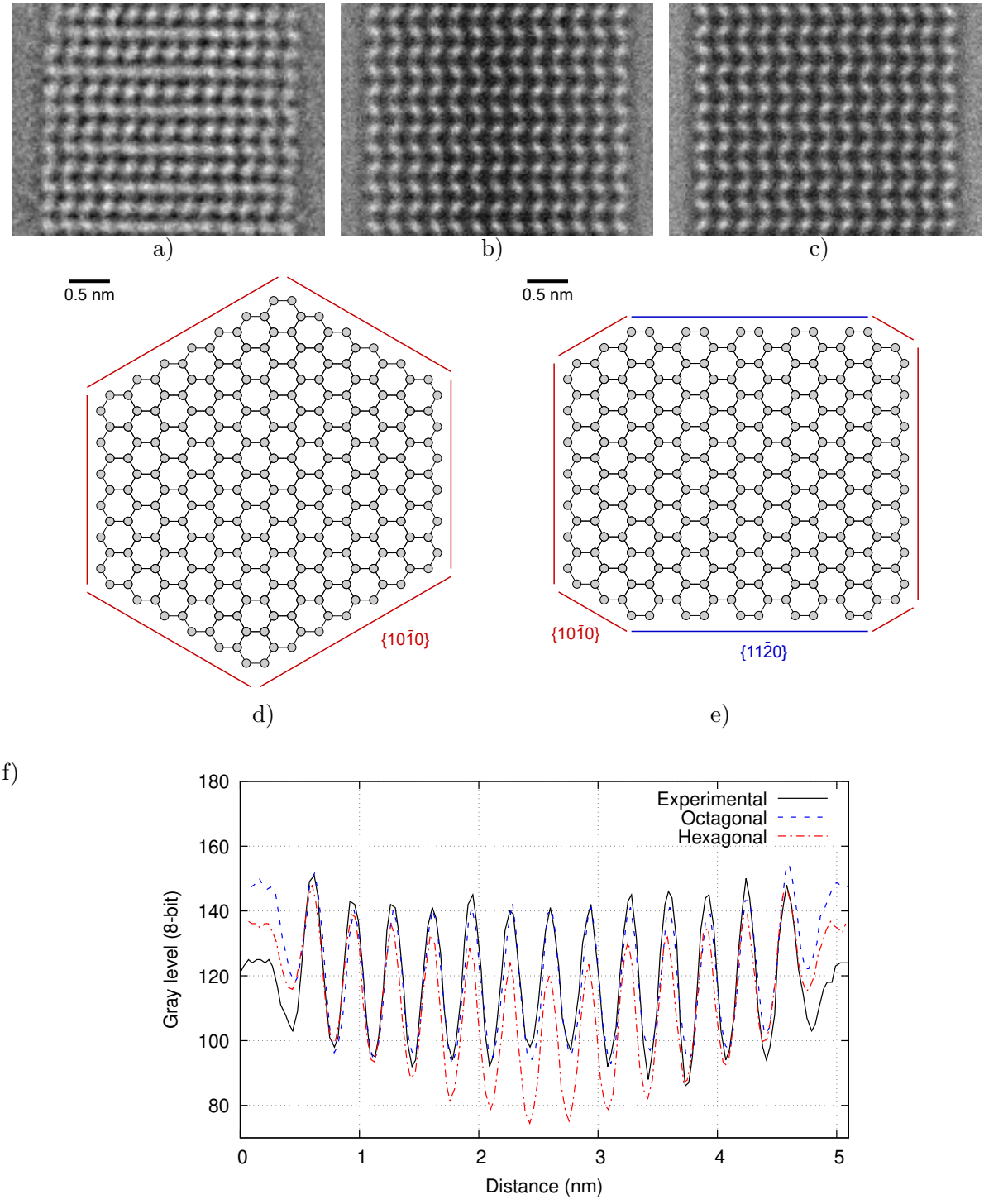

FIGURE 6.3: Simulation of the 2H nanowire cross-section. a) Close-up view of the yellow rectangle in Figure 6.2a. b) Simulated HRTEM image of the nanowire with a hexagonal cross-section in d). c) Simulated HRTEM image of the nanowire with an octagonal cross-section in e). d)-e) Top view of the two simulated configurations. f) Gray level profile along the nanowire width for the experimental image and the two simulated ones. Profiles are aligned so that their relative variation is more visible.

TABLE 6.1: Free surface energies in both 2H and 3C Si crystals calculated by DFT, accounting for eventual reconstructions and relaxations. Table extracted from [140].

Surface	3C ($eV \cdot Å^{-2}$)	2H ($eV \cdot Å^{-2}$)
$\{111\}_C/\{0001\}_H$	0.091	0.099
$\{110\}_C/\{11\bar{2}0\}_H$	0.106	0.091
$\{113\}_C/\{11\bar{2}2\}_H$	0.115	
$\{112\}_C/\{10\bar{1}0\}_H$	0.098	0.082

$\langle 112\rangle_C/\langle 10\bar{1}0\rangle_H$ oriented, some of the lateral facets should be of type $\{0001\}_H$. However, due to the two-fold symmetry of the $\langle 10\bar{1}0\rangle_H$ axis, there must be additional facets. One likely candidate is $\{11\bar{2}2\}_H$ which is analogous to the $\{113\}_C$ surface. The inclusion of this facet may make the $\langle 112\rangle_C/\langle 10\bar{1}0\rangle_H$ orientation unstable in the tested temperature range (380 °C to 800 °C), radical species concentration and both H_2 and SiH_4 partial pressure.

Because the previous experiments concerning the formation of polytype 2H were carried out in PECVD reactors without atomic characterization tools [110, 243], doubts remain on whether 2H is formed during the SiNW growth or after by cooling or by some form of strain relaxation. Thanks to *in situ* characterization capabilities of NanoMAX, we can clearly observe that the hexagonal phase in SiNWs is produced by the catalyst itself during the growth. This confirms experimentally that the 2H phase can develop preferentially over the 3C phase in specific growth conditions, which we will show later. Otherwise, it can only be metastable. However, it should be noted that most of the observed SiNWs which had a 2H section also contained a standard 3C phase. Thus, the advantage provided by nucleating the hexagonal structure instead of the cubic one seems to be rather small.

6.1.3 General stability of the 2H phase in SiNWs

As the hexagonal diamond phase is metastable, we then tested its stability during high temperature annealing on the nanowire of 6.2. In order to carry on this experiment, we have switched off the SiH_4, with the H_2 partial pressure set to 5×10^{-2} mbar and the plasma operating at a power of 50 W. From the initial growth temperature of 380 °C, the substrate is heated from 400 °C to 650 °C in steps of 50 °C with a plateau time of one minute each. Quite interestingly, during the first stages of the anneal, both the hexagonal and cubic sections gained width by epitaxial deposition of Si on the sidewalls. It is possible that in the presence of H radicals, Si from the plasma chamber walls is etched away and then redeposits on the sample [244], a process known as chemical transport. As the substrate temperature is increased, there were no visible changes on the SiNW: we did not observe any temperature-induced modifications of the crystalline structure. Cubic sections remained cubic while hexagonal sections retained their arrangement. The lack of transition at high temperature can be linked to its martensitic nature [93]. It requires a cohesive displacement of atoms which can be achieved by stress application.

Finally, Si from the NW itself started to be etched from 650 °C under the combined action of the electron beam and the hydrogen radicals through *in situ* annealing as shown in Figure 6.4. The substrate temperature of 650 °C is reached at 0 s. The etching starts from the thinner top of the SiNW and continues on the thicker base. Both polytype 2H and 3C are etched. If we had conducted the annealing without atomic hydrogen, the nanowire might have sustained even higher temperatures. We thus find that this metastable phase is able to sustain relatively

high temperatures, consistent with a previous study [110].

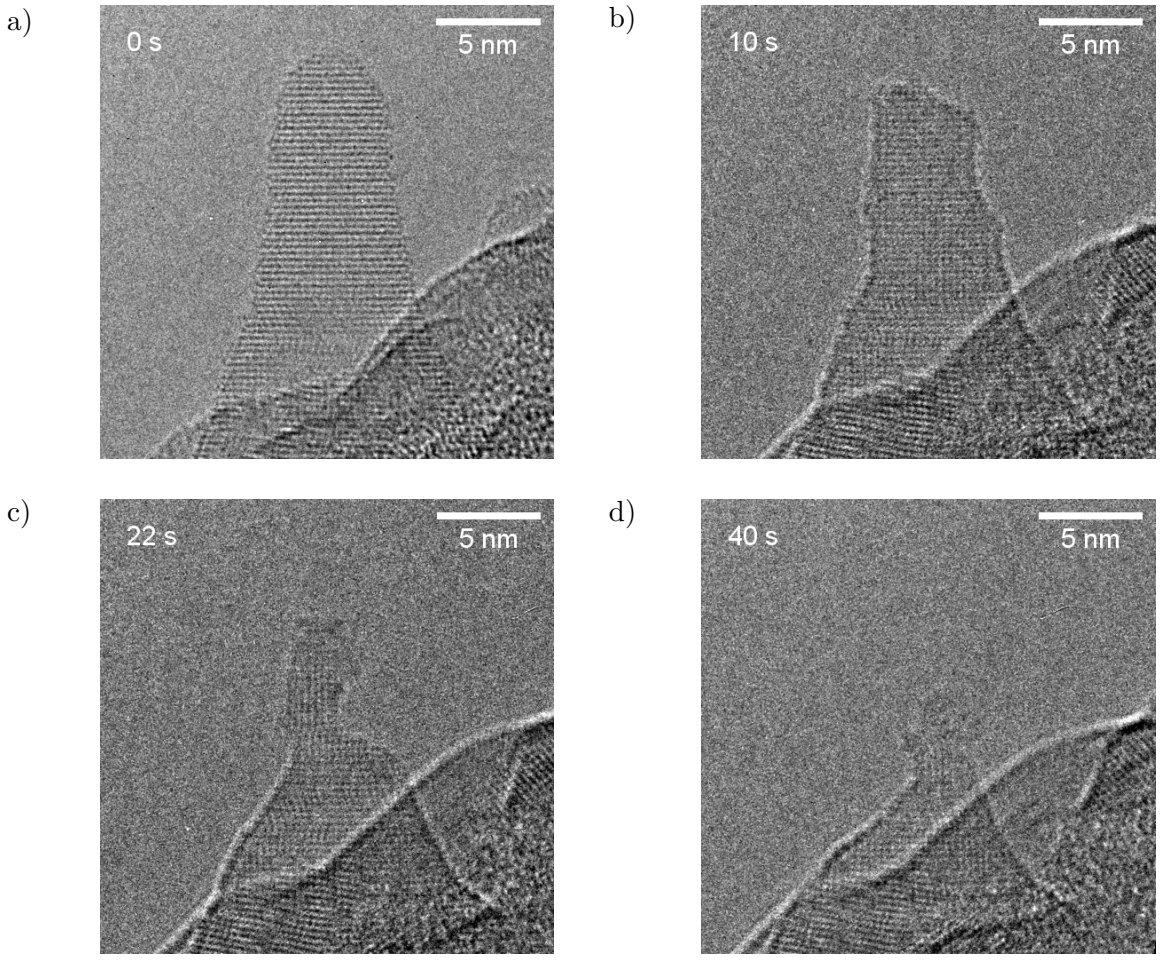

FIGURE 6.4: Etching of the SiNW of Figure 6.2 through the application of plasma conditions delivering hydrogen atoms at high temperature. The substrate reaches 650 °C at 0 s.

6.1.4 Scarcity of polytype 2H in SiNWs

While polytype 2H was observed in our SiNWs, it remains an uncommon occurrence. By only considering wires that grew in the $\langle 111\rangle_C/\langle 0001\rangle_H$ direction and which had the correct $[110]_C/[11\bar{2}0]_H$ zone axis for us to clearly distinguish between the cubic and the hexagonal structures, we obtain a ratio of hexagonal wires over cubic ones that ranges from 6 % to 40 %. All the growth experiments that involved CuSn double catalysts are summarized in Table 6.2. Let us recall that while the plasma power and H_2 partial pressure are initially kept constant and at the same value for both the SiC membrane and the Si cantilever, the SiH_4 partial pressure and temperature could change between the two types of substrate. In particular, the temperature influences the average diameter of the deposited catalytic seeds by promoting coalescence. SiNWs on the Si cantilever thus have larger diameter compared to ones on the SiC membrane. One can notice that wires in the correct zone axis are more numerous on the Si cantilever. This is because growth is generally epitaxial on this substrate that exhibits {111} surfaces. No fastidious sample tilting is required contrary to the SiC membrane.

Overall, for the growth experiments that used CuSn catalysts, 20 different SiNWs presented

the 2H structure over 150 which were both growing along $\langle 111\rangle_C/\langle 0001\rangle_H$ and in the right zone axis, which gives a total ratio of 13 %.

TABLE 6.2: Yield of SiNWs with a 2H section among those grown in NanoMAX with CuSn catalysts. In each experiment, the yield is given with respect to the total number of wires analyzed (i.e. in the $[110]_C/[11\bar{2}0]_H$ zone).

Cu at. %	Sn at. %	Substrate	Wires in zone	2H wires	Ratio
100		SiC membrane	1		
82	18	SiC membrane	16	4	25 %
77	23	Si cantilever	10	0	0 %
69	31	SiC membrane	2	0	0 %
69	31	Si cantilever	21	2	10 %
65	35	SiC membrane	6	1	17 %
65	35	Si cantilever	22	7	32%
48	52	SiC membrane	5	0	0 %
48	52	Si cantilever	54	4	7 %
30	70	Si cantilever	5	2	40%
	100	SiC membrane	8	0	0 %

6.2 Phase switching between polytype 2H and 3C

Some of the wires showed both the 3C and the 2H phase, meaning that they switched phase during the growth. One such wire is shown in Figure 6.5a. It was grown at 380 °C on the SiC membrane with a majority-Cu catalyst. Its growth direction is $\langle 111\rangle_C/\langle 0001\rangle_H$ and it has an average diameter of 5 nm. The *in situ* data does not have atomic resolution, hence we cannot directly observe what phase is nucleated at a specific time in the data. However, a HRTEM micrograph was taken just after. By counting the number of nucleated planes during the video, we can deduce both: (i) at what plane the *in situ* data began and (ii) know what phase nucleated at any time stamp. The yellow line in Figure 6.5a indicates where the recording starts.

On the *in situ* data of this nanowire, the 2H phase nucleated first until the 170 seconds mark. Then, there was a phase transition from 2H to 3C, and the wire stayed in 3C for the rest of the video. At the transition, shown in Figure 6.5b-c, the catalyst has visibly changed shape. This shows that there are some modifications of surface energies in the vicinity of the triple-phase boundary. It is important to note here that the observed phase transition was spontaneous: the growth conditions did not change at all. To better understand its evolution over the transition, we plotted the value of the contact angle of the catalyst particle β (defined in Figure 3.13) with the nanowire as a function of growth time. The results are shown in Figure 6.5d. In this plot, the phase transition is represented by a change of color of the curve. There is a clear variation of the contact angle through the transition: when the nucleated phase is 3C, the average contact angle is 111°; when the nucleated phase is 2H, the average is 99°.

The change in contact angle can be understood by considering that there exists an equilibrium of forces that pins the catalyst particle to the nanowires edge. If the nucleated phase changes, so do the interfacial surface energies between the solid nanowire and the other phases. As discussed before, surfaces in the cubic diamond are more energetic than those of the hexagonal diamond phase, see Table 6.1. That justifies the variation in contact angle observed. Theoreti-

cal models predicting a phase switch depending on the contact angle exists for III-V nanowires. They take into consideration some parameters such as the involved surface energies, the contact angle, tapering and the existence of surfaces wetted by catalysts [153, 154]. A relationship between these quantities and the formation energy of a new monolayer is derived. The grown phase will be the one that minimizes the formation energy. From this principle, three regimes are possible. Low contact angle favors a tapered nanowire with a zinc blende structure (cubic diamond). Intermediate values give a nanowire with perpendicular facets with a wurtzite structure (hexagonal diamond). High values yield a zinc blende nanowire with lateral facets that are partially wetted by the catalyst. Thus, the control of the contact angle allows to control which phase is nucleated. This has been demonstrated for III-V nanowires for both Au-catalyzed [151] and self-catalyzed growth [152] by modification of the III/V ratio of the gas flow.

The SiNW grown in NanoMAX (Figure 6.5) presents some of this behavior. The hexagonal section has perpendicular lateral facets while the cubic section at low contact angle is tapered. Thus, at first glance, we can expect from III-V models and experiments that the observed phase switch in Si could occur for the same reasons. However, their direct applicability to Si presents some conceptual problems. The III-V models assume that the catalyst is liquid. In Si, the catalyst is mostly solid Cu_3Si with possibly a pocket of liquid Sn which size will depend on the ratio of evaporated Sn compared to Cu. This means that there could be more interfacial energies involved and an additional contact angle to consider.

We now discuss why this phase transition occurred. The tapering of the nanowire is an important clue. It confirms that the catalyst is losing material during the growth [245]. The rate of tapering depends on the number of atoms lost per unit time, or loss rate. At the same time, before the transition, the equilibrium phase is the hexagonal diamond phase (due to the nanowire small diameter [140]), which tends to maintain vertical, $\{10\bar{1}0\}$ sidewalls parallel to the growth axis. As such, there is a competition between the tendency to create tapered sidewalls (and switch to 3C for this); and the tendency to keep those vertical sidewalls (and remain 2H). By losing volume, the catalyst particle will change shape and decrease its contact angle. This has a cost in energy. Once this cost becomes higher than that of creating a cubic/hexagonal phase interface, a phase transition to the cubic phase occurs, with the implied tapering.

Consequently, in order to have long 2H section in our small diameter nanowires, it is necessary to stop the catalyst from continuously losing atoms, avoiding frustration. Possible ways include increasing the partial pressure of SiH_4 to counterbalance the loss of Si, reducing temperature to reduce the desorption flux, lowering the energy of the electron beam to decrease the probability of Si knock-on. However, these would only slow-down the process. To stabilize the NW diameter, the only perennial solution is to maintain the Cu inside the catalyst: i.e. to stop its diffusion in the nanowire and/or at its surface. Volume diffusion should be limited by the very low solubility of Cu in Si. There remains surface diffusion. A means to stop it would be to saturate the surface sites by another element. Perhaps hydrogen would do it.

Another way would be to switch to another catalyst. The choice of the catalyst should influence the interface energy between itself, the vapor phase and the nanowire. Different catalysts indeed have different surface energies [25] which may change the critical angle of transitions. Furthermore, different catalysts have different eutectic temperatures when mixed with Si, which will influence its physical state, solid or liquid. For the present majority-Cu catalyst, we have shown that the metal in the catalyst is actually mostly Cu and in all of the temperature range that was achievable in our equipment, its state was solid. This leads us to mention yet another parameter, in the catalyst-NW equilibrium. That crystalline state should change surface energy

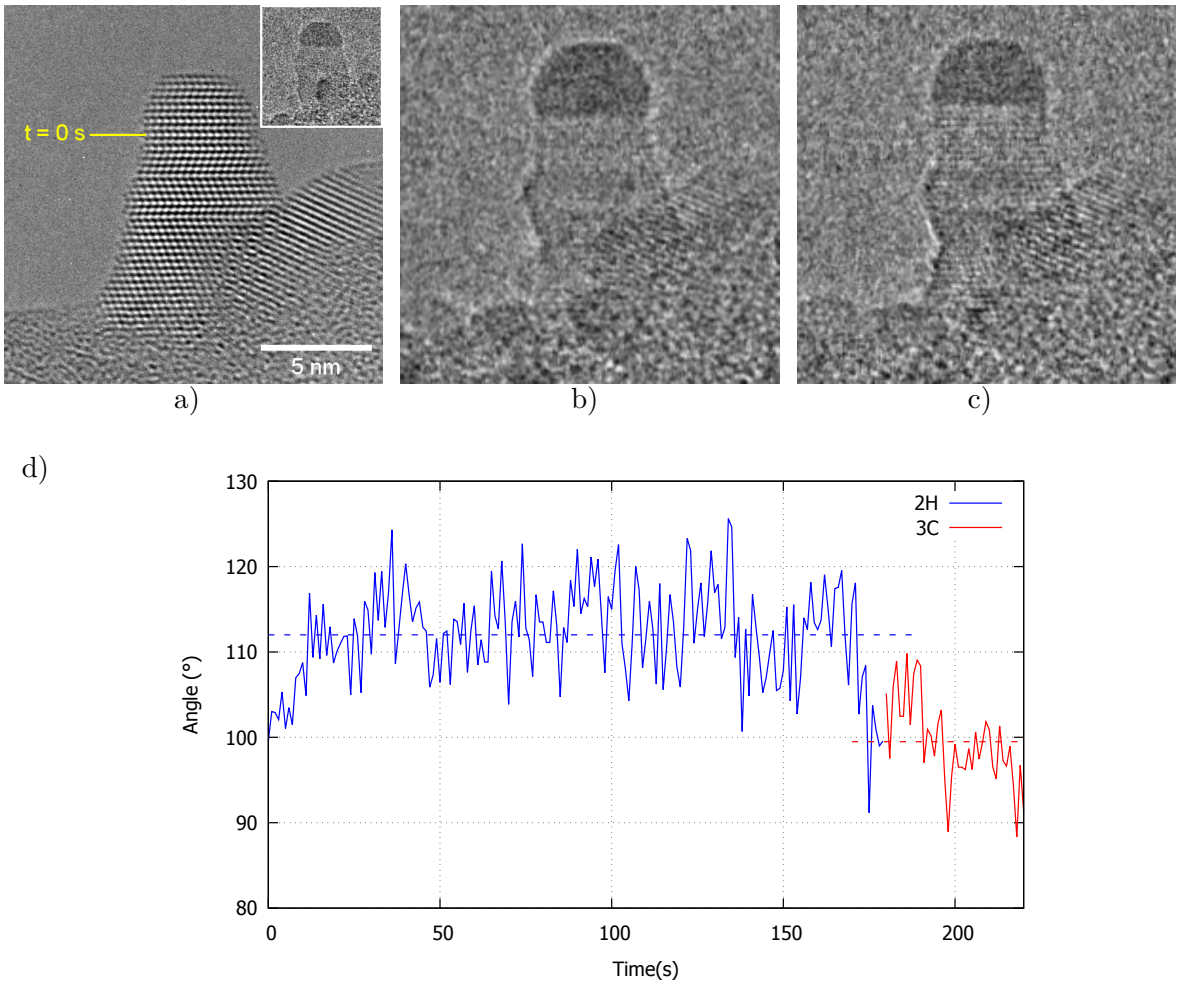

FIGURE 6.5: Phase transition from hexagonal diamond to cubic diamond. a) HRTEM image of a multi-phased SiNW after growth and after tilt in the zone axis. b) TEM image of the NW shown in a) just before the phase transition. c) TEM image of the same NW just after the phase transition. d) Evolution of the catalyst contact angle during the phase transition.

again and has also interesting consequences. Because the catalyst is solid, facets will naturally appear. This means that it may not be possible, for the catalyst particle, to vary its contact angle continuously, but rather to only take a set of discrete values. Additionally, we have seen in Section 5.4 for CuSn that, for the $\langle 111 \rangle$ growth direction, different epitaxial relationships were possible with the nanowire. Thus, the facet close to the triple-phase line may not always be the same, changing the equilibrium there. We then expect that some orientations would be more favorable for the stabilization of the 2H phase. To know which one would be the best, it would be necessary to precisely measure, through experiments or *ab initio* simulations, the relevant interface and surface energies in Cu_3Si.

6.3 Stability factors in nucleating the 2H phase

In this section, we investigate the possible factors that could contribute to the stabilization of polytype 2H in our SiNWs and increase the ratio of hexagonal wires over cubic shown in Table

6.2.

6.3.1 Diameter-dependent effect

It is worth noting that, with the CuSn-catalyzed growth, we have obtained SiNWs that had diameters from 5 nm to 60 nm. All of the identified 2H SiNWs had a small diameter below 10 nm. Tang *et al.* made a similar observation [110]. What this suggests is the existence of size effects concerning the stabilization of the 2H phase. *Ab initio* simulations [140] have shown that the contribution of surfaces to the Gibbs free energy stabilizes the 2H phase in small-diameter NWs (Section 1.5.2 and Table 6.2). They predicted the existence of a critical diameter where the stable phase changes. For Si, two values have been proposed: 6 nm [242] and 13 nm [140].

20 SiNWs with a diamond hexagonal section were observed to grow (Figure 6.6). Their diameters range from 4 nm to 8 nm with an average at 5.3 nm. This means that the critical diameter must not be far from 8 nm. 87 correctly oriented SiNWs with a diameter below 8 nm were synthesized in total over every growth session. If we only count SiNWs with a diameter below 8 nm, we find that the ratio of SiNWs that contain a 2H section over all those that have been characterized jumps up to 20 % compared to 9.5 % if diameter is not considered. This constitutes an experimental evidence on the role of nanowire diameter on the stabilization of polytype 2H in SiNWs. Thus, the equilibrium phase of our small diameter nanowires could be the hexagonal diamond phase. The above-described *ab initio* calculations, that do not take into account the kinetics of phase formation, are consistent with our growth experiments. If the 3C phase is still present, it could be due to an easier nucleation in most geometries. Only one in every five small-diameter SiNWs have the 2H phase, therefore, small diameter appears to be a necessary, but not sufficient, condition for polytype 2H formation.

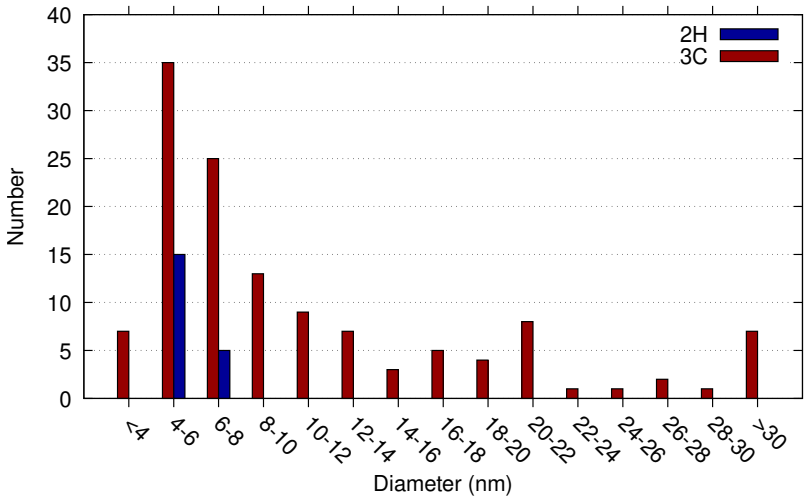

FIGURE 6.6: Number of ⟨111⟩-SiNWs observed in the $[110]_C/[11\bar{2}0]_H$ zone axis as a function of diameter and polytype.

Small diameter SiNWs are also more likely to contain one or more twin planes that their larger counterparts. In particular, those grown with majority-Sn catalyst showed a high density of twin planes perpendicular to the growth axis of ⟨111⟩ SiNWs as shown in Section 5.2.2. Twinning and other sorts of stacking faults generally require an energy input compared to a pristine structure. The cost in energy scales with the size of the faulted layer. In the case of a

twin plane in a Si crystal, the fault formation energy [246, 247] is $1.7\,\mathrm{meV}\cdot\mathrm{\AA}^{-2}$. For Si, polytype 2H and others can be considered as a faulted cubic diamond structure with periodically spaced twin planes. The number of $\{111\}_C/\{0001\}_H$ layers between successive twin planes determines the polytype nature. 2H for instance has a zero periodicity which means that all layers can be considered as twin planes. Thus, if the 2H phase is seen as a stacking of twin planes, then it is more likely to appear in small diameter nanowires because of the reduction of the energy cost of repeated twinning. Figure 6.7a shows a multi-twinned SiNW that also displays a short 2H section. While the wires' reduced size explains how twinning more easily occurs, it does not tell when it will occur. Indeed, other polytypes were observed during our experiments over small distances, such as the 10H structure spanning two periods shown in Figure 6.7b. For the catalytic seed to create these polytypes requires it to remember how many $\{111\}_C/\{0001\}_H$ planes it has created since the last twin plane. This suggests an involvement of some form of memory effect during the growth. Since nanowire growth is driven by the catalyst, it is possible that this memory effect originates from periodic fluctuations of some of its physical quantities such as Si atoms concentration in the catalyst or its contact angle with the nanowire. The period would determine which polytype is grown.

The fact that small nanowire diameter is an important factor for the stabilization of the 2H phase constitutes a conceptual challenge as current theoretical growth model which predict what will be the nucleated polytype do not consider the nanowire diameter as a relevant parameter [153, 154, 152]. In these models, only the balance between all the involved interfacial energies, excess chemical potential in precursors as well as the nanowire tapering angle are considered. The initial nucleus is unaware of the nanowire diameter. When applied to GaAs nanowires that can switch between the wurtzite (2H) and the zinc blende (3C) phase, these models predicting the stability domain of the wurtzite phase are in agreement with *in situ* data [151, 152]. However, given our observations, modifications in these models are required in order to explain the formation of the 2H phase in Si.

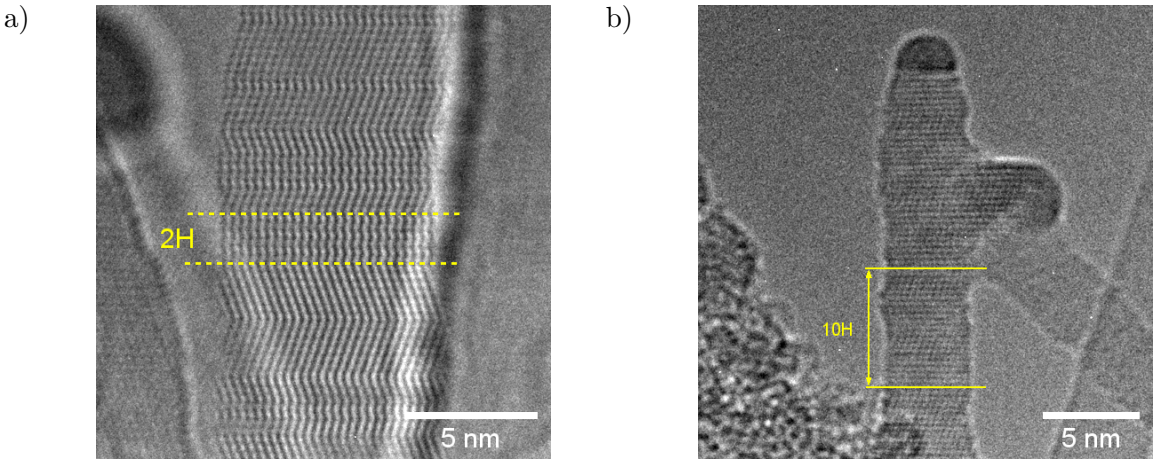

FIGURE 6.7: Twinning in small diameter CuSn-catalyzed SiNWs. a) Multi-twinned SiNW with a small 2H section. b) Formation of a 10H periodicity polytype in a SiNW grown with a majority-Sn catalyst.

6.3.2 Additional interface in biphasic catalyst

We have established that CuSn catalysts have two distinct phases: a solid Cu_3Si core and a Sn-rich liquid shell. Their respective sizes will depend on the deposited thickness Cu/Sn ratio during thermal evaporation. We have found that both phases are in contact with the growing nanowire. The coexistence of two different phases implies that there exists an interface inside the catalyst. Such an interface may play a role in the stabilization of polytype 2H as pure Sn did not yield a single 2H wire.

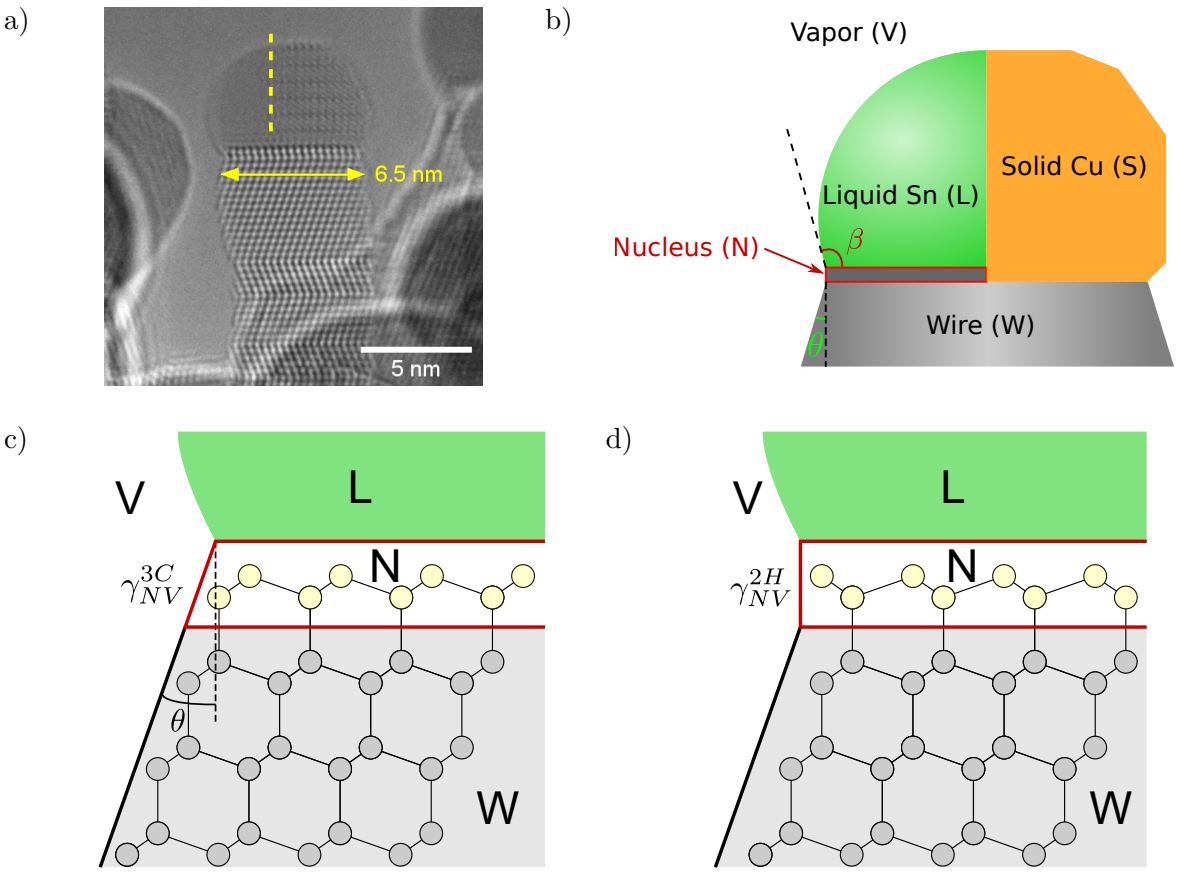

FIGURE 6.8: Schematic representing the nucleation of a new monolayer in a SiNW with a biphasic CuSn catalyst. a) Existence of an interface in small diameter SiNWs catalyzed by CuSn. b) Representation of the different phases and interfaces involved. c) Nucleus atoms positions (in yellow) for a 3C stacking with $\theta = -19.5°$. d) Same as c) but for a 2H stacking with $\theta = 0°$.

In situ evidence shown in Section 5.5.2 indicates that the nucleation of a new Si monolayer for a SiNW growing along $\langle 111 \rangle_C / \langle 0001 \rangle_H$ occurs in the liquid Sn-rich side. That can be explained by supersaturation first being reached in liquid Sn due to its low Si solubility. A schematic representation of the nanowire state is shown in Figure 6.8b. The Sn-rich liquid is denoted L while S is the Cu_3Si solid part. W is the SiNW itself and N is the initial Si nucleus of the newly forming monolayer. V designates the vapor phase containing SiH_4, H_2 and radical species created by the plasma. The nucleus N is assumed to appear close to one of the two quadruple points, separating the vapor, liquid, solid catalyst and solid nanowire; as that should minimize the length of newly created interfaces. Let h be the height of the monolayer. In Si, h is a multiple of the {111} spacing: $h = nd_{111}$ where $d_{111} = 3.14\,\text{Å}$. In CuSn growth, n is found to

be 1 or 2. S_{top} is the surface of the interface between the nucleus and the nanowire. S_{side} is the sum of the surfaces defined by the lateral edges of the nucleus. The formation of this nucleus has an energy cost ΔG^k that has a negative part that is due to the reduction of the excess Si chemical potential following the precipitation. The positive part rises from the creation of new interfaces or the replacement of existing ones by others of different nature. Thus, by modifying the model developed in [153], we have:

$$\begin{aligned}\Delta G^k = &- hS_{top}\Delta\mu + S_{side}[(1-\lambda-\sigma)\gamma_{NL} + \lambda(\gamma^k_{NV} - \gamma_{LV}\sin\beta) + \sigma(\gamma^k_{NS} - \gamma_{LS})] \\ &+ S_{top}(\gamma^k_{WN} + \gamma_{NL} - \gamma_{WL})\end{aligned} \tag{6.1}$$

where $\Delta\mu$ is the excess in Si chemical potential, γ_{ij} is the interfacial energy between phase i and j, β is the contact angle of the liquid Sn-rich phase with the SiNW, λ is the fraction of S_{side} which is in contact with the vapor phase and σ is its counterpart with the solid Cu_3Si. Some interfacial energies can vary depending on how the atoms of the nucleus are positioned with respect to the atoms of the top SiNW layer, see Figure 6.8c. This determines if a twin plane is created or not. γ^k_{ij} is thus the interfacial energy if the atoms of the nucleus are in position k, with $k = 2\text{H}$ or 3C. γ^k_{WN} is the interfacial energy between the nanowire and the newly nucleating monolayer. We expect that $\gamma^{3C}_{WN} = 0$ since this configuration is the continuation of the standard stacking while γ^{2H}_{WN} is simply the twinning energy with a value of $1.7\,\text{meV}\cdot\text{Å}^{-2}$. γ_{NL} and γ_{WL} are assumed to cancel out each other as both interfaces are identical. If we compare the energy cost between the 2H and 3C configurations, we find that:

$$\Delta G^{2H} - \Delta G^{3C} = S_{side}[\lambda(\gamma^{2H}_{NV} - \gamma^{3V}_{NV}) + \sigma(\gamma^{2H}_{NS} - \gamma^{3C}_{NS})] + S_{top}\gamma^{2H}_{WN} \tag{6.2}$$

Thus, the polytype 2H is preferred if the condition:

$$\lambda(\gamma^{3C}_{NV} - \gamma^{2H}_{NV}) + \sigma(\gamma^{3C}_{NS} - \gamma^{2H}_{NS}) > \frac{S_{top}}{S_{side}}\gamma^{2H}_{WN} \tag{6.3}$$

is satisfied.

Let us examine the left-hand side of Equation (6.3). $\gamma^{2H}_{NV} = 82\,\text{meV}\cdot\text{Å}^{-2}$ is simply the $\{10\bar{1}0\}_H$ surface energy [140] (Figure 6.8d). γ^{3C}_{NV}, on the other hand, is more complicated to quantify as a continuous 3C stacking prolongs a tilted surface exposed to the vapor (Figure 6.8c). Glas *et al.* [153] derived its expression as such:

$$\gamma^{3C}_{NV} = \frac{\gamma_{111}}{\cos\theta} + (\gamma_{LW} + \gamma_{LV}\cos\beta)\sin\theta \tag{6.4}$$

where $\gamma_{111} = 91\,\text{meV}\cdot\text{Å}^{-2}$ is the $\{111\}$ free surface energy. γ_{LW} is the interfacial energy between liquid Sn and the SiNW top $\{111\}$ surface. A crude way to estimate it for our growth conditions is to measure the contact angle β for a pure-Sn catalyst during steady growth. We find that $\gamma_{LW} = 44\,\text{meV}\cdot\text{Å}^{-2}$ for a contact angle $\beta = 112°$ on the nanowire of Figure 6.10. $\gamma_{LV} = 36\,\text{meV}\cdot\text{Å}^{-2}$ is the surface tension of liquid Sn [42]. $\theta = -19.5°$ is the angle between the normal to the top $\{111\}$ surface and the lateral $\{111\}$ facet. This angle is characteristic of the crystalline structure of Si.

Consider the growth of SiNWs with pure-Sn catalysts. Equation (6.3) becomes:

$$\lambda(\gamma^{3C}_{NV} - \gamma^{2H}_{NV}) > \frac{S_{top}}{S_{side}}\gamma^{2H}_{WN} \tag{6.5}$$

Taking β in a range from 60° to 150°, we find that γ^{3C}_{NV} takes value from $75\,\text{meV}\cdot\text{Å}^{-2}$ up to $92\,\text{meV}\cdot\text{Å}^{-2}$. The left-hand side of Equation (6.5) is shown in Figure 6.9. Assuming the

S_{top}/S_{side} ratio to be equal to 1, which corresponds to situations where the nucleus size is small (few atoms long), the 2H phase becomes favorable for energy differences $\lambda(\gamma_{NV}^{3C} - \gamma_{NV}^{2H}) > 1.7\,\text{meV} \cdot \text{Å}^{-2}$ (black horizontal line in Figure 6.9). If the opposite is true, then the 3C phase will become the most favorable polytype. Depending on the value of λ, i.e. the fraction of the nucleus that is in contact with the vapor, the threshold contact angle when the preferable phase switches go from 100° to more than 150°. Thus, at first glance, polytype 2H is possible with Sn-catalysts. However, only a small fraction of the nucleus is in contact with the vapor phase $\lambda \sim 0.3$. Consequently, polytype 2H can only occur for high values of contact angle $\beta > 120°$ which we never observed during our *in situ* growth. It is suspected that the surface tension of Sn is too low to achieve this low wetting level. In this case, polytype 2H is unlikely to happen in pure-Sn growth.

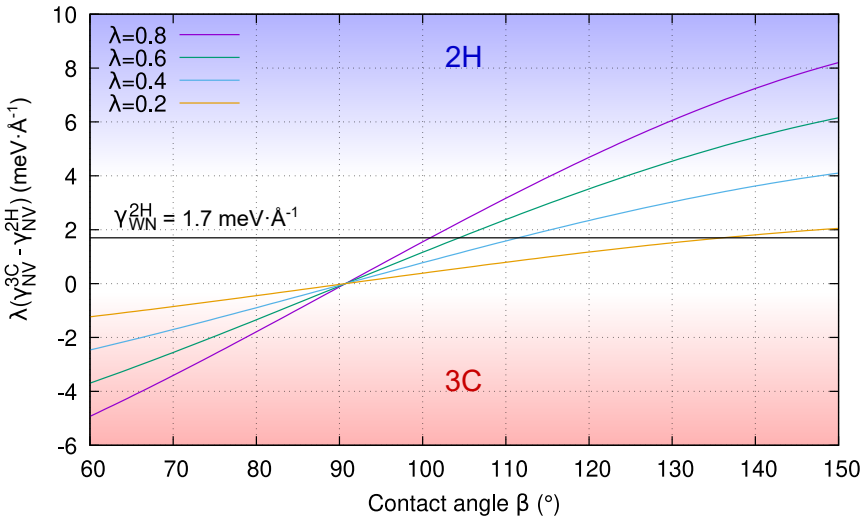

FIGURE 6.9: Evolution of the energy difference between the lateral facets in polytype 3C and 2H as a function of the liquid Sn droplet contact angle β for different values of the parameter λ.

By growing with CuSn biphasic catalysts, i.e. by introducing this additional interface, it might be possible that the balance of energy becomes in favor of polytype 2H if we have at least $\gamma_{NS}^{3C} > \gamma_{NS}^{2H}$ and if the nucleus has a shape that maximizes the one in contact with Cu_3Si. γ_{NS}^{3C} and γ_{NS}^{2H} are not known but they cannot be equal due to the different orientation of the nucleus terminating Si dimer (rightmost Si dimer in Figure 6.8c-d) in position 2H and 3C, especially if the Si nucleus is more than one monolayer high. If the new layer has nucleated in position 3C, then the interface between the nucleus and solid Cu_3Si will be tilted. The stacking along this interface would be $\{111\}_{Si}/\{10\bar{1}1\}_{Cu_3Si}$. This will not be the case in position 2H where the interface will be perpendicular to the SiNW top {111} surface. On this occasion, the stacking would be $\{10\bar{1}0\}_{Si}/\{10\bar{1}0\}_{Cu_3Si}$. For polytype 2H to be preferred, the latter must at least be of lower energy than the former.

This model relies on the assumption that the catalyst-nanowire interface is planar, and that the nucleus size is large enough to reach the Sn-Cu_3Si interface. Thus, it does not hold in large diameter SiNWs, where the interface is not planar due to the existence of truncated facets. However, it does hold in small SiNWs, where we found no truncated facets. Nuclei size in Sn are difficult to measure due to fast step velocity in liquid catalysts. In Cu_3Si, Figure 5.21 shows that it is around 1 nm. If we assume this nucleus size in liquid Sn, reaching the Sn-Cu_3Si liquid-solid interface becomes possible as soon as the interface is close enough to one edge of the SiNW. We

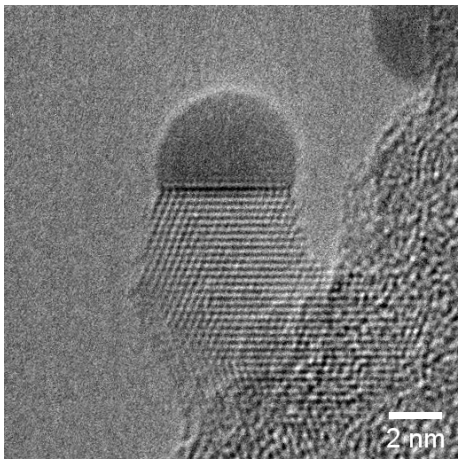

FIGURE 6.10: Estimation of γ_{LS} for a pure-Sn catalyst sitting on a growing $\langle 111 \rangle$ SiNW.

expect that the interface position can be partially controlled by tuning the Cu/Sn deposition ratio in favor of Cu, though the correlation between more Cu and higher 2H yield is not very clear in Table 6.2. In a small diameter SiNW, the maximum distance between nanowire edges and the Sn-Cu_3Si interface is reduced, which should increase the likelihood of a Si nucleus reaching the interface and the 2H proportion. The fact that a precise positioning of the nucleus plays such a great role, however, should explain why, even in small diameter SiNWs, the polytype 2H is not always present. Another assumption of this model is that the Sn-Cu_3Si interface exists at all diameters, which we only managed to confirm on small diameter SiNWs above 6 nm (Figure 6.8a) in diameter. Observation of a biphasic catalyst for smaller nanowire are difficult as those are the most unstable under the electron beam.

6.3.3 Chemical composition of the catalyst and supersaturation

The chemical composition of the catalyst used to grow SiNWs has an influence on nucleation. We are now going to discuss how the catalyst choice can help or not the nucleation of polytype 2H. First, if a small diameter of the SiNW is a necessary condition, then the chosen catalyst must be able to grow SiNWs with such sizes. In other words, the seeds should preserve their small sizes during the growth. Au droplets for instance are difficult to work with due to their tendency to coalesce together during the annealing phase prior to the growth. Thus, the SiNWs we obtained with this catalyst, described in Chapter 4, have a 30-nm average diameter for a total Au deposited thickness of 1 nm, far from the 7 nm critical diameter.

Given the considerations described in Section 6.3.2, the liquid catalyst choice will directly influence the interfacial energies γ_{LS} and γ_{LV}. Sn for instance has a low surface tension γ_{LV} when compared with other metal catalyst like Au and Cu. A higher surface tension should decrease the likelihood of obtaining polytype 2H as that would decrease the interfacial energy between the Si nucleus in position 3C and the vapor phase as described by Equation (6.4). In that case, the energy reduction of having an interface between the catalyst solid part and a 2H nucleus instead of that same interface but with a 3C nucleus would need to be higher. In addition, some catalysts like Sn have a tendency to unpin or leak from the nanowire tip even with the plasma on. This can result into a nanowire with a tapered geometry that is unfavorable for polytype 2H or the formation of a wetting layer. This wetting layer will change the surface

energies γ_{NV} involved in Equation (6.3). Fluctuations in the catalyst leakage rate will affect the coverage of the lateral walls by the wetting layer. It was also observed that the liquid and solid parts of the catalyst could swap positions over time. Contact angle variations can be expected during such movement. If fluctuations in catalyst leakage rate and contact angle are large enough, it might be possible that the favored phase switch repeatedly between 3C and 2H. This could explain why most 2H wires also have a 3C section.

The formation of polytype 2H in Section 6.3.2 should be easier if part of the initial nucleus is adjacent to the interface separating the liquid and solid part of the catalyst. Because the nucleation occurs at the triple phase boundary on the liquid part of the catalyst, large nuclei are important. According to nucleation theory, decreasing supersaturation should increase the size of the initial nucleus but at the cost of a higher nucleus formation energy. In Section 1.5.3, we have defined the supersaturation $s = c/c_{eq}$ as the ratio between the Si concentration in the catalyst and the equilibrium Si concentration. The latter is linked to the Si solubility. Consequently, catalysts like Sn, In or Ga with a low Si solubility can be problematic. Conversely, Au and Ag with their higher Si solubilities seem to be better suited. However, experiments seem to indicate that the supersaturation factor is secondary. Other studies successfully synthesized small diameter Au-catalyzed SiNWs through VLS and carried out TEM structural characterization. While they obtained SiNWs with diameters below 5 nm, they did not report the formation of wires with 2H sections [138].

The metals chosen as catalysts will also determine the growth temperature. It is preferable for the two chosen metals to have very different eutectic temperature. In that way, the catalyst will be biphasic and the presence of an interface guaranteed. The relevant characteristics of some metals are presented in Table 6.3. In addition, some metal catalysts preferentially grow SiNWs along a specific direction. Catalysts with large quantity of Cu for instance tend to create $\langle 112 \rangle$ wires that are detrimental to the stabilization of 2H.

With the previously described considerations, we can predict if some mixed catalysts are likely to yield 2H SiNWs. For a growth temperature of around 380 °C, a CuIn catalyst is a first candidate as In has an eutectic temperature of 157 °C and has a similar surface tension γ_{LS} as Sn. The Cu-In system also has a similar phase diagram as the Cu-Sn one, giving compounds with varying stoichiometry. SiNWs growth by PECVD has revealed that it is indeed possible to have polytype 2H with this catalyst [248]. CuGa should also produce good results but it has not been studied experimentally yet. Finally, Cu could be substituted by Ni thanks to its even higher eutectic temperature when mixed with Si. We thus expect catalysts such as NiSn and NiIn to also give good results.

TABLE 6.3: Characteristics of other catalysts known to grow SiNWs. T_e is the eutectic temperature when mixed with Si and γ_{LV} is the surface tension.

Catalyst	T_e (°C)	γ_{LV} (meV · Å^{-2})
Au	363	57
Cu	806	81
Sn	232	36
Ag	835	56
In	157	35
Ni	964	109
Ga	30	43
Bi	271	22

Conclusion of the chapter

In this chapter, we examined in greater detail the experimental results of the growth of column-IV nanowires by PECVD in both Plasfil and NanoMAX. We have found polytype 2H could be obtained in both Si and GeNWs. Although polytype 2H in GeNWs was only obtained once (in the Plasfil reactor) and doubts remain as to when the 2H section appeared, the evidence in SiNWs is clear. Growth in both apparatuses successfully yielded SiNWs with 2H sections with CuSn catalysts. The *in situ* data showed that polytype 2H appeared during the monolayer by monolayer growth mechanism. This proves that the 2H phase can be preferred over the 3C phase in specific growth conditions. Analysis of the HRTEM images suggests that the 2H SiNWs have a octogonal cross-section with six $\{10\bar{1}0\}_H$ and two $\{11\bar{2}0\}_H$ facets. Not a single $\langle 112\rangle_C/\langle 10\bar{1}0\rangle_H$ SiNW with a 2H section was found. In total, we have observed 150 SiNWs where we could clearly distinguish whether they were 3C or 2H. From these 150, only 20 wires were found to possess a 2H section, which gives a ratio of 13 %. Thus, while polytype 2H can be grown spontaneously, it remains uncommon.

During the growth in NanoMAX, we indirectly observed a spontaneous phase transition between polytype 2H to 3C. Measurements on the contact angle on the catalyst-nanowire interface revealed an evolution from high contact angle (around 110°) when 2H is grown to low contact angle (around 100°) for 3C. The change in contact angle shows a modification in surface energies when the grown phase switches. 2H favors $\{10\bar{1}0\}_H$ facets which are perpendicular to the interface while 3C prefers forming $\{111\}_C$ surfaces that are tilted. It is possible that the phase switch is due to the catalyst leaking atoms, reducing its overall volume. A non-tapered geometry might be more favorable when the catalyst is stable resulting in producing perpendicular $\{10\bar{1}0\}_H$ facets. Conversely, catalysts that are decreasing in volume may favor $\{111\}_C$ surfaces. Thus, we believe that an unperturbed growth should stabilize polytype 2H.

Other factors are also at play in order to obtain 2H reliably. First, SiNWs with small diameter is a major parameter. Indeed, if we only consider those, the ratio of 2H over 3C increases from 13 % to 20 %. This can be understood due to the increased aspect ratio of the wires with decreasing diameter. Surfaces will play a bigger role in the overall energy of the nanowire which should favor polytype 2H as its surfaces have lower energies than 3C [140]. Because 2H was grown with a biphasic catalyst, we expect that the additional interface might play an important role in stabilizing it. We modified an existing model to take this new interface into account. Finally, we discussed about catalyst choice if one wants to maximize 2H yield. For that purpose, two metals are chosen, with one that will remain solid and the other liquid when brought to the growth temperature and mixed with Si. The catalyst that remains liquid should preferably have a low surface tension and a high Si solubility. The high Si solubility should induce a low supersaturation, favoring large Si nuclei which allows for the additional interface in biphasic catalyst to be involved.

Conclusion and perspectives

In this thesis, we have studied the *in situ* growth of Si and GeNWs in the NanoMAX transmission electron microscope with the aim of understanding the formation mechanisms of a metastable crystalline structure of Si and Ge: the polytype 2H.

In Chapter 1, we have introduced the concept of nanowires. Their high aspect-ratio confers them interesting properties that can be used in various devices like sensors and solar cells. They can be grown using bottom-up approaches like the VLS technique. Then, we presented how atoms are arranged in a crystal. In particular, Si and Ge have a cubic diamond stacking. This structure has polytypes, notably the arrangement known as the hexagonal diamond structure or polytype 2H. The latter is interesting because it has unique electronic and optical properties like a direct band gap in small diameter nanowires. However, a literature review shows that this structure is difficult to obtain and no model tailored for Si and Ge exists yet that would explain why it forms.

To understand the growth mechanisms of its formation, we use a modified transmission electron microscope to watch it *in situ* and in real time. Gas sources, molecular beam epitaxy sources and an electron cyclotron resonance plasma source were used jointly for that purpose. Details on the experimental procedures and techniques were exposed in Chapter 2.

In Chapter 3, we first started to grow Au-catalyzed GeNWs by using both the molecular beam epitaxy and the gas sources in NanoMAX. The results of these growth experiments were then compared with ones obtained in a PECVD reactor. The important role of atomic hydrogen was highlighted. By covering the GeNWs sidewall, hydrogen is able to modify the sawtooth faceting as well as to stabilize the Au catalyst on top of the nanowire. In the absence of hydrogen, the Au catalyst leaks which results in the formation of an Au wetting layer on the nanowire sidewalls.

There is a wide variety of experimental results concerning the growth of Au-catalyzed SiNWs in the literature. This opportunity allowed us to validate the results obtained in the modified *in situ* microscope. In Chapter 4, we presented some of the SiNWs. obtained with Au catalyst. They displayed structures that were reported before such as kinks, specific configurations of sidewalls and sawtooth faceting. The validation of NanoMAX comes from the measurement of the SiNW growth activation energy which is consistent with past results.

These exciting results pushed us to substitute Au as catalyst with the double CuSn catalyst (with which 2H SiNWs had been obtained in a PECVD reactor) in Chapter 5. Several compositions of Cu and Sn were tried which gave different results in terms of the growth mechanisms themselves and the morphology of the SiNWs. Majority-Cu catalysts were found to be composed mostly of Cu_3Si. Majority-Sn catalysts on the other hand were made of two phases: a

solid Cu_3Si core and a liquid Sn-rich shell. Depending on the composition, the orientation of the nanowire with respect to the catalyst changes. Mixing Cu and Sn together also reveals a unique growth mode which combines characteristic of both VLS and VSS.

Finally, in Chapter 6, we examined all the previous results in order to find evidence of polytype 2H in Si and GeNWs. The endeavor is successful as polytype 2H is present in both Si and GeNWs. This phase has several characteristics. It is mainly found in nanowires growing along the $\langle 111\rangle_C/\langle 0001\rangle_H$ direction. Some parameters have an impact on whether polytype 2H is obtained or not. Smaller diameter nanowire is one of them. A second important factor is the existence of an interface consisting of liquid tin and solid Cu_3Si in biphasic catalysts like CuSn. We implemented this interface into an existing model to understand how both small diameter and this interface influence the stability of polytype 2H. At last, we suggested some other catalysts, such as CuIn, CuGa or CuBi which are viable candidates for obtaining more of this exotic structure.

While the utilization of the NanoMAX microscope brought a better understanding on the growth mechanism of both Si and GeNWs and the formation of polytype 2H, a certain number of questions remain about the PECVD growth. From an experimental point of view, the plasma environment constitutes a black box. It is clear that the radical species created by the plasma play an important role. However, we do not yet know how much radicals are sent towards the sample for a given ECR power. Furthermore, the relationship between coverage of the SiNWs sidewalls with atomic hydrogen and the number of radicals produced is unknown. This is particularly important given what was presented in this work as the areal coverage influences the surface energies which should decide if polytype 2H is formed or not. Direct observation of a sample during growth is also problematic. A high electron dose promotes the diffusion of materials under the beam and produces undesirable effects. Experimental improvements should implement the capability to directly measure the concentration of species produced by the plasma and the generalized use of direct electron detectors coupled with low dose observation. An infrared spectrometer could also be fitted on the *in situ* TEM to measure the hydrogen coverage. Finally, it is necessary to systematically calibrate the Si cantilevers, using a pyrometer or, better, an infra-red camera fitted on an optical microscope, to precisely measure the temperature.

A list of potential catalysts was proposed. Growth with these could provide supplementary information on polytype 2H on the one hand and the novel hybrid growth mode on the other hand. It can be very interesting to understand what triggers this hybrid growth mode, notably if the metal that remains solid must be a silicide. We have discussed some of this growth mode properties but there are still some open questions. The relative position of the liquid and solid parts in the catalyst is one of them. Indeed, the solid part can sometimes be completely immerged inside the liquid and sometimes be in contact with the vapor phase. Another question is how the solid part communicates with the liquid part in order to yield a homogeneous growth rate for the nanowire.

With the knowledge that a small diameter is an important factor in the stabilization of polytype 2H, growing GeNWs again in NanoMAX could prove fruitful. Au seeds are complicated to work with due to coalescence. We could replace Au with alternative catalysts like Sn or other double catalysts, coupled with the ECR source to aim for small diameter nanowires. Determining the 2H ratio in GeNWs should be interesting as the 2H phase is expected to be more difficult to obtain. If synthesizing 2H is successful in these nanowires, then we could attempt the growth of polytype 2H in Si_xGe_{1-x} NWs. These alloys currently attract a lot of attention due to the tunability of their electronic properties. Being able to control the phase will certainly provide

new useful applications.

The electronic properties of polytype 2H are only known through numerical simulations. If one wants to use 2H SiNWs to create novel devices, it is first necessary to use optical characterization techniques such as cathodoluminescence on them to assess the accuracy of the simulations. There is a major roadblock for this kind of experiments as of now. Indeed, in ideal conditions, SiNWs that are partially or completely 2H only represent around 20 % of below 7 nm diameter wires with CuSn catalysts. Thus, further works on this crystalline structure should aim towards the 2H yield maximization. To control what polytype is grown, an experimental technique less demanding than TEM would then be welcome; the discovery of luminescent signatures of the phase would be perfect for that. Such experimental works could now rely on the improvement of existing theoretical models and the calculation of surface energies in varying conditions by *ab initio* simulations.

Résumé de la thèse en français

L'objectif de cette thèse est de déterminer dans quelles conditions la phase hexagonal-diamant (2H) du silicium et du germanium peut apparaître dans des nanofils. Des propriétés électroniques intéressantes y ont été prédites. Toutefois, cette phase n'est pas dans les diagrammes de phases à l'équilibre de ces deux matériaux. C'est la phase cubique-diamant (3C) qui est la plus stable et non la phase 2H. Cette dernière est donc métastable. Or, des résultats expérimentaux récents ont pu démontrer qu'il était possible de la synthétiser grâce à une méthode de croissance bottom-up : le procédé vapeur-liquide-solide assisté par plasma. Afin de répondre à cette question, nous avons utilisé un microscope électronique en transmission modifié, capable de faire croître de tels nanofils et d'observer leur croissance en temps réel.

Cette thèse débute par une brève introduction des nanofils semi-conducteurs. Les nanofils, grâce à leur forme, ont des propriétés intéressantes qui peuvent être exploitées dans toute une gamme d'applications. En particulier, il est possible de les implémenter dans le but de fabriquer des cellules solaires ou des capteurs biochimiques. Une méthode couramment utilisée pour leur synthèse est le procédé vapeur-liquide-solide (VLS), dans lequel on apporte une vapeur contenant des atomes de précurseurs, qui dépend de ce que l'on veut faire croître, à un catalyseur métallique liquide. L'apport continu en précurseur augmente sa concentration dans le liquide qui finit par la précipitation d'un nanofil solide. On dresse ensuite un état de l'art sur la synthèse de la phase métastable 2H. Il existe plusieurs procédés à ce jour, mais la technique la plus prometteuse est celle utilisant la méthode VLS assistée par un plasma d'hydrogène utilisant des nanoparticules d'étain comme catalyseur et un substrat de cuivre. Bien qu'il n'existe pas encore de théorie expliquant la formation de cette phase dans le silicium et le germanium, il est possible de faire un parallèle avec ceux existant dans les nanofils III-V qui ont également cette dichotomie 3C/2H.

Pour mieux comprendre les mécanismes participant à l'apparition de la phase 2H dans les nanofils de silicium et de germanium, on peut essayer de reproduire la croissance assistée par plasma dans un microscope électronique en transmission (MET). Le MET NanoMAX est équipé de source de matière permettant la croissance et l'observation des nanofils en temps réel. Il est également complété par une source plasma à résonance cyclotron (ECR) produisant de lhydrogène atomique qui joue un rôle important lors de la croissance. Le dépôt des catalyseurs sur les substrats se fait par évaporation thermique. L'énergie des électrons dans le MET est de 300 keV. Cette haute énergie peut se transmettre aux atomes de l'échantillon, ce qui va modifier sa nature et sa température. On estime que l'échauffement provoqué ne dépasse pas 3 K. Pour faciliter l'identification de la phase 2H, des simulations numériques de diffraction électronique dynamique ont été effectués. Les résultats de ces simulations montrent que l'observation doit principalement se faire par l'axe de zone $[110]/[1\bar{2}10]$. Dans cet axe, l'interprétation des images MET peut se faire sans ambiguïté.

Les premières expériences in situ se sont déroulées sur des nanofils de germanium avec des nanoparticules d'or comme catalyseur. Dans un premier temps, une source solide d'épitaxie par jets moléculaires (MBE) fournit les atomes de germanium aux particules d'or. Nous avons observé les premiers instants de la croissance où un eutectique liquide or-germanium se forme, suivi de la précipitation de germanium solide. Les nanofils obtenus ont tous une structure 3C avec une direction de croissance $\langle 111 \rangle$ et une section transversale hexagonale. L'interface catalyseur-nanofil est complexe, avec une surface principale $\{111\}$ et des petites facettes tronquées au voisinage de la ligne triple liquide-solide-vapeur. La synthèse MBE est caractérisée par un faible taux de croissance non-constant. Il est constaté qu'une régression du fil pouvait s'opérer malgré un apport constant en germanium vers la goutte. Ce phénomène est suivi d'une restructuration des facettes latérales du fils : les facettes $\{113\}$, initialement créées pour maintenir le fil à un diamètre constant, disparaissent au profit des surfaces $\{111\}$ et $\{112\}$. Le catalyseur liquide or-germanium peut parfois se déstabiliser du sommet du fil et s'écouler sur les parois latérales des fils. En remplaçant la source MBE par une source gazeuse de Ge_2H_6, la croissance change radicalement notamment au niveau du facettage des parois latérales. On passe d'une alternance de surface $\{111\}$ et $\{113\}$ à un nano-facettage $\{111\}$ en dent de scie donnant une surface vicinale $\{112\}$. La déstabilisation des catalyseurs liquides n'est pas observée dans ces conditions. La présence d'hydrogène modifie les énergies de surface et empêche la formation d'une couche de mouillage d'or autour du fil, qui mène à la déstabilisation des catalyseurs observé en MBE. On montre ainsi que l'hydrogène et son effet sur les surfaces est un facteur décisif lors de la croissance.

Nous avons ensuite utilisé des catalyseurs mixtes étain-cuivre pour produire des nanofils de silicium à l'aide de la source de plasma ECR. La croissance avec de l'étain pur souligne l'importance de l'hydrogène atomique, car un apport insuffisant mène à un mouillage rapide de l'étain et à la fin de la croissance. Plusieurs ratios de cuivre-étain ont été testés. Selon la composition, les nanofils obtenues sont différents. Avec un catalyseur à majorité cuivre, le mode de synthèse est le procédé vapeur-solide-solide (VSS) où la croissance s'opère en général plan par plan. Un noyau de silicium se forme initialement à la ligne triple. L'incorporation graduelle d'atomes de silicium puis la propagation du nouveau plan par un mécanisme dit "step-flow" va étendre latéralement ce noyau jusqu'à couvrir entièrement la surface du plan inférieur. Les fils croissent en majorité dans la direction $\langle 112 \rangle$ et présentent de nombreux plans de macle. Le catalyseur solide est un cristal de Cu_3Si. Lorsque le ratio étain-cuivre est en faveur de l'étain, les catalyseurs deviennent biphasés avec à la fois une partie solide en Cu_3Si et une partie liquide riche en étain. La direction de croissance dominante est maintenant $\langle 111 \rangle$. Le mode de croissance devient plus compliqué avec des caractéristiques provenant à la fois des modes VLS et VSS. La nucléation d'une nouvelle couche débute dans la partie liquide et sa propagation y est rapide. La marche nouvellement créée va stationner pendant un moment à l'interface catalyseur solide-catalyseur liquide avant de reprendre sa propagation beaucoup plus lentement à travers Cu_3Si. Dans les catalyseurs étain-cuivre, un rôle de l'étain est d'abaisser la température à partir duquel la croissance d'un nanofil de silicium peut débuter.

Au cours de ces croissances in situ, des nanofils de silicium à structure 2H ont été observées. Tous ont cru selon l'orientation $\langle 0001 \rangle$ et des simulations numériques suggèrent qu'elles ont une section transverse octogonale. Les effets de taille jouent un rôle déterminant dans l'apparition de la phase 2H puisque tous les fils ayant cette structure ont un diamètre inférieur à 8 nm. Parmi tous les fils ayant un diamètre inférieur à ce seuil, 20 % ont la structure 2H recherchée. Nous expliquons l'influence du diamètre par d'une part le fait que les surfaces dans la phase 2H ont une plus faible énergie par rapport à la phase 3C, et d'autre part la propension des fils de petit diamètre à macler régulièrement. Nous avons aussi observé qu'un nanofil a changé

de phase pendant sa croissance, passant d'une structure 2H à 3C. Au cours de ce changement, l'angle de contact du catalyseur sur le fil passe d'une valeur moyenne à une autre. Ceci montre que des effets thermodynamiques sont aussi à l'uvre. Cependant, ces effets ne dépendent pas explicitement du diamètre. L'existence d'une interface dans les catalyseurs cuivre-étain biphasés peut expliquer et réunir les effets thermodynamiques et de taille. La structure 2H pourrait être la structure de plus basse énergie si sa nucléation a lieu proche de cette interface.

Bibliography

[1] van Delft, D. & Kes, P. The discovery of superconductivity. *Physics Today* **63**, 38–43 (2010). doi:10.1063/1.3490499.

[2] Haegel, N. M. *et al.* Terawatt-scale photovoltaics: Transform global energy. *Science* **364**, 836–838 (2019). doi:10.1126/science.aaw1845.

[3] Best Research-Cell Efficiency Chart.

[4] Jena, A. K., Kulkarni, A. & Miyasaka, T. Halide Perovskite Photovoltaics: Background, Status, and Future Prospects. *Chem. Rev.* **119**, 3036–3103 (2019). doi:10.1021/acs.chemrev.8b00539.

[5] Hall, R. N., Fenner, G. E., Kingsley, J. D., Soltys, T. J. & Carlson, R. O. Coherent Light Emission From GaAs Junctions. *Phys. Rev. Lett.* **9**, 366–368 (1962). doi:10.1103/PhysRevLett.9.366.

[6] Tsuruoka, T., Ohizumi, Y., Ushioda, S., Ohno, Y. & Ohno, H. Light emission spectra of AlGaAs/GaAs multiquantum wells induced by scanning tunneling microscope. *Appl. Phys. Lett.* **73**, 1544–1546 (1998). doi:10.1063/1.122200.

[7] Nakamura, S., Mukai, T. M. T. & Senoh, M. S. M. High-Power GaN P-N Junction Blue-Light-Emitting Diodes. *Jpn. J. Appl. Phys.* **30**, L1998 (1991). doi:10.1143/JJAP.30.L1998.

[8] Nannini, J. B. The Nobel Prize in Physics 2014 (2014).

[9] Yoffe, A. D. Low-dimensional systems: quantum size effects and electronic properties of semiconductor microcrystallites (zero-dimensional systems) and some quasi-two-dimensional systems. *Advances in Physics* **42**, 173–262 (1993). doi:10.1080/00018739300101484.

[10] Novoselov, K. S. *et al.* Electric Field Effect in Atomically Thin Carbon Films. *Science* **306**, 666–669 (2004). doi:10.1126/science.1102896.

[11] Huss, E. The Nobel Prize in Physics 2010 (2010).

[12] Yaroshevsky, A. A. Abundances of chemical elements in the Earths crust. *Geochem. Int.* **44**, 48–55 (2006). doi:10.1134/S001670290601006X.

[13] Pillarisetty, R. Academic and industry research progress in germanium nanodevices. *Nature* **479**, 324–328 (2011). doi:10.1038/nature10678.

[14] Bean, J. C. Silicon-based semiconductor heterostructures: column IV bandgap engineering. *Proceedings of the IEEE* **80**, 571–587 (1992). doi:10.1109/5.135380.

[15] El Kurdi, M., Sauvage, S., Fishman, G. & Boucaud, P. Band-edge alignment of SiGe/Si quantum wells and SiGe/Si self-assembled islands. *Phys. Rev. B* **73**, 195327 (2006). doi:10.1103/PhysRevB.73.195327.

[16] Zhang, T., Wang, J., Yu, L., Xu, J. & Roca i Cabarrocas, P. Advanced radial junction thin film photovoltaics and detectors built on standing silicon nanowires. *Nanotechnology* **30**, 302001 (2019). doi:10.1088/1361-6528/ab0e57.

[17] Khayrudinov, V. *et al.* Direct Growth of Light-Emitting IIIV Nanowires on Flexible Plastic Substrates. *ACS Nano* **14**, 7484–7491 (2020). doi:10.1021/acsnano.0c03184.

[18] Zhang, M.-L. *et al.* Preparation of Large-Area Uniform Silicon Nanowires Arrays through Metal-Assisted Chemical Etching. *J. Phys. Chem. C* **112**, 4444–4450 (2008). doi:10.1021/jp077053o.

[19] Tseng, A., Chen, K., Chen, C. & Ma, K. Electron beam lithography in nanoscale fabrication: recent development. *IEEE Transactions on Electronics Packaging Manufacturing* **26**, 141–149 (2003). doi:10.1109/TEPM.2003.817714.

[20] Melosh, N. A. *et al.* Ultrahigh-Density Nanowire Lattices and Circuits. *Science* **300**, 112–115 (2003). doi:10.1126/science.1081940.

[21] Morton, K. J., Nieberg, G., Bai, S. & Chou, S. Y. Wafer-scale patterning of sub-40 nm diameter and high aspect ratio >50:1 silicon pillar arrays by nanoimprint and etching. *Nanotechnology* **19**, 345301 (2008). doi:10.1088/0957-4484/19/34/345301.

[22] Fan, H. J., Werner, P. & Zacharias, M. Semiconductor Nanowires: From Self-Organization to Patterned Growth. *Small* **2**, 700–717 (2006). doi:https://doi.org/10.1002/smll.200500495.

[23] Wagner, R. S., Ellis, W. C., Jackson, K. A. & Arnold, S. M. Study of the Filamentary Growth of Silicon Crystals from the Vapor. *Journal of Applied Physics* **35**, 2993–3000 (1964). doi:10.1063/1.1713143.

[24] Das Kanungo, P. *et al.* Controlled in situ boron doping of short silicon nanowires grown by molecular beam epitaxy. *Appl. Phys. Lett.* **92**, 263107 (2008). doi:10.1063/1.2953702.

[25] Nebol'sin, V. A., Shchetinin, A. A., Dolgachev, A. A. & Korneeva, V. V. Effect of the Nature of the Metal Solvent on the Vapor-Liquid-Solid Growth Rate of Silicon Whiskers. *Inorg Mater* **41**, 1256–1259 (2005). doi:10.1007/s10789-005-0296-5.

[26] Morales, A. M. & Lieber, C. M. A Laser Ablation Method for the Synthesis of Crystalline Semiconductor Nanowires. *Science* **279**, 208–211 (1998). doi:10.1126/science.279.5348.208.

[27] Cao, L. *et al.* Instability and Transport of Metal Catalyst in the Growth of Tapered Silicon Nanowires. *Nano Lett.* **6**, 1852–1857 (2006). doi:10.1021/nl060533r.

[28] Misra, S., Yu, L., Chen, W. & Roca i Cabarrocas, P. Wetting Layer: The Key Player in Plasma-Assisted Silicon Nanowire Growth Mediated by Tin. *J. Phys. Chem. C* **117**, 17786–17790 (2013). doi:10.1021/jp403063d.

[29] Wagner, R. S. & Ellis, W. C. Vaporliquidsolid mechanism of single crystal growth. *Appl. Phys. Lett.* **4**, 89–90 (1964). doi:10.1063/1.1753975.

[30] Cui, Y., Lauhon, L. J., Gudiksen, M. S., Wang, J. & Lieber, C. M. Diameter-controlled synthesis of single-crystal silicon nanowires. *Appl. Phys. Lett.* **78**, 2214–2216 (2001). doi:10.1063/1.1363692.

[31] Wu, Y. *et al.* Controlled Growth and Structures of Molecular-Scale Silicon Nanowires. *Nano Lett.* **4**, 433–436 (2004). doi:10.1021/nl035162i.

[32] Kodambaka, S., Tersoff, J., Reuter, M. C. & Ross, F. M. Germanium Nanowire Growth Below the Eutectic Temperature. *Science* **316**, 729–732 (2007). doi:10.1126/science.1139105.

[33] Yao, Y. & Fan, S. Si nanowires synthesized with Cu catalyst. *Materials Letters* **61**, 177–181 (2007). doi:10.1016/j.matlet.2006.04.045.

[34] Wan, Y. *et al.* Silicon nanowires grown from copper oxalate. *Materials Letters* **64**, 1839–1842 (2010). doi:10.1016/j.matlet.2010.05.029.

[35] Yu, L. *et al.* Plasma-enhanced low temperature growth of silicon nanowires and hierarchical structures by using tin and indium catalysts. *Nanotechnology* **20**, 225604 (2009). doi:10.1088/0957-4484/20/22/225604.

[36] Liu, J., Huang, S.-H., Chen, L.-P. & He, L. Tin catalyzed silicon nanowires prepared by magnetron sputtering. *Materials Letters* **151**, 122–125 (2015). doi:10.1016/j.matlet.2015.03.065.

[37] Tang, J. *et al.* Plasma-Assisted Growth of Silicon Nanowires by Sn Catalyst: Step-by-Step Observation. *Nanoscale Research Letters* **11**, 455 (2016). doi:10.1186/s11671-016-1681-5.

[38] Sunkara, M. K., Sharma, S., Miranda, R., Lian, G. & Dickey, E. C. Bulk synthesis of silicon nanowires using a low-temperature vaporliquidsolid method. *Appl. Phys. Lett.* **79**, 1546–1548 (2001). doi:10.1063/1.1401089.

[39] Jeon, M., Tomitsuka, Y. & Kamisako, K. Synthesis of gallium-catalyzed silicon nanowires by hydrogen radical-assisted deposition method. *Journal of Industrial and Engineering Chemistry* **14**, 836–840 (2008). doi:10.1016/j.jiec.2008.06.004.

[40] Zardo, I. *et al.* Gallium assisted plasma enhanced chemical vapor deposition of silicon nanowires. *Nanotechnology* **20**, 155602 (2009). doi:10.1088/0957-4484/20/15/155602.

[41] Kohen, D. *et al.* Aluminum catalyzed growth of silicon nanowires: Al atom location and the influence of silicon precursor pressure on the morphology. *Journal of Crystal Growth* **341**, 12–18 (2012). doi:10.1016/j.jcrysgro.2011.12.057.

[42] Nebol'sin, V. A. & Shchetinin, A. A. Role of Surface Energy in the VaporLiquidSolid Growth of Silicon. *Inorganic Materials* **39**, 899–903 (2003). doi:10.1023/A:1025588601262.

[43] Fairfield, J. M. & Gokhale, B. V. Gold as a recombination centre in silicon. *Solid-State Electronics* **8**, 685–691 (1965). doi:10.1016/0038-1101(65)90036-5.

[44] Wen, C.-Y., Reuter, M. C., Tersoff, J., Stach, E. A. & Ross, F. M. Structure, Growth Kinetics, and Ledge Flow during VaporSolidSolid Growth of Copper-Catalyzed Silicon Nanowires. *Nano Lett.* **10**, 514–519 (2010). doi:10.1021/nl903362y.

[45] Hofmann, S. *et al.* Ledge-flow-controlled catalyst interface dynamics during Si nanowire growth. *Nature Mater* **7**, 372–375 (2008). doi:10.1038/nmat2140.

[46] Wen, C.-Y. *et al.* Formation of Compositionally Abrupt Axial Heterojunctions in Silicon-Germanium Nanowires. *Science* **326**, 1247–1250 (2009). doi:10.1126/science.1178606.

[47] Chou, Y.-C. *et al.* Controlling the Growth of Si/Ge Nanowires and Heterojunctions Using SilverGold Alloy Catalysts. *ACS Nano* **6**, 6407–6415 (2012). doi:10.1021/nn301978x.

[48] Yu, Z. *et al.* Bi-Sn alloy catalyst for simultaneous morphology and doping control of silicon nanowires in radial junction solar cells. *Appl. Phys. Lett.* **107**, 163105 (2015). doi:10.1063/1.4933274.

[49] Misra, S., Yu, L., Chen, W., Foldyna, M. & Roca i Cabarrocas, P. A review on plasma-assisted VLS synthesis of silicon nanowires and radial junction solar cells. *J. Phys. D: Appl. Phys.* **47**, 393001 (2014). doi:10.1088/0022-3727/47/39/393001.

[50] Yu, P. *et al.* Design and fabrication of silicon nanowires towards efficient solar cells. *Nano Today* **11**, 704–737 (2016). doi:10.1016/j.nantod.2016.10.001.

[51] Kayes, B. M., Atwater, H. A. & Lewis, N. S. Comparison of the device physics principles of planar and radial p-n junction nanorod solar cells. *Journal of Applied Physics* **97**, 114302 (2005). doi:10.1063/1.1901835.

[52] Faß, S., Steinhauser, J., Oliveira, N., Vallat-Sauvain, E. & Ballif, C. Opto-electronic properties of rough LP-CVD ZnO:B for use as TCO in thin-film silicon solar cells. *Thin Solid Films* **515**, 8558–8561 (2007). doi:10.1016/j.tsf.2007.03.130.

[53] Zhang, P. *et al.* Dense nanoimprinted silicon nanowire arrays with passivated axial p-i-n junctions for photovoltaic applications. *Journal of Applied Physics* **117**, 125104 (2015). doi:10.1063/1.4916535.

[54] Foldyna, M., Yu, L. & Roca i Cabarrocas, P. Theoretical short-circuit current density for different geometries and organizations of silicon nanowires in solar cells. *Solar Energy Materials and Solar Cells* **117**, 645–651 (2013). doi:10.1016/j.solmat.2012.10.014.

[55] Misra, S., Yu, L., Foldyna, M. & Cabarrocas, P. R. i. New Approaches to Improve the Performance of Thin-Film Radial Junction Solar Cells Built Over Silicon Nanowire Arrays. *IEEE Journal of Photovoltaics* **5**, 40–45 (2015). doi:10.1109/JPHOTOV.2014.2366688.

[56] Jie, J. *et al.* Surface-Dominated Transport Properties of Silicon Nanowires. *Advanced Functional Materials* **18**, 3251–3257 (2008). doi:10.1002/adfm.200800399.

[57] Chen, W. & Roca i Cabarrocas, P. Rational design of nanowire solar cells: from single nanowire to nanowire arrays. *Nanotechnology* **30**, 194002 (2019). doi:10.1088/1361-6528/aaff8d.

[58] Presnova, G. *et al.* Biosensor based on a silicon nanowire field-effect transistor functionalized by gold nanoparticles for the highly sensitive determination of prostate specific antigen. *Biosensors and Bioelectronics* **88**, 283–289 (2017). doi:10.1016/j.bios.2016.08.054.

[59] Bi, X., Agarwal, A. & Yang, K.-L. Oligopeptide-modified silicon nanowire arrays as multichannel metal ion sensors. *Biosensors and Bioelectronics* **24**, 3248–3251 (2009). doi:10.1016/j.bios.2009.04.007.

[60] Luo, L. *et al.* Silicon nanowire sensors for Hg2+ and Cd2+ ions. *Appl. Phys. Lett.* **94**, 193101 (2009). doi:10.1063/1.3120281.

[61] Cui, Y., Wei, Q., Park, H. & Lieber, C. M. Nanowire Nanosensors for Highly Sensitive and Selective Detection of Biological and Chemical Species. *Science* **293**, 1289–1292 (2001). doi:10.1126/science.1062711.

[62] Dorvel, B. R. *et al.* Silicon nanowires with high-k hafnium oxide dielectrics for sensitive detection of small nucleic acid oligomers. *ACS Nano* **6**, 6150–6164 (2012). doi:10.1021/nn301495k.

[63] Gao, A. *et al.* Enhanced Sensing of Nucleic Acids with Silicon Nanowire Field Effect Transistor Biosensors. *Nano Lett.* **12**, 5262–5268 (2012). doi:10.1021/nl302476h.

[64] Beaulieu, L. Y., Eberman, K. W., Turner, R. L., Krause, L. J. & Dahn, J. R. Colossal Reversible Volume Changes in Lithium Alloys. *Electrochem. Solid-State Lett.* **4**, A137 (2001). doi:10.1149/1.1388178.

[65] Yang, Y. *et al.* New Nanostructured Li2S/Silicon Rechargeable Battery with High Specific Energy. *Nano Lett.* **10**, 1486–1491 (2010). doi:10.1021/nl100504q.

[66] Zamfir, M. R., Nguyen, H. T., Moyen, E., Lee, Y. H. & Pribat, D. Silicon nanowires for Li-based battery anodes: a review. *J. Mater. Chem. A* **1**, 9566–9586 (2013). doi:10.1039/C3TA11714F.

[67] Wang, J. W. *et al.* Two-Phase Electrochemical Lithiation in Amorphous Silicon. *Nano Lett.* **13**, 709–715 (2013). doi:10.1021/nl304379k.

[68] Cui, L.-F., Ruffo, R., Chan, C. K., Peng, H. & Cui, Y. Crystalline-Amorphous CoreShell Silicon Nanowires for High Capacity and High Current Battery Electrodes. *Nano Lett.* **9**, 491–495 (2009). doi:10.1021/nl8036323.

[69] Chen, H., Xiao, Y., Wang, L. & Yang, Y. Silicon nanowires coated with copper layer as anode materials for lithium-ion batteries. *Journal of Power Sources* **196**, 6657–6662 (2011). doi:10.1016/j.jpowsour.2010.12.075.

[70] Jamieson, J. C. Crystal Structures at High Pressures of Metallic Modifications of Silicon and Germanium. *Science* **139**, 762–764 (1963). doi:10.1126/science.139.3556.762.

[71] Mujica, A., Rubio, A., Muñoz, A. & Needs, R. J. High-pressure phases of group-IV, III–V, and II–VI compounds. *Rev. Mod. Phys.* **75**, 863–912 (2003). doi:10.1103/RevModPhys.75.863.

[72] Olijnyk, H., Sikka, S. K. & Holzapfel, W. B. Structural phase transitions in Si and Ge under pressures up to 50 GPa. *Physics Letters A* **103**, 137–140 (1984). doi:10.1016/0375-9601(84)90219-6.

[73] Duclos, S. J., Vohra, Y. K. & Ruoff, A. L. Experimental study of the crystal stability and equation of state of Si to 248 GPa. *Phys. Rev. B* **41**, 12021–12028 (1990). doi:10.1103/PhysRevB.41.12021.

[74] McMahon, M. I. & Nelmes, R. J. New high-pressure phase of Si. *Phys. Rev. B* **47**, 8337–8340 (1993). doi:10.1103/PhysRevB.47.8337.

[75] Nelmes, R. J. *et al.* Imma phase of germanium at ~80 GPa. *Phys. Rev. B* **53**, R2907–R2909 (1996). doi:10.1103/PhysRevB.53.R2907.

[76] Takemura, K. *et al.* High-pressure Cmca and hcp phases of germanium. *Phys. Rev. B* **62**, R10603–R10606 (2000). doi:10.1103/PhysRevB.62.R10603.

[77] Yang, C. C., Li, J. C. & Jiang, Q. Temperature-pressure phase diagram of silicon determined by Clapeyron equation. *Solid State Communications* **129**, 437–441 (2004). doi:10.1016/j.ssc.2003.11.020.

[78] Van Vechten, J. A. Quantum Dielectric Theory of Electronegativity in Covalent Systems. III. Pressure-Temperature Phase Diagrams, Heats of Mixing, and Distribution Coefficients. *Phys. Rev. B* **7**, 1479–1507 (1973). doi:10.1103/PhysRevB.7.1479.

[79] Deb, S. K., Wilding, M., Somayazulu, M. & McMillan, P. F. Pressure-induced amorphization and an amorphousamorphous transition in densified porous silicon. *Nature* **414**, 528–530 (2001). doi:10.1038/35107036.

[80] Jayaraman, A., Klement, W. & Kennedy, G. C. Melting and Polymorphism at High Pressures in Some Group IV Elements and III-V Compounds with the Diamond/Zincblende Structure. *Phys. Rev.* **130**, 540–547 (1963). doi:10.1103/PhysRev.130.540.

[81] Bundy, F. P. Phase Diagrams of Silicon and Germanium to 200 kbar, 1000řC. *J. Chem. Phys.* **41**, 3809–3814 (1964). doi:10.1063/1.1725818.

[82] Cannon, J. F. Behavior of the Elements at High Pressures. *Journal of Physical and Chemical Reference Data* **3**, 781 (2009). doi:10.1063/1.3253148.

[83] Hu, J. Z., Merkle, L. D., Menoni, C. S. & Spain, I. L. Crystal data for high-pressure phases of silicon. *Phys. Rev. B* **34**, 4679–4684 (1986). doi:10.1103/PhysRevB.34.4679.

[84] Yang, C. C. & Jiang, Q. Temperature-pressure phase diagram of germanium determined by Clapeyron equation. *Scripta Materialia* **51**, 1081–1085 (2004). doi:10.1016/j.scriptamat.2004.08.001.

[85] Wentorf, R. H. & Kasper, J. S. Two New Forms of Silicon. *Science* **139**, 338–339 (1963). doi:10.1126/science.139.3552.338-a.

[86] Xiao, S.-Q. & Pirouz, P. On diamond-hexagonal germanium. *Journal of Materials Research* **7**, 1406–1412 (1992). doi:10.1557/JMR.1992.1406.

[87] Lopez, F. J., Hemesath, E. R. & Lauhon, L. J. Ordered Stacking Fault Arrays in Silicon Nanowires. *Nano Lett.* **9**, 2774–2779 (2009). doi:10.1021/nl901315s.

[88] den Hertog, M. I. *et al.* Hidden defects in silicon nanowires. *Nanotechnology* **23**, 025701 (2012). doi:10.1088/0957-4484/23/2/025701.

[89] Fasolato, C. *et al.* Crystalline, Phononic, and Electronic Properties of Heterostructured Polytypic Ge Nanowires by Raman Spectroscopy. *Nano Lett.* **18**, 7075–7084 (2018). doi:10.1021/acs.nanolett.8b03073.

[90] Cayron, C. *et al.* Odd electron diffraction patterns in silicon nanowires and silicon thin films explained by microtwins and nanotwins. *J Appl Cryst, J Appl Crystallogr* **42**, 242–252 (2009). doi:10.1107/S0021889808042131.

[91] Németh, P. *et al.* Lonsdaleite is faulted and twinned cubic diamond and does not exist as a discrete material. *Nat Commun* **5**, 1–5 (2014). doi:10.1038/ncomms6447.

[92] Eremenko, V. G. & Nikitenko, V. I. Electron microscope investigation of the microplastic deformation mechanisms of silicon by indentation. *physica status solidi (a)* **14**, 317–330 (1972). doi:10.1002/pssa.2210140139.

[93] Pirouz, P., Chaim, R., Dahmen, U. & Westmacott, K. H. The martensitic transformation in siliconI experimental observations. *Acta Metallurgica et Materialia* **38**, 313–322 (1990). doi:10.1016/0956-7151(90)90061-K.

[94] Dahmen, U., Westmacott, K. H., Pirouz, P. & Chaim, R. The martensitic transformation in siliconII. crystallographic analysis. *Acta Metallurgica et Materialia* **38**, 323–328 (1990). doi:10.1016/0956-7151(90)90062-L.

[95] Müllner, P. & Pirouz, P. A disclination model for the twin-twin intersection and the formation of diamond-hexagonal silicon and germanium. *Materials Science and Engineering: A* **233**, 139–144 (1997). doi:10.1016/S0921-5093(97)00058-0.

[96] Tan, T. Y., Föll, H. & Hu, S. M. On the diamond-cubic to hexagonal phase transformation in silicon. *Philosophical Magazine A* **44**, 127–140 (1981). doi:10.1080/01418618108244498.

[97] Cerofolini, G. F. *et al.* Damaged and reconstructed regions in silicon after heavy arsenic implantation. *Journal of Applied Physics* **56**, 2981–2983 (1984). doi:10.1063/1.333768.

[98] Komarov, F. F., Novikov, A. P., Samoilyuk, T. T., Solov'yev, V. S. & Shiryaev, S. Y. Modification of silicon structure during highly intensive Ar +ion implantation. *Radiation Effects* (2006). doi:10.1080/00337578508222540.

[99] Korolev, D. S. *et al.* Formation of hexagonal 9R silicon polytype by ion implantation. *Tech. Phys. Lett.* **43**, 767–769 (2017). doi:10.1134/S1063785017080211.

[100] Williams, J. S. *et al.* Hexagonal germanium formed via a pressure-induced phase transformation of amorphous germanium under controlled nanoindentation. *physica status solidi (RRL) Rapid Research Letters* **7**, 355–359 (2013). doi:10.1002/pssr.201307079.

[101] Dushaq, G., Nayfeh, A. & Rasras, M. Hexagonal germanium formation at room temperature using controlled penetration depth nano-indentation. *Sci Rep* **9**, 1–10 (2019). doi:10.1038/s41598-018-38440-3.

[102] Zhang, Y., Iqbal, Z., Vijayalakshmi, S., Qadri, S. & Grebel, H. Formation of hexagonal-wurtzite germanium by pulsed laser ablation. *Solid State Communications* **115**, 657–660 (2000). doi:10.1016/S0038-1098(00)00259-3.

[103] Vincent, L. *et al.* Novel Heterostructured Ge Nanowires Based on Polytype Transformation. *Nano Lett.* **14**, 4828–4836 (2014). doi:10.1021/nl502049a.

[104] Vincent, L. *et al.* Shear-driven phase transformation in silicon nanowires. *Nanotechnology* **29**, 125601 (2018). doi:10.1088/1361-6528/aaa738.

[105] Qiu, Y. *et al.* Epitaxial diamond-hexagonal silicon nano-ribbon growth on (001) silicon. *Sci Rep* **5**, 1–10 (2015). doi:10.1038/srep12692.

[106] Algra, R. E. *et al.* Crystal Structure Transfer in Core/Shell Nanowires. *Nano Lett.* **11**, 1690–1694 (2011). doi:10.1021/nl200208q.

[107] Hauge, H. I. T. *et al.* Hexagonal Silicon Realized. *Nano Lett.* **15**, 5855–5860 (2015). doi:10.1021/acs.nanolett.5b01939.

[108] Fadaly, E. M. T. *et al.* Direct-bandgap emission from hexagonal Ge and SiGe alloys. *Nature* **580**, 205–209 (2020). doi:10.1038/s41586-020-2150-y.

[109] Ren, Y., Leubner, P., Verheijen, M. A., Haverkort, J. E. M. & Bakkers, E. P. A. M. Hexagonal silicon grown from higher order silanes. *Nanotechnology* **30**, 295602 (2019). doi:10.1088/1361-6528/ab0d46.

[110] Tang, J. *et al.* Natural occurrence of the diamond hexagonal structure in silicon nanowires grown by a plasma-assisted vapourliquidsolid method. *Nanoscale* **9**, 8113–8118 (2017). doi:10.1039/C7NR01299C.

[111] He, Z., Maurice, J.-L., Li, Q. & Pribat, D. Direct evidence of 2H hexagonal Si in Si nanowires. *Nanoscale* **11**, 4846–4853 (2019). doi:10.1039/C8NR10370D.

[112] Dínek, V., Fajgar, R., Klementová, M. & ubrt, J. Deposition of Germanium Nanowires from Hexamethyldigermane: Influence of the Substrate Pretreatment. *J. Electrochem. Soc.* **157**, K218–K222 (2010). doi:10.1149/1.3476288.

[113] Galvão Tizei, L. H. & Amato, M. Electronic structure and optical properties of semiconductor nanowires polytypes. *Eur. Phys. J. B* **93**, 16 (2020). doi:10.1140/epjb/e2019-100375-7.

[114] Rödl, C. *et al.* Wurtzite silicon as a potential absorber in photovoltaics: Tailoring the optical absorption by applying strain. *Phys. Rev. B* **92**, 045207 (2015). doi:10.1103/PhysRevB.92.045207.

[115] Kaewmaraya, T., Vincent, L. & Amato, M. Accurate Estimation of Band Offsets in Group IV Polytype Junctions: A First-Principles Study. *J. Phys. Chem. C* **121**, 5820–5828 (2017). doi:10.1021/acs.jpcc.6b12782.

[116] Rödl, C. *et al.* Accurate electronic and optical properties of hexagonal germanium for optoelectronic applications. *Phys. Rev. Materials* **3**, 034602 (2019). doi:10.1103/PhysRevMaterials.3.034602.

[117] Diarra, M., Niquet, Y.-M., Delerue, C. & Allan, G. Ionization energy of donor and acceptor impurities in semiconductor nanowires: Importance of dielectric confinement. *Phys. Rev. B* **75**, 045301 (2007). doi:10.1103/PhysRevB.75.045301.

[118] Björk, M. T., Schmid, H., Knoch, J., Riel, H. & Riess, W. Donor deactivation in silicon nanostructures. *Nature Nanotech* **4**, 103–107 (2009). doi:10.1038/nnano.2008.400.

[119] Yan, J.-A., Yang, L. & Chou, M. Y. Size and orientation dependence in the electronic properties of silicon nanowires. *Phys. Rev. B* **76**, 115319 (2007). doi:10.1103/PhysRevB.76.115319.

[120] Amato, M., Kaewmaraya, T., Zobelli, A., Palummo, M. & Rurali, R. Crystal Phase Effects in Si Nanowire Polytypes and Their Homojunctions. *Nano Lett.* **16**, 5694–5700 (2016). doi:10.1021/acs.nanolett.6b02362.

[121] Ma, D. D. D., Lee, C. S., Au, F. C. K., Tong, S. Y. & Lee, S. T. Small-Diameter Silicon Nanowire Surfaces. *Science* **299**, 1874–1877 (2003). doi:10.1126/science.1080313.

[122] Shockley, W. & Queisser, H. J. Detailed Balance Limit of Efficiency of pn Junction Solar Cells. *Journal of Applied Physics* **32**, 510–519 (1961). doi:10.1063/1.1736034.

[123] Dixit, S. & Shukla, A. K. Optical properties of lonsdaleite silicon nanowires: A promising material for optoelectronic applications. *Journal of Applied Physics* **123**, 224301 (2018). doi:10.1063/1.5025856.

[124] Fabbri, F., Rotunno, E., Lazzarini, L., Fukata, N. & Salviati, G. Visible and Infra-red Light Emission in Boron-Doped Wurtzite Silicon Nanowires. *Scientific Reports* **4**, 3603 (2014). doi:10.1038/srep03603.

[125] Mamur, H., Bhuiyan, M. R. A., Korkmaz, F. & Nil, M. A review on bismuth telluride (Bi2Te3) nanostructure for thermoelectric applications. *Renewable and Sustainable Energy Reviews* **82**, 4159–4169 (2018). doi:10.1016/j.rser.2017.10.112.

[126] Nozariasbmarz, A. *et al.* Thermoelectric silicides: A review. *Jpn. J. Appl. Phys.* **56**, 05DA04 (2017). doi:10.7567/JJAP.56.05DA04.

[127] Weber, L. & Gmelin, E. Transport properties of silicon. *Appl. Phys. A* **53**, 136–140 (1991). doi:10.1007/BF00323873.

[128] Walkauskas, S. G., Broido, D. A., Kempa, K. & Reinecke, T. L. Lattice thermal conductivity of wires. *Journal of Applied Physics* **85**, 2579–2582 (1999). doi:10.1063/1.369576.

[129] Khitun, A., Balandin, A., Wang, K. L. & Chen, G. Enhancement of the thermoelectric figure of merit of Si1xGex quantum wires due to spatial confinement of acoustic phonons. *Physica E: Low-dimensional Systems and Nanostructures* **8**, 13–18 (2000). doi:10.1016/S1386-9477(00)00119-3.

[130] Hochbaum, A. I. *et al.* Enhanced thermoelectric performance of rough silicon nanowires. *Nature* **451**, 163–167 (2008). doi:10.1038/nature06381.

[131] Lee, S.-M., Cahill, D. G. & Venkatasubramanian, R. Thermal conductivity of SiGe superlattices. *Appl. Phys. Lett.* **70**, 2957–2959 (1997). doi:10.1063/1.118755.

[132] Larroque, J., Dollfus, P. & Saint-Martin, J. Phonon transmission at Si/Ge and polytypic Ge interfaces using full-band mismatch based models. *Journal of Applied Physics* **123**, 025702 (2018). doi:10.1063/1.5007034.

[133] Raya-Moreno, M., Aramberri, H., Seijas-Bellido, J. A., Cartoixà, X. & Rurali, R. Thermal conductivity of hexagonal Si and hexagonal Si nanowires from first-principles. *Appl. Phys. Lett.* **111**, 032107 (2017). doi:10.1063/1.4985278.

[134] Amor, A. B. *et al.* Si and Ge allotrope heterostructured nanowires: experimental evaluation of the thermal conductivity reduction. *Nanotechnology* **30**, 375704 (2019). doi:10.1088/1361-6528/ab29a6.

[135] Raffy, C., Furthmüller, J. & Bechstedt, F. Properties of hexagonal polytypes of group-IV elements from first-principles calculations. *Phys. Rev. B* **66**, 075201 (2002). doi:10.1103/PhysRevB.66.075201.

[136] Kagimura, R., Nunes, R. W. & Chacham, H. Structures of Si and Ge Nanowires in the Subnanometer Range. *Phys. Rev. Lett.* **95**, 115502 (2005). doi:10.1103/PhysRevLett.95.115502.

[137] Garcia-Castello, N., Prades, J. D., Orlando, R. & Cirera, A. Stability Model of Silicon Nanowire Polymorphs and First-Principle Conductivity of Bulk Silicon. *J. Phys. Chem. C* **116**, 22078–22085 (2012). doi:10.1021/jp307449y.

[138] Puglisi, R. A. *et al.* Chemical Vapor Deposition Growth of Silicon Nanowires with Diameter Smaller Than 5 nm. *ACS Omega* (2019). doi:10.1021/acsomega.9b01488.

[139] Oehler, F. *et al.* The Importance of the Radial Growth in the Faceting of Silicon Nanowires. *Nano Lett.* **10**, 2335–2341 (2010). doi:10.1021/nl904081g.

[140] Béjaud, R. & Hardouin Duparc, O. Stabilizing the hexagonal diamond metastable phase in silicon nanowires. *Computational Materials Science* **188**, 110180 (2021). doi:10.1016/j.commatsci.2020.110180.

[141] Kashchiev, D. *Nucleation: basic theory with applications* (Oxford, Royaume-Uni de Grande-Bretagne et d'Irlande du Nord, 2000).

[142] Dubrovskii, V. G., Sibirev, N. V., Harmand, J. C. & Glas, F. Growth kinetics and crystal structure of semiconductor nanowires. *Phys. Rev. B* **78**, 235301 (2008). doi:10.1103/PhysRevB.78.235301.

[143] Dubrovskii, V. G. *et al.* Gibbs-Thomson and diffusion-induced contributions to the growth rate of Si, InP, and GaAs nanowires. *Phys. Rev. B* **79**, 205316 (2009). doi:10.1103/PhysRevB.79.205316.

[144] Yeh, C.-Y., Lu, Z. W., Froyen, S. & Zunger, A. Zinc-blende–wurtzite polytypism in semiconductors. *Phys. Rev. B* **46**, 10086–10097 (1992). doi:10.1103/PhysRevB.46.10086.

[145] Soshnikov, I. P. *et al.* Atomic structure of MBE-grown GaAs nanowhiskers. *Phys. Solid State* **47**, 2213–2218 (2005). doi:10.1134/1.2142881.

[146] Koguchi, M., Kakibayashi, H., Yazawa, M., Hiruma, K. & Katsuyama, T. Crystal Structure Change of GaAs and InAs Whiskers from Zinc-Blende to Wurtzite Type. *Jpn. J. Appl. Phys.* **31**, 2061 (1992). doi:10.1143/JJAP.31.2061.

[147] Patriarche, G. *et al.* Wurtzite to Zinc Blende Phase Transition in GaAs Nanowires Induced by Epitaxial Burying. *Nano Lett.* **8**, 1638–1643 (2008). doi:10.1021/nl080319y.

[148] Krogstrup, P. *et al.* Structural Phase Control in Self-Catalyzed Growth of GaAs Nanowires on Silicon (111). *Nano Lett.* **10**, 4475–4482 (2010). doi:10.1021/nl102308k.

[149] Lehmann, S., Jacobsson, D., Deppert, K. & Dick, K. A. High crystal quality wurtzite-zinc blende heterostructures in metal-organic vapor phase epitaxy-grown GaAs nanowires. *Nano Res.* **5**, 470–476 (2012). doi:10.1007/s12274-012-0232-3.

[150] Lehmann, S., Jacobsson, D. & Dick, K. A. Crystal phase control in GaAs nanowires: opposing trends in the Ga- and As-limited growth regimes. *Nanotechnology* **26**, 301001 (2015). doi:10.1088/0957-4484/26/30/301001.

[151] Jacobsson, D. *et al.* Interface dynamics and crystal phase switching in GaAs nanowires. *Nature* **531**, 317–322 (2016). doi:10.1038/nature17148.

[152] Panciera, F. *et al.* Phase Selection in Self-catalyzed GaAs Nanowires. *Nano Lett.* (2020). doi:10.1021/acs.nanolett.9b04808.

[153] Glas, F., Harmand, J.-C. & Patriarche, G. Why Does Wurtzite Form in Nanowires of III-V Zinc Blende Semiconductors? *Phys. Rev. Lett.* **99**, 146101 (2007). doi:10.1103/PhysRevLett.99.146101.

[154] Dubrovskii, V. G. Development of Growth Theory for VaporLiquidSolid Nanowires: Contact Angle, Truncated Facets, and Crystal Phase. *Crystal Growth & Design* **17**, 2544–2548 (2017). doi:10.1021/acs.cgd.7b00076.

[155] Ando, T. High-speed atomic force microscopy. *Microscopy* **62**, 81–93 (2013). doi:10.1093/jmicro/dfs093.

[156] Gai, P. L. & Kourtakis, K. Solid-State Defect Mechanism in Vanadyl Pyrophosphate Catalysts: Implications for Selective Oxidation. *Science* **267**, 661–663 (1995). doi:10.1126/science.267.5198.661.

[157] Boyes, E. D. & Gai, P. L. Environmental high resolution electron microscopy and applications to chemical science. *Ultramicroscopy* **67**, 219–232 (1997). doi:10.1016/S0304-3991(96)00099-X.

[158] Taheri, M. L. *et al.* Current status and future directions for in situ transmission electron microscopy. *Ultramicroscopy* **170**, 86–95 (2016). doi:10.1016/j.ultramic.2016.08.007.

[159] Xu, C. *et al.* In situ transmission electron microscope studies on one-dimensional nanomaterials: Manipulation, properties and applications. *Progress in Materials Science* **113**, 100674 (2020). doi:10.1016/j.pmatsci.2020.100674.

[160] Sterling, H. F. & Swann, R. C. G. Chemical vapour deposition promoted by r.f. discharge. *Solid-State Electronics* **8**, 653–654 (1965). doi:10.1016/0038-1101(65)90033-X.

[161] Hogness, T. R., Wilson, T. L. & Johnson, W. C. The Thermal Decomposition of Silane. *J. Am. Chem. Soc.* **58**, 108–112 (1936). doi:10.1021/ja01292a036.

[162] Schmitz, J. Low temperature thin films for next-generation microelectronics (invited). *Surface and Coatings Technology* **343**, 83–88 (2018). doi:10.1016/j.surfcoat.2017.11.013.

[163] Droes, S. R., Kodas, T. T. & Hampden-Smith, M. J. Plasma-Enhanced Chemical Vapor Deposition (PECVD). In Weimer, A. W. (ed.) *Carbide, Nitride and Boride Materials Synthesis and Processing*, 579–603 (Springer Netherlands, Dordrecht, 1997).

[164] Kim, B. & Kim, S. Room-temperature high radio-frequency source power effects on silicon nitride films deposited by using a plasma-enhanced chemical vapor deposition. *Met. Mater. Int.* **14**, 637 (2008). doi:10.3365/met.mat.2008.10.637.

[165] Minea, T. M., Point, S., Granier, A. & Touzeau, M. Room temperature synthesis of carbon nanofibers containing nitrogen by plasma-enhanced chemical vapor deposition. *Appl. Phys. Lett.* **85**, 1244–1246 (2004). doi:10.1063/1.1781352.

[166] Lee, J. H., Kim, D. S. & Lee, Y. H. Room Temperature Deposition of Silicon Dioxide Films by IonAssisted Plasma Enhanced Chemical Vapor Deposition. *J. Electrochem. Soc.* **143**, 1443 (1996). doi:10.1149/1.1836657.

[167] Heitz, T., Drévillon, B. & Godet, C. Improvement of sensitivity in the analysis of vibrational properties of thin films by use of in situ ellipsometry: applications to hydrogenated amorphous carbon films. *J. Opt. Soc. Am. B, JOSAB* **16**, 1044–1048 (1999). doi:10.1364/JOSAB.16.001044.

[168] Fetisov, G. V. X-ray diffraction methods for structural diagnostics of materials: progress and achievements. *Phys.-Usp.* **63**, 2 (2020). doi:10.3367/UFNe.2018.10.038435.

[169] Williams, D. B. & Carter, C. B. *Transmission Electron Microscopy: A Textbook for Materials Science* (Springer US, 2009), 2 edn.

[170] Buseck, P., Cowley, J. & Leroy, E. *High-Resolution Transmission Electron Microscopy and Associated Techniques* (Oxford University Press, Inc., New York, 1988), oxford edn.

[171] Zaefferer, S. & Elhami, N.-N. Theory and application of electron channelling contrast imaging under controlled diffraction conditions. *Acta Materialia* **75**, 20–50 (2014). doi:10.1016/j.actamat.2014.04.018.

[172] Schwartz, A. J., Kumar, M., Adams, B. L. & Field, D. P. (eds.) *Electron Backscatter Diffraction in Materials Science* (Springer US, 2009), 2 edn.

[173] Hetherington, C. Aberration correction for TEM. *Materials Today* **7**, 50–55 (2004). doi:10.1016/S1369-7021(04)00571-1.

[174] Freitag, B., Kujawa, S., Mul, P. M., Ringnalda, J. & Tiemeijer, P. C. Breaking the spherical and chromatic aberration barrier in transmission electron microscopy. *Ultramicroscopy* **102**, 209–214 (2005). doi:10.1016/j.ultramic.2004.09.013.

[175] Slater, T. J. A. *et al.* STEM-EDX tomography of bimetallic nanoparticles: A methodological investigation. *Ultramicroscopy* **162**, 61–73 (2016). doi:10.1016/j.ultramic.2015.10.007.

[176] McRae, E. G. Electron diffraction at crystal surfaces: II. The double-diffraction picture. *Surface Science* **11**, 492–507 (1968). doi:10.1016/0039-6028(68)90059-9.

[177] Cowley, J. M. & Moodie, A. F. The scattering of electrons by atoms and crystals. I. A new theoretical approach. *Acta Crystallographica* **10**, 609–619 (1957). doi:10.1107/S0365110X57002194.

[178] Goodman, P. & Moodie, A. F. Numerical evaluations of N-beam wave functions in electron scattering by the multi-slice method. *Acta Crystallographica Section A* **30**, 280–290 (1974). doi:10.1107/S056773947400057X.

[179] Stadelmann, P. A. EMS - a software package for electron diffraction analysis and HREM image simulation in materials science. *Ultramicroscopy* **21**, 131–145 (1987). doi:10.1016/0304-3991(87)90080-5.

[180] Cartier, E., Stathis, J. H. & Buchanan, D. A. Passivation and depassivation of silicon dangling bonds at the Si/SiO2 interface by atomic hydrogen. *Appl. Phys. Lett.* **63**, 1510–1512 (1993). doi:10.1063/1.110758.

[181] Weber, J. R., Janotti, A., Rinke, P. & Van de Walle, C. G. Dangling-bond defects and hydrogen passivation in germanium. *Appl. Phys. Lett.* **91**, 142101 (2007). doi:10.1063/1.2793184.

[182] Hitz, D. Recent Progress in High Frequency Electron Cyclotron Resonance Ion Sources. In Hawkes, P. W. (ed.) *Advances in Imaging and Electron Physics*, vol. 144, 1–164 (Elsevier, 2006).

[183] Drentje, A. G. Techniques and mechanisms applied in electron cyclotron resonance sources for highly charged ions. *Review of Scientific Instruments* **74**, 2631–2645 (2003). doi:10.1063/1.1569408.

[184] Egerton, R. F., Li, P. & Malac, M. Radiation damage in the TEM and SEM. *Micron* **35**, 399–409 (2004). doi:10.1016/j.micron.2004.02.003.

[185] Egerton, R. F., McLeod, R., Wang, F. & Malac, M. Basic questions related to electron-induced sputtering in the TEM. *Ultramicroscopy* **110**, 991–997 (2010). doi:10.1016/j.ultramic.2009.11.003.

[186] Konobeyev, A. Y., Fischer, U., Korovin, Y. A. & Simakov, S. P. Evaluation of effective threshold displacement energies and other data required for the calculation of advanced atomic displacement cross-sections. *Nuclear Energy and Technology* **3**, 169–175 (2017). doi:10.1016/j.nucet.2017.08.007.

[187] Kim, Y.-K. & Rudd, M. E. Binary-encounter-dipole model for electron-impact ionization. *Phys. Rev. A* **50**, 3954–3967 (1994). doi:10.1103/PhysRevA.50.3954.

[188] Ali, M. A., Kim, Y.-K., Hwang, W., Weinberger, N. M. & Rudd, M. E. Electron-impact total ionization cross sections of silicon and germanium hydrides. *J. Chem. Phys.* **106**, 9602–9608 (1997). doi:10.1063/1.473842.

[189] Hwang, W., Kim, Y. & Rudd, M. E. New model for electronimpact ionization cross sections of molecules. *J. Chem. Phys.* **104**, 2956–2966 (1996). doi:10.1063/1.471116.

[190] Wilson, G. & Dennison, J. R. Approximation of Range in Materials as a Function of Incident Electron Energy. *IEEE Transactions on Plasma Science* **40**, 291–297 (2012). doi:10.1109/TPS.2011.2176515.

[191] Sikora, T. & Serin, V. The EELS spectrum database. In Luysberg, M., Tillmann, K. & Weirich, T. (eds.) *EMC 2008 14th European Microscopy Congress 15 September 2008, Aachen, Germany*, 439–440 (Springer, Berlin, Heidelberg, 2008).

[192] Schmid, G. & Corain, B. Nanoparticulated Gold: Syntheses, Structures, Electronics, and Reactivities. *European Journal of Inorganic Chemistry* **2003**, 3081–3098 (2003). doi:10.1002/ejic.200300187.

[193] Kallesøe, C., Wen, C.-Y., Mølhave, K., Bøggild, P. & Ross, F. M. Measurement of Local Si-Nanowire Growth Kinetics Using In situ Transmission Electron Microscopy of Heated Cantilevers. *Small* **6**, 2058–2064 (2010). doi:https://doi.org/10.1002/smll.200902187.

[194] Gamalski, A. D., Ducati, C. & Hofmann, S. Cyclic Supersaturation and Triple Phase Boundary Dynamics in Germanium Nanowire Growth. *J. Phys. Chem. C* **115**, 4413–4417 (2011). doi:10.1021/jp1095882.

[195] Dau, M. T. *et al.* Growth of germanium nanowires on silicon(111) substrates by molecular beam epitaxy. *J Nanosci Nanotechnol* **11**, 9292–9295 (2011). doi:10.1166/jnn.2011.4288.

[196] Searcy, A. W. The Vapor Pressure of Germanium. Tech. Rep. UCRL-1403, Radiation Laboratory, University of California, Berkeley, California (1951).

[197] Wen, C.-Y., Tersoff, J., Reuter, M. C., Stach, E. A. & Ross, F. M. Step-Flow Kinetics in Nanowire Growth. *Phys. Rev. Lett.* **105**, 195502 (2010). doi:10.1103/PhysRevLett.105.195502.

[198] Gamalski, A. D., Tersoff, J. & Stach, E. A. Atomic Resolution in Situ Imaging of a Double-Bilayer Multistep Growth Mode in Gallium Nitride Nanowires. *Nano Lett.* **16**, 2283–2288 (2016). doi:10.1021/acs.nanolett.5b04650.

[199] Harmand, J.-C. *et al.* Atomic Step Flow on a Nanofacet. *Phys. Rev. Lett.* **121**, 166101 (2018). doi:10.1103/PhysRevLett.121.166101.

[200] Tran, R. *et al.* Surface energies of elemental crystals. *Scientific Data* **3**, 160080 (2016). doi:10.1038/sdata.2016.80.

[201] Schwarz, K. W., Tersoff, J., Kodambaka, S., Chou, Y.-C. & Ross, F. M. Geometrical Frustration in Nanowire Growth. *Phys. Rev. Lett.* **107**, 265502 (2011). doi:10.1103/PhysRevLett.107.265502.

[202] Gamalski, A. D., Tersoff, J., Sharma, R., Ducati, C. & Hofmann, S. Metastable Crystalline AuGe Catalysts Formed During Isothermal Germanium Nanowire Growth. *Phys. Rev. Lett.* **108**, 255702 (2012). doi:10.1103/PhysRevLett.108.255702.

[203] Gamalski, A. D., Tersoff, J., Sharma, R., Ducati, C. & Hofmann, S. Formation of Metastable Liquid Catalyst during Subeutectic Growth of Germanium Nanowires. *Nano Lett.* **10**, 2972–2976 (2010). doi:10.1021/nl101349e.

[204] Zhang, S. B. & Wei, S.-H. Surface Energy and the Common Dangling Bond Rule for Semiconductors. *Phys. Rev. Lett.* **92**, 086102 (2004). doi:10.1103/PhysRevLett.92.086102.

[205] Sivaram, S. V., Hui, H. Y., de la Mata, M., Arbiol, J. & Filler, M. A. Surface Hydrogen Enables Subeutectic VaporLiquidSolid Semiconductor Nanowire Growth. *Nano Lett.* **16**, 6717–6723 (2016). doi:10.1021/acs.nanolett.6b01640.

[206] Gamalski, A. D. *et al.* The Role of Surface Passivation in Controlling Ge Nanowire Faceting. *Nano Lett.* **15**, 8211–8216 (2015). doi:10.1021/acs.nanolett.5b03722.

[207] Sivaram, S. V., Shin, N., Chou, L.-W. & Filler, M. A. Direct Observation of Transient Surface Species during Ge Nanowire Growth and Their Influence on Growth Stability. *J. Am. Chem. Soc.* **137**, 9861–9869 (2015). doi:10.1021/jacs.5b03818.

[208] Stekolnikov, A. A., Furthmüller, J. & Bechstedt, F. Absolute surface energies of group-IV semiconductors: Dependence on orientation and reconstruction. *Phys. Rev. B* **65**, 115318 (2002). doi:10.1103/PhysRevB.65.115318.

[209] Kolíbal, M., Kalousek, R., Vystavl, T., Novák, L. & ikola, T. Controlled faceting in 110 germanium nanowire growth by switching between vapor-liquid-solid and vapor-solid-solid growth. *Appl. Phys. Lett.* **100**, 203102 (2012). doi:10.1063/1.4714765.

[210] den Hertog, M. I. *et al.* Control of Gold Surface Diffusion on Si Nanowires. *Nano Lett.* **8**, 1544–1550 (2008). doi:10.1021/nl073356i.

[211] Dailey, E., Madras, P. & Drucker, J. Au on vapor-liquid-solid grown Si nanowires: Spreading of liquid AuSi from the catalytic seed. *Journal of Applied Physics* **108**, 064320 (2010). doi:10.1063/1.3487971.

[212] Madras, P., Dailey, E. & Drucker, J. Spreading of Liquid AuSi on VaporLiquidSolid-Grown Si Nanowires. *Nano Lett.* **10**, 1759–1763 (2010). doi:10.1021/nl100249j.

[213] Chen, W. *et al.* Atomic characterization of Au clusters in vapor-liquid-solid grown silicon nanowires. *Journal of Applied Physics* **118**, 104301 (2015). doi:10.1063/1.4930143.

[214] Boukhicha, R. *et al.* Gold anchoring on Si sawtooth faceted nanowires. *EPL* **95**, 18004 (2011). doi:10.1209/0295-5075/95/18004.

[215] Kolmakov, A., Chen, X. & Moskovits, M. Functionalizing Nanowires with Catalytic Nanoparticles for Gas Sensing Application. *Journal of Nanoscience and Nanotechnology* **8**, 111–121 (2008). doi:10.1166/jnn.2008.N10.

[216] Gai, Z., Yu, H. & Yang, W. S. Adatom diffusion on Ge(111) and the corresponding activation energy barrier. *Phys. Rev. B* **53**, 13547–13550 (1996). doi:10.1103/PhysRevB.53.13547.

[217] Dubrovskii, V. G. *et al.* Diffusion-induced growth of GaAs nanowhiskers during molecular beam epitaxy: Theory and experiment. *Phys. Rev. B* **71**, 205325 (2005). doi:10.1103/PhysRevB.71.205325.

[218] Wen, C.-Y. *et al.* Periodically Changing Morphology of the Growth Interface in Si, Ge, and GaP Nanowires. *Phys. Rev. Lett.* **107**, 025503 (2011). doi:10.1103/PhysRevLett.107.025503.

[219] Ross, F. M., Tersoff, J. & Reuter, M. C. Sawtooth Faceting in Silicon Nanowires. *Phys. Rev. Lett.* **95**, 146104 (2005). doi:10.1103/PhysRevLett.95.146104.

[220] Vincent, L. *et al.* Faceting mechanisms of Si nanowires and gold spreading. *J Mater Sci* **47**, 1609–1613 (2012). doi:10.1007/s10853-011-5939-0.

[221] Gentile, P. *et al.* The growth of small diameter silicon nanowires to nanotrees. *Nanotechnology* **19**, 125608 (2008). doi:10.1088/0957-4484/19/12/125608.

[222] Madras, P., Dailey, E. & Drucker, J. Kinetically Induced Kinking of VaporLiquidSolid Grown Epitaxial Si Nanowires. *Nano Lett.* **9**, 3826–3830 (2009). doi:10.1021/nl902013g.

[223] Kodambaka, S., Tersoff, J., Reuter, M. C. & Ross, F. M. Diameter-Independent Kinetics in the Vapor-Liquid-Solid Growth of Si Nanowires. *Phys. Rev. Lett.* **96**, 096105 (2006). doi:10.1103/PhysRevLett.96.096105.

[224] Bootsma, G. A. & Gassen, H. J. A quantitative study on the growth of silicon whiskers from silane and germanium whiskers from germane. *Journal of Crystal Growth* **10**, 223–234 (1971). doi:10.1016/0022-0248(71)90188-6.

[225] Alchagirov, B. B. & Chochaeva, A. M. Temperature dependence of the density of liquid tin. *High Temp* **38**, 44–48 (2000). doi:10.1007/BF02755565.

[226] Yu, L., Fortuna, F., ODonnell, B., Patriache, G. & Roca i Cabarrocas, P. Stability and evolution of low-surface-tension metal catalyzed growth of silicon nanowires. *Appl. Phys. Lett.* **98**, 123113 (2011). doi:10.1063/1.3569817.

[227] Arbiol, J., Kalache, B., Roca i Cabarrocas, P., Morante, J. R. & Morral, A. F. i. Influence of Cu as a catalyst on the properties of silicon nanowires synthesized by the vapoursolidsolid mechanism. *Nanotechnology* **18**, 305606 (2007). doi:10.1088/0957-4484/18/30/305606.

[228] Renard, V. T. *et al.* Catalyst preparation for CMOS-compatible silicon nanowire synthesis. *Nature Nanotech* **4**, 654–657 (2009). doi:10.1038/nnano.2009.234.

[229] David, T., Buttard, D., Schülli, T., Dallhuin, F. & Gentile, P. Structural investigation of silicon nanowires using GIXD and GISAXS: Evidence of complex saw-tooth faceting. *Surface Science* **602**, 2675–2680 (2008). doi:10.1016/j.susc.2008.06.022.

[230] Wang, Z. W. & Li, Z. Y. Structures and Energetics of Indium-Catalyzed Silicon Nanowires. *Nano Lett.* **9**, 1467–1471 (2009). doi:10.1021/nl803345u.

[231] Arbiol, J. *et al.* Influence of the (111) twinning on the formation of diamond cubic/diamond hexagonal heterostructures in Cu-catalyzed Si nanowires. *Journal of Applied Physics* **104**, 064312 (2008). doi:10.1063/1.2976338.

[232] Alcock, C. B., Itkin, V. P. & Horrigan, M. K. Vapour Pressure Equations for the Metallic Elements: 2982500K. *Canadian Metallurgical Quarterly* **23**, 309–313 (1984). doi:10.1179/cmq.1984.23.3.309.

[233] Akasaka, Y., Horie, K., Nakamura, G., Tsukamoto, K. & Yukimoto, Y. Study of Tin Diffusion into Silicon by Backscattering Analysis. *Jpn. J. Appl. Phys.* **13**, 1533 (1974). doi:10.1143/JJAP.13.1533.

[234] Trumbore, F. A. Solid Solubilities of Impurity Elements in Germanium and Silicon*. *Bell System Technical Journal* **39**, 205–233 (1960). doi:10.1002/j.1538-7305.1960.tb03928.x.

[235] Olesinski, R. W. & Abbaschian, G. J. The CuSi (Copper-Silicon) system. *Bulletin of Alloy Phase Diagrams* **7**, 170–178 (1986). doi:10.1007/BF02881559.

[236] Sufryd, K., Ponweiser, N., Riani, P., Richter, K. W. & Cacciamani, G. Experimental investigation of the CuSi phase diagram at x(Cu)>0.72. *Intermetallics* **19**, 1479–1488 (2011). doi:10.1016/j.intermet.2011.05.017.

[237] Wen, C.-Y. & Spaepen, F. In situ electron microscopy of the phases of Cu3Si. *Philosophical Magazine* **87**, 5581–5599 (2007). doi:10.1080/14786430701675829.

[238] Palatinus, L., Klementová, M., Dínek, V., Jaroová, M. & Petíek, V. An Incommensurately Modulated Structure of -Phase of Cu3+xSi Determined by Quantitative Electron Diffraction Tomography. *Inorg. Chem.* **50**, 3743–3751 (2011). doi:10.1021/ic200102z.

[239] Antunes Correa, C. *et al.* Phase transitions and crystal structures of -Cu(3+x)Si and -Cu(3+x)Si. vol. A73, C1122 (Acta Crystallographica, Hyderabad, India, 2017).

[240] Smaalen, S. v. *Incommensurate Crystallography.* International Union of Crystallography Monographs on Crystallography (Oxford University Press, Oxford, New York, 2007).

[241] Bradby, J. E., Williams, J. S., Wong-Leung, J., Swain, M. V. & Munroe, P. Nanoindentation-induced deformation of Ge. *Appl. Phys. Lett.* **80**, 2651–2653 (2002). doi:10.1063/1.1469660.

[242] Scalise, E. *et al.* Thermodynamic driving force in the formation of hexagonal-diamond Si and Ge nanowires. *arXiv:2009.13630 [cond-mat, physics:physics]* (2020).

[243] Morral, A. F. i., Arbiol, J., Prades, J. D., Cirera, A. & Morante, J. R. Synthesis of Silicon Nanowires with Wurtzite Crystalline Structure by Using Standard Chemical Vapor Deposition. *Advanced Materials* **19**, 1347–1351 (2007). doi:10.1002/adma.200602318.

[244] Kail, F. *Etude in-situ par ellipsométrie et spectrométrie de masse du transport de l'hydrogène dans a-Si:H : Cinétique de diffusion et modifications de structure.* These de doctorat, Reims (2005).

[245] Schwarz, K. W. & Tersoff, J. From Droplets to Nanowires: Dynamics of Vapor-Liquid-Solid Growth. *Phys. Rev. Lett.* **102**, 206101 (2009). doi:10.1103/PhysRevLett.102.206101.

[246] Davidson, F. M., Lee, D. C., Fanfair, D. D. & Korgel, B. A. Lamellar Twinning in Semiconductor Nanowires. *J. Phys. Chem. C* **111**, 2929–2935 (2007). doi:10.1021/jp0672205.

[247] Takeuchi, S. & Suzuki, K. Stacking Fault Energies of Tetrahedrally Coordinated Crystals. *physica status solidi (a)* **171**, 99–103 (1999). doi:https://doi.org/10.1002/(SICI)1521-396X(199901)171:1<99::AID-PSSA99>3.0.CO;2-B.

[248] Wang, W. *Plasma-enhanced CVD growth of cubic and hexagonal diamond silicon nanowires with liquid-solid mixed catalysts for photovoltaic applications.* Ph.D. thesis, Institut Polytechnique de Paris (2021).

List of Figures

List of Tables

ECOLE DOCTORALE

Titre : Croissance *in situ* de nanofils de silicium et germanium dans la phase métastable hexagonale-diamant

Mots clés : croissance, nanofils de silicium/germanium, microscopie électronique,

Résumé : Ce travail a trait à l'identification et la compréhension des mécanismes de formation de la phase cristalline métastable hexagonale-diamant (polytype 2H) dans des nanofils de silicium ou germanium. D'après les simulations numériques, cette phase présente des propriétés électroniques et optiques spécifiques et intéressantes. Notre principal outil d'investigation a été NanoMAX, un microscope électronique en transmission modifié, équipé de sources atomiques et d'un générateur de radicaux, permettant l'observation *in situ*, à l'échelle atomique et en temps réel, de la synthèse de cette phase.
Pour faire croître les nanofils de silicium et de germanium, nous avons utilisé la méthode de croissance dite "VLS" (vapeur-liquide-solide) où le nanofil précipite à partir d'atomes de silicium ou de germanium en solution dans une nanoparticule formant un eutectique liquide avec l'élément à déposer. Les atomes étaient apportés par le craquage de molécules gazeuses et également, dans le cas du germanium, depuis une source à effusion.
Nous montrons que la phase hexagonale-diamant est principalement présente dans les nanofils de silicium dont la croissance a été catalysée par une particule de cuivre-étain. Des nanofils de petit diamètre facilitent la formation de cette phase, ce qui est cohérent avec les prédictions des simulations *ab initio*. En considérant uniquement les nanofils de diamètre inférieur à 8 nm, le ratio de nanofils présentant cette phase est de 20 %. Aux températures de croissance et en présence de silane, il se passe une ségrégation spatiale du cuivre et de l'étain dans les catalyseurs. Une interface entre de l'étain liquide et un siliciure de cuivre solide se créée alors. Cette interface semble faciliter la formation de la phase métastable hexagonale-diamant.

Title : *In situ* growth of silicon and germanium nanowires in the metastable hexagonal-diamond phase

Keywords : growth, silicon/germanium nanowires, electron microscopy,

Abstract : The topic of this work is the identification and the understanding of the formation mechanisms of the metastable hexagonal-diamond crystalline phase (2H polytype) in silicon and germanium nanowires. Following numerical simulations, that phase presents specific and interesting electronic and optical properties. Our main investigation tool has been NanoMAX, an advanced transmission electron microscope equipped with atomic sources and a radical generator, allowing the *in situ* observation, at the atomic scale and in real time, of the synthesis of this phase.
To grow silicon and germanium nanowires, we used the so-called "VLS" (vapor-liquid-solid) method, where the nanowire precipitates from Si or Ge atoms in solution in a liquid catalyst eutectic droplet. The atoms were brought to the catalyst by cracked gas molecules or also, in the case of Ge, directly from an effusion source.
We show that the diamond-hexagonal phase is found to form mainly in silicon nanowires with the help of a copper-tin catalyst. A small nanowire diameter is found to stabilize this phase consistently with *ab initio* simulations. The yield of silicon nanowires with a hexagonal-diamond part is 20 % when the diameter is below 8 nm. At the growth temperature and in the presence of silane, there is a spatial segregation of copper and tin in the catalysts, which leads to the creation of an interface between liquid tin and solid copper silicide. This interface is thought to facilitate the formation of the metastable hexagonal-diamond phase.

Institut Polytechnique de Paris
91120 Palaiseau, France